Journal of Engineering

ISSN 1726-4073

A Scientific Refereed Journal Published by College of Engineering University of Baghdad

April 2014

Number 4

Volume 20

مجلـــة الهندســـــــــة

ISSN 1726-4073

مجلة علمية محكمة تصدرها
كلية الهندسة ـ جامعة بغداد

نيسان

2014

العدد 4

المجلد 20

ENGINEERING

College of Engineering University of Baghdad

List of Contents

English Section: Page

English Section

القسم العربي

JOURNAL OF ENGINEERING

ISSN 1726-4073

College of Engineering | Baghdad University | Baghdad

The Journal of Engineering is a monthly refereed periodical
Correspondence should be addressed to:

THE EDITOR
JOURNAL ENGINEERING

COLLEGE of ENGINEERING
P. O. BOX 47024 JADERIYAH
BAGHDAD - IRAQ

ISSN 1726-4073

مجلة الهندسة

كلية الهندسة جامعة بغداد

مجلة الهندسة: مجلة شهريه محكمة

تعنون كافة المراسلات وطلبات الاشتراك الى:

رئيس التحرير
مجلة الهندسة
كلية الهندسة
صندوق بريد **47024** الجادرية
بغداد - العراق

Heave Behavior of Granular Pile Anchor-Foundation System (GPA-Foundation System) in Expansive Soil

Dr. Ala Nasir Aljorany
Professor
Engineering College
Baghdad University
Email: alajorany@yahoo.com

Dr. Saad Farhan Ibrahim
Assistant Professor
Engineering College
Al-Mustansiriya University
Email: drsaaBarhan@yahoo.com

Dr. Ahmed Ibrahim Al-Adly
Lecturer
Engineering College
Baghdad University
Email: ahmed_aladly81@yahoo.com

ABSTRACT

Granular Pile Anchor (GPA) is one of the innovative foundation techniques, devised for mitigating heave of footing resulting from the expansive soils. This research attempts to study the heave behavior of (GPA-Foundation System) in expansive soil. Laboratory tests have been conducted on an experimental model in addition to a series of numerical modeling and analysis using the finite element package PLAXIS software. The effects of different parameters, such as (GPA) length (L) and diameter (D), footing diameter (B), expansive clay layer thickness (H) and presence of non-expansive clay are studied. The results proved the efficiency of (GPA) in reducing the heave of expansive soil and showed that the heave can be reduced with increasing length and diameter of (GPA). The heave of (GPA-Foundation System) is controlled by three independent variables these are (L/D) ratio, (L/H) ratio and (B/D) ratio. The heave can be reduced by up to (38 %) when (GPA) is embedded in expansive soil layer at (L/H=1) and reduced by about (90 %) when (GPA) is embedded in expansive soil and extended to non-expansive clay (stable zone) at (L/H=2) at the same diameter of (GPA) and footing. An equation (mathematical mode1) was obtained by using the computer package (SPSS 17.0) for statistical analysis based on the results of finite element analysis relating the maximum heave of (GPA-Foundation System) as a function of the above mentioned three independent variables with coefficient of regression of (R^2 = 92.3 %).

Keywords: expansive soil, sand, heave, granular pile anchor (GPA), PLAXIS, foundation, finite element.

سلوك الانتفاخ لمنظومة (اساس - ركيزة رملية مربوطة) في التربة الانتفاخية

أ.د.علاء ناصر الجوراني
استاذ
كلية الهندسة-جامعة بغداد

أ.م.د. سعد فرحان ابراهيم
استاذ مساعد
كلية الهندسة-الجامعة المستنصرية

د.احمد ابراهيم العادلي
مدرس
كلية الهندسة-جامعة بغداد

الخلاصــة

تعتبر الركائز الرملية المربوطة المسماة بـ (GPA) احدى الطرق المبتكرة والحديثة المستخدمة للحد من الرفع او الازاحة العامودية الحاصلة في الاساس والناتجة من الترب الانتفاخية. هذا البحث يهدف الى دراسة مدى استجابة وسلوكية منظومة الاساس الجديدة تحت تأثير الانتفاخ وتعيين كفاءة وقدرة الركائز الرملية المربوطة في تقليل الازاحة العامودية الحاصلة في الاساس. تضمنت الدراسة انجاز عمل مختبري على موديل مختبري مصغر تم ابتكاره لهذا الغرض بالاضافة الى اجراء سلسلة من النمذجة والتحليلات بأستخدام نظرية العناصر المحددة بأستخدام برنامج البلاكسس (PLAXIS) تم اعداده لهذا الغرض. تم دراسة عدة متغيرات مثل طول وقطر الركائز الرملية المربوطة, قطر الاساس, سمك طبقة التربة الانتفاخية بالاضافة الى تأثير طبقة التربة الطينية الغير منتفخة. لقد اثبتت النتائج كفاءة وقدرة الركائز الرملية المربوطة في تقليل الازاحة العامودية الحاصلة في الاساس وقد تبين ان الازاحة العامودية للاساس تقل بزيادة طول و قطر الركائز الرملية المربوطة وان هذه الازاحة تتأثر بثلاثة متغيرات رئيسية وهي نسبة الطول المدفون الى القطر للركائز الرملية المربوطة (L/D), نسبة الطول المدفون الى سمك طبقة التربة الانتفاخية (L/H) ونسبة قطر الاساس الى قطر الركيزة الرملية المربوطة (B/D). وقد تبين ان الازاحة العاموية للاساس تقل بنسبة (38%) عندما تدفن الركائز الرملية المربوطة بطول مساوي الى سمك طبقة التربة الانتفاخية وتقل بنسبة تصل الى (90%) عندما تدفن في التربة الانتفاخية وتمتد الى تربة طينية غير انتفاخية بطول مساوي الى

ضعف سمك طبقة التربة الانتفاخية بسبب الحصول على مقدار ازاحة ضئيل للاساس. تم استنباط معادلة احصائية وتكوين موديل رياضي تم الحصول عليه بأستخدام البرنامج الاحصائي المعروف بـ (SPSS 17) بالاعتماد على النتائج المستحصلة من التحليل بأستخدام نظرية العناصر المحددة بحيث يمكن ايجاد اقصى ازاحة عامودية لمنظومة الاساس الجديدة تحت تأثير الانتفاخ بدلالة المتغيرات الثلاثة التي ذكرت سابقا بدرجة عالية مقدارها (92.3%).

1. INTRODUCTION

Many plastic types of clay swell considerably when water is added to them and then shrink with loss of water. Foundations constructed on such clays are subjected to large uplifting forces caused by swelling. These forces induce heaving, cracking, and the breakup of both building foundations and slab-on-grade members **Das, 2011**. Expansive soil is a term applied to any soil that undergo detrimental changes in volume because of variations in moisture content. These soils subject to cycles of wetting-drying and swell when taking up water during wet seasons and shrink because of evaporation of water in dry spells **,Chen, 1988, Nelson** and **Miller, 1992**. Such soils are considered natural hazards that pose challenges to civil engineers, construction firms, and owners. Based on **,Chen, 1988,** the six major natural hazardous are earthquakes, landslides, expansive soils, hurricanes, tornados and floods. Over the last four decades, relentless efforts were made to understand and solve the problems associated with engineering on expansive soils. Several methods can be used to minimize the effect of the damage caused by expansive soils. These include soil replacement, physical and chemical treatment and use of special techniques. The application of these methods will keep intact over a long period of time. Many of them, however, have certain limitations and may be very costly, **Dafalla** and **Shamrani, 2012**. Keeping these shortcomings in view, an attempt to develop a simple, easy to install and cost-effective alternative foundation system, this research presents a simple foundation technique in the name of Granular Pile Anchor (GPA) foundation system as a dependable solution to suppress or tolerate heaving developed by expansive soils.

2. CONCEPT OF (GPA-FOUNDATION SYSTEM)

The granular pile anchor (GPA) is an innovative foundation technique, devised for mitigating heave of expansive clay and improving their engineering behavior. It is a modification of the conventional granular pile, wherein an anchor is provided in the pile to render it tension-resistant. Granular piles are a well-known ground improvement technique used for reducing the settlement and increasing load-carrying capacity of soft clay beds **,Hughes** and **Withers, 1974.** In a granular pile anchor, the foundation is anchored at the bottom of the granular pile to an anchored steel plate with the help of a mild steel road. This renders the granular pile tension-resistant and enables it to offer resistance to the uplift force exerted on the foundation by the swelling soil, **Phanikumar, 1997, Phanikumar et al., 2004, Rao et al., 2007** and **Phanikumar et al., 2008)**. **Fig. 1** shows a typical schematic representation of the fundamental concept of a granular pile anchor (GPA) and the various forces acting on the foundation. The uplift force (P_{Uplift}) acting on the base of the foundation in the vertical direction is due to the swelling pressure (P_s) of the expansive soil. This uplift force is resisted by the weight of the granular pile (W) acting in the downward direction. The friction mobilized along the pile-soil interface also resists the upward movement of the foundation. This friction is generated mainly because of the anchor in the system. The upward resistance is further augmented by the lateral swelling pressure, which confines the granular pile anchor radially, increases the friction along the pile-soil interface, and prevents it from being uplifted, **Phanikumar, 1997, Phanikumar et al., 2004, Rao et al., 2007 and Phanikumar et al., 2008**.

3. OBJECTIVES

Due to limited knowledge currently available in the literature about (GPA), the present study is an attempt aiming at insight understanding to the behavior and performance of (GPA) in expansive soils in reduce the heave. The following aspects are covered:

1- The behavior of (GPA-Foundation System) under heave.

2- The validity and suitability of (GPA) as a dependable solution for problems in expansive soils. Different parameters will be investigated that would be account for in the design of (GPA), such as (GPA) length (L), diameter (D), expansive soil layer thickness (H), shallow footing diameter (B), (L/D) ratio, (L/H) ratio, (B/D) ratio and presence of non-expansive soil.

4. METHODOLOGY

The study is divided into two phases including:

1- Experimental Phase: A cylindrical physical steel model with (30 cm) diameter and (50 cm) height has been built up and planned experimental laboratory testing program has been performed on expansive soil bed prepared from silty clayey soil.

2- Numerical Phase: A numerical model has been used and solved to analyze the described problem in the field. A software finite element program PLAXIS 2D-Version 8.2 packages is used to solve such problem depending on the adopted non-linear elastoplastic models.

5. EXPERMINTAL WORKS

The expansive clay used in this investigation was collected from Al-Wahda Discrete at Al-Mosul governorate in the north of Iraq, from a depth of about (1-1.5) m below the ground level. A series of rotten laboratory tests was carried out on the expansive soil samples to obtain physical, mechanical, and swelling soil properties. **Table 1** shows the properties of expansive soil used. The granular material used for the installation of the granular piles was dense sand with (75 %) relative density. **Table 2** shows the properties of sand used. Heave tests were performed in metal cylindrical container of (0.3 m) diameter and (0.5 m) height. The expansive soil bed is prepared firstly by laying a filter paper covered with thin layer (30 mm) of poorly graded sand, as a drainage layer. All internal sides of container are covered with petroleum jelly to diminish friction effect. After thorough mixing with water, the soil lumps are spread inside the model container at maximum dry unit weight of (16.3 kN/m^3) and optimum moisture content of (21.5 %)which is obtained using standard compaction testin form of eight layers. Each layer have a compacted thickness of (5 cm) and contain (5.76 kg) of soil to give the total depth and weight of expansive soil inside the model container of (40 cm) and (46 kg).The uniformity in the soil bed is checked by measuring the unit weight and moisture content at various depths of the soil bed.

The (GPA) installed in expansive soil bed by made a holein the center of the expansive soil bed surface by driving a steel pipe gradually in specified diameter up to the required depth. The unit of anchor rod with the bottom anchor plate of specified diameter and depth is placed vertically in the hole. Simultaneously, the hole is filled with poorly graded sand gradually and compacted gently using steel tamping rod in required relative density (75 %). Finally, granular pile anchor (GPA) is formed in specified depth and diameter at an average dry unit weight of (16.9 kN/m^3). The (GPA) length was varied as (10, 20, 30, and 40) cm and the diameter as (1, 2, 3, and 4) cm to give a different ratios of (L/D). A circular mild steel plate of (20 cm) diameter was used as the surface shallow footing in the heave tests. A total of (16) test was conducted for studying the heave behaviour of (GPA-Foundation System). **Fig. 2** and **3** show the experimental setup of heave test. The soil bed is wetted gradually by adding the water from the top and continuously pumping water from the base of model container using water pump and controlled valve. Water pump system is used as a vacuum to accelerate the saturation of expansive soil bed by continuously suction the water from model container.The model was left under the saturation and amount of heave is measured and continuously monitored with time until there is no further swelling. At this stage, saturation of soil bed is conformed and the test is completed.

6. RESULTS AND DISCUSSIONS OF EXPERMINTAL WORKS

The results of unreinforced and reinforced expansive soil bed with (GPA) are obtained as shown in **Table 3** and **Fig 4** to **7.** Generally, the heave response appears non-linear behavior and increases continuously with time until reach the equilibrium after (7) days for unreinforced expansive soil bed and (4) days for reinforced expansive soil bed with (GPA). The results showed that the unreinforced expansive soil attained a final heave of (26 mm) and the heave of (GPA-Foundation System) decreases with installation of (GPA) in expansive soil. This may indicate the efficiency of (GPA) in reducing the heave. This in agreement with **,Phanikumar, 1997, Phanikumar et al., 2004, Rao et al., 2007, Phanikumar et al., 2008, Ismail** and **Shahin, 2011 and Krishna et al, 2013**. The results showed that, there are three main variables controlling heave behavior of (GPA-Foundation System) that can be categorized as [(L/D) ratio, (L/H) and (B/D) ratio]. The heave of (GPA-Foundation System) is affected by one or all theses variable, the heave reduction and degree of improvement increases with increasing (L/D) ratio, (L/H) ratio and decreases with increasing (B/D) ratio at a given two variables. The percentage heave reduction and degree of improvement can be expressed as a percentage from the maximum heave without (GPA) by the following equation:

$$\text{Degree of Improvment (\%)} = \left(\frac{\mathrm{H_{vo}} - \mathrm{H'_v}}{\mathrm{H_{vo}}}\right) \times 100 \tag{1}$$

Where:
H_{vo}: is the maximum heave of footing without (GPA) reinforcement.
H'_v: is the maximum heave of footing with (GPA) reinforcement.

It can be noted that, slightly reduction in heave was observed at [(L/D=10), (L/H=0.25) and (B/D=20)] with (7.8 %) degree of improvement, while higher reduction in heave was observed at [(L/D=10), (L/H=1) and (B/D=2.5)] with (38.1 %) degree of improvement. This reflects the ability and efficiency of a single (GPA) in reducing the heave when embedded in an expansive soil and anchored to the shallow footing. This performance agrees with the results obtained from, **Phanikumar, 1997, Phanikumar et al., 2004, Rao et al., 2007, Phanikumar et al., 2008,**and **Krishna et al, 2013**. The results of (GPA-Foundation System) showed that, there is a great effect on the time of heave development. The time period required for attaining the final amount of heave in the case of reinforced expansive soil with (GPA) was (4/7) of that for unreinforced expansive soil. This performance agrees with the results obtained from,**Phanikumar, 1997, Phanikumar et al., 2004** and **Phanikumar et al., 2008.**

7. NUMERICAL MODELLING OF HEAVE OF (GPA-FOUNDATION SYSTEM)

In this study, PLAXIS 2D-Version 8.2 program is used in numerical modelling and analysis of heave problems of (GPA-Foundation System). The problem deals with shallow circular footing rest on the expansive soil layer reinforced with (GPA) models with different length and diameter. For comparison, the circular footing rest on the expansive soil without (GPA) is also modelled here. The purpose of the problems is to calculate the maximum heave under the footing. The expansive soil layer is located above a layer of saturated stable clay with (6 m) thickness. The active zone of the expansive soil is chosen to be (4 m); at this depth, the water table rising causes a considerable swelling in expansive soil. **Fig. 8** shows the sketch of described problem. Axisymmetric type model is chosen, it is the best option for circular models. The soil parts are modelled using 15-node triangular element. The shallow footing and anchor plate are modelled using plate element, while the anchor rod is modelled using node-to-node element. The footing diameter was fixed at (2 m), and the (GPA) length was varied from (2-8) m and diameter was varied from (0.2-0.8) m. So, the ratio of length to diameter was ranged as (2.5 to 40) and the ratio of the footing diameter to (GPA) diameter varied as (2.5 to 10). The thickness of expansive clay layer is fixed at (4 m) and thickness of non-expansive clay layer is fixed at (6 m), so, the ratio of (GPA) length to expansive soil thickness was varied as (0.5-2). The boundary conditions are assumed using standard fixity. This means a full fixity at the base of the geometry and, roller conditions at the vertical sides. **Figs. 9, 10** and **11** show the finite element models of heave problems. The clay of expansive and non-expansive soil layers are modelled using Mohr-Coulomb (MC) model, assumed to behave in an undrained manner. The granular pile sand is modelled using Mohr-Coulomb (MC) also. It is assumed to behave in a drained manner. The rigid steel is used as a material for both anchor plate, anchor rod and shallow footing and assumed as linear elastic model. The flexural rigidity of anchor plate, anchor rod and footing assumed as very high to avoid unnecessary buckling and deformation. All materials and models with set of parameters are listed in **Tables 4** and **5**. The simple global finite element mesh of model is generated using the coarse setting to allow a more accurate stress distribution as shown in **Figs. 12** and **13.** The swelling of expansive soil layer is modelled by applying a positive volumetric strain of (6.5 %) to the expansive clay cluster. In reality, the rate at which expansive clay would normally swell depends on the location from the source of moisture and magnitude of overburden pressure. However, for simplicity, in the analyses presented herein, the volumetric strain was applied uniformly across the full thickness of the expansive soil layer.

8. RESULTS AND DISCUSSIONS OF NUMERICAL MODELING

The numerical results of heave of unreinforced and reinforced expansive clay with (GPA) are obtained as shown in **Table 6**, and **Figs. 14, 15** and **16**. The results reflect the efficiency of (GPA) to reduce the heave (GPA-Foundation System). The maximum heave of footing resting on unreinforced expansive soil with (GPA) is observed as (260 mm). In case of footing resting on reinforced expansive soil with (GPA) models, i.e. (GPA-Foundation System), the results showed that the maximum heave of footing decrease with increasing the (GPA) size, the heave decrease with increasing (GPA) length and diameter due to anchorage action of (GPA) and there are three main variables controlling behavior of (GPA-Foundation System) under the heave. These variables are (L/D) ratio, (B/D) ratio and (L/H) ratio, this performance in agreement with the experimental modeling. The results also showed that, the (GPA) could be extended to the non-expansive soil layer or stable zone at sufficient depth to provide the anchorage zone help the (GPA) to resist the heave. (69%) reduction in heave when single (GPA) embedded in the expansive soil depth layer and (90.4 %) reduction in heave can be obtained when single (GPA) embedded in expansive clay layer and extended into non-expansive clay layer at the same embedded length. The efficiency of the (GPA-Foundation System) in arresting the heave induced by expansive soil layer is illustrated in **Fig. 17**. The figure relates the normalized maximum heave ratio (H_v'/H_{vo}) with (L/D) ratio of (GPA) for different ratios of (B/D), where (H_v') represent the maximum heave of footing with (GPA) reinforcement, while (H_{vo}) represent the maximum heave of footing without (GPA) reinforcement. It can be noted that for a given (B/D) ratio, the maximum heave decrease with increasing (L/D) ratio due to increasing (GPA) length. This means the (GPA) movement strongly dependent on the (GPA) size; the ability of the system to resist various rates of swelling seems to improve with increasing the (GPA) size. As interpreted previously in the experimental works, this attributed to the anchorage action (GPA) that resulting from (GPA) weight and shear stress mobilized along (GPA) body, of them increases when (GPA) size increases. The heave can be reduced from (260 mm to 25 mm) at (L=8 m and D=0.8 m) i.e., (L/D=10) with (90.4 %) reduction in heave. **Fig. 18** displays the relationship between normalized maximum heave ratio (H_v'/H_{vo}) with (L/H) ratio for different (B/D) ratios. It can be seen that for a given (B/D) ratio, the heave decreases when (L/H) increases due to increasing the (GPA) length. Dramatic reducing in heave was observed when (GPA) penetrated in non-expansive clay layer at sufficient length, this means the (GPA) can be penetrate the non-expansive clay layer (stable zone) to provide a sufficient anchorage in the base of (GPA) help it in arresting the heave. This behavior can be attributed to increase the shear resistance in circumference of penetrate length of (GPA). The results showed that, the (GPA) could be extended to non-expansive clay layer with thickness not less than thickness of expansive clay layer thickness to provide a sufficient anchorage at (GPA) base. The heave dropped from (260 mm) to (25 mm) when (L/H=2) at (D=0.8 m and L=8 m) with (90.4 %) reduction in heave, while, the heave reduced to (204 mm) when (L/H=0.5) and to (81 mm) when (L/H=1) at the same size of (GPA) with (21.54 %) and (69 %) reduction in heave respectively. **Fig. 19** shows the relationship between normalized maximum heave ratio (H_v'/H_{vo}) and (B/D) ratio for different ratios of (L/H). The figure presents the effect of the footing diameter (B) on the heave response of (GPA- Foundation System). It can be seen that for a given (L/H) ratio, the maximum heave increases with increasing (B/D) ratio due to increasing footing diameter. The reason of this behavior can be understood as the following: when the footing diameter increases with constant (GPA) diameter, the annular area of the footing on which the swelling pressure acts is increased resulting increases in the heave of the (GPA-Foundation System). Dramatic reduction in heave can be obtained at (B/D=2.5), where the heave reduced from (260 mm to 25 mm) with (90.4 %) reduction in heave.

9. MATHEMATICAL MODELLING OF HEAVE OF (GPA-FOUNDATION SYSTEM)

An attempt is made to develop a mathematical modelling relate the heave of footing resting on reinforced expansive soil with a single (GPA) with three effective variables (L/D), (B/D) and (L/H). The results of finite element analysis are merged and entered in a multiple linear regressions statistical analysis using SPSS Statistics 17.0 to develop a mathematical model that relates the ratio of (H_v'/H_{vo}) as a dependent variable to (L/D), (B/D) and (L/H) as independent variables. A general equation relates all variables were obtained in the following form with very good degree of correlation (R^2=0.923):

$$\mathbf{\frac{H_v'}{H_{vo}} = 0.94 + 0.011\left(\frac{L}{D}\right) + 0.008\left(\frac{B}{D}\right) - 0.5\left(\frac{L}{H}\right)} \quad \mathbf{(2)}$$

Where:
H_{vo}: Maximum heave without (GPA) reinforcement
H_v': Maximum heave of with (GPA) reinforcement
L: Length of (GPA)
D: Diameter of (GPA)
H: Depth of expansive soil layer
B: Diameter of shallow footing

The derived equation is valid within the ranges of the variables they were developed from. The ranges of variables can be seen in **Table 7**. To verify the validity of the equation, the predicted values of heave are compared with observed values obtained previously from laboratory test results as shown in **Table 8)**and **Fig. 20**. It can be seen that, the values agree well with (98 %) degree of correlation and consider under estimation, conforming the validity of derived equation.

10. CONCLUSIONS

An extensive laboratory testing and numerical modeling and analysis was conducted to study the performance of Granular Pile Anchor (GPA) in expansive soil. The research work focuses on studying the efficacy and ability of the innovative (GPA) system in minimizing heave of foundations laid on expansive clay. The conclusions drawn from the different aspects of the study in this paper may be summarized as follows:

1- Installation of (GPA) in expansive soil reduces the amount of heave effectively. Of the various combinations of length (L) and diameter (D) of (GPA), the amount of heave reduces with increasing both length and diameter.

2- The maximum heave of (GPA-Foundation System) is controlled by three main independent variables, (GPA) length to diameter (L/D) ratio, (GPA) length to expansive soil active thickness (L/H) ratio and footing diameter to (GPA) diameter (B/D) ratio.

3- The efficacy of (GPA) in reducing the heave can be improved when (GPA) embedded in expansive soil layer and extend to non-expansive clay layer (stable zone) at sufficient depth. The maximum of about (38 %) reduction in heave is observed when (GPA) embedded in expansive soil layer at (L=H) and reaches to (90.4%) at (L=2H) i.e. (GPA) extend to stable zone at length equal to thickness of expansive soil layer, this performance was observed at (L/D=10) and (B/D=2.5).

4- Reduction in (GPA-Foundation System) can be attributed to the (GPA) weight, the frictional resistance mobilized along the (GPA)-soil face, the effect of anchorage which made the (GPA) to resist the uplift force applied on the foundation. In addition, the developed lateral swelling pressure resulting from surrounding expansive clay which confines the (GPA) radially increases the upward resistance.

5- Installation of (GPA) in expansive soil reduces the time of heave and the rate of heave become faster. The expansive soil reinforced with (GPA) adjusted quickly to moisture changes because of the higher permeability of the granular material. The high permeability characteristics of (GPA) allowed a quick circulation and absorption of water and the path of radial inflow of water became shorter, which led to a rather quick attainment of the final heave.The time period required for attaining the final amount of heave in the case of reinforced expansive soil with (GPA) was (3/7) of that for unreinforced expansive soil.

6- An equation is obtained to calculate the maximum heave of (GPA-Foundation System). The equation is derived basing on statistical analysis of the obtained analysis results.

REFRENCES

-ASTM D4253-2007, *Standard Test Method for Maximum Index Density and Unit Weight of Soils Using a Vibratory Table*.

-ASTM D4254-2007, *Standard Test Method for Minimum Index Density and Unit Weight of Soils and Calculation of Relative Density*.

-ASTM D854-2007, *Standard Test Method for Specific Gravity of Soil Solids by Water Pycnometer*.

-ASTM D422-2007, *Standard Test Method for Liquid Limit, Plastic Limit and Plasticity Index of Soils*.

-ASTM D24884-2007, *Standard Test Method for Classification of Soils for Engineering Purposes (Unified Soil Classification System).*

-ASTM D698-2007, *Standard Test Method for Laboratory Compaction Characteristics of Soil Using Standard Effort.*

-ASTM D3084-2007, *Standard Test Method for Direct Shear Test of Soil Under Consolidated Drained Condition.*

-ASTM D2435-2007, *Standard Test Method for One-Dimensional Consolidation Properties.*

-ASTM D2166-2007, *Standard Test Method for Unconfined Compression Strength of Cohesive Soil.*

-ASTM D4546 (A)-2007, *Standard Test Method for One-Dimensional Swell or Settlement Potential of Cohesive Soils*.

-British Standard BS 1377-1990, *Methods of Test for Soils for Civil Engineering Purposes, London, UK.*

-Chen, F. H. 1988, *Foundations on Expansive Soils, 2nd Edition, Elsevier Scientific Publishing Company.*

-Dafalla, M.A. and Shamrani, M.A. 2012, *Expansive Soil Properties in a Semi-Arid Region*, Research Journal of Environmental and Earth Sciences, Vol. (4), No. (11): 930-938.

-Das, B.M. ,2011, *Principles of Foundation Engineering*, 7th Edition, Cengage Learning, USA.

-Hughes, J.M., and Withers, N.J. ,1974, *Reinforcing of Soft Cohesive Soils with Stone Columns*, Ground Engineering, London, Vol. (17), No. (3): 42-49.

-Ismail, M.A. and Shahin, M.,2011, *Finite Element Analysis of Granular Pile Anchors as A Foundation Option for Reactive Soils*, International Conference on Advances in Geotechnical Engineering, Perth, Australia.

-Krishna, P.H., Murty, V.R. and Vakula, J. ,2013, *A Filed Study on Reduction of Flooring Panels Resting on Expansive Soils Using Granular Anchor Piles and Cushions*, The International Journal of Engineering and Science (IJES), Vol. (2), No. (3): 111-115.

-Nelson, J. D. and Miller, D. J. ,1992, *Expansive Soils: Problem and Practice in Foundation and Pavement Engineering*, John Wiley and Sons, Inc., New York, USA.

-Phanikumar, B.R. 1997, *A Study of Swelling Characteristics of and Granular Pile-Anchor Foundation System in Expansive Soils*, Ph.D Thesis, JNTU, Hyderabad, India.

-Phanikumar, B.R., Sharma R.S., Srirama, R.A and Madhav, M.R. 2004, *Granular Pile-Anchor Foundation (GPAF) system for Improving Engineering Properties of Expansive Clay Beds*, Geotechnical Testing Journal, ASTM, Vol. (27), No. (3): 279-287.

-Phanikumar, B.R., Rao, A.S. and Suresh, K. ,2008, *Field Behavior of Granular Pile Anchors in Expansive Soils*, Ground Improvement Journal, Proceeding of Institution of Civil Engineering (ICE), Vol. (4): 199-206.

-Phanikumar, B.R. and Amrutha, K. ,2011, *Bulging Capacity of Granular Pile-Anchors, Pullout Capacity or Uplift Capacity of Granular Pile-Anchors through Bulging*, VDM Verlag, USA.

-Rao, A.S., Phanikumar, B.R., Babu, R.D. and Suresh, K. ,2007, *Pullout Behavior of Granular Pile Anchors in Expansive Clay Beds In-situ*, Journal of Geotechnical and Geoenvironmental Engineering, ASCE, Vol. (133), No. (5): 531–538, Via Iraqi Virtual Science Library (IVSL), www.IVSL.com.

NOMENCLATURE

ASTM	American society for testing and materials
B	Footing width or diameter
Cc	Compression Index
Cc	Coefficient of curvature
Cs	Swelling index
Cu	Coefficient of uniformity
c	Soil cohesion
CH	Clay with high plasticity
D	Diameter of granular pile anchor
D_r	Relative density of soil
B/D	Ratio of footing diameter to granular pile anchor diameter
E	Modulus of elasticity
e	Void ratio of soil
e_o	Initial void ratio
e_{max}	Maximum void ratio
e_{mim}	Minimum void ratio
Gs	Specific gravity of soil
GPA	Granular pile anchor
H	Expansive soil layer or bed thickness
H_{vo}	Maximum heave of footing without reinforcement with (GPA)
H_v'	Maximum heave of footing with (GPA) reinforcement
L	Length of granular pile anchor
L/D	Ratio of length to diameter of granular pile anchor
L/H	Ratio of length of granular pile anchor to expansive soil layer or bed thickness
L.L	Liquid limit
MC	Mohr-coulomb
O.M.C	Optimum moisture content
PLAXIS	Finite element code for soil and rock
Ps	Swelling pressure
P.L	Plastic limit
P.I	Plasticity index
USCS	Unified soil classification system
W	Granular pile anchor weight
ΔH	Heave or shrinkage
ϕ^o	Angle of internal friction of soil
ψ^o	Dilatancy angle
ν_u	Undrained poison's ratio
γ_{unst}	Unsaturated unit weight
γ_{sat}	Saturated unit weight
γ_{dry}	Dry unit weight

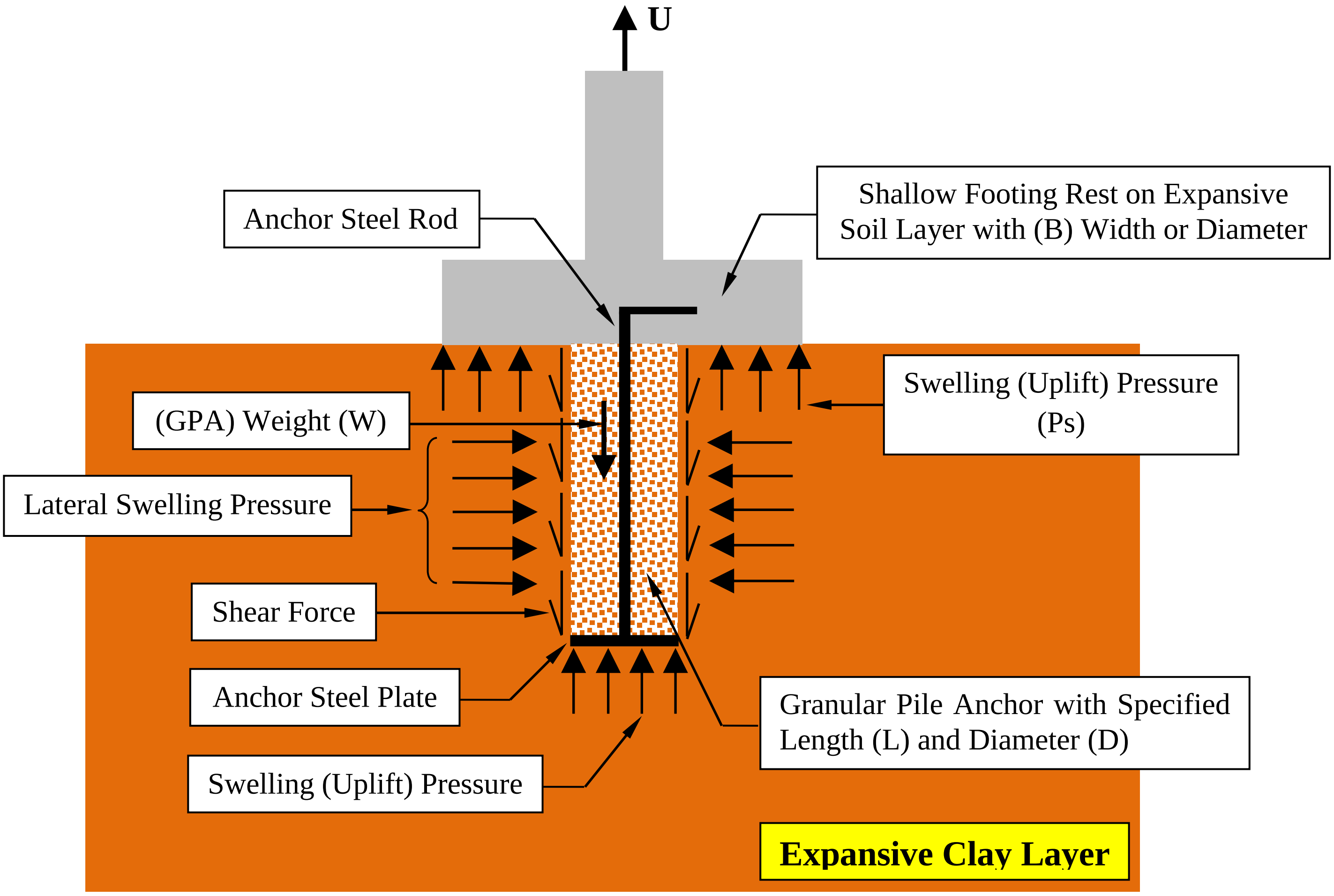

Figure 1. Concept of Granular Pile Anchor foundation system and forces acting on a Granular Pile Anchor (GPA) (After Rao et al., 2007).

Table 1. Summary of physical, mechanical and chemical properties of expansive soil used.

Test Name	Standard	Soil Property	Value
Specific Gravity	(ASTM D-854)	Specific Gravity (Gs)	2.73
Atterberg Limits	(ASTM D-4318)	Liquid Limit (L.L) %	59
		Plastic limit (P.L) %	23
		Plasticity Index (P.I) %	36
Grain Size Analysis Hydrometer	(ASTM D-422)	% Clay	51
		% Silt	42
		% Sand	7
		% Gravel	0
		Unified Soil Classification System (USCS)	CH
Standard Compaction	(ASTM D-1557)	Maximum Unit Weight (γ_{dry}), kN/m³	16.3
		Optimum Moisture Content (O.M.C)%	21.5
		Initial Void Ratio (eo)	0.674
Unconfined Compression	(ASTM D-2216)	Unconfined Compressive Strength (q_u), kPa	165
Undrained Unconsolidated	(ASTM D-2850)	Undrianed Cohesion (c_u), kPa	70

Triaxial (UU)		Undrained Angle of Internal Friction (ϕ_u)°	10
Direct Shear at (0.02 mm/min) adjusted Velocity	(ASTM D-3084)	Drained Cohesion (c'), kPa	5
		Drained Angle of Internal Friction (ϕ')°	24
One-Dimensional Swell or Consolidation	(ASTM D-3084) Method (A)	Compression Index (Cc)	0.332
		Swelling Index (Cs)	0.076
		Free Swelling (%)	6.5
		Swelling Pressure (kPa)	170
Chemical Properties	BS 1377: 1990 Part 3	Organic Matters Content (%)	1.93
		Gypsum Content (%)	1.85
		Total Soluble Salts Content (%)	1.05
		Sulphate (So_3) Content (%)	0.86

Table 2. Summary of physical, mechanical and chemical properties of sand used.

Test Name	Standard	Property	Value
Specific Gravity	(ASTM D-854)	Specific Gravity (Gs)	2.66
Grain Size Analysis Sieve Analysis	(ASTM D-422)	D_{10}	0.179
		D_{30}	0.308
		D_{60}	0.5
		Coefficient of Uniformity (Cu)	2.793
		Coefficient of Curvature (Cc)	1.06
		Unified Soil Classification System (USCS)	SP
Maximum Unite Weight	(ASTM D-253)	Maximum Unit Weight (γ_{max}), kN/m³	18.1
Maximum Unite Weight	(ASTM D-4254)	Minimum Unit Weight (γ_{min}), kN/m³	13.6
Chosen	---	Experimental Relative Density (Dr) %	75
Calculated	---	Experimental Unit Weight (γ_{dry}), kN/m³	16.72
Calculated	---	Maximum Void Ratio (e_{max})	0.956
Calculated	---	Minimum Void Ratio (e_{mim})	0.469
Calculated	---	Experimental Void Ratio (e_o)	0.591
Direct Shear	(ASTM D-3084)	Cohesion (c), kPa	0
		Angle of Shearing Resistance (ϕ)°	40
Chemical Properties	(BS 1377: 1990 Part 3)	Organic Matters Content (%)	0.31
		Gypsum Content (%)	0.78
		Total Soluble Salts Content (%)	0.88
		Sulphate (So_3) Content (%)	0.36

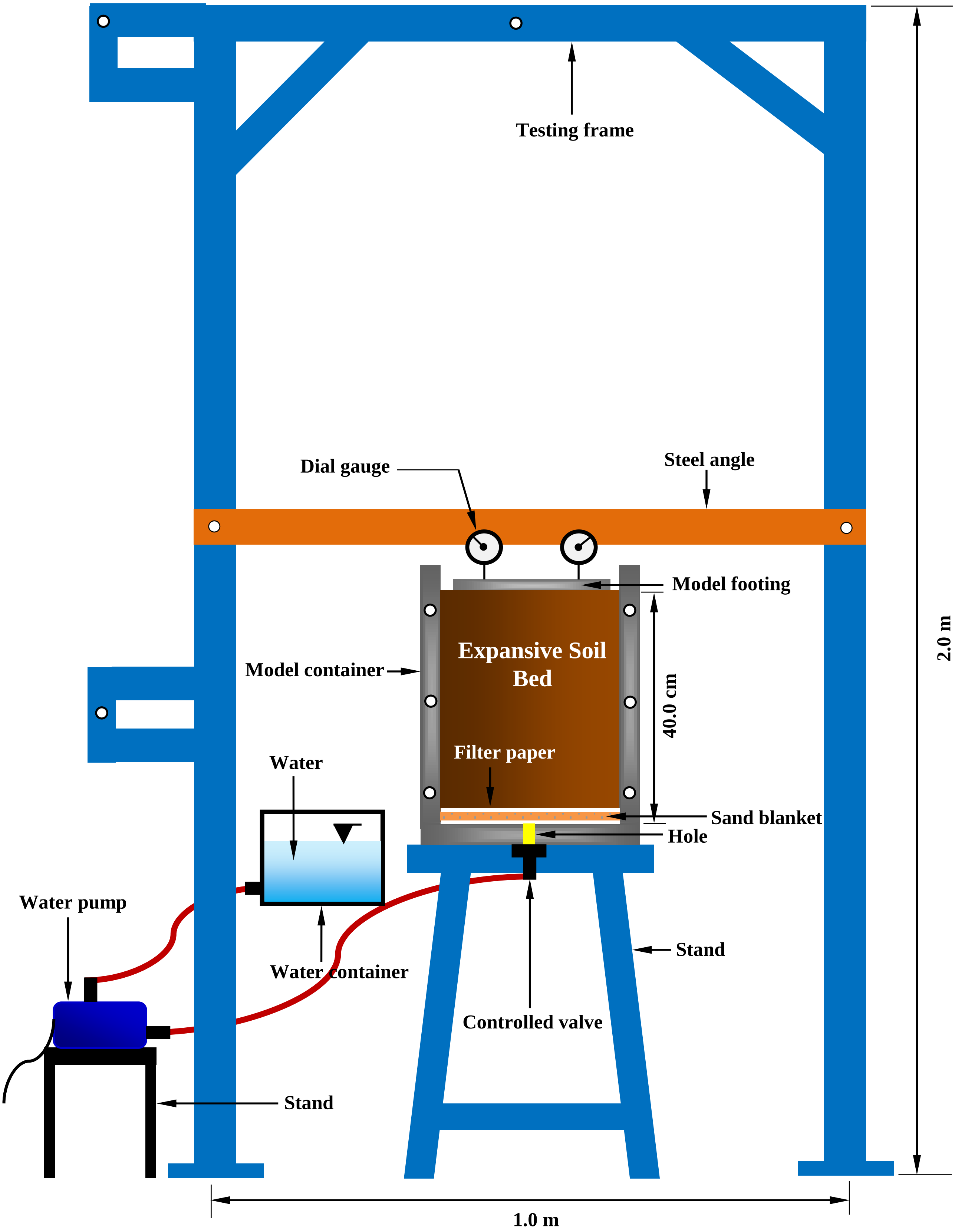

Figure 2. Schematic details of heave test of unreinforced expansive soil bed.

Figure 3. Plate of (GPA-Foundation System) under the heave.

Table 3. Summary of the maximum heave of expansive soil reinforced with (GPA) models at different lengths and diameters.

(GPA) Diameter (cm)	(GPA) Length (cm)	(L/D) Ratio	(L/H) Ratio	(B/D) Ratio	Maximum Heave (mm)
1	10	10	0.25	20	24.0
	20	20	0.5		23.2
	30	30	0.75		22.4
	40	40	1		21.2
2	10	5	0.25	10	23.1
	20	10	0.5		22.7
	30	15	0.75		21.6
	40	20	1		19.2
3	10	3.3	0.25	6.6	22.0
	20	6.6	0.5		21.0
	30	10	0.75		19.2
	40	13.3	1		17.1
4	10	2.5	0.25	2.5	21.0
	20	5	0.5		20.1
	30	7.5	0.75		18.3
	40	10	1		16.1

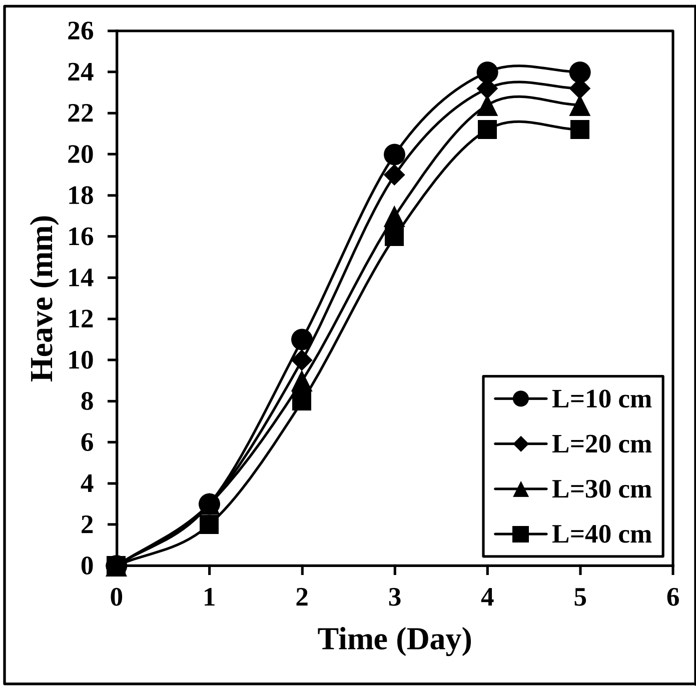

Figure 4. Heave–time relationship for reinforced expansive soil with (GPA) at 1 cm diameter.

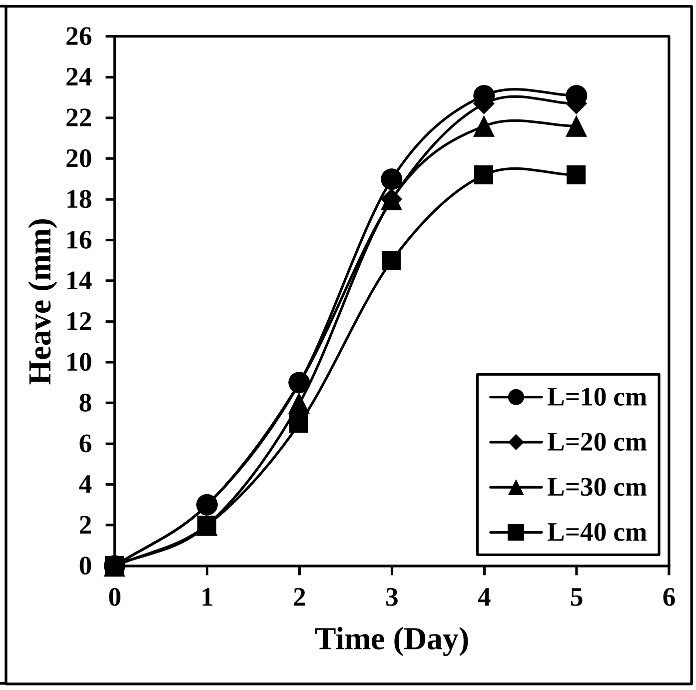

Figure 5. Heave–time relationship for reinforced expansive soil with (GPA) at 2 cm diameter.

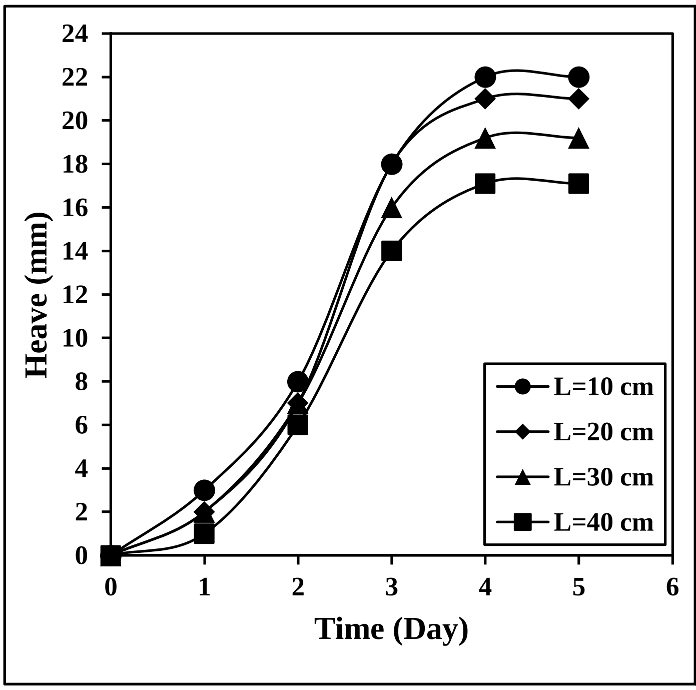

Figure 6. Heave–time relationship for reinforced expansive soil with (GPA) at 3 cm diameter.

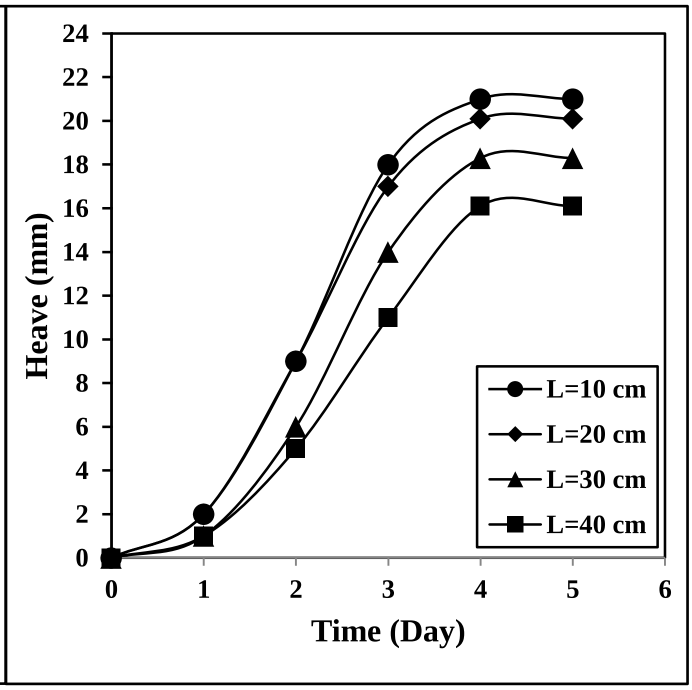

Figure 7. Heave–time relationship for reinforced expansive soil with (GPA) at 4 cm diameter.

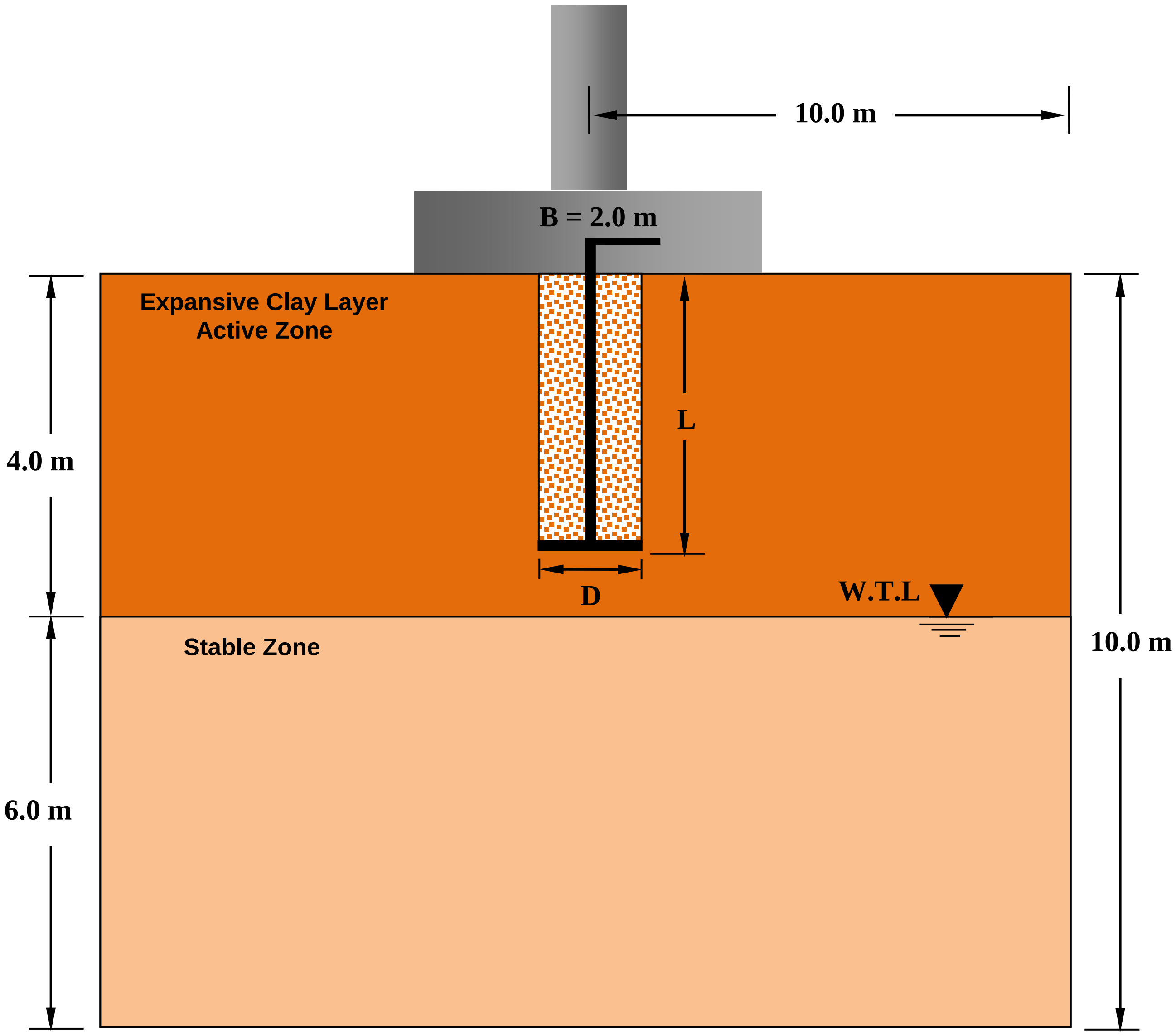

Figure 8. Descriptive sketch of large scale heave problems.

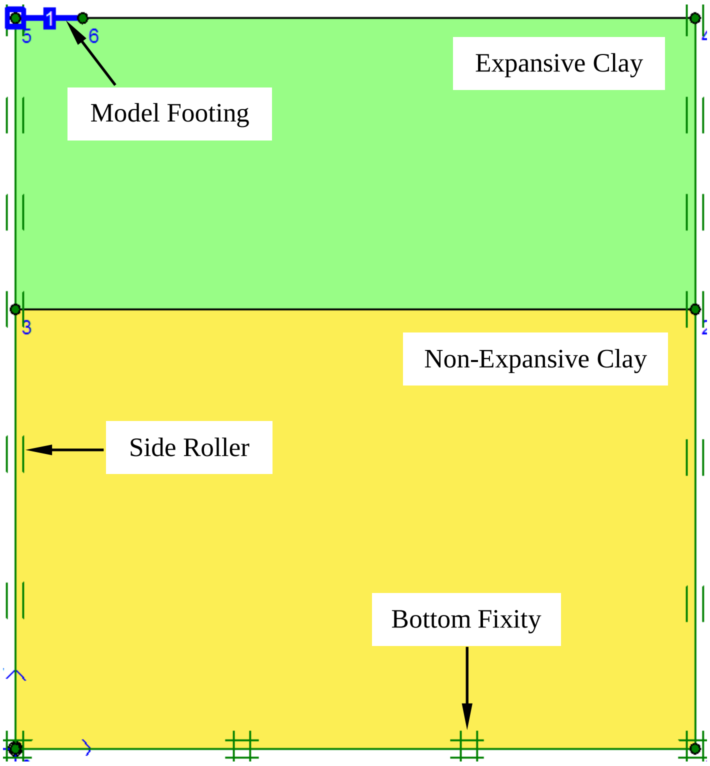

Figure 9. 2D-Axisymmetric model, unreinforced expansive clay.

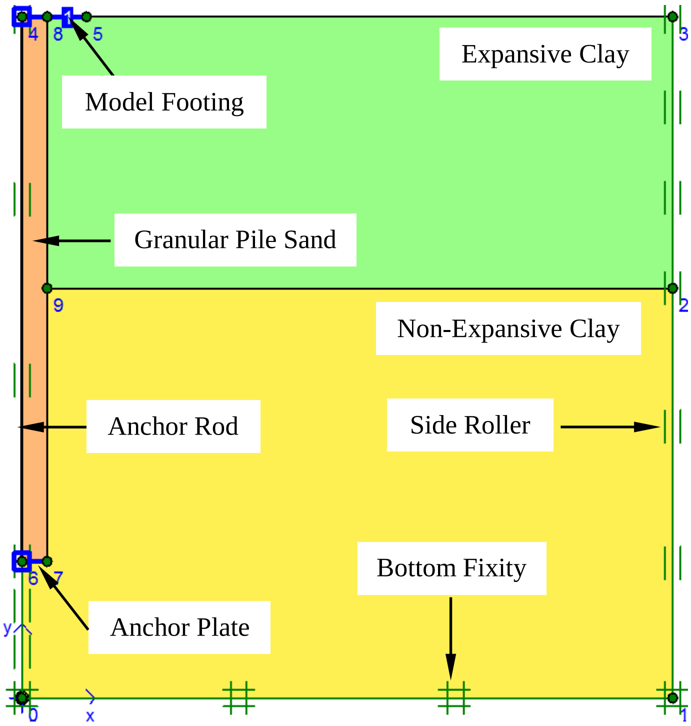

Figure 11. 2D-Axisymmetric model, (GPA) extended to the non-expansive clay layer.

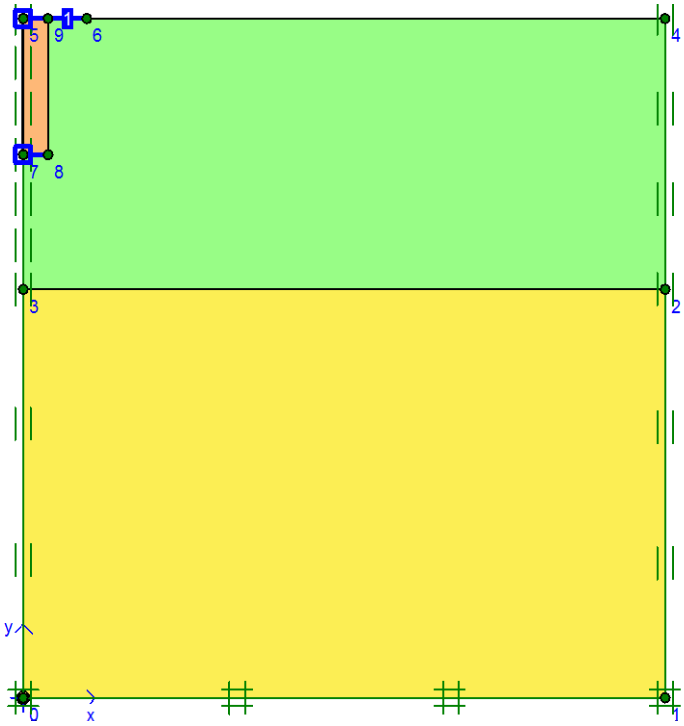

Figure 10. 2D-Axisymmetric model, (GPA) within the expansive clay layer.

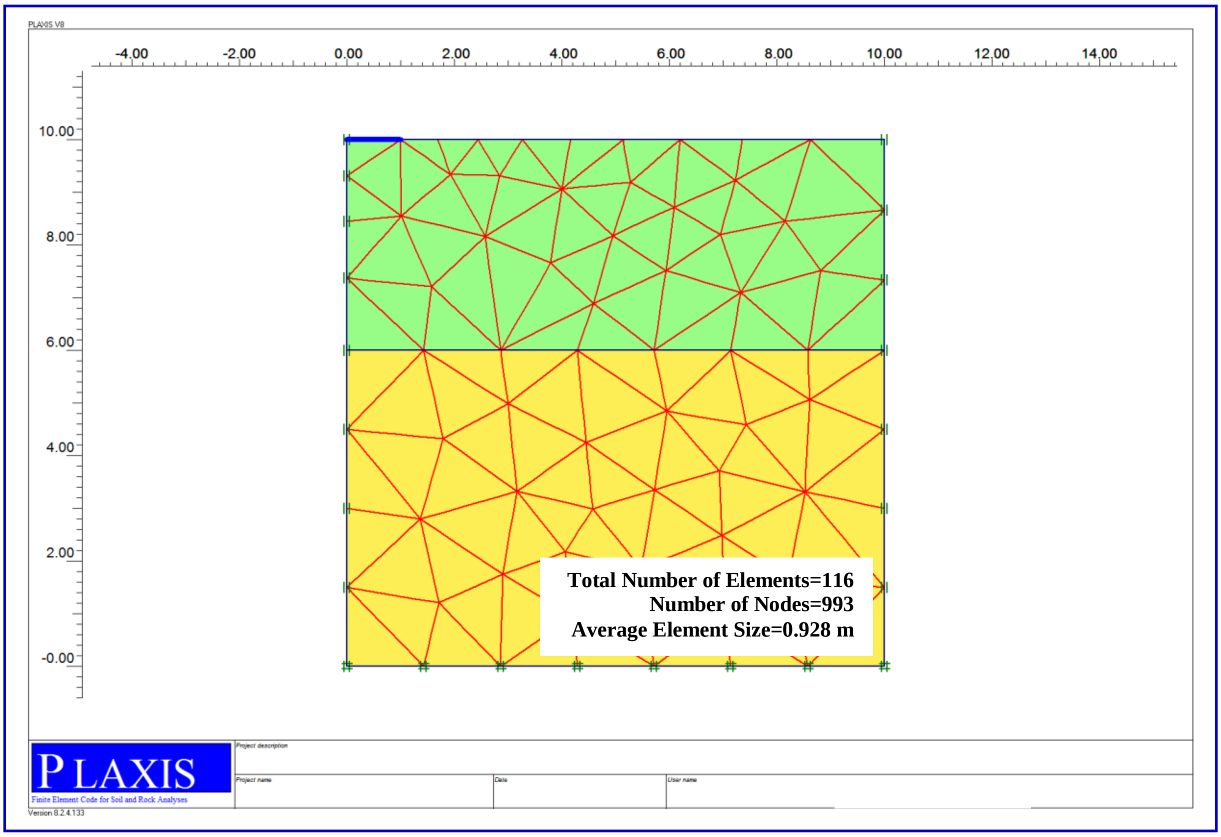

Figure 12. Finite element mesh of foundation system without (GPA).

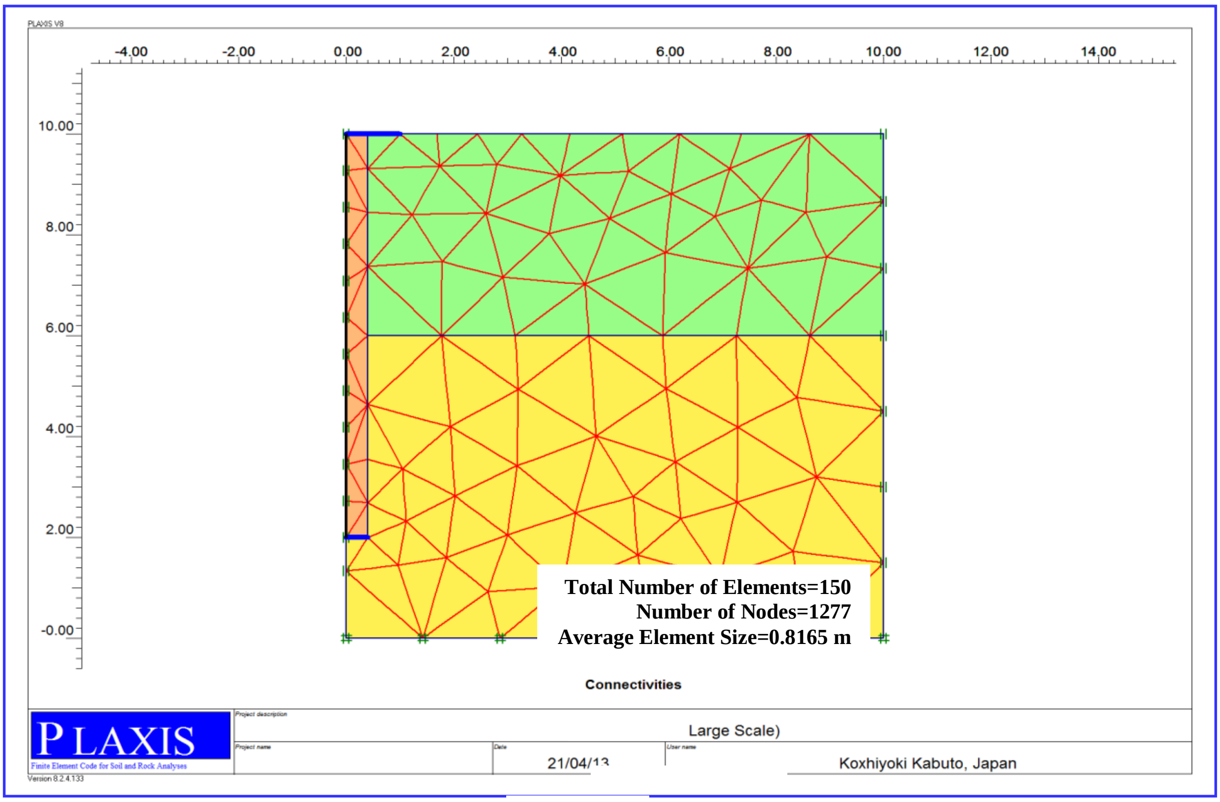

Figure 13. Finite element mesh of (GPA-Foundation System), GPA extended to the non-expansive clay layer.

Table 4. Soil parameters set considered for heave response problems.

Model Type	Model Parameters	Expansive Clay Undrained Method (A)	Granular Pile Sand Drained ---	Non-Expansive Clay Undrained Method (A)
Mohr-Coulomb (MC) Model	γ_{usat} (kN/m³)	16	17	16
	γ_{sat} (kN/m³)	19	20	19
	E'_{ref} (kPa)	5000	50000	5000
	c'_{ref} (kN/m^2)	5	0.1	5
	ϕ'^{o}	24	40	24
	ψ°	0	0	0
	ν_{nu}	0.35	0.3	0.35

Table 5. Steel properties set considered for heave response problems.

Model Type	Model Parameters	Footing Model	Anchor Plate	Anchor Rod
		Steel	Steel	Steel
Linear Elastic	EA (kN/m^2)	5×10^6	5×10^6	2×10^6
	EI (kN/m^2/m)	4×10^4	1×10^4	-
	ν	0.15	0.15	0.15

Table 6. Summary of the maximum heave of unreinforced and expansive soil reinforced with (GPA) models at different lengths and diameters.

(GPA) Diameter (m)	(GPA) Length (m)	(L/D) Ratio	(L/H) Ratio	(B/D) Ratio	Maximum Heave (mm)
Footing Resting on Unreinforced Expansive Soil					260
0.2	2	10	0.5	10	225
	4	20	1		189
	6	30	1.5		130
	8	40	2		115
0.4	2	5	0.5	5	215
	4	10	1		170
	6	15	1.5		100
	8	20	2		84
0.6	2	3.3	0.5	3.3	209
	4	6.6	1		124
	6	10	1.5		56
	8	13.3	2		40
0.8	2	2.5	0.5	2.5	204
	4	5	1		81
	6	7.5	1.5		38
	8	10	2		25

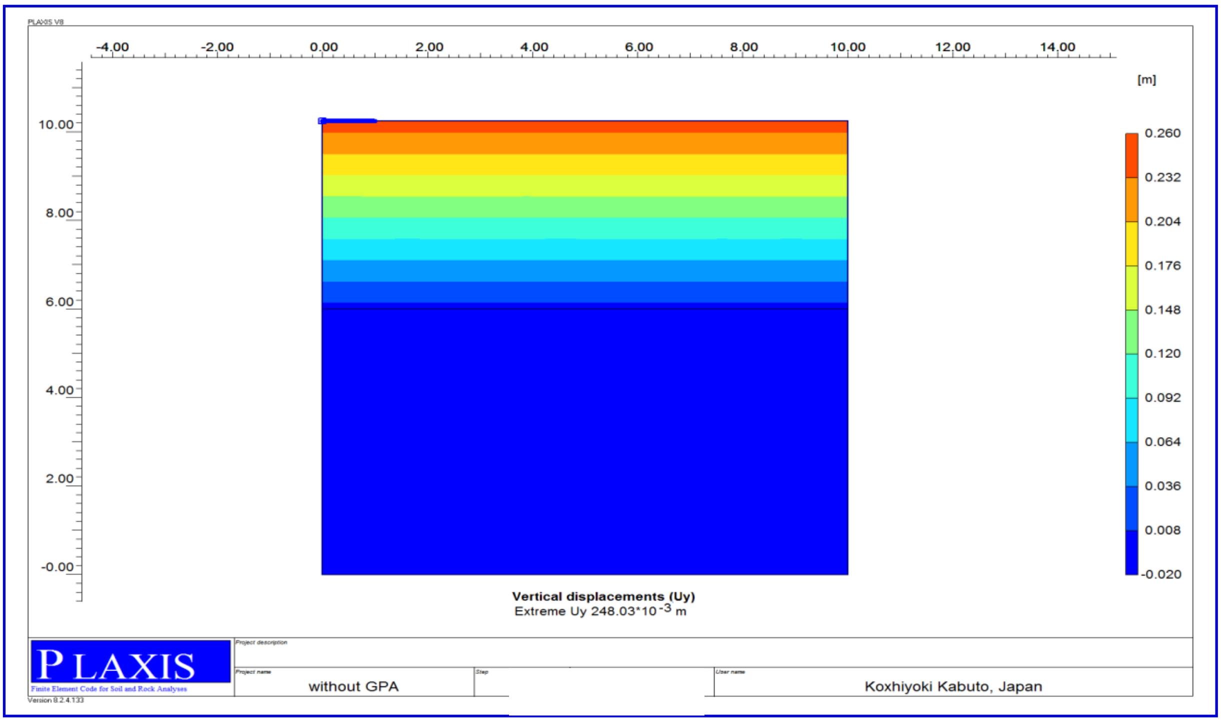

Figure 14. Shading diagram of the vertical displacement distribution resulting from the heave for unreinforced expansive clay in (m).

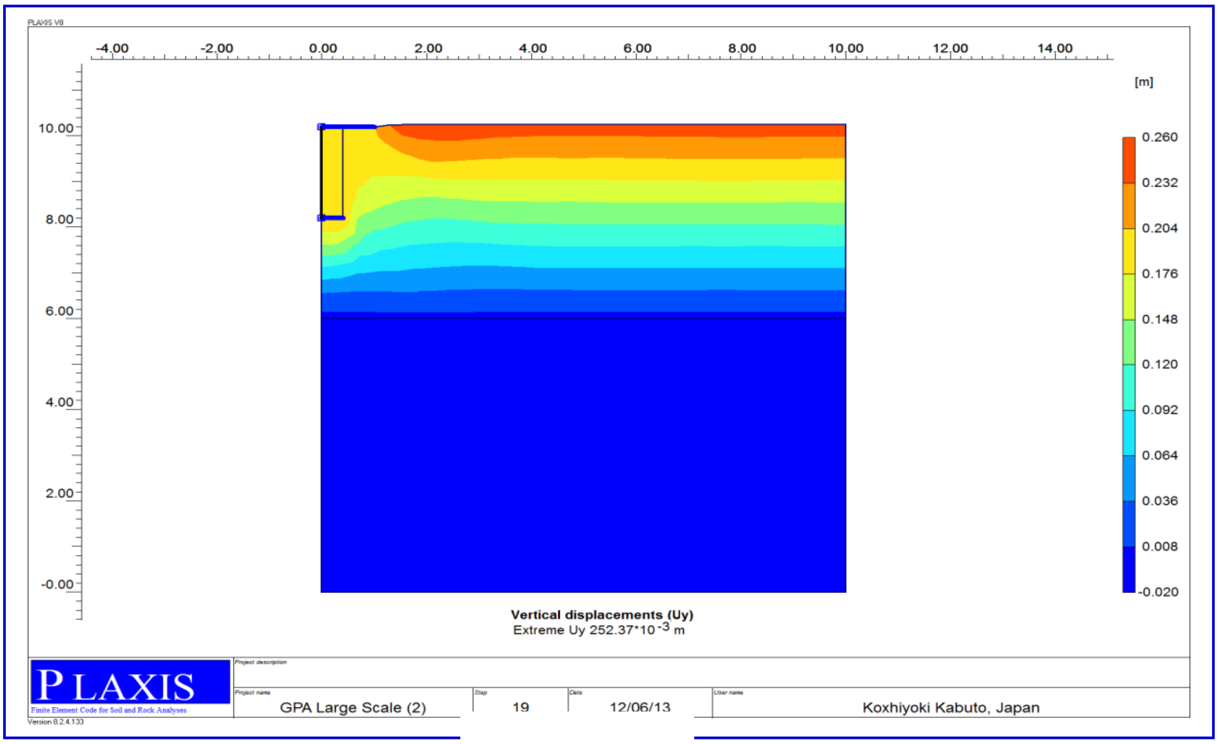

Figure 15. Shading diagram of the vertical displacement distribution resulting from the heave for (GPA at L=2 m and D=0.8 m) in (m).

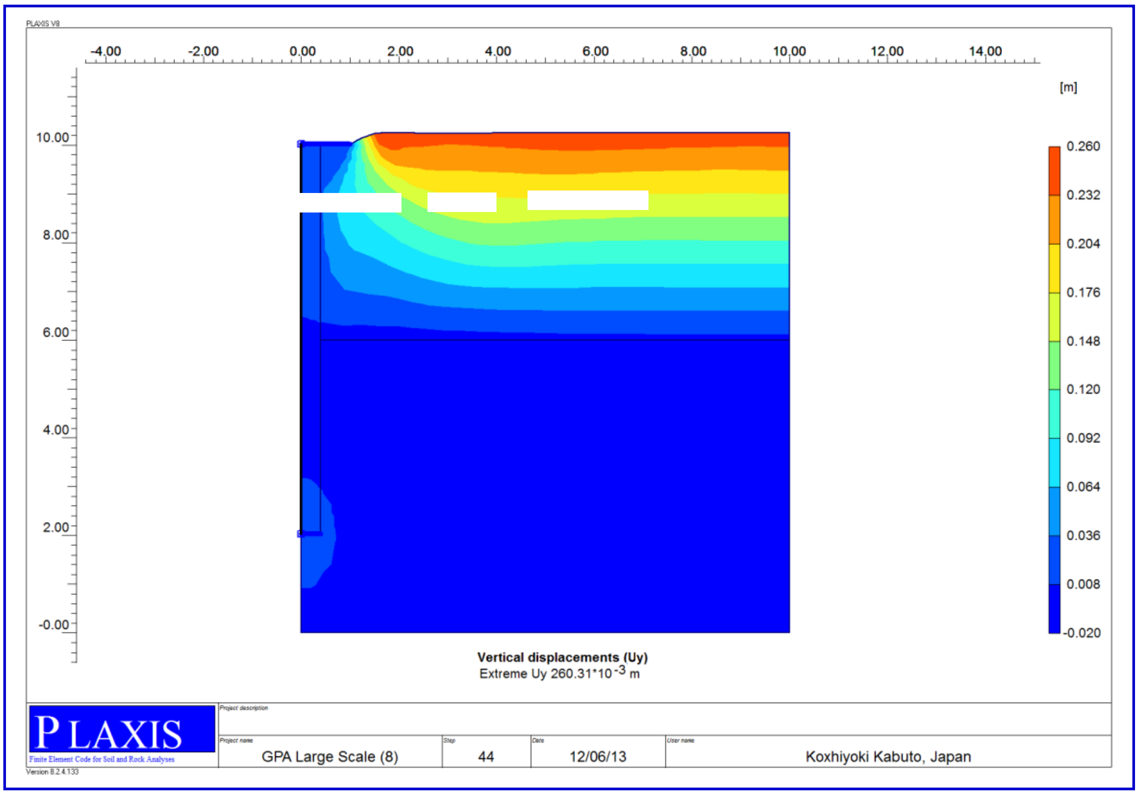

Figure 16. Shading diagram of the vertical displacement distribution resulting from the heave for (GPA at L=8 m and D=0.8 m) in (m).

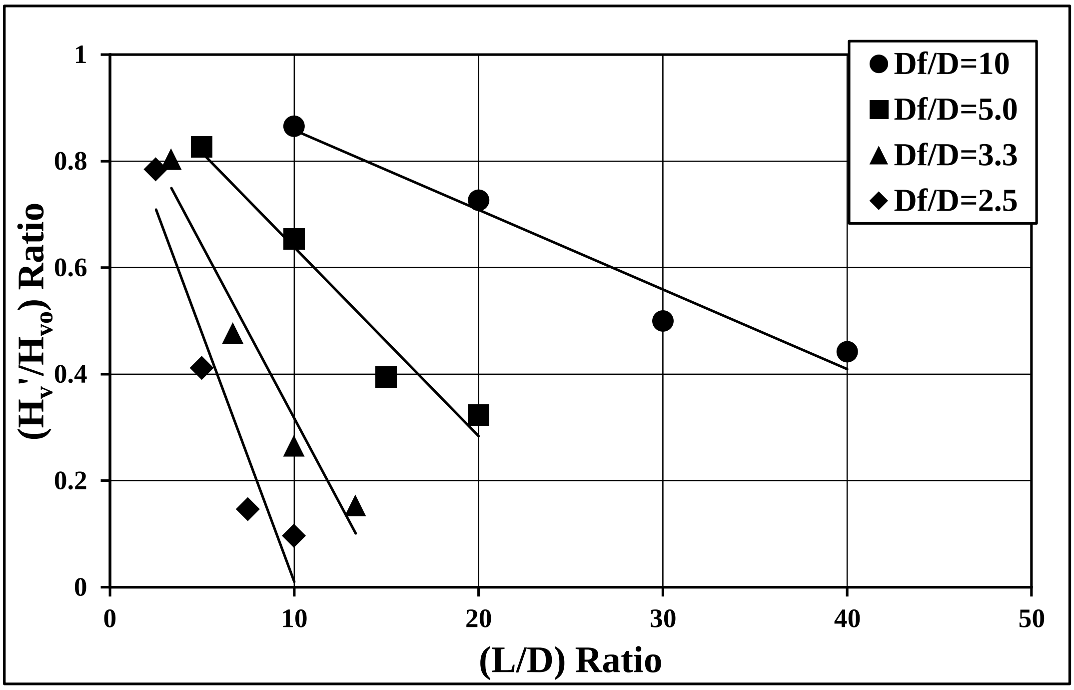

Figure 17. Relationship between the normalized maximum heave (H_v'/H_{vo}) and (L/D) ratio of (GPA) for different ratios of (B/D) - (L/D) ratio effect.

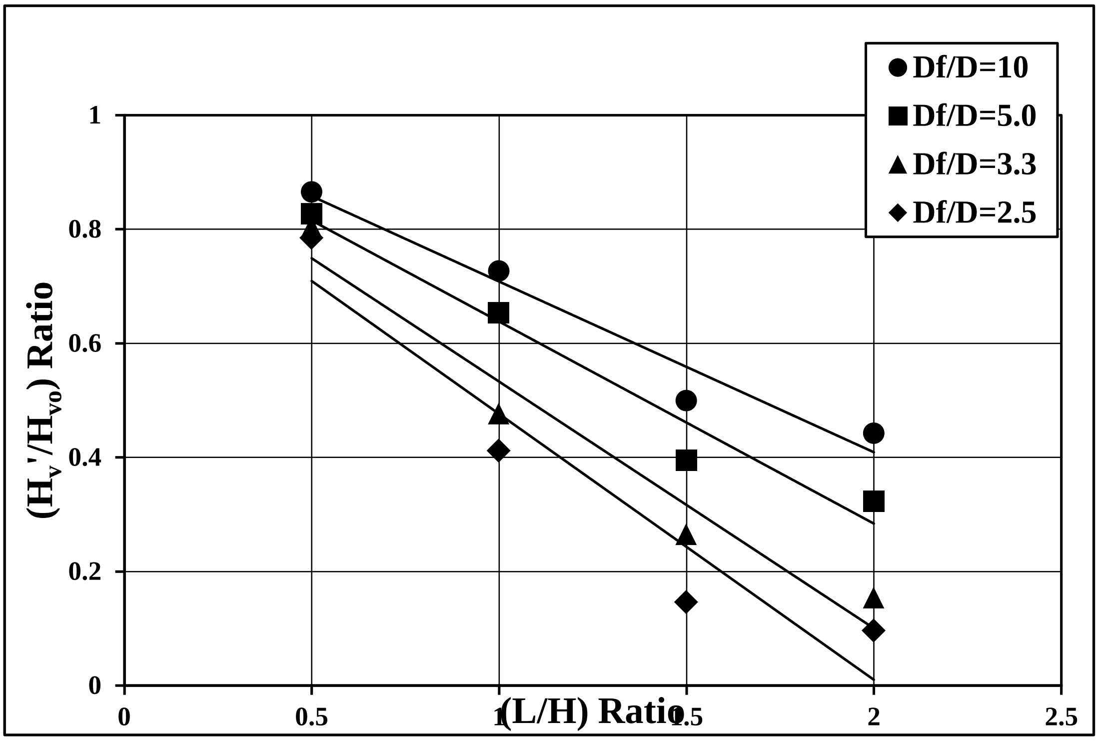

Figure 18. Relationship between the normalized maximum heave (H_v'/H_{vo}) and (L/H) ratio of (GPA) for different ratios of (B/D) - (L/H) ratio rffect.

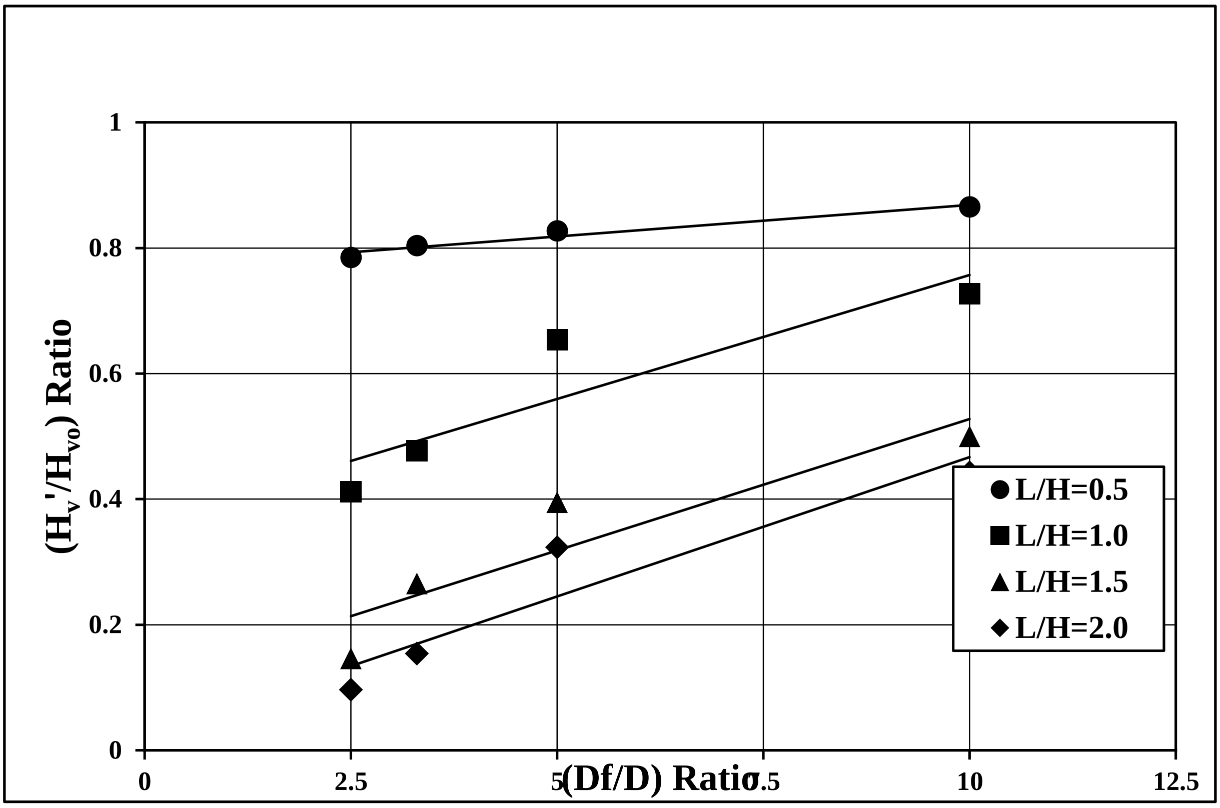

Figure 19. Relationship between the normalized maximum heave (H_v'/H_{vo}) and (B/D) ratio of (GPA) for different ratios of (L/H) - (B/D) ratio effect.

Table 7. Variables limitation for the heave equation.

Variable	Minimum	Maximum
(L/D) Ratio	2.5	40
(B/D) Ratio	2.5	10
(L/H) Ratio	0.5	2

Table 8. Comparison between the predicted and observed heave.

(GPA) Diameter (cm)	(GPA) Length (cm)	(L/D) Ratio	(L/H) Ratio	(B/D) Ratio	Predicted Heave (mm)	Observed Heave (mm)
2	20	10	0.5	10	22.88	22.7
	30	15	0.75		21.06	21.6
	40	20	1		19.24	19.2
3	20	6.67	0.5	6.67	21.24	21.0
	30	10	0.75		18.94	19.2
	40	13.33	1		16.64	17.1
4	20	5	0.5	5	20.41	21.1
	30	7.5	0.75		17.87	18.3
	40	10	1		15.34	16.1

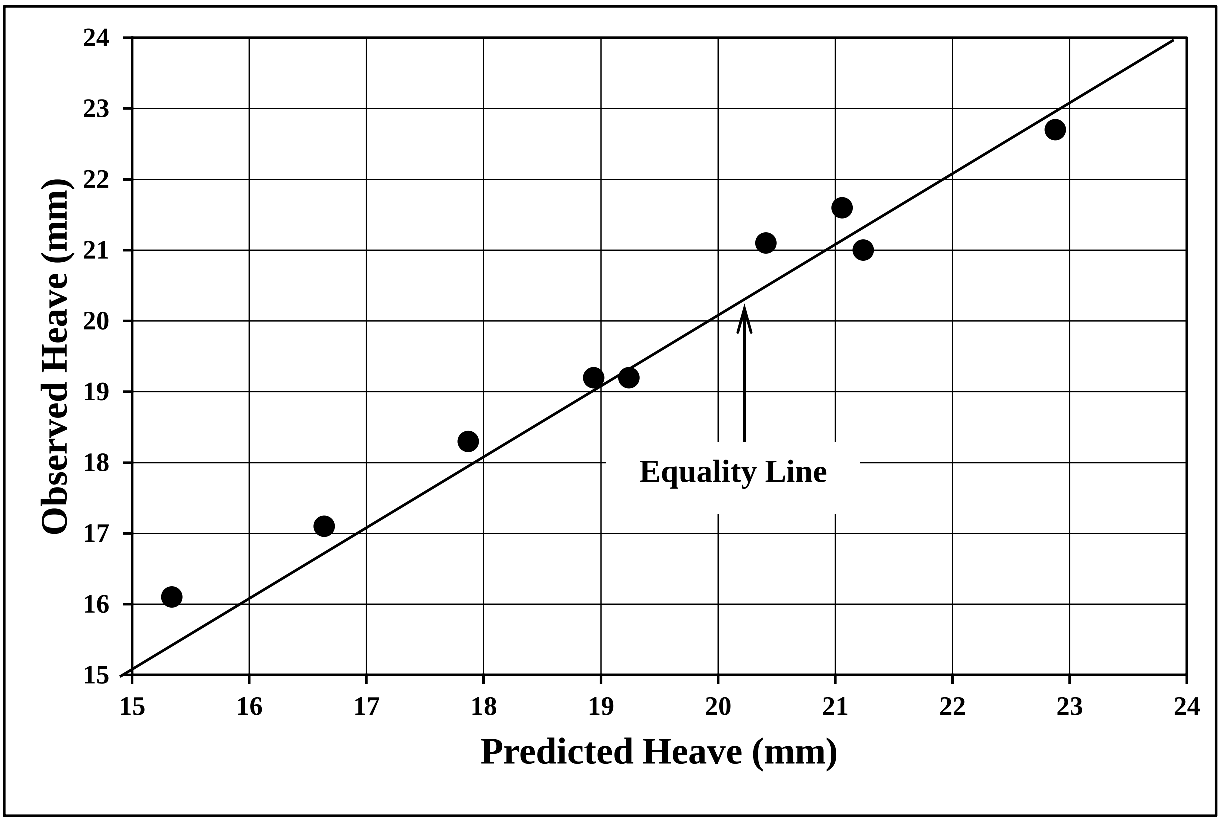

Figure 20. Relationship between the predicted and observed heave of (GPA-Foundation System).

A Linear Programming Method Based Optimal Power Flow Problem for Iraqi Extra High Voltage Grid (EHV)

Dr. Firas Mohammed Tuaimah
Assistant Professor
College of Engineering-University of Baghdad
Email: Dr.Firas@coeng.uobaghdad.edu.iq

Montather Fadhil Meteb
Department of Electrical Engineering
College of Engineering-University of Baghdad
Email: montather87@gmail.com

ABSTRACT

The objective of an Optimal Power Flow (OPF) algorithm is to find steady state operation point which minimizes generation cost, loss etc. while maintaining an acceptable system performance in terms of limits on generators real and reactive powers, line flow limits etc. The OPF solution includes an objective function. A common objective function concerns the active power generation cost. A Linear programming method is proposed to solve the OPF problem. The Linear Programming (LP) approach transforms the nonlinear optimization problem into an iterative algorithm that in each iteration solves a linear optimization problem resulting from linearization both the objective function and constrains. A computer program, written in MATLAB environment, is developed to represent the proposed method. The adopted program is applied for the first time on Iraqi 24 bus Extra High Voltage (EHV) network (400 kV). The required are data taken from the operation and control office, which belongs to the ministry of electricity.

Keywords: Optimal power flow, linear programming, active power dispatch.

السريان الأمثل للطاقة بأستخدام طريقة البرمجة الخطية لشبكة الضغط الفائق العراقية

د. فراس محمد طعيمة
أستاذ مساعد
كلية الهندسة/ جامعة بغداد

منتظر فاضل متعب
قسم هندسة الكهرباء
كلية الهندسة/ جامعة بغداد

الخلاصة

الهدف من الخوارزمية المقترحة لسريان القدرة الأمثل (OPF) هو العثور على نقطة عمل موحدة ومستقرة تؤدي إلى تقليل تكلفة التوليد، أو الخسائر مع الحفاظ على أداء مقبول لمجمل الشبكة من حيث الحدود المفروضة على القدرة الفعالة والغير فعالة المتولدة، وحدود سريان القدرة بخط النقل. الحل بأستخدام OPF يتضمن دالة هدف. ودالة الهدف الشائعة هي فيما يتعلق بكلفة توليد القدرة الفعالة، حيث تم اقتراح طريقة البرمجة الخطية (LP) لحلOPF. طريقة البرمجة الخطية (LP) تحول مسالة التحسين غير الخطية إلى خوارزمية تكرارية حيث في كل تكرار يحل مسالة التحسين الخطية الناتجة عن عملية التحويل إلى دالة خطية لكل من دالة الهدف والقيود. تمت كوين برنامج بأستخدام الحاسب الآلي، وكتب في بيئة MATLAB، لتمثيل الطريقة المقترحة.ويطبق البرنامج الذي اعتمد لأول مرة على شبكة الضغط الفائق العراقية (400 كيلوفولت) التي تتكون من 24 عقدة. حيث تم اخذ البيانات اللازمة من دائرة التشغيل والتحكم، التابعة الى وزارة الكهرباء العراقية.

الكلمات الرئيسية: السريان الأمثل للطاقة، البرمجة الخطية، نقل الطاقة الحقيقية

I. INTRODUCTION

Throughout the entire world, the electric power industry has undergone a considerable change in the past decade, and will continue to do so for the next several decades. In the past, the electric power industry has been either a government-controlled or a government-regulated Industry which existed as a monopoly in its service region. All people, businesses, and industries were required to purchase their power from the local monopolistic power company. This was not only a legal requirement, but a physical engineering requirement as well. It just did not appear feasible to duplicate the resources required to connect everyone to the power grid. Over the past decade, however, countries have begun to split up these monopolies in favor of the free market **Barkovich 1996, Morgan 1996**and **Rudnick 1996**.

Optimal Power Flow (OPF) solution methods have been developed over the years to meet this very practical requirement of power system operation **Acha 2000, El-Hawary 1986,Giacomoni 2010** and **Huneault 1991**.

The optimal power flow problem has been discussed since its introduction by Carpentier **Khaled 2008**. Because the OPF is a very large, non-linear mathematical programming problem, it has taken decades to develop efficient algorithms for its solution. Many different mathematical techniques have been employed for its solution. The majority of the techniques discussed in the literature use one of the following five methods **Alsac 1990, Dommel 1968, Sun 1984** and **Wood 1996**.

1. Lambda iteration method, also called the equal incremental cost criterion (EICC) method.
2. Gradient method.
3. Newton's method.
4. Linear programming method.
5. Interior point method.

The Linear Programming (LP) approach transforms the nonlinear optimization problem into an iterative algorithm that in each iteration solves a linear optimization problem resulting from linearizing both the objective function and constrains **Alsac 1990, Chamorel 1983, Tareq 2008 and Ye Tao 2009**.

The large - scale application of LP - based methods has traditionally been limited to network constrained real and reactive dispatch calculations whose objectives are separable, comprising the sum of convex cost curves. The accuracy of calculation may be lost if the oversimplified approximation is adopted in LP - based OPF. The piecewise linear segmentation of the generator fuel cost curve should be good for avoiding this problem. The piecewise approach can fit an arbitrary curve convexly to any desired accuracy with a sufficient number of segments. Originally, a separable LP variable had to be used for each segment, with the resulting large problems with multi segments cost curve modeling were prohibitively time and storage consuming. The difficulty was alleviated considerably by a separable programming procedure that uses a single variable per cost curve, regardless of the number of the segments. However, the number of segments still affects the solution speed and precision, **Jizhong Zho 2009**.

This paper presents an LP-based OPF for generation cost minimization using as control variables the generator active power and generator voltage. It is intended to overcome the constraints of current LP-based OPF algorithms. The main problem of the current algorithms is the loss of accuracy of the linear approximation of the objective function when the changes of the control variables are not small enough. An attempt to address this issue consists of imposing limits to the deviation of control variables, **Alsac 1990** . Although this approach solves the problem, the convergence of the algorithm becomes very slow. The LP based OPF proposed in this paper improves the accuracy of the linear approximation of the objective function. The objective function is approximated by a piecewise linear function determined iteratively by segmented the objective function in each iteration.

2. PIECEWISE LINEAR APPROXIMATION OF OBJECTIVE FUNCTION

Assuming that the objective function is a quadratic characteristic, the objective function can be linearized by a piecewise linear approach. If the objective function is divided into N linear segments, the real power variable of each generator will also be divided into N variables. **Fig. 1** is an objective function with three linear segments. The corresponding slopes are b_1, b_2, and b_3, respectively **Jizhong Zho 2009**.

From **Fig. 1**, the generator power output variables for each segment can be presented as below:

$$P_{Gi\,min} \leq P_{Gi\,1} \leq P_{G1\,max} \tag{1}$$

$$P_{G1\,max} \leq P_{Gi\,2} \leq P_{G2\,max} \tag{2}$$

$$P_{G2\,max} \leq P_{Gi\,3} \leq P_{Gi\,max} \tag{3}$$

If $P_{Gi\,min}$ is selected as the initial generator output power, the incremental generator power outputs for each segment can be expressed as:

$$\Delta P_{Gi\,1} = P_{Gi\,1} - P_{Gi\,min} \tag{4}$$

$$\Delta P_{Gi\,2} = P_{Gi\,2} - P_{Gi\,1max} \tag{5}$$

$$\Delta P_{Gi\,3} = P_{Gi\,3} - P_{Gi\,2max} \tag{6}$$

Thus the constraint **Eq. (1)** to **Eq. (3)** become

$$0 \leq \Delta P_{Gi\,1} \leq P_{Gi\,1max} - P_{Gi\,min} \tag{7}$$

$$0 \leq \Delta P_{Gi\,2} \leq P_{Gi\,2max} - P_{Gi\,1max} \tag{8}$$

$$0 \leq \Delta P_{Gi\,3} \leq P_{Gi\,max} - P_{Gi\,2max} \tag{9}$$

The piecewise linear objective function becomes

$$\boldsymbol{F} = \sum_{i=1}^{NG} f_i(P_{Gi}) = \sum_{k=1}^{N} \sum_{i=1}^{NG} b_k\,\Delta P_{Gik} \tag{10}$$

Where;

N_G: The number of generators

$P_{Gi\,min}$: The minimal real power output at generator i

$P_{Gi\,max}$:The maximal real power output at generator i

3. MATHEMATICAL FORMULATION OF THE ALGORITHM

The objective function contains real power generation cost. Mathematically, it is formulated as follows:

$$\boldsymbol{F} = \sum_{i=1}^{NG} f_i(P_{Gi}) \tag{11}$$

Subject to

$$\sum_{i=1}^{NG} P_{Gi} = \sum_{k=1}^{ND} P_{Dk} + P_L \tag{12}$$

$$|P_{ij}| \leq P_{ij\,max} \quad ij \in N_T \tag{13}$$

$$P_{Gi\,min} \leq P_{Gi} \leq P_{Gi\,max} \quad i \in N_G \tag{14}$$

Where;
P_D : The real power load
P_{ij}: The power flow of transmission line *ij*
$P_{ij\,max}$: The power limits of transmission line *ij*
P_L: The network losses
f_i: The cost function of the generator *i*
N_T: The number of transmission lines
N_D: The number of loads
Since loads are constant for the given time, we can get the following expression through linearizing the real power balance equation:

$$\sum_{i=1}^{NG} \left(1 - \frac{\partial P_L}{\partial P_{Gi}}\right)\Big| P_{Gi}^0 \Delta P_{Gi} = 0 \tag{15}$$

The real power flow equation of a branch can be written as follows:

$$P_{ij} = V_i^2 G_{ij} - V_i V_j(G_{ij} \cos \delta_{ij} + B_{ij} \sin \delta_{ij}) \tag{16}$$

Where;
P_{ij}: The sending end real power on transmission branch *ij*
V_i: The node voltage magnitude of node *i*
δ_{ij}: The difference of node voltage angles between the sending end and receiving end of the line *ij*
B_{ij}: The susceptance of transmission branch *ij*
G_{ij}: The conductance of transmission branch *ij*

Through linearizing Eq. **(16),** we get the incremental branch power expression as below:

$$\Delta P_{ij} = - V_i^0 V_j^0 \left(-G_{ij} \sin \delta_{ij}^0 \Delta\delta_{ij} + B_{ij} \cos \delta_{ij}^0 \Delta\delta_{ij}\right) \tag{17}$$

In a high - voltage power network, the value of $\delta_{ij}$is very small, and the following approximate equations are easily obtained:

$$\sin\delta_{ij} \cong 0 \tag{18}$$

$$\cos\delta_{ij} \cong 1 \tag{19}$$

In addition, assume that the magnitudes of all bus voltages are the same and equal to 1.0 p.u. Furthermore, suppose the reactance of the branch is much bigger than the resistance of the branch, so that we can neglect the resistance of the branch. Thus,

$$G_{ij} = \frac{R_{ij}}{R_{ij}^2 + X_{ij}^2} \approx 0 \tag{20}$$

$$B_{ij} = -\frac{X_{ij}}{R_{ij}^2 + X_{ij}^2} \approx -\frac{X_{ij}}{X_{ij}^2} \approx -\frac{1}{X_{ij}} \tag{21}$$

Substituting **Eq. (18)** to **Eq. (21)** in to **Eq. (17)** , we get

$$\Delta P_{ij} = -B_{ij}\Delta\delta_{ij} = -B_{ij}(\Delta\delta_i - \Delta\delta_j) = \frac{(\Delta\delta_i - \Delta\delta_j)}{X_{ij}} \tag{22}$$

The above equation can also be written in matrix form, i.e.,

$$\Delta Pb = B'\Delta\delta \tag{23}$$

Where the elements of the susceptance matrix B′ are

$$B'_{ij} = B_{ij} = -\frac{1}{X_{ij}} \tag{24}$$

$$B'_{ii} = -\sum_{\substack{j=1 \\ j\neq i}}^{n} B_{ij} \tag{25}$$

The bus power injection equation can be written as

$$P_{Gi} - P_{Di} = V_i \sum_{j=1}^{n} V_j \left(G_{ij}\cos\delta_{ij} + B_{ij}\sin\delta_{ij} \right) \tag{26}$$

Since the load demand is constant, the linearization expression of **Eq.(26)** can be written as below:

$$\Delta P_{Gi} = V_i^0 \sum_{j=1}^{n} V_j^0 \left(-G_{ij}\sin\delta_{ij}^0 \Delta\delta_{ij} + B_{ij}\cos\delta_{ij}^0 \Delta\delta_{ij}\right) \tag{27}$$

$$= V_i^0 \sum_{j=1}^{n} V_j^0 \left(-G_{ij}\sin\delta_{ij}^0 + B_{ij}\cos\delta_{ij}^0\right)\Delta\delta_{ij} \tag{28}$$

The above equation can also be written in the following matrix form

$$\Delta P_G = H\Delta\delta \tag{29}$$

Eq. (29) stands for the relationship between the incremental generator output power (except for the generator that is taken as slack unit) and the incremental bus voltage angle. Matrix *H* can also be simplified by using **Eq. (18)** and **Eq. (21).**

According to **Eq. (23)** and **Eq. (29),** we can get the direct linear relationship between the incremental branch power flow and incremental generator output power, i.e.,

$$\Delta P_b = B'\Delta\delta = B'H^{-1}\Delta P_G = D\,\Delta P_G \tag{30}$$

Where

$$D=B'H^{-1} \tag{31}$$

It is also called as the linear sensitivity of the branch power flow with respect to the generator power output.

Thus the linear expression of the branch power flow constraints can be written as:

$$|D\ \Delta P_G| \leq \Delta P_{b\,max} \tag{32}$$

The element of the matrix $\Delta P_{b\,max}$ is the incremental power flow limit $\Delta P_{ij\,max}$ of the branch *ij*, i.e.,

$$\Delta P_{ij\,max}=P_{ij\,max}-P_{ij}^{0} \tag{33}$$

The incremental form of the generator output power constraint is , **Jizhong Zho 2009**

$$P_{Gi\,min}-P_{Gi}^{0} \leq \Delta P_{Gi} \leq P_{Gi\,max}-P_{Gi}^{0} \qquad i \in N_G \tag{34}$$

4. THE PROPOSED METHOD IMPLEMENTATION

The above mentioned method for solving optimal power by LP uses an iterative technique to obtain the optimal solution, so it is also called a successive linear programming (SLP) method. The solution procedures of SLP for optimal power flow are summarized below:

Step1. Select the set of initial control variables

Step2. Solve the power flow problem to obtain a feasible solution that satisfies the power balance equality constraint.

Step3. Linearize the objective function and inequality constraints around the power flow solution and formulate the LP problem. Then solve the LP problem and obtain the optimal incremental control variables ΔP_{Gi}.

Step4. Update the control variables :

$$P_{Gi}^{k+1} = P_{Gi}^{k} + \Delta P_{Gi}$$

Step5. Obtain the power flow solution with updated control variables.

Step6. Check the convergence. If ΔP_{Gi} in Step 4.Are bellow the user-defined tolerance, the solution converges. Otherwise, go to Step 3.

Fig. 2 shows the flowchart of linear programming method Based optimal power flow problem.

5. CASE STUDY

The Iraqi 400kV (EHV) network shown in **Fig. 3** was chosen to implement the proposed LP algorithm for OPF.

The Iraqi EHV network consists of 24 bus bars, 38 transmission lines and 11 generating stations. Two operational case studies for the Iraqi network were chosen to be studied by this paper for optimal power flow solution. These two case studies are with cheap and expensive international fuel price conditions.

All the data for this work was taken from the Iraqi operation and control office that belongs to the ministry of electricity.

Table 1 indicates transmission system parameters in p.u. / km (at a base of 100 MVA) for the three types of the transmission lines used in the Iraqi network.

6. RESULTS

The algorithm described in this paper has been coded in MATLAB (R2008a) language. The performance of the algorithm is illustrated considering for a state of load of the operation of the Iraqi power system. The results obtained from using Linear Programming (LP) method are compared with the results obtained from power flow solution using Newton-Raphson method. It is worth mentioning that the distribution of loads on the power plants identified for Newton-Raphson so that we get less losses. There are four power plants run on two types of fuel to generate electric power, so we compared the results when they operate on the cheap fuel type and expensive fuel type. **Fig.4** shows the voltage magnitude in per unit for each bus when cheap fuel price is used to generate power in power plants that operate on two types of fuel and for the two algorithms (Newton-Raphson and Linear Programming).

Fig. 5 shows the generation of each plant for Newton-Raphson power flow solution compared with Linear Programming method when cheap fuel price is used, **Fig. 6** shows the production cost when cheap fuel price is used

Fig.7 shows the voltage magnitude for each bus when expensive fuel price is used to generate power in power plants that operate on two types of fuel and for the two algorithms (Newton-Raphson and Linear Programming).

Fig. 8 shows the generation of each plant for Newton-Raphson power flow solution compared with Linear Programming method when expensive fuel price is used.
Fig. 9 shows the variation of production cost through optimization using Linear Programming method (LP).

7. CONCLUSION

The Linear Programming (LP) algorithm is used for the first time on the Iraqi Extra High Voltage (EHV 400kV) Grid for optimal power flow to minimize the active power generation cost. paper has presented a LP based.

The problem constraints are the coupled linearized power flow equations and the system variable limits. A piecewise linear approximation of the objective function is built by adding iteratively a tangent cut in each iteration.
It can be also note that the results of the production cost are significantly decreased when using Linear Programming with the results derived in the case of Newton–Raphson. From **Table 2** there is about 30.16% decrease in the production costs when using cheap fuel type, whereas there is about 28.2% decrease in production costs when using expensive fuel type as given in **Table 3**.

REFERENCES

Acha, E., Ambriz-Pe´rez, H., Fuerte-Esquivel, C.R , 2000, *Advanced Trans-former Control Modeling in An Optimal Power Flow Using Newton's Method, IEEE Trans. Power Systems* 15(1), pp. 290–298.

Alsac O., J. Bright, M. Prais and B. Stott, , 1990, *Further Developments in LP-Based Optimal Power Flow*, IEEE Transactions on Power Systems, Vol. 5(3), pp. 697-711.

Barkovich B.R. and D. Hawk, 1996, *Charting a New Course in California, IEEE Spectrum*, Vol. 33, No. 7, July, pp. 26-31.

KhaledZehar& Samir Sayah, 2008, *Optimal Power Flow with Environmental Constraint using a Fast Successive Linear Programming Algorithm*, Application to the Algerian power system, Elsevier, Volume 49, Issue 11, November pp. 3362–3366.

Chamorel P-A., A. J. Germond, 1983, *Optimal Voltage and Reactive Power Control in an Interconnected Power System with Linear Programming*, CIGRE Study Committee 38, Montreaux.

Dommel H. W. and W. F. Tinney, 1968, *Optimal Power Flow Solutions, IEEE Transactions on Power Apparatus and Systems*, Vol. PAS-87, October, pp. 1866-1876.

El-Hawary, M.E., Tsang, D.H., 1986, *The Hydro-Thermal Optimal Power Flow, A Practical Formulation and Solution Technique Using Newton's Approach,* IEEE Trans. Power Systems PWRS-1(3), pp. 157–167,.

Huneault, M., Galiana, F.D., A, , 1991, *Survey of the Optimal Power Flow Literature, IEEE Trans. Power Systems* volume:6, Issue:2, pp. 762–770.

JizhongZho, 2009, *Optimization Of Power System Operation, Institute Of Electrical and Electronics Engineers John Wiley & Sons, Inc., Hoboken, New Jersey*.

Tareq A. Al-Muhawesh&Isa S. Qamber, 2008,*The Established Mega Watt Linear Programming-Based Optimal Power Flow Model Applied to The Real Power 56-Bus System In Eastern Province of Saudi Arabia, Elsevie*r, Volume 33, Issue 1, January, pp. 12–21.

Giacomoni A.M.&Wollenberg B.F.,2010, *Linear Programming Optimal Power Flow Utilizing A Trust Region Method, IEEE, North American Power Symposium (NAPS)* .

Morgan M.G. and S. Talukdar, 1996 ,*Nurturing R&D, IEEE Spectrum*, Vol. 33, No.7, July pp. 32-33.

Ye Tao,A , 2009, *Sequential Linear Programming Algorithm for Security-Constrained Optimal Power Flow*, IEEE, North American Power Symposium (NAPS) Conference**.**

Rudnick H., 1996, *Pioneering Electricity Reform in South America, IEEE Spectrum*, Vol. 33, No. 8, August pp. 38-44.

Sun D.I., B. Ashley, B. Brewer, A. Hughes and W. F. Tinney, 1984, *Optimal Power Flow by Newton Approach, IEEE Transactions on Power Apparatus and Systems*, Vol. PAS-103, October pp. 2864-2880.

Wood J. and B. F. Wollenberg, 1996, *Power Generation Operation and Control, New York, NY*: John Wiley & Sons, Inc., pp. 39-517,.

9. ABBREVIATIONS AND SYMBOLS

EHV	Extra high voltage
LP	Linear programming
OPF	Optimal power flow
B_{ii}	Self susceptance
B_{ij}	Mutual susceptance

F_i The generator fuel cost function
G_{ii} Self conductance
G_{ij} Mutual conductance
P_{Di} Active load power at bus i
P_{Gi} Active power generated by unit i
$P_{Gi\,min}$ Minimum generator active power limit
$P_{Gi\,max}$ Maximum generator active power limit

V_i Bus voltage at bus i
ΔP Change in active power
$\Delta\delta$ Change in voltage angle
ΔV Change in voltage magnitude
δ_i Bus voltage angle at bus i

Table1. Iraqi transmission line system parameters.

Conductor Type	R p.u. / km	X p.u. / km	B p.u. / km
AAAC	0.00002167	0.000197	0.005837
ACSS	0.0000228	0.0001868	0.005784
ACSD	0.0000228	0.0001897	0.005962

Table 2. Results when cheap fuel price is used.

	NR	LP
Total Active Gen.	4188.97 [MW]	4192.63 [MW]
Total Reactive Gen.	11.74 [Mvar]	63.99 [Mvar]
Total Active Load	4177 [MW]	4177 [MW]
Total Reactive Load	1998 [Mvar]	1998 [Mvar]
Total Active Loss	11.967 [MW]	15.633 [MW]
Total Reactive Loss	104.97 [Mvar]	136.20 [Mvar]
ProductionCost ($/h)	688960	481158.11

Table 3. Results when expensive fuel price is used.

	NR	LP
Total Active Gen.	4188.97 [MW]	4195.76 [MW]
Total Reactive Gen.	11.74 [Mvar]	91.23 [Mvar]
Total Active Load	4177 [MW]	4177 [MW]
Total Reactive Load	1998 [Mvar]	1998 [Mvar]
Total Active Loss	11.967 [MW]	18.756 [MW]
Total Reactive Loss	104.97 [Mvar]	164.64 [Mvar]
Production Cost ($/h)	974630	699679.68

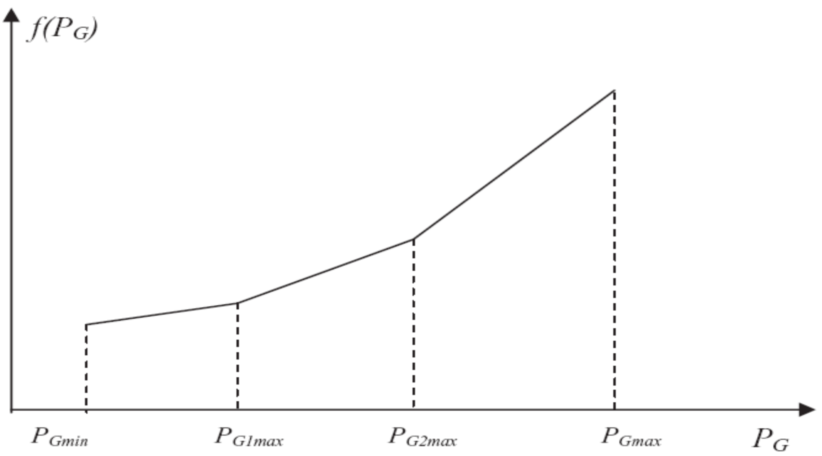

Figure 1. Piecewise linear objective function.

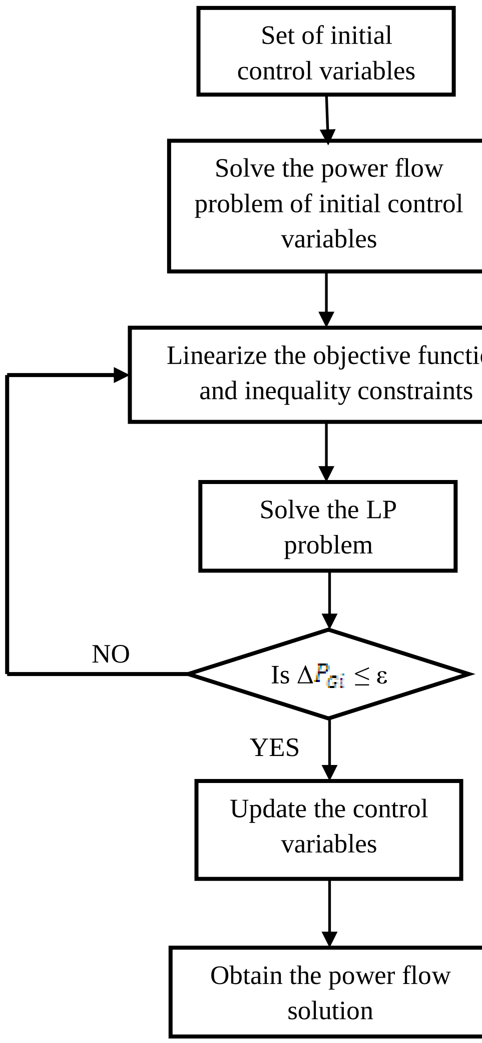

Figure 2. The flowchart of linear programming method based-optimal power flow problem**.**

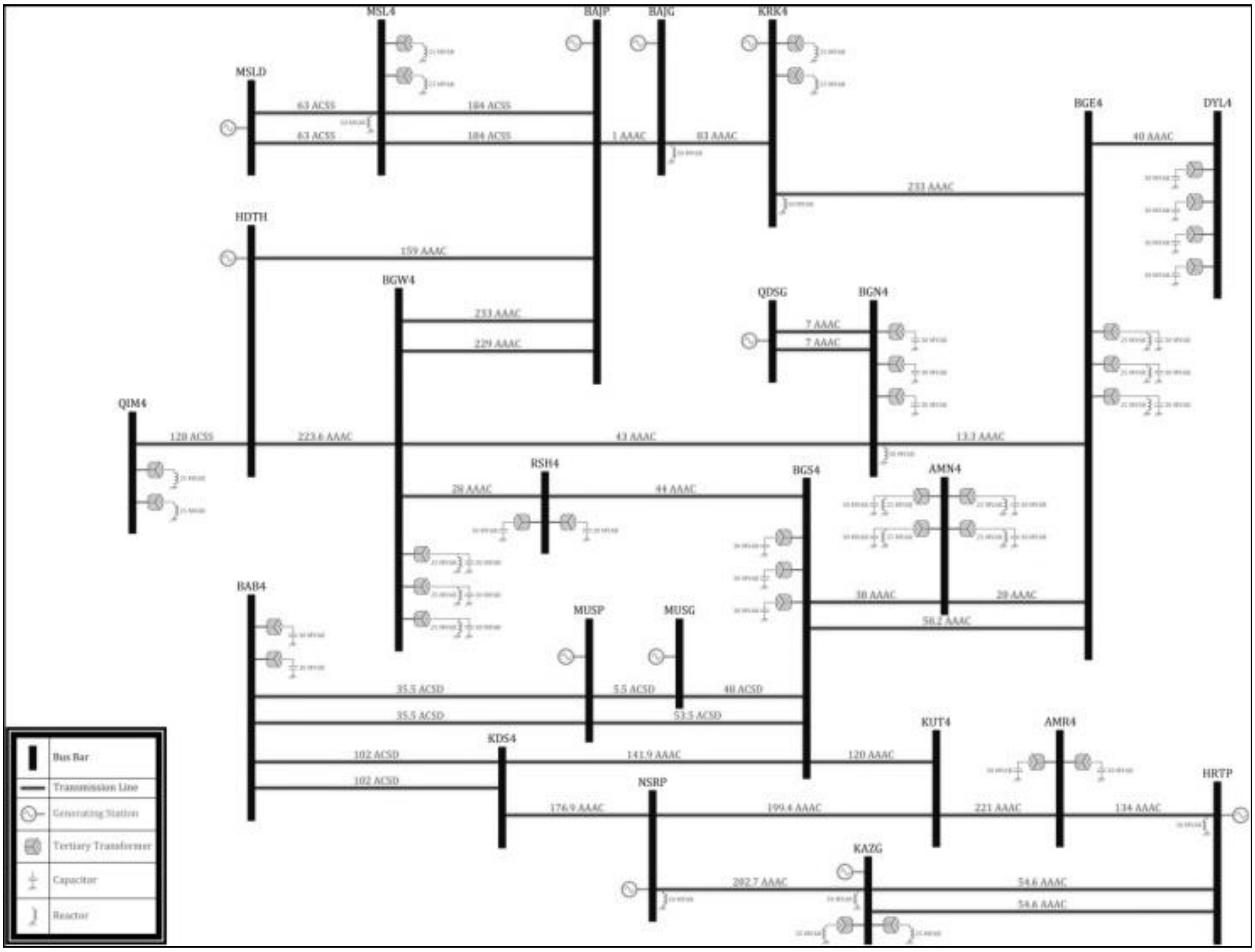

Figure 3. Single line diagram of the Iraqi network 400kV.

Figure 4. Voltage magnitude at each bus with cheap fuel price.

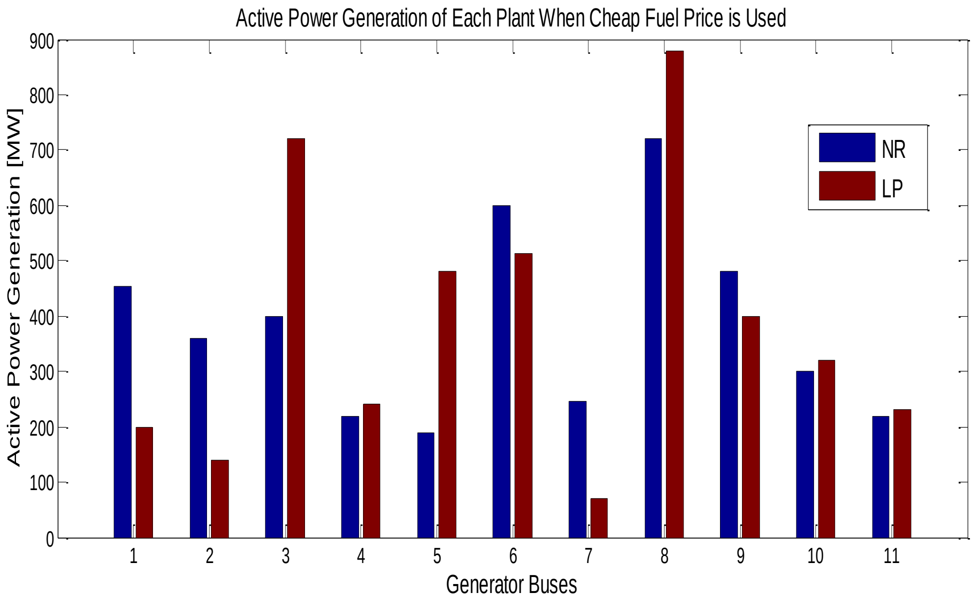

Figure 5. Active power generation for each plant with cheap fuel price.

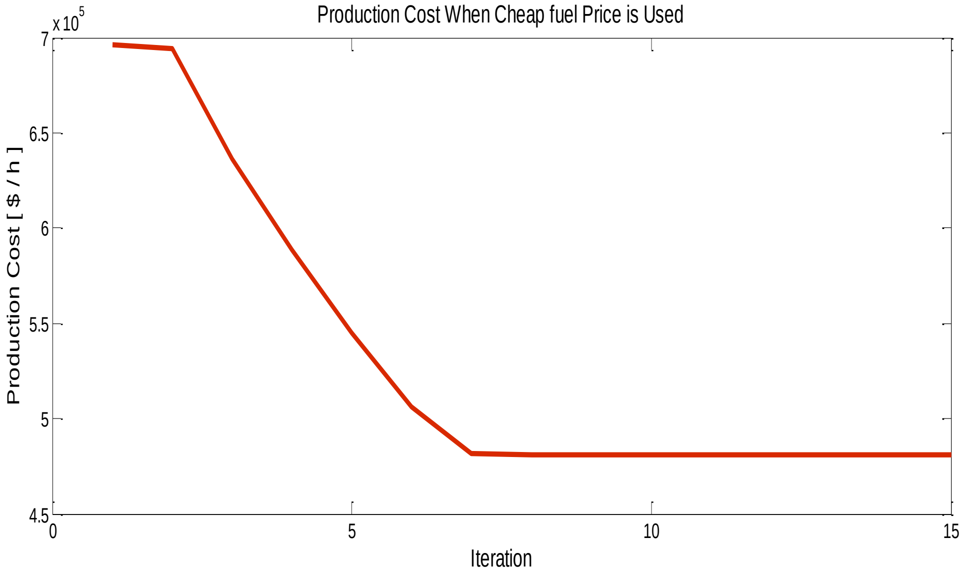

Figure 6. Production cost when cheap fuel price is used.

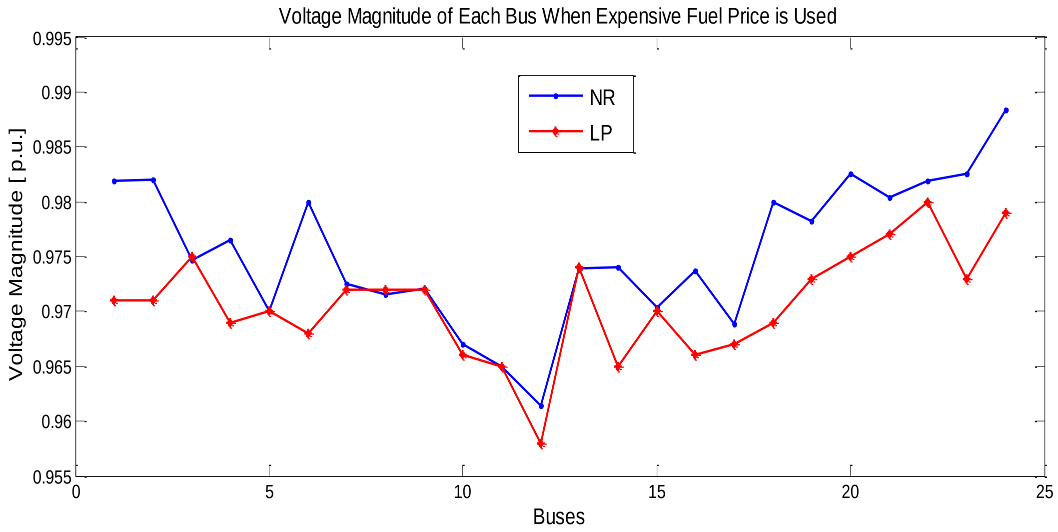

Figure 7. Voltage magnitude at each Bus with expensive fuel price.

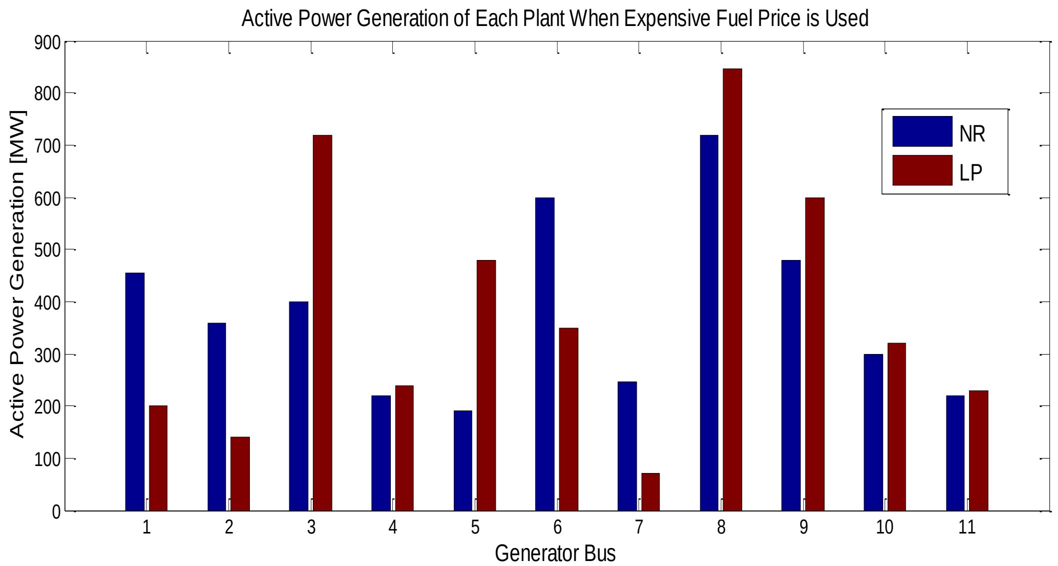

Figure 8. Active power generation for each plant with expensive fuel price.

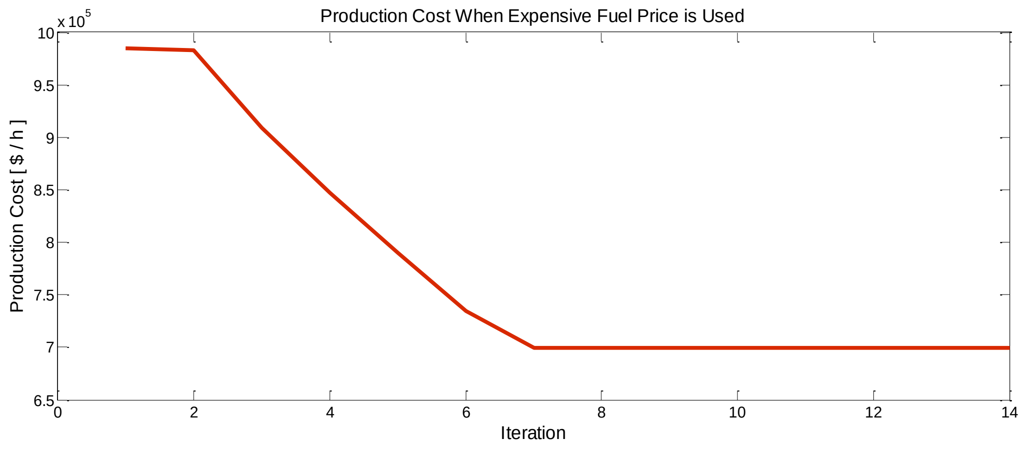

Figure 9. Production cost when expensive fuel price is used.

Data Classification using Quantum Neural Network

Dr. Ghassan H. Abd Al- Majeed
Professor.
Computer center- Baghdad University
Baghdad, Iraq
Email: ghmajeed@gmail.com

Dr. Zainab T. Alisa
Assistant Professor.
Electrical Engineering- Baghdad University
Baghdad, Iraq
Email: zainab_alisa@yahoo.com

Hassan Saadallah Naji
Department of Electrical Engineering
College of Engineering
Baghdad University
Email: hassanmaster79@yahoo.com

ABSTRACT

In this paper, integrated quantum neural network (QNN), which is a class of feedforward neural networks (FFNN's), is performed through emerging quantum computing (QC) with artificial neural network(ANN) classifier. It is used in data classification technique, and here **iris flower data** is used as a classification signals. For this purpose independent component analysis (ICA) is used as a feature extraction technique after normalization of these signals, the architecture of (QNN's) has inherently built in fuzzy, hidden units of these networks (QNN's) to develop quantized representations of sample information provided by the training data set in various graded levels of certainty. Experimental results presented here show that (QNN's) are capable of recognizing structures in data, a property that conventional (FFNN's) with sigmoidal hidden units lack. In addition, (QNN) gave a kind of fast and realistic results compared with the (FFNN). Simulation results indicate that QNN is superior (with total accuracy of 97.778%) than ANN (with total accuracy of 93.334%).

Keywords: signal classification, artificial neural network, quantum computing, data analysis and fuzziness.

تصنيف البيانات بأستخدام الشبكة العصبية الكمية

أ.د. غسان حميد عبد المجيد
مركز الحاسبة / جامعة بغداد

أ.م.د. زينب توفيق باقر
قسم الهندسة الكهربائية / جامعة بغداد

حسن سعد الله ناجي
قسم الهندسة الكهربائية / جامعة بغداد

الخلاصة

يتطرق البحث الى الشبكة العصبية الكمية كاحدى اصناف الشبكات العصبية الاصطناعية والتي تتم من خلال دمج مجالين مهمين وهما مجال الاحتساب الكمي مع مجال الشبكة العصبية الاصطناعية . تستخدم هذه الدائرة في مجال تقنية تصنيف البيانات, ان بيانات ازهار السوسن (Iris flower database) قد تم اعتمادها هنا كأشارات تصنيف. ولهذا الغرض تم اعتماد تقنية تحليل المركبة الاساس (ICA) كتقنية استخلاص الخصائص من اشارات التصنيف بعد مرحلة المعالجة الاولية للبيانات لغرض تهيئة البيانات, ان الطبقة الوسطية المعروفة بالطبقة الخفية تتألف من عدد من الخلايا العصبية التي تكون متعددة المستويات لغرض

معالجة بيانات التدريب و الاختبار لتعطي بذالك مستويات متعددة من التأكيد. النتائج التجريبية تشير بأن الشبكة العصبية الكمية لها قدرة تمييز البيانات افضل مقارنة بالشبكة العصبية الصناعية و لنفس الغرض, بالاضافة لذالك النتائج تشير بأن الشبكة العصبية الكمية تعطي نتائج تمييز(تصنيف) اسرع و اكثر واقعية اي ان دوائر QNN تعتبر الافضل(بدقة تصل97.778%) مقارنة بالشبكة العصبية الاصطناعية(التي تصل دقتها 93.334%).

الكلمات المفتاحية:تصنيف الاشارات,الشبكة العصبية الصناعية,الاحتساب الكمي, تحليل البيانات, و المنطق المضبب.

1. INTRODUCTION

Quantum neural network (QNN's) is a promising area in quantum computation and quantum information field. In 1997, Lov K. Grover proposed a method that can speed up a range of search applications over unsorted data using Quantum mechanics, **Lov K. Grover, 1997**.

Several models have been proposed in the literature but most of them need clear hardware requirements to implement such models, one of the most exciting emerging technologies is quantum computation, which attempts to overcome limitations of classical computers by employing phenomena unique to quantum-level events, such as nonlocal entanglement and superposition. It is therefore not surprising that many researchers have conjectured that quantum effects in the brain are crucial for explaining psychological phenomena, including consciousness, **Abninder, 2006**.

Jarernsri. L. Mitrpanont, and Ananta Srisuphab, presented the approach of the quantum complex-valued backpropagation neural network or QCBPN, the challenge of their research is the expected results from the development of the quantum neural network using complex-valued backpropagation learning algorithm to solve classification problems, **Jarernsri, 2003**.

Independent component analysis (ICA) is essentially a method for extracting useful information from data. It separates a set of *signal mixtures* into a corresponding set of statistically independent component signals or *source signals*. ICA belongs to a class of *blind source separation* (BSS) methods for separating data into underlying informational components, **Isabelle, 2006**.

The mixtures can be sounds, electrical signals, e.g., electroencephalographic (EEG) signals or images (e.g., faces, and Functional Magnetic Resonance Imaging (FMRI) data). The defining feature of the extracted signals is that each extracted signal is statistically independent of all the other extracted signals, **James, 2004.**

2. METHODLOGY FOR INTEGRATED QNN SIGNAL CLASSIFIER SYSTEM

The overall block diagram that shows the structure of integrated QNN as signal classifier system is shown in **Fig.1**. Every single recorded input signal Iris signals database is depicted or formed by [1X50] discrete data matrix, and represents a vector pattern. Two different Iris data sets are formed for training and testing purposes. The discrete dataset has three different classes species, the structure of integrated QNN signal classifier system can be shown by the following principal steps**:**

2.1 Normalization

Normalization is a process to simplify data as feature extraction. It is usually affected by peak-to-peak magnitudes and offset of input data because of physiology conditions surrounding, psychological state, artifacts; therefore, normalization mainly required to decrease the effects of undesirable parameters and offset.

2.2 Feature Extraction

Feature extraction or dimensionality reduction is the process of extracting useful information from the signal, features are characteristics of a signal that are able to distinguish between different classes species. Feature extraction requires reducing the size of the data by selecting appropriate features, selected features should be minimally redundant and the expected results should maximally depend on these features, and preserve all information from the signal that is needed for classification.

In ICA, each signal is described as a scalar variable, and a set of signals as a vector of variables, and the process of obtaining signal mixtures from signal sources using a set of mixing coefficients, **Isabelle, 2006**.

$$x_1 = a_{11}s_1 + a_{12}s_2 \tag{1}$$

$$x_2 = a_{21}s_1 + a_{22}s_2 \tag{2}$$

Above equations can be rewritten using matrix –by-vector form as:

$$\mathbf{X} = \begin{bmatrix} x_1 \\ x_2 \end{bmatrix} \tag{3}$$

$$\mathbf{S} = \begin{bmatrix} s_1 \\ s_2 \end{bmatrix} \tag{4}$$

$$A = \begin{bmatrix} a_{11} & a_{12} \\ a_{21} & a_{22} \end{bmatrix} \tag{5}$$

Then **Eq. (1)** can be written in matrix by vector form as follow:

$$\mathbf{X = A\ S} \tag{6}$$

Where, (a_{11}, a_{12}, a_{21}, a_{22}), a set of mixing coefficients, (s_1, s_1) are original signals(source signals), and(x_1, x_2) set of “mixture” points which can be transformed back to the source signals (s_1, s_1) using a set of unmixing coefficients, which reverse the effects of the original geometric transformation from source signals to signal mixtures, **Joshua, 2000**.

$$s_1 = \mu x_1 + \sigma x_2 \tag{7}$$

$$s_2 = \gamma x_1 + \delta x_2 \tag{8}$$

Above equations can be rewritten using matrix –by-vector form as:

$$\begin{bmatrix} s_1 \\ s_2 \end{bmatrix} = \begin{bmatrix} \mu & \sigma \\ \gamma & \delta \end{bmatrix} \begin{bmatrix} x_1 \\ x_2 \end{bmatrix} \tag{9}$$

$$W = \begin{bmatrix} \mu & \sigma \\ \gamma & \delta \end{bmatrix} \tag{10}$$

Then **Eq. (9)** can be rewritten using matrix –by-vector form as:

$$S = W X \tag{11}$$

Where (μ, σ, γ, δ), a set of unmixing coefficients.

2.3 QNN and its Learning Algorithm

FFNNs must use the sample information as a mere reference for creating the internal representations, thus, it should not encode the sample information accurately into the internal representations. Such an exact or faithful encoding of the sample information results in the FFNN memorizing the “crispness” in the training data set. But an inherently fuzzy architecture should be capable of generalizing the sample information into various graded levels of certainty over the entire feature space. This may be possible if the architecture is capable of creating graded internal representations from the sample information. The QNN is as architecture capable of allowing the sample information to be encoded into certain levels grades of certainty/uncertainty only, **Jarernsri, 2003**.

One simple way of incorporating the ability to form consistent multilevel partitions in the hidden layer is to create hidden unit partitions with the property of “spreading-out” over regions of uncertainty in the feature space and collapsing-in over regions of certainty. If all the hidden unit transfer functions have the ability to form “graded” partitions instead of the crisp linear partitions, then these partitions can be “collapsed-in” or “spread-out” as required, using a suitable algorithm. Such an algorithm will not require that the fuzzy measures on the feature space be known, but will be a general procedure for learning the imprecision and uncertainty in the data set. This motivates the study of hidden units with *multilevel* transfer functions, **Jarernsri, 2003** and **Gopathy, 1996**.

Suppose the multilevel hidden unit has n_s discrete *states* or *levels*. Then its transfer function can be written as a superposition of ns sigmoidal functions, each shifted by θ^r. The output of this multilevel unit can be written as $(1/n_s)\sum_{r=1}^{n_s}$ sgm$(v^T x - \theta^r)$ where v is the connected weight matrix between input and the hidden units in hidden layers, and x is the input feature vector . The step widths of the multilevel transfer function, which may be called the quantum intervals, will be representative of discrete localized cells in the feature space consisting of feature vectors with approximately the same level of uncertainty as to their membership to the classes in the data set. These quantum intervals “jump-positions” θ^r unlike the step widths, step heights need not be learned by independent parameters because several sigmoid can be shifted to the same location and added together to give steps of desired heights, to an approximation which reduces total number of parameters to be learned by almost one-third, **Gopathy, 1996**.

QNN consists of n_i inputs, one hidden layer of n_h nodes, each one represents a multilevel units and n_o outputs. Output units can be linear or sigmoid. Let $\mathbf{x_k}=[x_{1,k}, x_{2,k}, \ldots, x_{n,k}]^T$, k=1,..,.m , be the k^{th} feature vector of the data set **X**. Then the input to the j^{th} hidden unit from the k^{th} feature vector is:

$$\bar{h}_{j,k} = \sum_{l=0}^{n_i} v_{jl}\, x_{l,k} \tag{12}$$

$$\tilde{h}_{j,k} = \frac{1}{n_s}\sum_{r=1}^{n_s} h_{j,k}^r \quad = \frac{1}{n_s}\sum_{r=1}^{n_s} \mathrm{sgm}(\beta_h(\bar{h}_{j,k} - \theta_j^r)) \tag{13}$$

Where $h_{j,k}^{\sim}$: the response of the j^{th} multilevel hidden unit from k^{th} is feature , $sgm(\tau) = \frac{1}{1 + e^{(-\tau)}}$: is a sigmoid function (unipolar), β_h a slope factor for all multilevel hidden units in hidden layer, θ_j^r define the jump positions in transfer function, and n_s is the number of levels or sigmoids in the multilevel hidden unit, **Fig. 2 (a)** plots the response $h_{j,k}^{\sim}$ of j^{th} four level quantum neuron as a function of its input $h_{j,k}^{-}$ with equal step heights and **Fig. 2 (b)** demonstrates multilevel transfer function with unequal step heights through simple shifting ,**Jarernsri, 2003**.

$$y_{i,k}^{-} = \sum_{j=0}^{n_h} w_{ij}\, h_{j,k}^{\sim} \tag{14}$$

With $h_{0,k}^{\sim} = 1$, $\forall k$ therefore, the response of the i^{th} output unit for the k^{th} input feature vector can be written as:

$$y_{i,k}^{\wedge} = sgm(\beta_o\,(y_{i,k}^{-})) \tag{15}$$

The major steps of QNN learning algorithm are summarized and presented as follows:

A) Update the synaptic weights:

Step 1: Select $\alpha, \alpha_\theta, \beta_h, \beta_o$ (by trail and error) and randomly initialize the weights (**W** & **V**) and values of jump positions θ_j^r.

Step 2: Present k^{th} input pattern and specify the desired output.

Step 3: Calculate actual output $y_{i,k}^{\wedge}$, using the present values of V_{jl} and W_{ij}.

Step 4: Find the error terms ($\overset{o}{e}_{i,k}$) and ($\overset{h}{e}_{j,k}$).

Calculate the output error.

$$\overset{o}{e}_{i,k} = (y_{i,k} - y_{i,k}^{\wedge})\; y_{i,k}^{\wedge}(1 - y_{i,k}^{\wedge}) \tag{16}$$

Calculate the hidden layer error term.

$$e_{j,k}^{h} = \left(\frac{1}{n_s}\sum_{r=1}^{n_s} h_{j,k}^{r}(1 - h_{j,k}^{r})\right)\sum_{p=1}^{n_o} e_{p,k}^{o} w_{pj} \tag{17}$$

p is over all nodes in the layer above node j.

Step 5: Adjust the synaptic weights:

$$w_{ij,k} = w_{ij,k-1} + \alpha e_{i,k}^{o} \frac{1}{n_s}\sum_{r=1}^{n_s} sgm(\beta_h\,(h_{j,k}^{-} - \theta_j^{r})) \tag{18}$$

$$v_{jl,k} = v_{jl,k-1} + \alpha\,\beta_h\,(\frac{1}{n_s}\sum_{r=1}^{n_s} h_{j,k}^{r}\,(1 - h_{j,k}^{r})\; x_{l,k} \tag{19}$$

Where, k + l , k , and , k - l index next, present, and previous respectively, and is a learning rate.

Step 6: Present another input pattern and go back to step 2
All of the training samples are presented cyclically.

B) Update the quantum intervals:
Step 1: In each training cycle, calculate the outputs $\hat{y}_{i,k}$, and $v^r_{q,k}$ for each hidden node.
Then, take the average values for each class, $\langle \tilde{h}_{j,c_m} \rangle$, $\langle v^s_{j,c_m} \rangle$, for m^{th} class during the training of QNN is as:

$$\langle \tilde{h}_{j,c_m} \rangle = \frac{1}{|c_m|} \sum_{x_k : x_k \in c_m} \tilde{h}_{j,k} \tag{20}$$

$$\langle v^r_{j,c_m} \rangle = \frac{1}{|c_m|} \sum_{x_k : x_k \in c_m} v^r_{j,k} \tag{21}$$

$|c_m|$ = The cardinality of m^{th} class

Step 2: Calculate the quantum interval adjustment $\Delta\theta^r_q$ for each level:

$$\Delta\theta^r_j = \alpha_\theta \frac{\beta_h}{n_s} \sum_{m=1}^{n_o} \sum_{x_k : x_k \in c_m} \left(\langle \tilde{h}_{j,c_m} \rangle - \tilde{h}_{j,k} \right) \left(\langle v^s_{j,c_m} \rangle - v^s_{j,k} \right) \tag{22}$$

Where α_θ **is** the learning rate.

Step 3: Update jump-positions by:

$$\theta^r_j = \theta^r_j + \Delta\theta^r_j \tag{23}$$

Step 4: Continue next cycle and go back to step 2.

Nomenclature:
n_o= number of output nodes.
n_i= number of input nodes.
n_s= number of quantum interval.
θ^r_j = value of r^{th} jump-position of hidden node j.
w_{ij} = the strength of connection between j^{th} hidden node and i^{th} output node.
v_{jl}= the strength of connection between l^{th} input node and j^{th} hidden node.
$\hat{y}_{i,k}$ = actual output at output node i for k^{th} input pattern.
$y_{i,k}$= desired output at output node i.
$e^o_{i,k}$ & $e^h_{j,k}$ = error terms of output node i and hidden node j for k^{th} input pattern.
$h^r_{j,k} = \mathrm{sgm}\,(\bar{h}_{j,k} - \theta^r_j))$
$\bar{h}_{j,k} = \sum_{l=0}^{n_i} v_{jl}\, x_{l,k}$, the internal state of hidden node j for k^{th} input pattern.
$\tilde{h}_{j,k} = \frac{1}{n_s} \sum_{r=1}^{n_s} h^r_{j,k}$, the output of j^{th} hidden node.

$v_{j,k}^{r} = h_{j,k}^{r}(1 - h_{j,k}^{r})$.

3. RESULTS AND DISCUSSION

3.1 Results of using ANN Classifier

Three layer ANN was employed as classifier, for Iris data set signal, network structure is 4-16-3 namely input vector (n_i) is equal to (4) representing number of input variables. The 4 rows (sepal length, sepal width, petal length, and petal width) contained a single hidden layer, number of hidden units was chosen by trial and error; which revealed that number of neurons at hidden layer (n_h) is at least greater than twice of input nodes (n_i) correspond to features of each species, as an assumption (n_h = 4*n_i) for good performance (n_h = 16) traditional neuron with sigmoid activation function (unipolar), and output layer contains number of neuron equivalent to classes (species), (n_o= 3), structure of the ANN classifier is shown in **Fig.3** with number of nodes at each layer.

Three layers ANN was employed as classifier of Iris data signal, randomly select input feature vectors to achieve the uncertainty principle. Randomly selected 70% samples as training samples and 30% for testing samples. Learning rate (η) is chosen by trial and error for weigh adjusting(W_{ij}, V_{jl}) is set to (0.01) MATLAB programming test, the number of iteration (epochs) is set to 1500.

The performance of ANN classifier (for both training and testing phases) is shown in **Fig.4** and for training data set; ANN gave a Mean Square Error (MSE) of (0.0054) and accuracy of (100.00%).

For testing phase, ANN classifier showed a mean square error MSE of (0.1174) with accuracy of (93.334%). **Fig.4** shows the relationship between MSE and number of iteration for ANN classifier. As can be seen that MSE is decreasing with increasing number of iterations, which revealed that the network is converged with iteration number of (1500) and MSE of (0.0054).

3.2 Results of using QNN Classifier

Three layers QNN was employed as classifier of Iris data signal, the performance of the QNN was tested to perform classification on Iris data signal. Randomly selected 70% of the samples are used for training (training input feature vectors) and 30% for testing (testing input feature vectors), the structure is 4-8-3 for the neural network, input vector(n_i) is equal to (4).

The number of multi-level hidden units (which are used in the hidden layer of QNN rather than traditional neurons as in ANN) with the number of multi-level neurons (n_h) is no more than twice of the input nodes (n_i), in such structure of (2*n_i), i.e. (n_h=8) multi-level hidden units with sigmoidal activation function (unipolar), and the output layer contains neurons equivalent to number of species (n_o= 3). The major difference between QNN and ANN is that the QNN uses quantum neuron (multi-level neuron (graded) with sigmoid activation function), structure of QNN classifier is shown in **Fig.5**). It contains a single hidden layer with (n_h = 8) units, three output units (no. of species) and 4 input nodes, also identifies by existence of jump-positions (thetas' values) of multi-level hidden units of the QNN hidden units were chosen by trial and error.

The QNN is composed of multi-level hidden units with (**n_s** = 3) (chosen by trial and error) levels for each hidden unit, the learning rate (learning ratio) (η) for weigh adjusting(W_{ij}, V_{jl}**)** is set to (0.07) training by MATLAB test, and the learning rate for quantum interval adjusting (eta_theta η_θ) is set to (0.001), and slop factor for unit at hidden layer $\beta_h = 2$, but for output layer slop factor β_o = 1.5, the number of iteration (epochs) is set to (300). Synaptic weights(W_{ij}, V_{jl}**)** are adjusted by minimizing quadratic error function with respect to particular weights, in training itself; jump-positions of multi-level hidden units adjusted also.

Results are done with (70%) of input feature vectors for training phase and (30%) of input feature for testing phase, performance of QNN classifier shown in **Fig.6** and summarized with (1)MSE of (0.1258) and accuracy of (97.143%) for training phase (2) MSE (0.3780) with accuracy of (97.778%) for testing phase. **Fig.6** displayed the relationship between MSE and number of iteration for QNN classifier, in which reveals that MSE is decreasing with increasing number of iterations, but when the iteration number exceeded 150 the MSE decreases very slightly which means the network is converged with iteration number of (150) and MSE of (0.1258). As in **Fig.4**, **Fig.6** shows an inverse relationship between MSE and number of iterations.

Main difference between two figures is that QNN converges with less iteration, **Fig.6** shows convergence occurs at (150) in QNN classifier compared with (1500) for ANN.

3.3 QNN vs. ANN Classifiers

To discuss the results of ANN and QNN classification for Iris data signals (QNN vs. ANN classifiers), table 1 shows a comparison between them. Two issues can be concluded from table1, first one is that QNN classifier gave better accuracy for testing phase compared with ANN classifier (97.778% compared with 93.334%) and second issue is that QNN converged with less number of iterations (150 epochs for QNN compared with 1500 epochs for ANN), and this indicates that the time required for QNN convergence is about (90%) less than that of ANN.

The reason is that ANN is unable to correctly assign class membership to data samples belonging to regions of the feature space where there is overlapping among the classes. The reason for this is that FFNNs use sharp decision boundaries (due to crisp membership function) to partition the feature space. As a result, the outputs of trained ANNs cannot generally be interpreted as membership values. Also it can be found that QNN is more reliable than the ANN because QNN generates a more structured representation of the input data at the hidden layer than that of the ANN as QNN use multilevel hidden units, this is not surprising, given the fact that the jump-positions of the multi-level hidden units of the QNN are updated by minimizing some measure based on the class-conditional variances at the outputs of the hidden units.

Another advantage is that QNN systems are using quantum neuron instead of traditional neuron which is often able to learn faster and require less number of neurons in the hidden layer which could lead to a smaller number of weights and reduction of the number of neurons in the hidden layer which could lead to smaller number of weights, or it can be said generally that this means reducing the total number of parameters (input weights, output weights, jump position) to be learned by almost half, as an assumption to the total number for hidden units in hidden layer is with($4*n_i$) empirically for best accuracy in ANN classifier, while assumption to the total number for multilevel hidden units in hidden layer is with($2*n_i$) empirically for best accuracy in QNN classifier. This means that the total number of parameters (input weights, output weights, jump position) to be learned is reduced by almost half which represents another advantage for QNN.

Here the number of multilevel hidden units in the hidden layer was set to (8) by QNN but (16) by ANN, the input weights is (**V**(8x4)) and output weight (**W**(3x8)) and jump position with (8x3)matrix by QNN while the input weight is (**V**(16x4)) and output weight is (**W**(3x16)) for ANN.

4. CONCLUSSIONS

In this paper, a data classification system based on multi-level transfer function integrated Quantum Neural Networks (QNN) is proposed. The classification system methodology consists of ion signals which here iris data. First, the classification signals should be normalized then feature extraction is applied using independent component analysis technique then classification task is to be achieved firstly using artificial neural network classifier and secondly using integrated Quantum Neural Networks (QNN).

The architecture of (QNN's) has inherently built in fuzzy, hidden units of these networks (QNN's) to develop quantized representations of sample information provided by the training data set in various graded levels of certainty. Experimental results presented here show that (QNN's) are capable of recognizing structures in data, a property that conventional (FFNN's) with sigmoidal hidden units lack. In addition, (QNN) gave a kind of fast and realistic results compared with the (FFNN). Simulation results indicate that QNN is superior (with total accuracy of 97.778%) than ANN (with total accuracy of 93.334%).

REFRENCES

Abninder L., Chris E., Frederick W. K., Steven W., and Paul T.,2006, *Is the Brain a Quantum Computer?,* Cognitive Science Society, University of Waterloo, No.30, pp. 593–603.

Gopathy Purushothaman and Nicolas. B. Karayiannis, 1996, *Quantum Neural Networks (QNNs): Inherently Fuzzy Feedforward Neural Networks*, IEEE Transactions On Neural Networks, Vol.2, pp. 1085-1090.

Isabelle G., Steve ., Masoud N., and Lotfi A. Z., 2006, *Feature Extraction Foundations and Applications, USA and United Kingdom.*

James V. Stone, 2004, *Independent Component Analysis A Tutorial Introduction*, A Bradford Book The MIT Press Cambridge, Massachusetts London, England.

Jarernsri. L. Mitrpanont, and Ananta Srisuphab**,** 2003 *The Realization of Quantum Complex-Valued Backpropagation Neural Network in Pattern Recognition Problem*.The 9th. International Conference on Neural Information Processing (ICONIP'OZ) Vol. 1.

Joshua B. T., Vin de Silva, and John C. L., A, 2000 *Global Geometric Framework for Nonlinear Dimensionality Reduction, Science,* Vol.290, pp. 2319-2323, USA.

Lov. K. Grover, 1997 *Quantum Mechanics Helps in Searching for a Needle in a Haystack*, American Physical Society, Vol 79,Issue 2, pp. 325–328.

Xin-Yi T., Yu-ju J. Chen, S. C., and Rye C. Hwang, 2005, *Quantum NN vs. NN in Signal Recognition*, Proceedings of the Third IEEE International Conference on Information Technology and Applications.

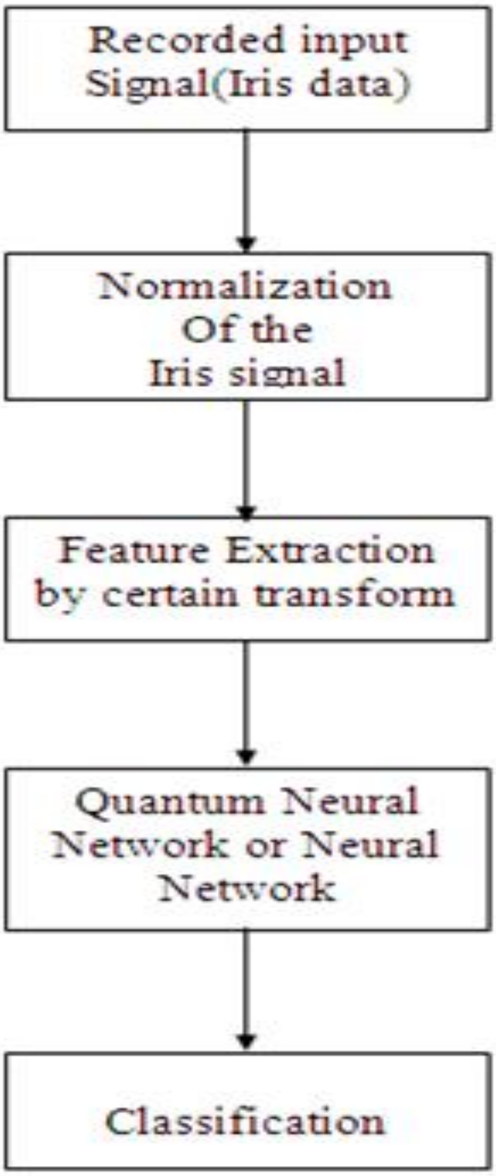

Figure 1. Block diagram of the methodlogy for signal classification system.

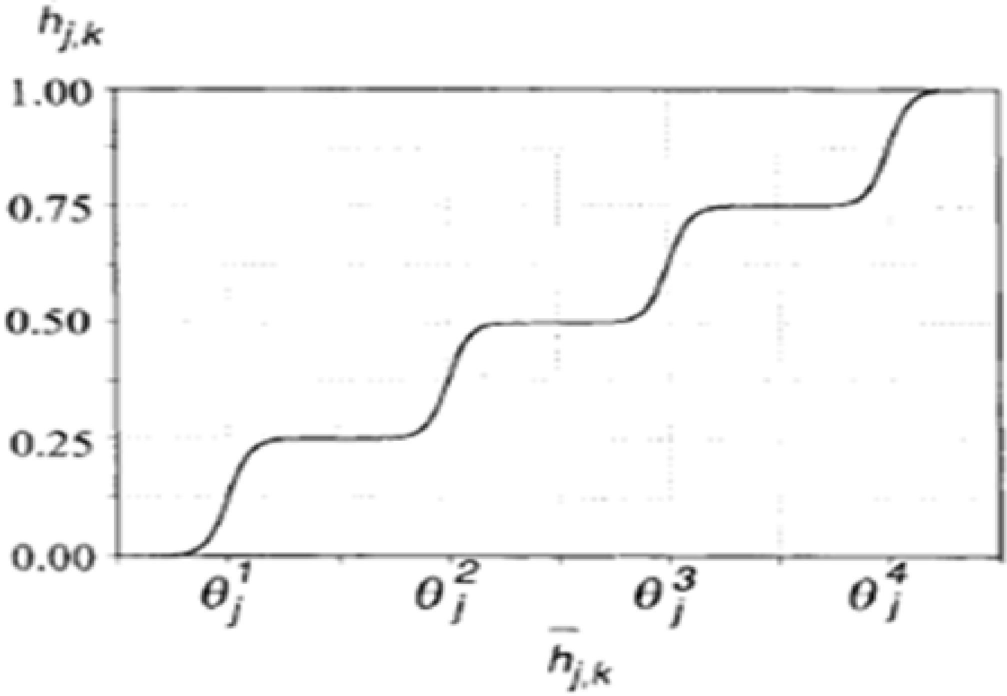

(a)

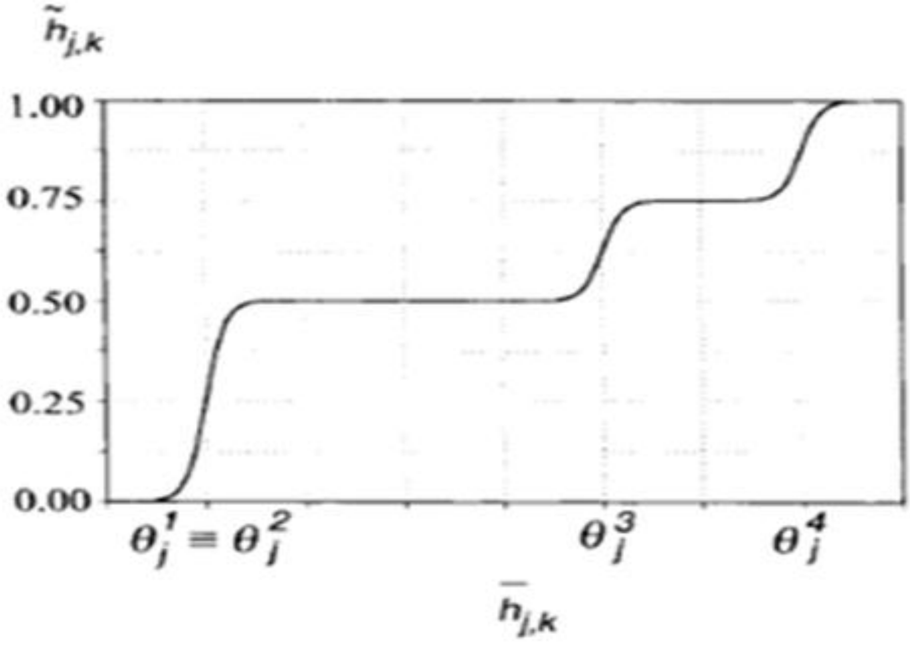

(b)

Figure 2. Multilevel transfers function with (a): equal step heights (b): unequal step heights.

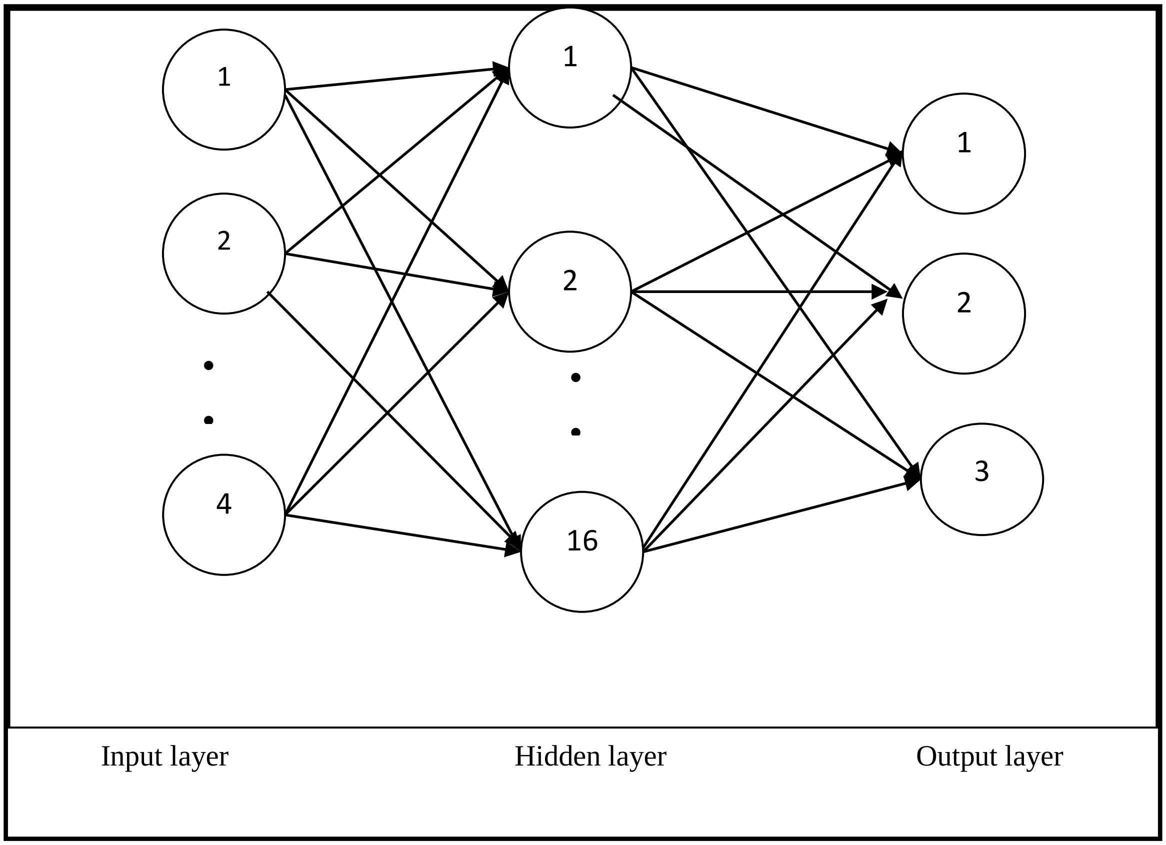

Figure 3. Structure of the Artificial Neural Network (ANN) classifier.

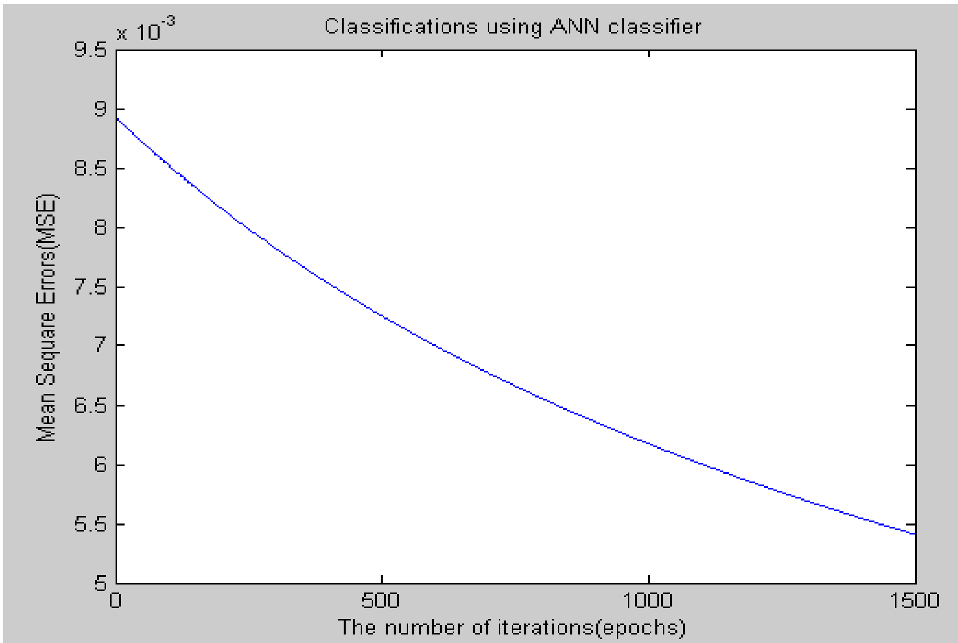

Figure 4. Classification of signals by ANN classifier.

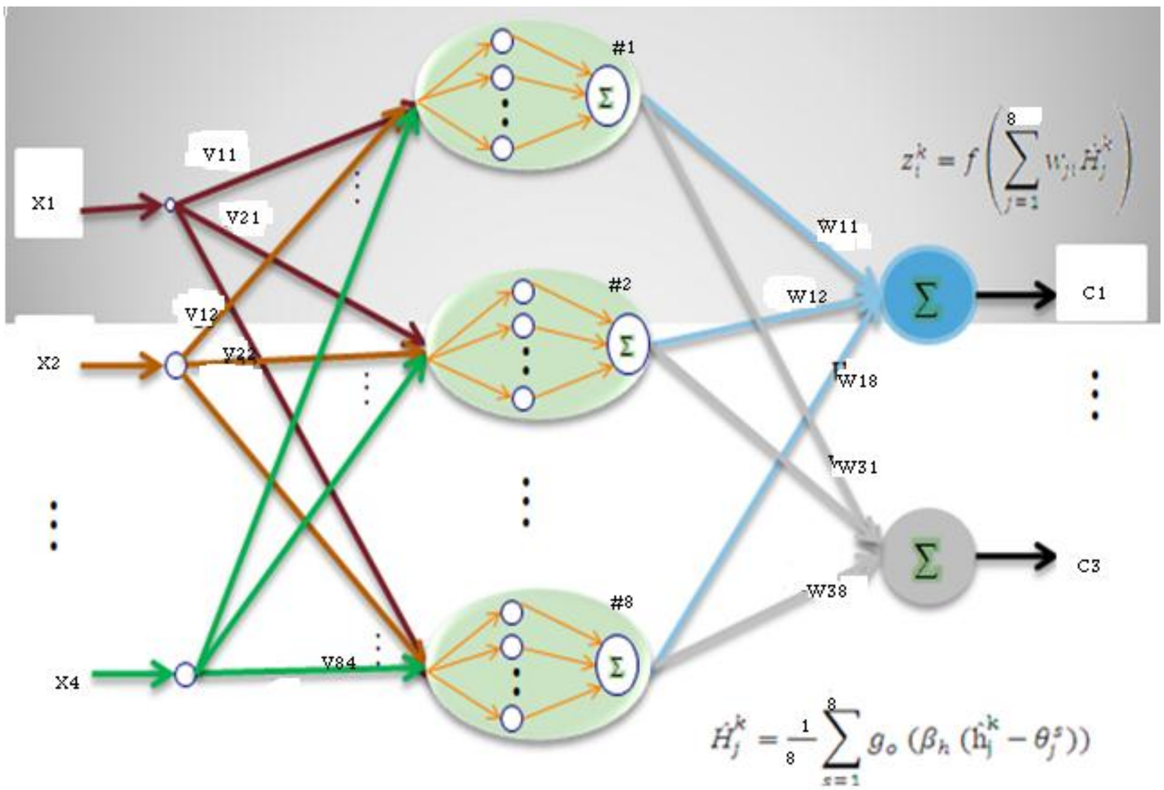

Figure 5. Structure of Quantum Neural Network (QNN) classifier.

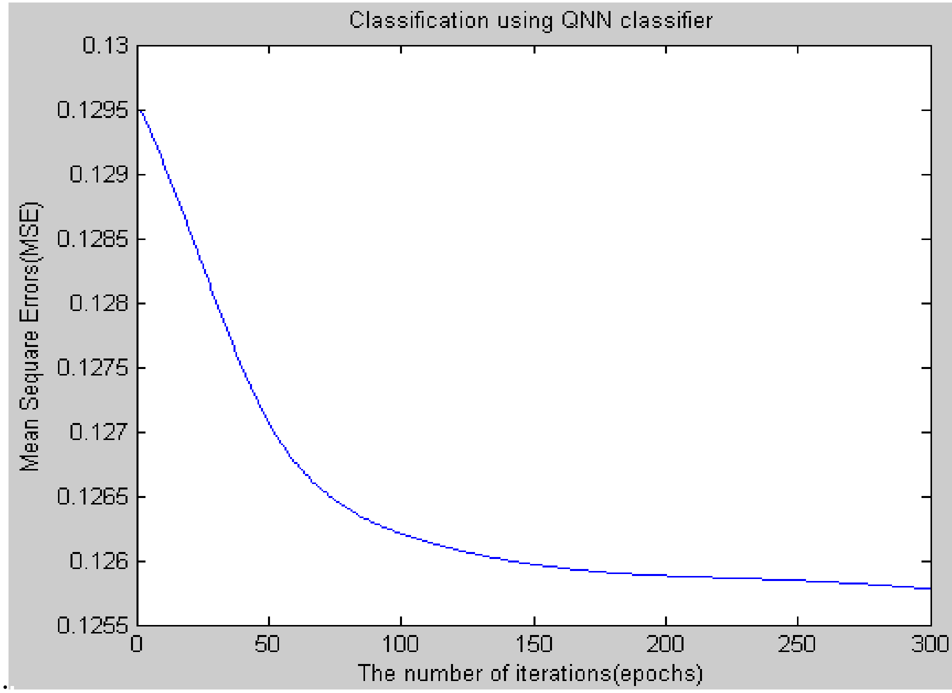

Figure 6. classification of signals by QNN classifier.

Table 1. Classification and performance using ANN and QNN classifiers.

Network classifier type	MSE for training set	Accuracy for training set (%)	No. of epochs for convergence	MSE for testing set	Accuracy for testing set (%)
ANN classifier	0.0054	100.00	1500	0.1174	93.334
QNN classifier	0.1258	97.143	150	0.3780	97.778

Linguistic Fuzzy Trust Model over Oscillating Wireless Sensor Networks

Firas Ali Al-Juboori
Ph. D.
College of Engineering - University of Baghdad
Email: firasaljuboori@yahoo.com

Sura Fawzi Ismail
M.Sc. Student
College of Engineering - University of Baghdad
Email: surafawzi7789@yahoo.com

ABSTRACT

Simulation of the Linguistic Fuzzy Trust Model (LFTM) over oscillating Wireless Sensor Networks (WSNs) where the goodness of the servers belonging to them could change along the time is presented in this paper, and the comparison between the outcomes achieved with LFTM model over oscillating WSNs with the outcomes obtained by applying the model over static WSNs where the servers maintaining always the same goodness, in terms of the selection percentage of trustworthy servers (the accuracy of the model) and the average path length are also presented here. Also in this paper the comparison between the LFTM and the Bio-inspired Trust and Reputation Model for Wireless Sensor Networks (BTRM-WSN) in terms of the accuracy and the average path length suggested by each model is presented. Both models give quite good and accurate outcomes over oscillating WSNs. Also it must be mentioned that the evaluation environment used here is Trust and Reputation Model Simulator for WSN.

Key words: oscillating WSN, linguistic fuzzy trust model, bio-inspired trust and reputation model for wireless sensor networks, trustworthy servers, and malicious servers.

اختبار نموذج ضبابي الثقة على شبكات الاستشعار الاسلكية المتأرجحة

فراس علي الجبوري
مدرس
كلية الهندسة - جامعة بغداد

سرى فوزي اسماعيل
طالبة ماجستير
كلية الهندسة - جامعة بغداد

الخلاصة

هذا البحث يتناول برنامج محاكاة بالحاسبة لنموذج ضبابي الثقة على شبكة استشعار لاسلكية متأرجحة حيث كفاءة الخوادم التابعة لها متغيرة مع الزمن وايضا هذا البحث يتناول المقارنة بين النتائج المكتسبة من تطبيق النموذج على شبكة استشعار لاسليكة متأرجحة مع النتائج التي حصل عليها من التطبيق على شبكة استشعار لاسلكية ثابتة حيث كفاءة الخوادم ثابتة والمقارنة هنا من ناحية دقة النموذج ومتوسط طول المسار .هذا البحث يتناول أيضا المقارنة بين النتائج من تطبيق النموذج ضبابي الثقة مع نموذج ذو استيحاء حيوي لقياس الثقة من حيث دقة وطول الطريق وكلا النموذجين يعطي نتائج جيدة جدا ودقيقة على شبكات الاستشعار اللاسلكية المتأرجحة.

1. INTRODUCTION

Wireless sensor networks or sensor networks are composed of a large number of sensor nodes deployed densely in a closed proximity to collect data to a specific function. Sensors have limited memory, computational capability, and limited transmission capacity. The sensors primarily preprogrammed to collect the data and forward to the base station through defined communication path. If the information is sensitive, the nodes and communication path must be trustworthy. The sensor network possesses the self-organizing capability if the positions of nodes are not predetermined. Irrespective of the topology, each node must trust the successive node in the path. If any node in the path is suspicious, the decision node must calculate the alternative path.

This paper take the scheme that assumes some nodes of the network request some services (and act, therefore, as clients) and some others provide those services (thus acting as servers or services providers). Here suppose that every sensor is only able to communicate with its direct neighbors (that is, it cannot establish a direct communication with a node more than one hop ahead. They are, however, susceptible to a large number of security threats, **Mármol**, and **Pérez**, **2009a**, some of which might be effectively mitigated with an accurate trust and reputation management, **Marsh**, **1994**, **Marti**, and **Garcia-Molina**, **2006**. Many researches about trust and reputation management models have been recently proposed as an innovative solution for guaranteeing a minimum level of security between two entities belonging to a distributed system that want to have a transaction or interaction. Thus, many models have been designed and developed in this direction.

Many methods, technologies and mechanisms like fuzzy logic, **Tajeddine**, **et al.**, **2006**, bayesian networks, **Wang**, **et al.**, **2006**, or even bio-inspired algorithms, **Mármol**, and **Pérez**, **2011**, have been proposed in order to manage and model trust and reputation in systems such as P2P networks, **Almen´arez**, **et al.**, **2004**, ad-hoc ones, **Moloney**, and **Weber**, **2005**, wireless sensor networks, **Boukerche**, **et al.**, **2007**, or even multi-agent systems, **Sabater**, and **Sierra**, **2001**.

The simulation of the trust model, Linguistic Fuzzy Trust Model (LFTM) over oscillating Wireless Sensor Networks is presented here. This model enhances the interpretability of previous model, BTRM-WSN (Bio-inspired Trust and Reputation Model for Wireless Sensor Networks), **Mármol**, and **Pérez**, **2011**, and makes it closer to the final user with relatively improvement in the accuracy of it. BTRM-WSN is a model based on a bio-inspired algorithm called ant colony system (ACS), **Dorigo**, and **Gambardella**, **1997**, where ants build paths fulfilling certain conditions in a graph. These ants leave some pheromone traces that help next ants to find and follow those routes.

The simulation of the BTRM-WSN model over oscillating WSNs is presented in paper, **Mármol**, and **Pérez**, **2011**, while in this paper the simulation of the LFTM model over oscillating WSNs is presented, and the comparison between the simulations of the two models over oscillating Wireless Sensor Networks is also presented here. Here the simulation is focused in two targets. First, interesting in finding out how many times a model is able to select the right benevolent server to interact with. In other words, the selection percentage of trustworthy servers is calculated; Second, in calculating the average path length suggested by a model. The rest of this paper is organized as follows: An overview of the Linguistic Fuzzy Trust model is presented in section 2. In section 3 simulation results of experiments and comparison between simulation of the BTRM-WSN and LFTM models over oscillating Wireless Sensor Networks are discussed. In section 4 conclusions is described.

2. LINGUISTIC FUZZY TRUST MODEL

This model is an enhancement for the pervious trust and reputation model, BTRM-WSN model, **Mármol**, and **Pérez**, **2011**, which uses linguistic fuzzy sets and fuzzy logic for the enhancement. On one hand, it will be enjoyed the representation power of linguistically labeled fuzzy sets, as is the case, for instance, of the satisfaction of a client or the goodness of a server. On the other hand, it will be exploited the inference power of fuzzy logic, as in the imprecise dependencies between the originally requested service and the actually received one, or the punishment to apply in case of fraud. The expected outcome will be an easy-to-interpret system with competitive performance.

A set of linguistic labels describing several levels of a variable or concept could be associated to a fuzzy set. The set is defined in a way that captures the underlying notion of such word for that particular concept. Typical linguistic labels include 'very low', 'low', 'medium', 'high', and 'very high'. The defined fuzzy sets associated to such labels for the case of client satisfaction are depicted in **Fig. 1**.

Fuzzy rules can be expressed in several forms. A rule is composed of an antecedent part, where the activation condition is expressed, and a consequent part, where an action or a conclusion is presented. The antecedent is usually a logic expression. In fuzzy rules, a basic logic expression is the membership of a variable value to a set. These basic expressions are then connected with logic connectives, being the most common, the AND operator. Likewise, the most common consequent is the membership of an output variable to a fuzzy concept. These are known in fuzzy terminology as Mamdani-type rules. In fuzzy logic, the truth value of logical expressions is not binary but ranges from zero to one allowing for partial truth. The fuzzy logic operators, AND, OR, and NOT are adapted to allow for such partial truth. Fuzzy operators also produce a partial truth value to the whole logic expression. A typical if–then linguistic fuzzy rule would look like:(**If *quality* is Good AND *price* is Low THEN *satisfaction* is Very High)**

The perception of quality being good or price being low may vary from total confidence to no confidence at all. But, unlike traditional logic, it may also be any value in between. In other words, a price being low can be partially true. This partial truth for each condition is combined through the fuzzy AND operator and the whole logic sentence of the antecedent is so evaluated. As can be guessed, the truth value of the consequent part is precisely that one achieved by the whole antecedent logic expression. For example, the truth value of the expression 'quality is Good AND price is Low' is 0.3, then the system concludes that the expression 'satisfaction is Very High' has a truth value of 0.3. When in a given situation, several fuzzy rules are activated; a collection of conclusions is produced. These separate conclusions are aggregated into a final result and, defuzzified back into a numerical value. Details of how fuzzification, fuzzy inference, aggregation, and defuzzification work can be found in, **Pedrycz**, and **Gomide**, **1998**, **Jang**, **et al.**, **1997**. The defuzzification method chosen to be used in this paper is Center of Gravity.

The flow of the Linguistic Fuzzy Trust Model is depicted in **Fig. 2**, emphasizing those steps where it actually applied linguistic fuzzy sets and fuzzy logic. Such steps are:

1) The trust and reputation model BTRM-WSN selects the server to have a transaction with.
2) Such server has a perceived certain goodness ("Very high", "High", "Medium", etc.).
3) According to the required service attributes and the server goodness, the server provides a better, worse or equal service than the expected.

4) Both the required service and the actually received one are compared, using certain subjective weights for the services attributes.
5) The client satisfaction is assessed by means of the services comparison performed in previous step, and the client conformity.
6) Finally, the punishment level is determined by the client satisfaction with the received service, together with his/her goodness.
More detailed about the use of linguistic fuzzy sets in the Linguistic Fuzzy Trust Model is described in, **Mármol**, **et al.**, **2011**.

3. EXPERIMENTS AND RESULTS

The tested scenario consisted of Wireless Sensor Networks where the goodness of the servers belonging to them could change along the time. How a sensor decides to be benevolent or malicious at each time is out of scope of this paper.
The following proposal takes in this paper: after every 20 transactions are carried out (i.e., after every client has had 20 transactions) all the benevolent servers composing the Wireless Sensor Network become malicious. **Fig. 3** shows this proposal.
In **Fig. 3** when the peer behavior is 1, the server is benevolent server but when the peer behavior is 0, then the server is malicious server. In order to preserve the same percentage of malicious servers, the number of previous benevolent servers, say *nb*, is kept. Then *nb* random servers are selected (note that all of them will be malicious) and their goodnesses are swapped so they become benevolent and the percentage of malicious servers remains equal to the stage previous the oscillation. With an oscillation scheme like this a benevolent server could maintain its positive goodness since it could be randomly selected to become benevolent when it indeed previously was benevolent.
The evaluation environment used is Trust and Reputation Model Simulator for WSN, **Mármol**, and **Pérez**, **2009b**, which is a generic framework serving as an assistant tool to easily implement trust and reputation mechanisms in distributed environments and to compare between them.
Here the experiments focused on two main targets. First, interesting in finding out how many times the model is able to select the right benevolent server to interact with. In other words, the selection percentage of trustworthy servers or the accuracy of the model is calculated. In order to consider a trust and reputation model as acceptable (with a minimum quality level), it is assumed that the model is not useful at all if the selection percentage of the trustworthy servers is less than 50%, since a smaller percentage would result in a model with certain security deficiencies. Secondly, it is aimed to find the closest benevolent servers to the client requesting the service. On the one hand it is more secure and robust if the lesser number of intermediaries present in a transaction. On the other hand, due to the specific restrictions related to Wireless Sensor Networks, the resources consumption saving is a critical issue. Therefore, a shorter path leading to the final trustworthy server implies less involved sensors and, consequently, less global utilization of resources such as energy or bandwidth.
The experiments that carried out here had the following structure. The model is launched 100 times (i.e. each client applied for a service 100 times) over 100 WSNs randomly generated, each one composed of 100 sensors. On each network, the percentage of sensors acting as clients was always a 15%, 5% acts as relay servers (those that not providing the service requested by the clients) and the 80% left were, therefore, sensors acting as trustworthy or malicious servers. With tried the model over 100 random WSNs having a 10% (over the 80% left) of malicious servers.

100 with 20%, other 100 with 30%, and so on until a 90% of malicious servers (the worst simulated situation). But even more, those experiments are repeated over WSNs composed of 200, 300, 400 and 500 sensors. This parameters and others used to perform the experiments are listed in **Table 1**.

3.1 Experiments and Results of Linguistic Fuzzy Trust Model over Oscillating Wireless Sensor Networks

3.1.1 Selection percentage of trustworthy servers

Fig. 4 shows the results achieved with LFTM model over static and oscillating WSNs. It is observed from **Fig. 4(a)** which is outcomes achieved with LFTM model over static networks that the selection percentage of trustworthy servers is quite high (above the 90%) when the percentage of malicious servers is greater than or equal to 60% regardless the size of the networks. And the maximum accuracy reached when the percentage of malicious servers is 90% and the size of the network is 300 nodes which it is (99.62%), and even in the worst case when the percentage of malicious servers is 90% and the size of the networks is 500 nodes, the accuracy is (97.96%) which it is still a high value. In general the selection percentage of trustworthy servers increases as the percentage of malicious servers increases regardless the size of the networks; the reason for the increase in the accuracy of the model as the number of malicious servers increases is that the ants spread a given total amount of pheromone and that when the number of good servers is small, the paths to these are more strongly selected. In a way, the fewer the number of good servers is, the easier is for them to shine or excel.

While it is observed from **Fig. 4(b)** which is the corresponding result for LFTM over oscillating WSNs that the selection percentage of trustworthy servers is (less than 50) when the percentage of malicious servers is 10% regardless the size of the network, which makes the model not useful at all, because here assume that if the selection percentage of trustworthy servers is under the 50%, then the model is completely useless, and the accuracy began to increase by increasing the percentage of the malicious servers. The selection percentage of trustworthy servers is quite high (above the 90%) when the percentage of malicious servers is greater than or equals to 70% regardless the size of the networks. The maximum accuracy reached here, when the percentage of malicious servers is 90% and the size of the network is 300 nodes which it is (99.13%), and even in the worst case when the percentage of malicious servers is 90% and the size of the networks is 500 nodes, the accuracy is (97.03%) which it is still high value. The selection percentage of trustworthy servers increases as the percentage of malicious servers increases regardless the size of the network, the reason again for the increase in the accuracy by increasing the number of malicious servers is that the ants spread a given total amount of pheromone and that when the number of good servers is small, the paths to these are more strongly selected. And in general the accuracy of the model over oscillating WSNs are slightly less than the accuracy of the model over static WSNs and this differences in the accuracy achieved with the model over static WSNs and over oscillating WSNs decreases as the percentage of malicious servers increases.

It is observed from the two figures **Fig. 4(a)** and **Fig. 4(b)** that for a certain percentage of malicious servers the results about the selection percentage of trustworthy servers is close to each other when the size of the network is less than or equal to 400 nodes while when the size of the network is 500 nodes the outcomes about the selection percentage of trustworthy servers is different from each other.

3.1.2 Average path length leading to trustworthy servers

The results achieved with LFTM model over static and oscillating Wireless Sensor Networks are shown in **Fig. 5**. It is observed from **Fig. 5(a)** which is the results achieved with LFTM model over static WSNs that the average path length decreases as the percentage of fraudulent servers increases regardless the size of the network, and it is also observed that when the percentage of malicious servers is greater than or equal to 80% the average path length is approximately equal to (2.2) which it is small value.

While it is observed from the simulation of the model over oscillating WSNs, **Fig. 5(b)** that the average path length decreases as the percentage of malicious servers increases regardless the size of the network, it is also observed that when the percentage of malicious servers is greater than or equal to 80% the average path length is never exceed (2.5) which it is still small value. But for a certain percentage of malicious servers and a certain size of network the average path length suggested by LFTM model over oscillating WSNs is longer than the average path length suggested by the model over static WSNs, such as for example when the percentage of malicious servers is 10% and the size of network is 300 nodes then the average path length suggested by the model over static WSNs is (5.01) while the average path length suggested by the model over dynamic WSNs is (10.68) and this differences between the average path length suggested by the model over static WSNs and the average path length suggested by the model over oscillating WSNs decreases as the percentage of malicious servers increases.

Finally, the appreciation that can be given from the results of the average path length together with the selection percentage of trustworthy servers constitute the proof that LFTM obtains quite good, accurate outcomes with slight differences in outcomes over oscillating Wireless Sensor Networks as compared with static scenario, since with an oscillation scheme the same percentage of malicious servers remains equal to the stage previous the oscillation. And also the outcomes in general slightly differ from one set of random WSNs to another when the percentage of malicious servers fixed and vary the size of the Wireless Sensor Networks, which constitutes a demonstration of the scalability of the model.

3.2 Comparison between Simulation of Bio-inspired Trust and Reputation Model and Linguistic Fuzzy Trust Model over Oscillating WSNs

In this section, the comparison between the two models, BTRM-WSN and LFTM according to the selection percentage of trustworthy servers and the average path length suggested by each model is described.

3.2.1 Selection percentage of trustworthy servers

Fig. 6 shows the selection percentage of trustworthy servers achieved with BTRM-WSN over oscillating WSNs composed of 100 to 500 sensors with a percentage of malicious servers from 10% to 90%.

It can be checked that the selection percentage of trustworthy servers is greater than 90% if the percentage of malicious servers is approximately less than or equal to 40%, regardless the size of the Wireless Sensor Network. Moreover, reasonably good outcomes (those with a selection percentage above the 60%) are obtained when the proportion of fraudulent servers is less than or equal to 80%. But the selection percentage of trustworthy servers decreases as the percentage of malicious servers increases, so when the percentage of malicious servers is equal to 90% the outcomes began to be (less than 50%) which makes the system not useful at all because here it is assumed that if the selection percentage of trustworthy servers is under the 50%, then the model is completely useless.

While the corresponding results obtains for the LFTM model over oscillating WSNs are shown in **Fig. 4(b)**, here the selection percentage of trustworthy servers is (less than 50) when the percentage of malicious servers is 10% which makes the model not useful at all. The accuracy began to increase by increasing the percentage of the malicious servers. The selection percentage of trustworthy servers is quite high (above the 90%) when the percentage of malicious servers is greater than or equals to 70% regardless the size of the networks.

The comparison between the two figures **Fig. 6** and **Fig. 4(b)** gives the conclusion that in the case of the BTRM-WSN model, the selection percentage of trustworthy servers decreases as the percentage of malicious servers increases while in the case of LFTM model, the selection percentage of trustworthy servers increases as the percentage of untrustworthy servers increases. This means that BTRM-WSN model gives higher accuracy in Wireless Sensor Networks with small number of malicious servers while LFTM model gives higher accuracy in Wireless Sensor Networks with large number of malicious servers.

Also it can be observes from the comparison, that the selection percentage of the trustworthy servers of the two models is slightly different from one set of random WSNs to another when the percentage of malicious servers fixed and vary the size of the Wireless Sensor Network, which constitutes a demonstration of the scalability of the two models.

3.2.2 Average path length leading to trustworthy servers

In this work, the measuring of the length (number of hops) of those paths found by BTRM-WSN and LFTM models leading to trustworthy servers is presented.

Fig. 7 shows the outcomes achieved with BTRM-WSN model over oscillating WSNs, here when the percentage of malicious servers is less than or equal to 40%, the results about the average path length is small and the differences between results when varying the size of tested networks are also small but when the percentage of untrustworthy servers is greater than 40% then the results about the average path length began to increase and the differences between results when varying the size of the networks also began to increase. It is also observes that whatever the size of the network and the number of malicious servers can reach high values the average path length never exceeds (8.5) hops in any case, which is still a good outcome for Wireless Sensor Networks, and in general when the percentage of malicious servers composing the network is greater, then the average path length also increases regardless the size of the networks.

The outcomes in **Fig. 5(b)** shows the results that achieved with LFTM model over oscillating WSNs, here the differences in the average path length suggested by the model when varying the size of the tested networks decreases as the percentage of malicious servers increases, so when the percentage of malicious servers is 10% the differences is very high but when the percentage is 90% the differences is very small and it is approximately equal. And also here in general, the average path length decreases as the percentage of malicious servers increases regardless the size of the network.

In the comparison between the two figures **Fig. 7** and **Fig. 5(b)**, it can be observed that in the case of the BTRM-WSN model, the average path length leading to trustworthy servers increases as the percentage of malicious servers increases while in the case of LFTM model, the average path length leading to trustworthy servers decreases as the percentage of untrustworthy servers increases. This means that BTRM-WSN model gives shorter path length in Wireless Sensor Networks with small number of malicious servers while LFTM model gives shorter path length in Wireless Sensor Networks with large number of malicious servers.

Also it can be observed from the comparison, that the average path length leading to trustworthy servers suggested by the two models is slightly different from one set of random WSNs to another with varying in the size of the Wireless Sensor Networks when the percentage of malicious servers is less than 50% in the case of BTRM-WSN model and when the percentage of malicious servers is greater than or equal to 50% in the case of LFTM model, which gives an evidence about the scalability of the two models.

4. CONCLUSION

Trust and reputation management over distributed systems has been proposed in the last few years as a novel and accurate way of dealing with some security deficiencies which are inherent to those environments. Tackling those risks not fully covered by traditional network security scheme.

In this paper the effect of one of these risks was shown, this risk is the oscillating behavior of the server nodes where the goodness of the servers could change along the time. The results is about the selection percentage of trustworthy servers and the average path length achieved with Linguistic Fuzzy Trust Model over oscillating WSNs. The experiment of the LFTM model over oscillating WSNs gives the proof that LFTM obtains quite good and accurate outcomes over oscillating Wireless Sensor Networks, with a low influence from the size of the networks and the percentage of malicious servers, which makes LFTM therefore presents a technique to identify trustworthy servers that is suitable for oscillating Wireless Sensor Networks.

Also, a comparison between BTRM-WSN and LFTM models over oscillating WSNs is presented. The results achieved by both models are slightly differ from one set of random WSNs to another when the percentage of malicious servers fixed and vary the size of the Wireless Sensor Network, which gives a confirmation about the scalability of the two models.

REFERENCES

- Almen´arez, F., Marı´n, A., Campo, C., and Garcı´a, C., 2004, *PTM: A Pervasive Trust Management Model for Dynamic Open Environments*, First Workshop on Pervasive Security and Trust, Boston, USA.

- Boukerche, A., Xu, L., and El-Khatib, K., 2007, *Trust-Based Security for Wireless Ad Hoc and Sensor Networks*, Computer Communications, Vol. 30, PP. 2413-2427.

- Dorigo, M., and Gambardella, L. M, 1997, *Ant Colony System: A Cooperative Learning Approach in the Traveling Salesman Problem*, IEEE Transaction on Evolutionary Computing, Vol. 1, Issue 1, PP. 53-66.

- Jang, J. S. R., Sun, C. T., and Mizutani, E., 1997, *Neuro-Fuzzy and Soft Computing*, Prentice Hall: Upper Saddle River, New Jersey, USA.

- Mármol, F. G, and Pérez, G. M, 2009a, *Security Threats Scenarios in Trust and Reputation Models for Distributed Systems,* Elsevier Computers & Security, Vol. 28, Issue 7, PP. 545-556.

- Mármol, F. G, and Pérez, G. M, 2009b, *TRMSim-WSN, Trust and Reputation Models Simulator for Wireless Sensor Networks*, Proceedings of the IEEE International Conference on Communications, Communication and Information Systems Security Symposium, PP. 1-5, Dresden, Germany.

- Mármol, F. G, and Pérez, G. M., 2011, *Providing Trust in Wireless Sensor Networks Using A Bio Inspired Technique*, Telecommunication Systems Journal, Vol. 46, Issue 2, PP. 163-180.

- Mármol, F. G, Marín-Blázquez, J. G, and Pérez, G. M, 2011, *Linguistic Fuzzy Logic Enhancement of A Trust Mechanism for Distributed Networks*, Proceedings of the Third IEEE International Symposium on Trust, Security and Privacy for Emerging Applications, PP. 838-845, Bradford, UK.

- Marsh, S. P., 1994, *Formalising Trust As A Computational Concept*, Ph.D. Dissertation, Department of Computing Science and Mathematics, University of Stirling.

- Marti, S., and Garcia-Molina, H., 2006, *Taxonomy of Trust: Categorizing P2P Reputation Systems*, Computer Networks, Vol. 50, Issue 4, PP. 472-484.

- Moloney, M., and Weber, S., 2005, *A Context-Aware Trust-Based Security System for Ad Hoc Networks*, In Workshop of the 1st International Conference on Security and Privacy for Emerging Areas in Communication Networks, PP. 153-160, Athens, Greece.

- Pedrycz, W., and Gomide, F., 1998, *An Introduction to Fuzzy Sets: Analysis and Design*, The MIT Press: Cambridge, Masssachusetts, USA.

- Sabater, J., and Sierra, C., 2001, *REGRET: Reputation in Gregarious Societies*, Proceedings of the Fifth International Conference on Autonomous Agents, ACM Press, PP. 194-195, Montreal, Canada.

- Tajeddine, A., Kayssi, A., Chehab, A., and Artail, H., 2006, *PATROL-F- A Comprehensive Reputation-Based Trust Model with Fuzzy Subsystems*, Third International Conference, ATC, LNCS, Wuhan, China: Springer, Vol. 4158, PP. 205-216.

- Wang, Y., Cahill, V., Gray, E., Harris, C., and Liao, L., 2006, *Bayesian Network Based Trust Management*, Third International Conference, ATC, LNCS, Wuhan, China: Springer, Vol. 4158, PP. 246-257.

Table 1. Experiment parameters.

Network	NumExecutions NumNetworks MinNumSensors MaxNumSensors	100 100 {100,200,300, 400,500} {100,200,300, 400,500}	%Clients %Relay %Malicious Radio range	15% 5% {10%,20%,30%,40%, 50%,60%,70%,80%, 90%} {8,6,5,4,3}
BTRM	phi rho Transition threshold alpha beta Punishment threshold	0.01 0.87 0.66 1.0 1.0 0.48	Num ants Num iteration Path length factor q0 Initial pheromone	0.35 0.59 0.71 0.45 0.85
LFTM	Server goodness		Client	
	Benevolent	'High' or ' very high'	Conformity	Random
	Malicious	'Low' or 'very low'	Goodness	Random
	Cost weight	0.25	Price weight	0.25
	Deliver weight	0.25	Quality weight	0.25

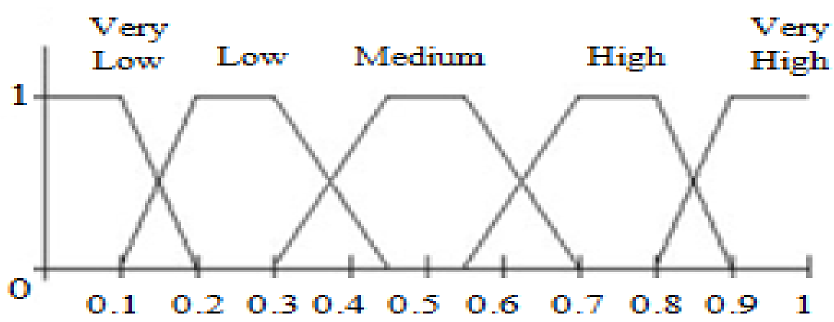

Figure 1. Linguistic labels and its defining fuzzy sets.

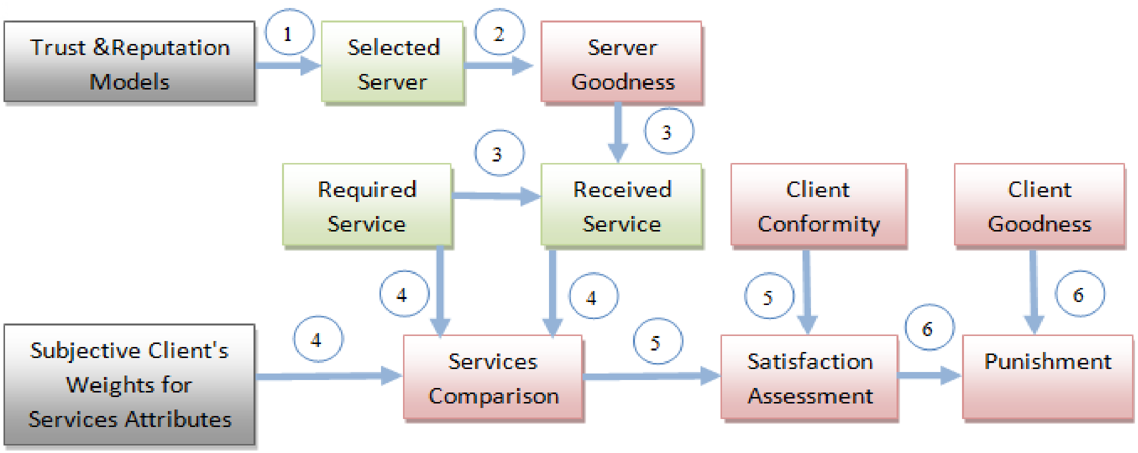

Figure 2. Linguistic fuzzy trust model steps.

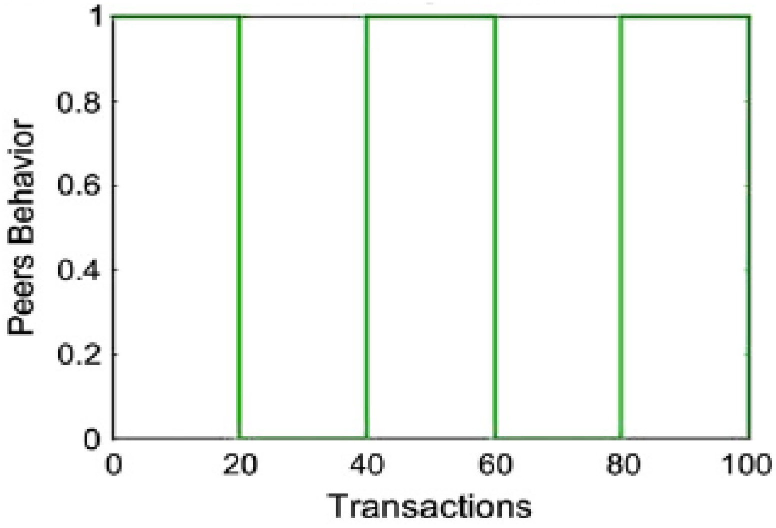

Figure 3. Oscillating behavior.

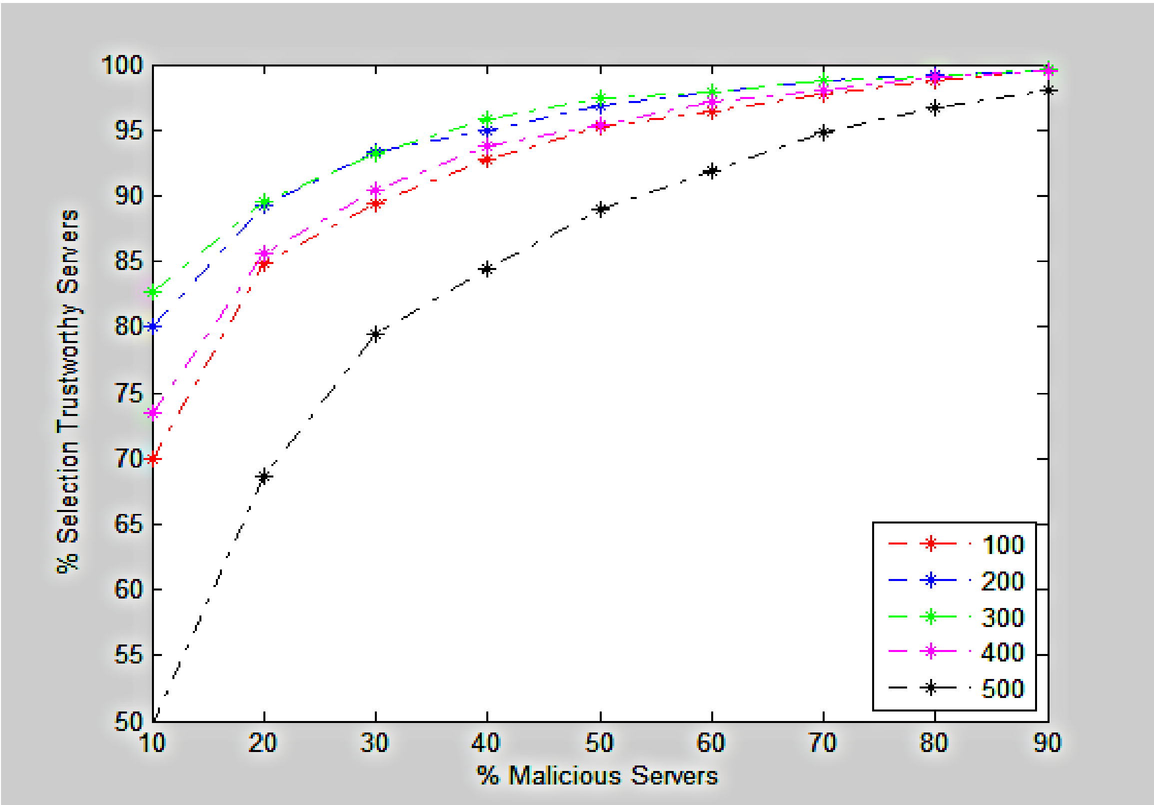

Figure 4(a). Selection percentage of trustworthy servers from linguistic fuzzy trust model over static WSNs.

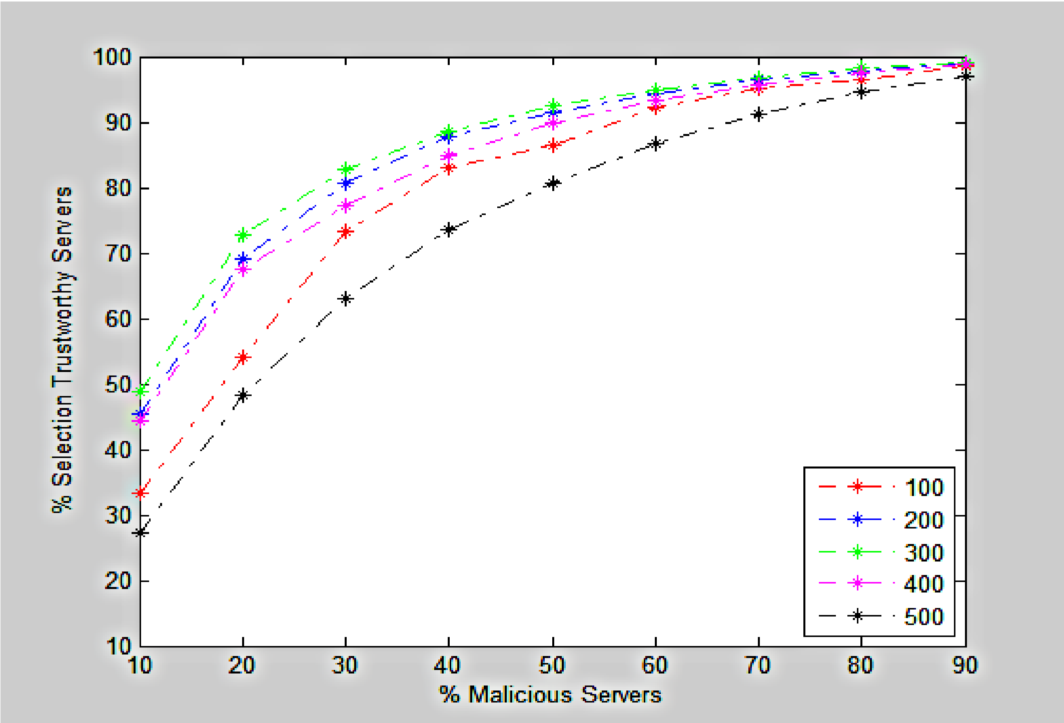

Figure 4(b). Selection percentage of trustworthy servers from linguistic fuzzy trust model over oscillating WSNs.

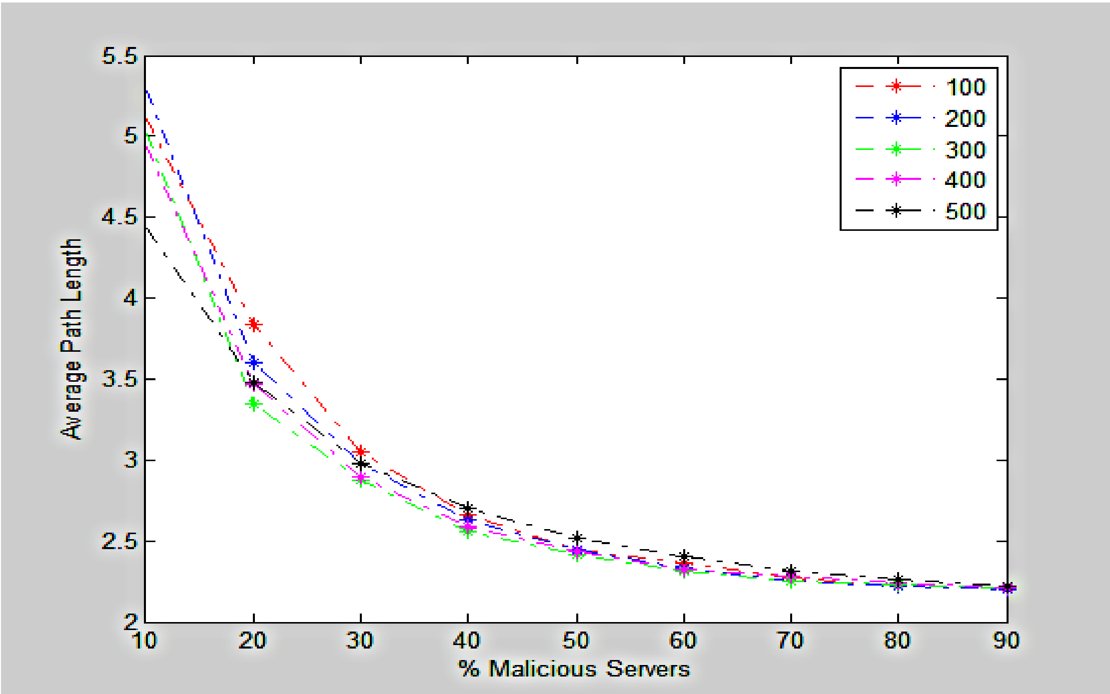

Figure 5(a). Average path length leading to trustworthy servers from linguistic fuzzy trust model over static WSNs.

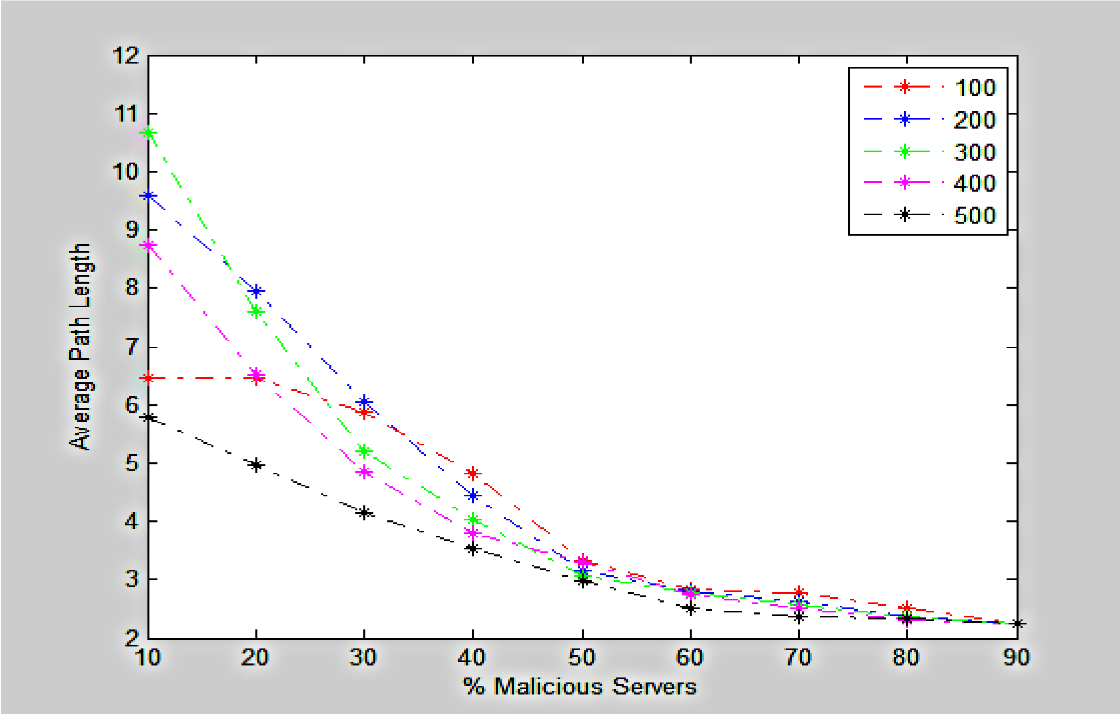

Figure 5(b). Average path length leading to trustworthy servers from linguistic fuzzy trust model over oscillating WSNs.

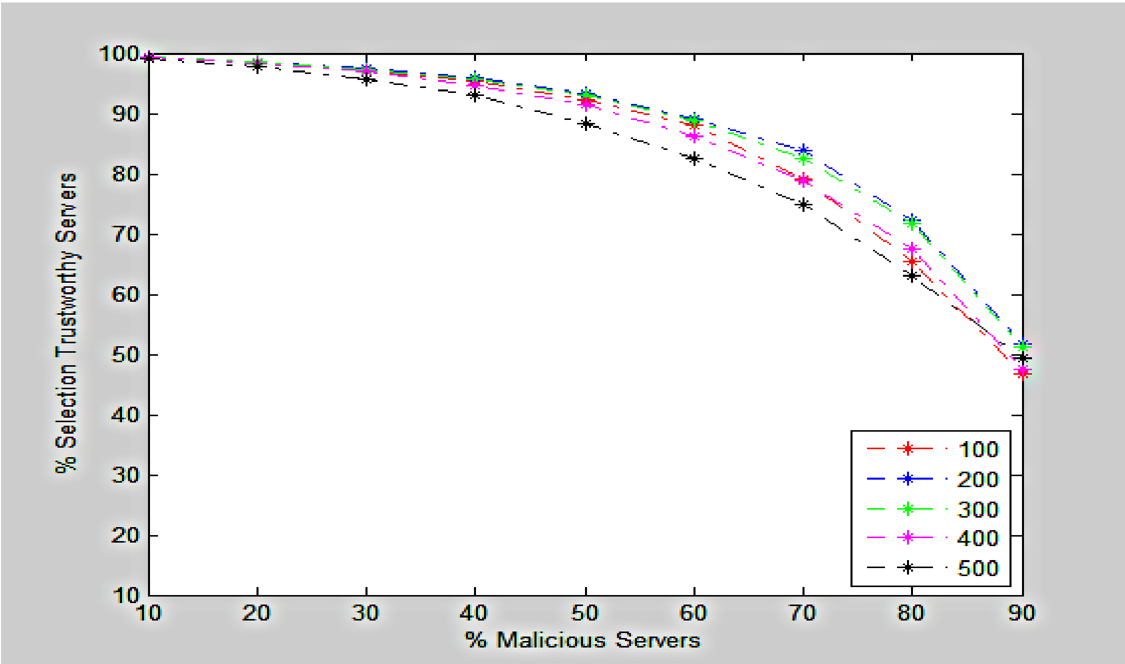

Figure 6. Selection percentage of trustworthy servers form bio-inspired trust and reputation model over oscillating WSNs.

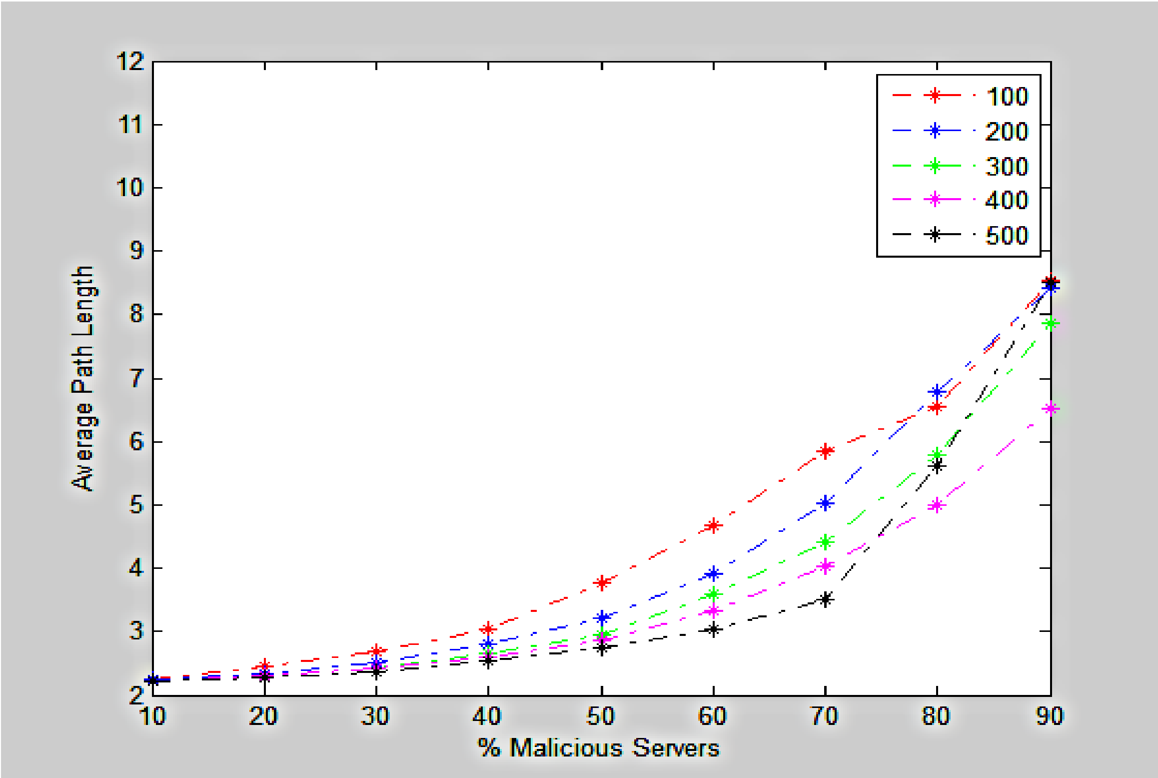

Figure 7. Average path length leading to trustworthy servers form bio-inspired trust and reputation model over oscillating WSNs.

Priority Based Transmission Rate Control with Neural Network Controller in WMSNs

Dr. Nadia Adnan Shiltagh
Lecturer
Computer Engineering/ University of Baghdad
dr-nadiaat@hotmail.co

Ali H. Wheeb
M.SC. Student
Computer Engineering / University of Baghdad

ABSTRACT

Wireless Multimedia Sensor Networks (WMSNs) are networks of wirelessly interconnected sensor nodes equipped with multimedia devices, such as cameras and microphones. Thus a WMSN will have the capability to transmit multimedia data, such as video and audio streams, still images, and scalar data from the environment. Most applications of WMSNs require the delivery of multimedia information with a certain level of Quality of Service (QoS). This is a challenging task because multimedia applications typically produce huge volumes of data requiring high transmission rates and extensive processing; the high data transmission rate of WMSNs usually leads to congestion, which in turn reduces the Quality of Service (QoS) of multimedia applications. To address this challenge, This paper proposes the Neural Control Exponential Weight of Priority Based Rate Control (NEWPBRC) algorithm for adjusting the node transmission rate and facilitate the problem of congestion occur in WMSNs. The proposed algorithm combines Neural Network Controller (NC) with the Exponential Weight of Priority Based Rate Control (EWPBRC) algorithms. The NC controller can calculate the appropriate weight parameter λ in the Exponential Weight (EW) algorithm for estimating the output transmission rate of the sink node, and then ,on the basis of the priority of each child node , an appropriate transmission rate is assigned . The proposed algorithm can support four different traffic classes namely, Real Time traffic class (RT class); High priority, Non Real-Time traffic class (NRT1 class); Medium priority, Non Real-Time traffic class (NRT2 class); and Low priority, Non Real-Time traffic class (NRT3 class). Simulation result shows that the proposed algorithm can effectively reduce congestion and enhance the transmission rate. Furthermore, the proposed algorithm can enhance Quality of Service (QoS) by achieve better throughput, and reduced the transmission delay and loss probability.

Keywords:-wireless multimedia sensor network; congestion control; QoS; neural network.

أولوية معدل انتقال مبني على السيطرة مع وحدة تحكم الشبكة العصبية في شبكات الا ستشعار الاسلكية ذات الوسائط المتعددة

د.نادية عدنان شلتاغ
مدرس
هندسة الحاسبات
كلية الهندسة\ جامعة بغداد

علي حسين وهيب
هندسة حاسبات
كلية الهندسة\ جامعة بغداد

الخلاصة

شبكات الاستشعار اللاسلكية ذات الوسائط المتعددة هي شبكات مترابطة لاسلكيا بمجموعة من عقد الاستشعار المزودة بأجهزة الوسائط المتعددة، مثل الكاميرات و الميكروفونات .وبالتالي فإن هذة الشبكات لديها القدرة على نقل البيانات والوسائط المتعددة، مثل الفيديو والصوت ، الصور الثابتة ، والبيانات العددية من البيئة .معظم تطبيقات شبكات الاستشعار اللاسلكية ذات الوسائط المتعددة تتطلب إيصال المعلومات الوسائط المتعددة مع مستوى معين من جودة الخدمة . هذه هي مهمة صعبة لأن تطبيقات الوسائط المتعددة عادة ما تنتج كميات ضخمة من البيانات التي تتطلب معدلات نقل عالية ومعالجة واسعة النطاق ، معدل نقل البيانات السريع في شبكات الاستشعار اللاسلكية ذات الوسائط المتعددة عادة ما يؤدي إلى الازدحام ، والذي بدوره يقلل من جودة الخدمة (QoS) في تطبيقات الوسائط المتعددة. ولمواجهة هذا التحدي، تم اقتراح خوارزمية (NEWPBRC)تهدف لضبط معدل ارسال العقدة وتقليل مشكلة الازدحام الذي يحدث في شبكات الاستشعار اللاسلكية ذات الوسائط المتعددة . الخوارزمية المقترحة تجمع بين وحدة تحكم الشبكة العصبية (NC) مع خوارزميات (EWPBRC). وحدة تحكم الشبكة العصبية (NC) يمكنها حساب القيمة المناسبة لمعامل الوزن (λ) المستخدم في خوارزمية الوزن الاسي (EW) لتخمين معدل الارسال الخارج من العقدة الاساسية، ومن ثم، على أساس أولوية كل عقدة تابعة، يتم تعيين معدل ارسال مناسب لها . الخوارزمية المقترحة يمكن أن تدعم أربع اصناف مرور مختلفة وهي ، صنف مرور وقت حقيقي (RT)؛ صنف مرور وقت غير حقيقي , أولوية عالية (NRT1), صنف مرور وقت غير حقيقي , أولوية متوسطة (NRT2) , صنف مرور وقت غير حقيقي , أولوية منخفضة (NRT3) .النتائج العملية اظهرت أن الخوارزمية المقترحة يمكن أن تقلل بشكل فعال الازدحام وتحسن معدل ارسال البينات. وعلاوة على ذلك الخوارزمية المقترحة ، يمكن أن تعزز جودة الخدمة (QoS) من خلال تحقيق إنتاجية أفضل ، وتقليل تأخير الارسال لتجنب احتمالية فقدان الحزم.

الكلمات الرئيسية: شبكات الاستشعار ذات الوسائط المتعددة, التحكم في الازدحام؛ جودة الخدمة؛ الشبكات العصبية.

1. INTRODUCTION

Most of the research before in the Wireless Sensor Network (WSN) is concerned with scalar sensor networks that measure physical phenomena, such as pressure, temperature, humidity, or location of objects that can be conveyed through low-bandwidth and delay-tolerant data streams. Recently, the focus is shifting toward research aimed to enable delivery of multimedia content, such as audio and video streams, as well as scalar data. This effort resulted in distributed networked systems, referred as Wireless Multimedia Sensor Networks (WMSNs**), Akyildiz, et al.,2007.** WMSNs are set of sensor nodes, whereby the nodes are equipped with multimedia devices such as cameras, and microphones. Thus a WMSN will have the capability to transmit multimedia data, such as still pictures, stream video, voice, animal sounds, and monitoring data. One important requirement of applications in WMSNs is low delay bounds. Furthermore, some applications of WMSNs need relative resilience to losses. WMSNs can support different types of traffic classes, **Akyildiz, et al.,2007.**

There are many different resource constraints in WMSNs involving energy, bandwidth, memory, buffer size and processing capability .Given the physically small nature of the sensors, and that multimedia applications typically produce huge volumes of data requiring high transmission rates and extensive processing, this may cause congestion in the sensor nodes. Thus, developing protocols, algorithms and architectures to maximize the network lifetime while satisfying the quality of service (QoS) requirements of the applications represents a critical problem. In most WSN and WMSN applications, traffic mainly flows from a large number of sensor nodes to a base station (sink) node, **Akyildiz, et al., 2002.**

Congestion control is an important issue in transport protocols. Congestion is also a difficult problem in wireless sensor networks. It not only wastes the scarce energy due to a large number of retransmissions and packet drops, but also hampers the event detection reliability. Congestion in WSNs and WMSNs has a direct impact on energy efficiency and application, **QoS Ee ,** and **Bajcsy, 2004.** Usually, congestion occurs in the bottleneck since it receives more data than it is capable of sending out. In this situation, packets will be queued and sometimes get dropped. As a consequence, response time will increase which causes throughput to be degraded, **Samiullah,** and **Karim, 2011**.

Two types of congestion could occur in sensor network, as show in **Fig. 1** and **Fig.2.** The first type is Node –Level congestion that is common in conventional network.it is caused by buffer overflow in the node and can result in packet loss, and increased queuing delay, **Malar, 2010.** Not only can packet loss degrade reliability and application QoS, but it can also waste the limited node energy and degrade link utilization. In each sensor node, when the packet-arrival rate exceeds the packet service rate, buffer overflow may occur. This is more likely to occur at sensor nodes close to the sink, as they usually carry more combined upstream traffic, **Yaghmaee,** and **Adjeroh, 2008**. The second type is Link-Level congestion, which occurs in wireless transmission and occurs when the nodes are in the same utilization channel, for example, Carrier Sense Multiple Access with Collision Detection (CSMA/CD). Such a situation occurs when multiple active nodes perform access on the same channel and collision is then the result, **Wan, and Siphon, 2005.**

2. RELATED WORK

Various congestion control techniques have been studied for wireless multimedia sensor networks .the congestion control mechanisms all have the same basic objective: they all try to detect congestion, notify the other nodes of the congestion status, and reduce the congestion and/or its impact using rate adjustment algorithms. **Wang, et al.,2007**, proposed Priority Based Congestion Control Protocol (PCCP). **Yaghmaee, and Adjeroh, 2009**, proposed Priority Based Rate Control Algorithm (PBRC) used for congestion control and service differentiation in WMSNs. **Chen, and Lai, 2012**, proposed an algorithm where a Fuzzy Logical Controller (FLC) is used to estimate the output transmission rate of the sink node. The FLC is associated with the Exponential Weight (EW) algorithm for selecting the appropriate weight parameter, and then, on the basis of the priority of each child node, an appropriate transmission rate is assigned. **Pawar**l, and **Kasliwal, 2012**, proposed a QoS-based sensory Media Access Control (MAC) protocol, which does not only adapts to application oriented QoS, but also attempts to conserve energy without violating QoS-constraints. proposed MAC layer protocol for WMSNs satisfy feature like Maximize network throughput, Enhance transmission reliability, and Minimize control overhead, be energy-efficient, Guarantee a certain level of QoS.

3. THE NETWORK MODEL

Fig. 3 shows a simplified experimental model for WMSN .This network model consist of ten nodes, nine sensor nodes, one sink node and the Base Station (BS). The locations of sensor nodes and the base station are fixed. Each sensor node has the knowledge of its own geographic location and the locations of its 1-hop neighbor nodes. Each of the nodes can sense different

types of data at the same time and sends those to BS. For each node in the network, there is a single path to reach to the BS.
In this network model node may generate different types of traffic .for example node 9 produces only NRT3 traffic, node 6 produces two type of traffic NRT1 and NRT2, while node 8 produces four type of traffic RT, NRT1, NRT2, and NRT3.
The queuing model of each node is shown in **Fig.4**. Each traffic class well be buffered in a separate queue, To discriminate traffic classes from each other, the wireless node adds a traffic class identifier to its local sensor packets; hence, when a data packet enters a transmission traffic classifier, the data type will be classified to enter the respective queue that it belongs to, then priority queue scheduler has been provisioned to schedule the diverse traffic with different priority from the priority queues.

4. PROPOSED NEWPBRC ALGORITHM

Fig. 5 shows the block diagram of the proposed algorithm which is called Neural controller Exponential Weight Priority-Based Rate Control (NEWPBRC), for the proposed algorithm which combines the Neural Controller (NC) with the Exponential Weight of Priority-Based Rate Control (EWPBRC) algorithm. The NC controller is used to adjust the weight parameter λ in the EWPBRC algorithm to obtain the optimal $\mathrm{r(sink\,)_{out}}$ as shown in **Fig. 5**, where $\mathrm{r(sink\,)_{out}}$ denotes as the rate of the output of the sink node. And $\mathrm{r(sink)_{in}}$ is the sum of input transmission rates for all the childe nodes for transmission data to the sink node. Furthermore, the transmission rate adjusts according to the priority of each child node.
In the proposed algorithm, The NC controller follow $\mathrm{r(sink)_{in}}$ to estimate the output transmission rate $\mathrm{r(sink)_{out}}$ of the sink node, where $\mathrm{r(sink)_{out}}$ is the transmission rate for the sink node to transmit data to the BS. In addition, the transmission rate of the node is adjusted according to the priority of the data type and the geographical location of the node .The structure of the proposed algorithm that contains NC controller is based on neural network which is shown in **Fig. 6** .The Feed Forward neural network is constructed in three layers. One unit in the input layer, four units in hidden layer, and one unit in the output layers .the output signal from the controller is the weight parameter (λ) that is used in EWPBRC algorithm. The activation function of the hidden layer is sigmoid. In **Fig. 6** ,W denotes the connection weights between the input layer and the hidden layer , and V denotes the connection weights between the hidden layer and the output layer .The NC controller is trained off-line using The Back Propagation (BP) training algorithm .The simulation of BP algorithm is done using MATLAB program . During the Training process weights in NC controller are adapted to optimize the controller response.
The congestion control unit in the proposed NEWPBRC algorithm is shown in **Fig. 7**, when input rate $\mathrm{r(sink)_{in}}$ passes through the CDU unit, calculate error, and then after the adjustment of the output transmission rate by the NEWPBRC controller and RMU unit, a new rate is generated to adjust the rate for transmitting from the sink node to the BS and the transmission rate for transmitting from all the child nodes to the sink node.

5 . RATE MANAGEMENT ALGORITHM

NEWPBRC algorithm used for adjustment the transmission rate while congestion occurs. This algorithm can be divided into three steps:

Step 1: Computing the new output transmission rate of sink node.

The error e is used as the input variable to the NC controller. E (t) is the error between $r(sink)_{in}$(t) and $r(sink)_{out}$(t) at time instant t, which is represented by

$$e(t) = r(sink)_{in}(t) - r(sink)_{out}(t) \quad (1)$$

The NC controller used to adjust weight parameter λ of the EW algorithm ,calculation of weight parameter λ is given by :

$$\text{net } 1 = (e * w) \quad (2)$$

$$\text{fnet1} = f_1 .(\text{net1}) \quad (3)$$

$$\text{net } 2 = (\text{fnet1} * v) \quad (4)$$

$$\lambda = f_2. (\text{net } 2) \quad (5)$$

Where λ is a constant, $0 \le \lambda \le 1$. f_1 sigmoid activation function and f_2 is linear activation function, w and v are connection weights .

Using the transmission rates of $r(sink)_{in}$(t) and $r(sink)_{out}$ (t) at time instant t, and from optimal value of weight parameter λ, we can calculated the $r(sink)_{out}$ (t+1) output transmission rate at time instant t+1 :

$$r(sink)_{out}(t+1) = r(sink)_{in}(t).(1-\lambda) + \lambda . r(sink)_{out}(t) \quad (6)$$

Step 2: Calculating the new output transmission rate for child node.

In WMSNs, based on the functionality, different types of sensor node will be equipped, and a node will be deployed at a related geographical location according to the different levels of importance.

In data transmission, on the basis of the geographical location, an appropriate priority and transmission rate will be given. $P(i)_{GEO}$ is the geographical location priority of node i. The total priorities $TP(i)$ of node i are the traffic class priority $P(i)_{TRC}$ and geographical location priority $P(i)_{GEO}$, defined as follows:

$$TP(i) = P(i)_{TRC} . P(i)_{GEO} \quad (7)$$

Let C(i) is the set of child nodes of node i; the global priority $GP(i)$ is defined as the sum of priorities of all nodes in sub tree node *i*. the global priority $GP(i)$ is given by:

$$GP(i) = \sum_{k \in c(i)} GP(k) + TP(i) \quad (8)$$

If node i doesn't have any child nodes, Then its global priority will be equal to its total priority $TP(i)$ value.

Note that global priority $GP(i)$ is calculated only for active traffic sources .On the other hand ,if the traffic sources is not active ,then the value of total priority $TP(i)$ is set to zero. This ensures that the algorithm will share the existing capacity only between active nodes.

$GP(sink)$ is the sum of global priorities of the sink node, C(Sink) is the set of all the child nodes with the sink as their parent, and $GP(sink)$ is the sum of the priorities of all the nodes, and is represented as follows:

$$GP(sink) = \sum_{k \in c(sink)} GP\ (k) \tag{9}$$

To calculate the optimal output transmission rate $r(i)_{out}$ of node i, $r(i)_{out}$ is calculated on the basis of the distribution of the output transmission rate $r(sink)_{out}$ from the sink node to node i according to the proportion between the global priority of child node $GP(i)$ and the global priority of the sink node $GP(sink)$:

$$r(i)_{out} = r(sink)_{out} \cdot \frac{GP(i)}{GP(sink)} \tag{10}$$

Step 3: Computing a new output transmission rate for each parent node.

$r(i)_{in}$ is the input transmission rate of node i, which is obtained through the summation of the $r(k)_{out}$ of the connected child nodes, and $r(i)_{in}$ is calculated as follows:

$$r(i)_{in} = \sum_{k \in c(i)} r(k)_{out} \tag{11}$$

where C(i) is the set of node i, and $r(k)_{out}$ represents the output rate of the k^{th} child of parent node i. $\Delta\, r(i)$ is the transmission rate difference of node i and is as follows:

$$\Delta\, r(i) = \mu \,.\, r(i)_{out} - r(i)_{in} \tag{12}$$

where μ is a constant close to 1.

Node i generates a new transmission rate to be distributed to all the child node k output transmission rates; this is calculated as follows:

$$r(i)_{out} = r(k)_{out} \cdot \frac{GP(i)}{GP(sink)} \tag{13}$$

Fig. 8 explain the rate management process of the NEWPBRC algorithm.

6. SIMULATION RESULTS

The proposed algorithm is implemented using the Network simulator 2 (NS-2) [www.isi.edu/nsnam/ns]. The NS-2 simulation environment is a flexible tool for network engineers to investigate how various algorithms perform with different configurations and topologies. To evaluate the performance of the proposed algorithm, three important parameters are considered. These parameters are throughput, delay, and packet loss probability. The simulation model consists of ten wireless multimedia sensor nodes, nine multimedia sensor node, one sink node and BS. The transmission route of that model is a single-path transmission. The transmission data collected by multimedia sensor nodes are generated randomly, All senders transmit data traffic to a single sink node. In the simulation model, there are four types of traffic class, namely RT, NRT1, NRT2 and NRT3. The simulated traffic is Pareto [www.wikipedia.org]. Each packet size is 500 bytes, the buffer size of each child node is set up as 50 packets, and the buffer size of the sink node is 100 packets. All multimedia sensor nodes start to send their data at the start of the simulation rounds and stop at the end of simulation rounds. The simulation rounds are 100 seconds. The performance measured after 30 simulation rounds. The channel capacity of each multimedia sensor node is set to the same value: 2 Mbps. The combination of traffic classes that each node could have in the simulation model is shown in Table (1) .where the symbol PV indicates Priority Value of traffic.

Assuming that all sensor nodes have the same geographical priority equal to 1. Suppose the assigned priority for RT, NRT1, NRT2, and NRT3 classes are equal to 4, 3, 2 and 1, respectively. For example , the sensor node 8 which has all traffic classes , the traffic class priority , $P(8)_{TRC}$ is 10 (4 + 3 + 2 + 1 = 10) ,while for sensor node 9 which has only NRT3 traffic classes, the traffic class priority , $P(9)_{TRC}$ is 1 .The performance of the proposed NEWPBRC algorithm is compared with FEWPBRC and EWPBRC algorithms. The performance is evaluated mainly according to the following metrics:

1- Throughput : measured in terms of number of packets received.
2- Sink Delay : is the time for the sink node to transmit data to BS.
3- End to End Delay: the packet transmission time between sources and sink node.
4- Packet Loss probability : it is a percent between number of packets lost in the network and number of packet generated by the sensing nodes .

Fig. 9 shows a comparison for the output transmission rate $r(sink)_{out}$ of three algorithms, namely the EWPBRC algorithm with λ = 0.5, the FEWPBRC algorithm, and the NEWPBRC algorithm. From the simulation results, It can be seen that the proposed algorithm has a slightly better throughput than FEWPBRC algorithm and EWPBRC algorithm**. Fig.10** shows a comparison for the delay of sink node of the EWPBRC algorithm with λ = 0.5,the FEWPBRC algorithm, and the NEWPBRC algorithm . Simulation result show that both the FEWPBRC and the NEWPBRC algorithm have average delay smaller than that of EWPBRC algorithm .The proposed algorithm has the shortest average delay time. **Fig. 11** shows a comparison for the end to end delay of the EWPBRC algorithm with λ = 0.5,and the NEWPBRC algorithm. **Fig. 12** shows a comparison for the loss probability of three algorithms, namely, the EWPBRC algorithm with λ = 0.5, the FEWPBRC algorithm, and the NEWPBRC algorithm .From the simulation result , it can be seen that the proposed algorithm has the lowest loss probability .

7. CONCLUSIONS

NEWPBRC algorithm is implemented in WMSN using NS2 simulator .then take average of performance parameters to get a more accurate result. The proposed algorithm enhancement the transmission rate and tries to avoid congestion, resulting to enhance the Performance of WMSN. The proposed algorithm provides good QoS in terms of minimizing delay and packet loss ratio and enhances the throughput of the network. The Average throughput achieved by NEWPBRC algorithm is slight better than of FEWPBRC algorithm. The Average sink delay achieved by the proposed algorithm is low by (13%) than that achieved by FEWPBRC algorithm. The proposed algorithm can be (4.61%) less average loss probability than FEWPBRC algorithm.

REFERENCES

Akyildiz I. F., Melodia T., Chowdhury K. R.,2007, *A Survey on Wireless Multimedia Sensor Networks, Computer Networks.*(Elsevier) ,vol.51, pp. 921–960.

Akyildiz I.F., Su W., Sankarasubramaniam Y., E. Cayirci, 2002, *Wireless Sensor Networks: a survey, Computer Networks.* (Elsevier), vol. 38, no. 4, pp. 393–422.

Chen Y. L., Lai H. P., 2012, *Priority-based Transmission Rate Control with a Fuzzy Logical Controller in Wireless Multimedia sensor Networks* , Computers and Mathematics with Applications. (Elsevier), vol. 64, pp. 688–698.

Ee C. T., Bajcsy R., 2004, Congestion *control and fairness for many-to one routing in sensor networks,* in: Proceedings of ACM Sensys, November.

Malar R.T., 2010, *Congestion Control in Wireless Sensor Networks Based Multi-Path Routing In Priority Rate Adjustment Technique*, International Journal of Advanced Engineering & Applications, January.

Pareto distribution : www.wikipedia.org .

Pawar S., and Kasliwal P., 2012, *A QoS Based Mac Protocol for Wireless Multimedia Sensor Network,* IOSR Journal of Electronics and Communication Engineering (IOSRJECE), Vol.1, No.5, pp.30–35.

Samiullah M., Karim M. Z., 2011, *Rate-Based Congestion Control and Reliable Data Dissemination in Wireless Sensor Network*, International Journal of Computer Networks and Wireless Communications (IJCNWC),vol. 1, no. 1, December.

The Network Simulator NS-2, Information Science Institute of the University of Southern California, March 2004, www.isi.edu/nsnam/ns.

Wang C., Li v, Sohraby K., Daneshmand M., Y. Hu, 2007, *Upstream Congestion Control in Wireless Sensor Networks Through Cross-Layer Optimization* , IEEE Journal On Selected Areas In Communications, vol.25, no. 4, pp. 786-795.

Wan C.Y., Siphon et al., 2005, *Overload Traffic Management using Multi-Radio Virtual Sinks in Sensor Networks*, In: Proc. Of ACM Sensys, San Diego, CA, Pp. 2–4.

Yaghmaee M. H., Adjeroh D., 2008, *A New Priority Based Congestion Control Protocol for Wireless Multimedia Sensor Networks,* proceedings of the 2008 International Symposium on a World of Wireless, Mobile and Multimedia Networks, IEEE Computer Society Washington, DC, USA pp. 1-8.

Yaghmaee M.H., Adjeroh D.A., 2009, *Priority-Based Rate Control for Service Differentiation and Congestion Control in Wireless Multimedia Sensor Networks*, Computer Networks. (Elsevier), vol.53, pp.1798–1811.

8. LIST OF SYMBOLS

PV	Priority value
W	*Weight matrix*
Thr	Throughput
Del	Delay
C(S)	The number of the child nodes for a parent node S
e	Error
λ	Weight parameter
$r(sink)_{in}$	Input transmission rate to sink node
$r(sink)_{out}$	Output transmission rate of sink node
$P(i)_{TRC}$	Traffic class priority
$P(i)_{GEO}$	Geographical priority
$SP(i)_j$	The traffic source priority j in sensor node i
e (t)	The error between $r(sink)_{in}(t)$ and $r(sink)_{out}$ (t) at time instant t
$r(sink)_{out}$ (t+1)	Output transmission rate at time instant t+1
TP(i)	The total priorities of node i
GP(i)	The global priority
GP(sink)	The sum of global priorities of the sink node
C(Sink)	The set of all the child nodes with the sink as their parent
$r(i)_{out}$	The optimal output transmission rate of node i
$r(i)_{in}$	The input transmission rate of node i
$r(k)_{out}$	The output rate of the kth child of parent node i
$\Delta\, r(i)$	The transmission rate difference of node i
μ	Constant close to 1

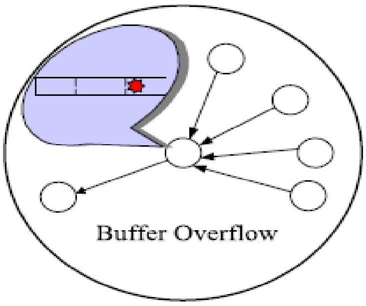

Figure1. Node–level congestion **Malar, 2010.**

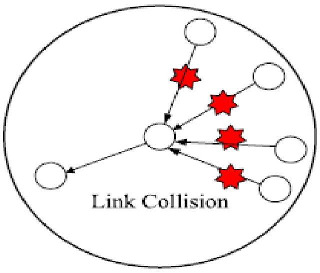

Figure2. Link – level congestion **Malar,2010.**

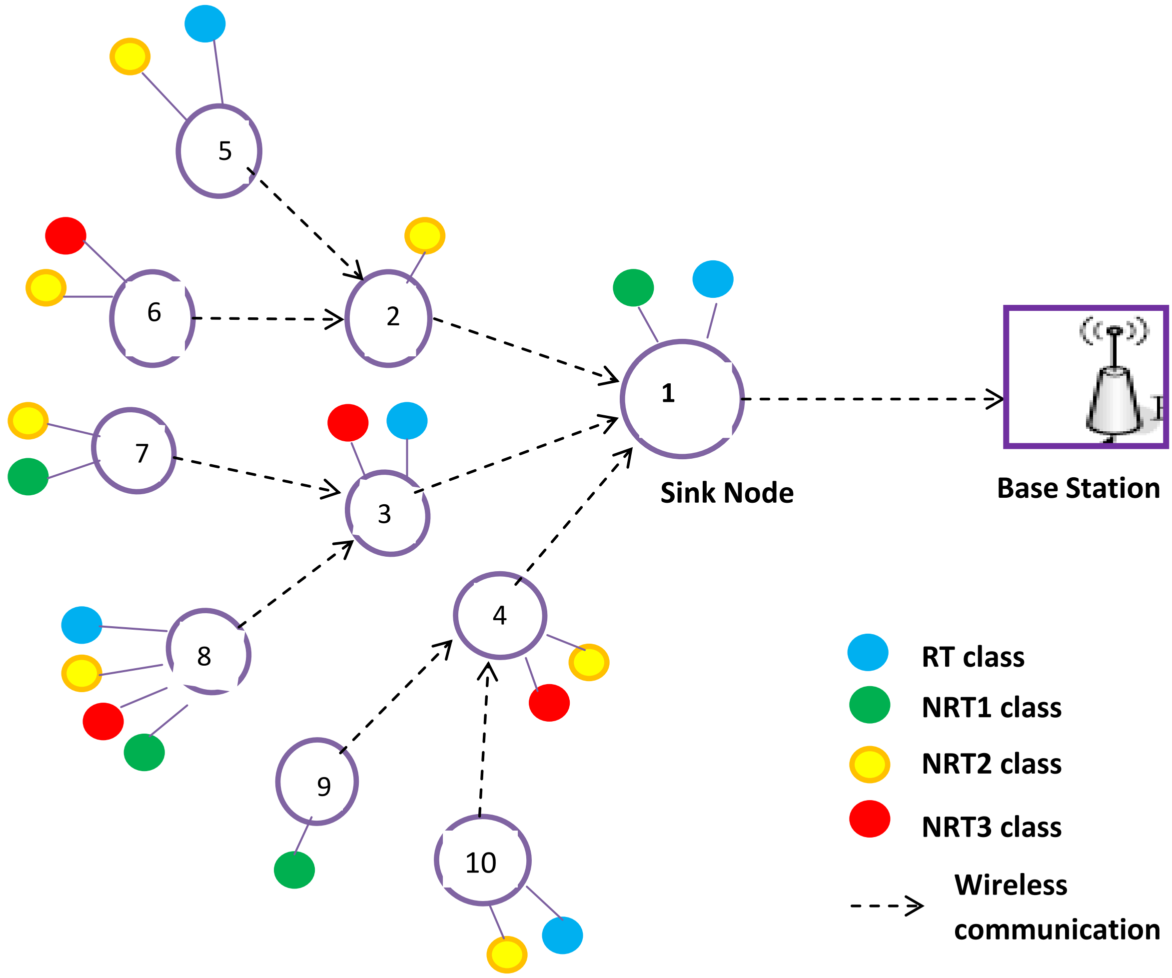

Figure 3. WMSN model **Chen, and Lai, 2012.**

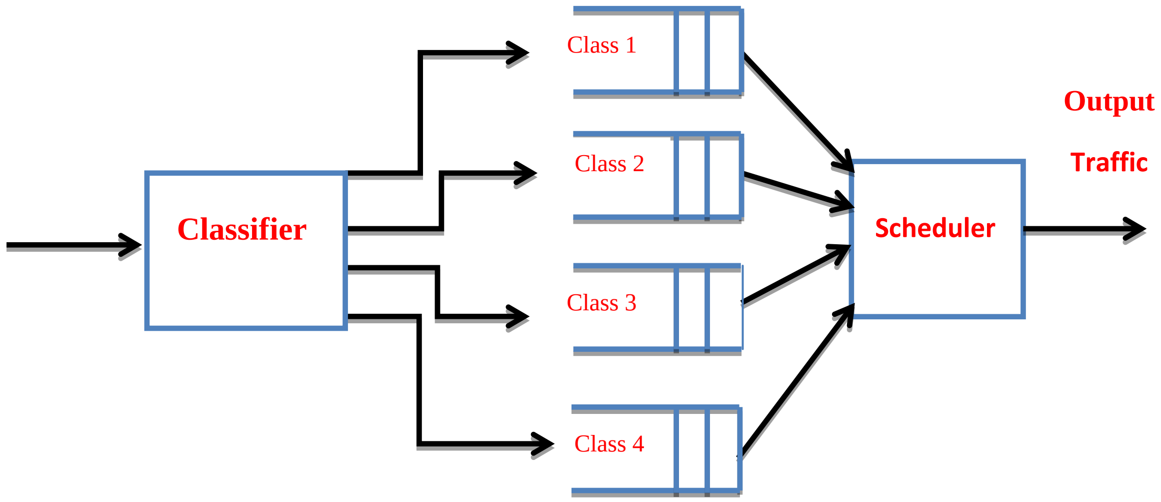

Figure 4. Queue model for each sensor node **Chen, and Lai, 2012**.

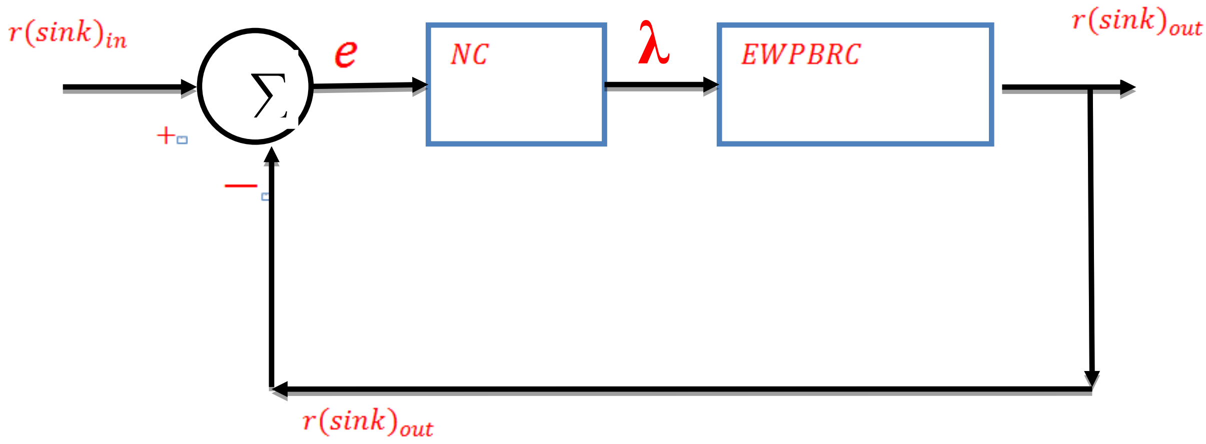

Figure 5. Block diagram of NEWPBRC algorithm.

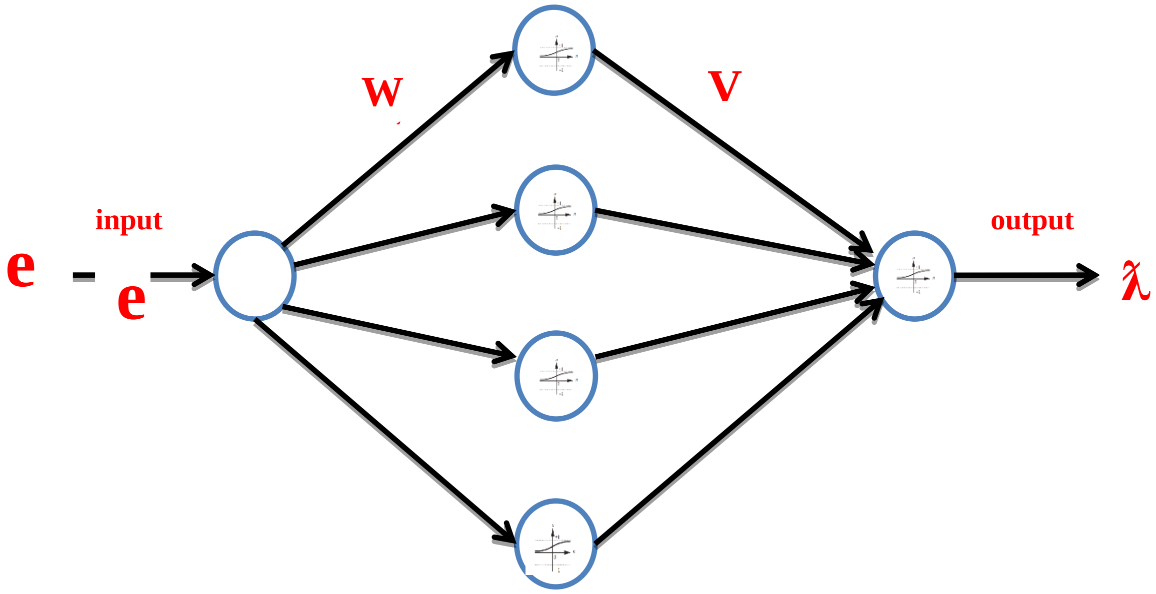

Figure 6. Structure of NC controller .

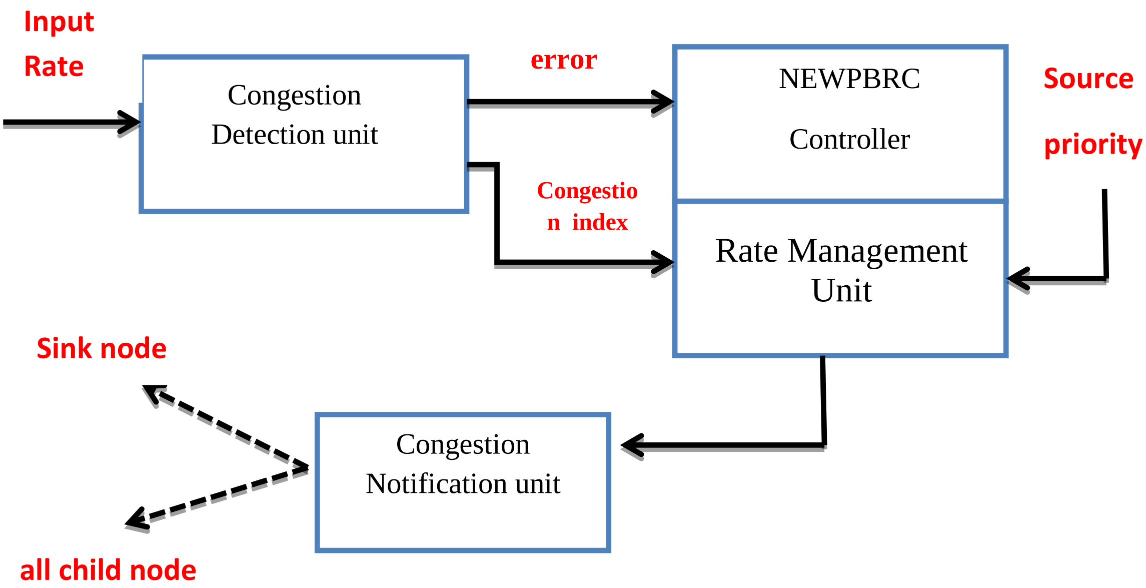

Figure 7. Structure of NEWPBRC congestion control unit.

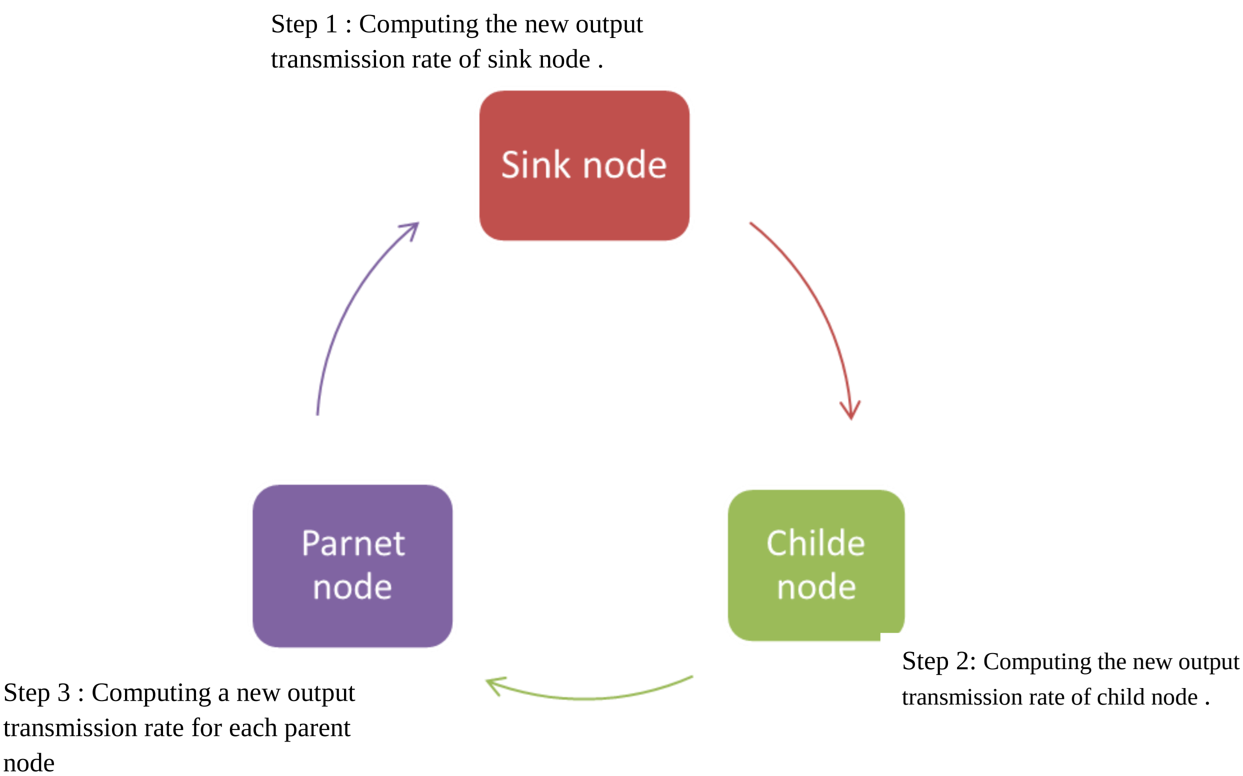

Figure 8. Rate management for NEWPBRC algorithm.

Table 1. The state of traffic classes in each sensor node .

Sensor node No.	RT (PV = 4)	NRT 1 (PV = 3)	NRT 2 (PV= 2)	NRT 3 (PV = 1)	Traffic Priority
1	ON	OFF	OFF	ON	5
2	OFF	ON	OFF	OFF	3
3	ON	OFF	ON	OFF	6
4	OFF	ON	ON	OFF	5
5	ON	ON	OFF	OFF	7
6	OFF	ON	ON	OFF	5
7	OFF	ON	OFF	ON	4
8	ON	ON	ON	ON	10
9	OFF	OFF	OFF	ON	1
10	ON	ON	OFF	OFF	7

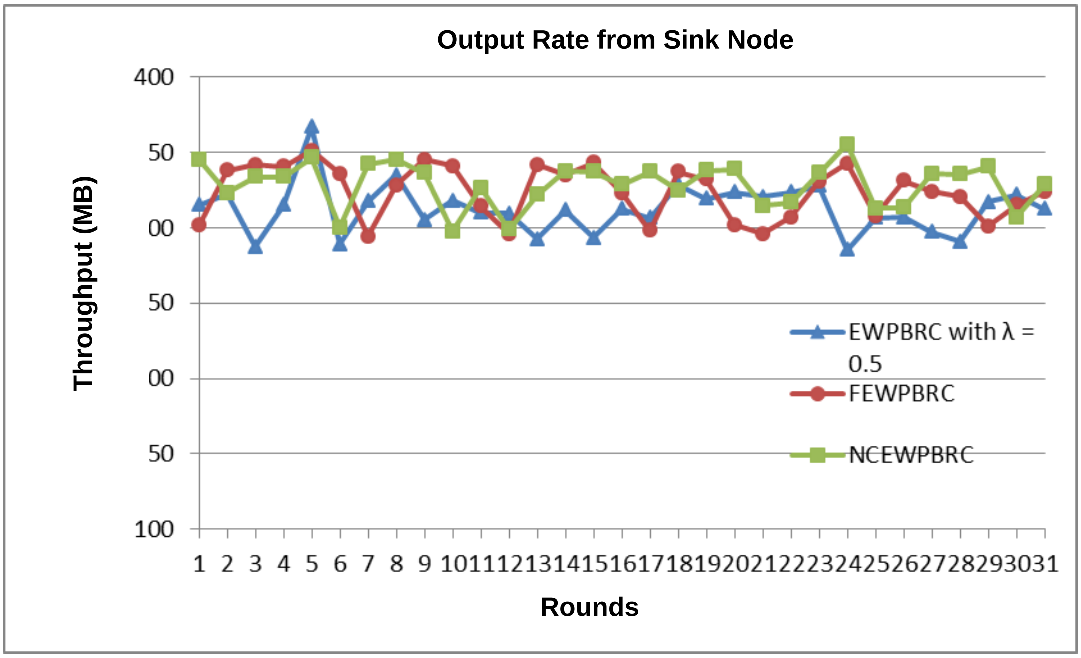

Figure 9. Compared performance of different algorithms for output transmission rate $r(sink)_{out}$.

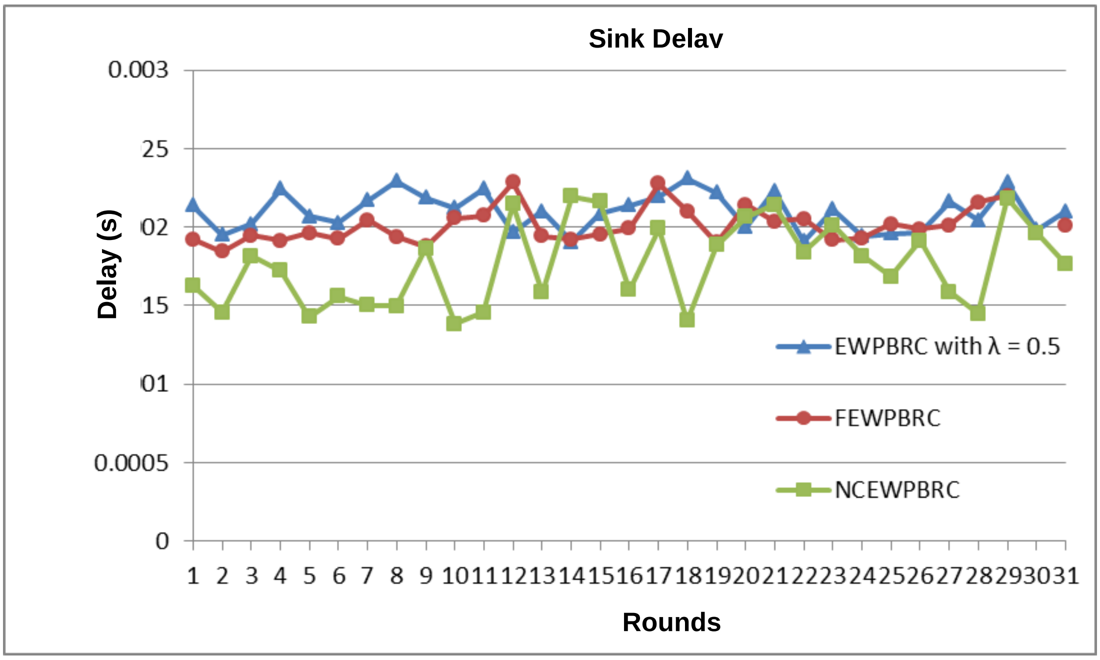

Figure 10. Compared the delay of sink node for different algorithms.

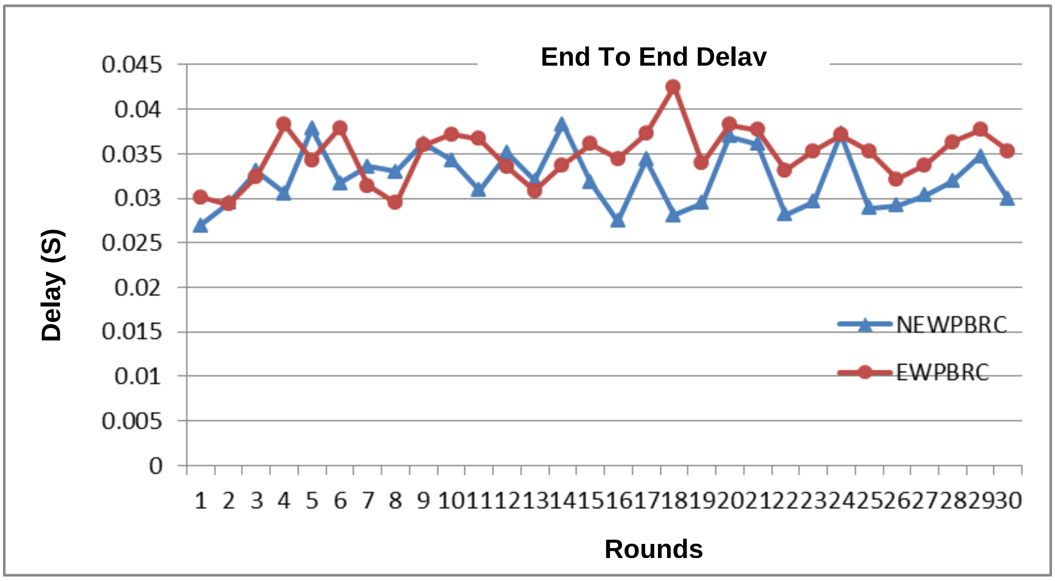

Figure 11. Comparison of end to end delay for different algorithms.

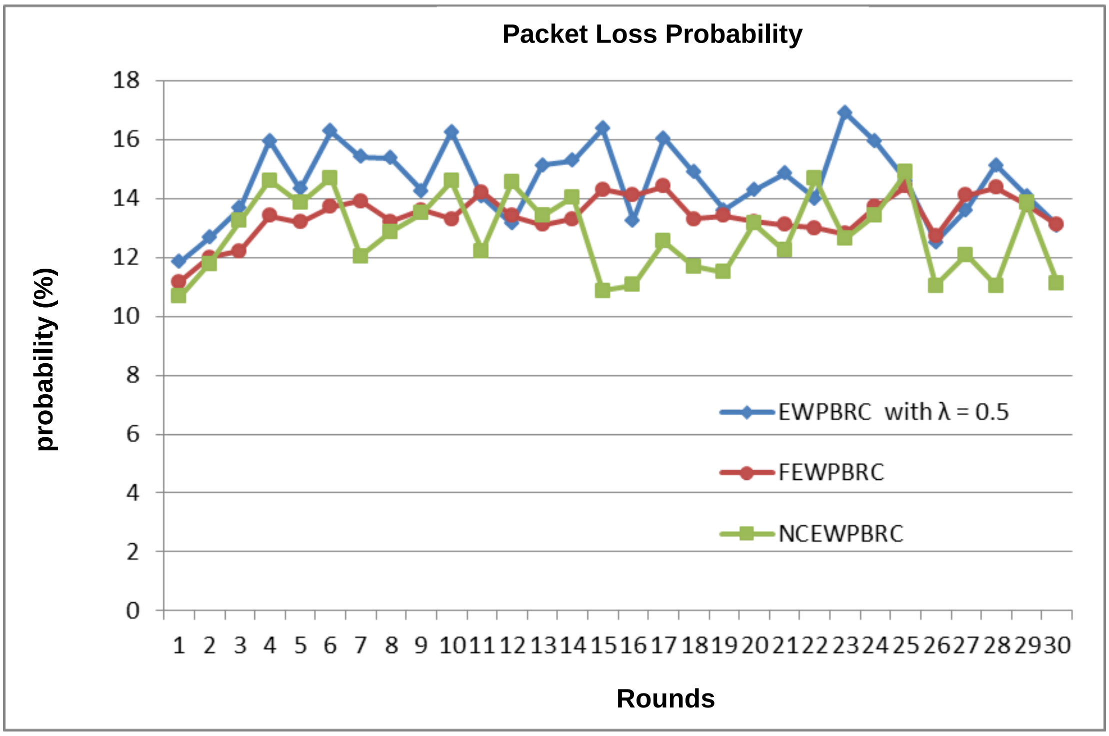

Figure 12. Compared of loss probability for different algorithms.

Study the Impact Behavior of the Prosthetic Lower Limb Lamination Materials Due to Low Velocity Impactor

Dr. Jumaa Salman Chiad
Assistant Professor
Engineering College -Al-Mustansiriya University
E-mail: jumaachiad@yahoo.com

ABSTRACT
This work involves three parts , first part is manufacturing different types of laminated below knee prosthetic socket materials with different classical laminated materials used in Baghdad center for prosthetic and orthotic (4perlon layers+2carbon fiber layer+4 perlon layers) , two suggested laminated materials(3perlon layers+2carbon fiber layer+3 perlon layers) and (3perlon layers+1carbon fiber layer+3 perlon layers)) in order to choose perfect laminated socket . The second part tests (Impact test) the laminated materials specimens used in socket manufacturing in order to get the impact properties for each socket materials groups using an experimental rig designed especially for this purpose. The interface pressure between the residual leg and prosthetic socket is also measured to cover all the surface area of the B-K prosthetic socket by using piezoelectric sensor in order to estimate the resulting stress according to loading conditions . A male with age, length, mass, and stump length of 42 years, 164 cm, 67 Kg and 13 cm respectively with a right transtibial amputation is chosen to achieve the above mentioned test procedures. The last part suggests a theoretical and analytical models for each group of specimen to find out the absorbed energy behavior and subjected maximum stress for each laminated B-K prosthetic socket materials .

Keywords :prosthetic, transtibial, impact, composite material

دراسه سلوك الصدم الواطئ السرعه للمواد المركبه المستخدمة في صناعه وقب الطرف الصناعي لبتر تحت الركبه

د. جمعه سلمان جياد
استاذ مساعد
كليه الهندسة/الجامعه المستنصرية

الخلاصة
يتضمن هذا العمل ثلاثة اجزاء رئيسية الاول شمل تصنيع وقب طرف صناعي وفق طريقة الخلط وعدد الطبقات المستخدمة كلاسيكيا في مركز بغداد للاطراف الصناعية وهي (4طبقة برلون+2طبقة كاربون فايبر +4 طبقة برلون) وايضا تم اقتراح نموذجين اخريين هما (3طبقة برلون+2طبقة كاربون فايبر +3 طبقة برلون) و(3طبقة برلون+1طبقة كاربون فايبر +3 طبقة برلون) .اما الجزء الثاني فكان تصنيع وفحص العينات لمختلف الفحوصات الميكانيكية كفحص الشد بالاضافة الى فحص الصدم من خلال استخدام منظومة فحص صممت وصنعت لغرض اجراء فحص الصدم الواطئ السرعة للمواد المركبة المستخدمة في تصنيع وقب طرف صناعي لبتر تحت الركبة.كما تم قياس ضغط التلامس بين وقب الطرف الصناعي ومتبقي الطرف لحالة بحثية تعرضت لبتر تحت الركبة بعمر 42سنة وطول 164 سم ووزن 67 كيلوغرام وطول بتر 13 سم من خلال استخدام منظومة قياس ضغط التلامس صممت وصنعت لهذا الغرض بهدف حساب الاجهادات التي يتعرض لها الطرف الصناعي اثناء تعرضة لظروف العمل المختلفة.الجزء الثالث والاخير تضمن اقتراح حل نظري ونموذج عددي للحالة البحثية

لكل مجموعة من العينات لكل مادة مقترحة لتصنيع وقب الطرف الصناعي لايجاد سلوك الطاقة المخزونة وايجاد الاجهاد الاعظم الذي يتعرض له وقب الطرف الصناعي اثناء الخدمة وظروف التحميل المختلفة .

1. INTRODUCTION

There are several levels of lower limb amputation, including partial foot, ankle disarticulation, transtibial (below the knee), knee disarticulation, transfemoral (above the knee), and hip disarticulation. The lower Limb Prosthesis is an artificial external device that replaces all or part of the lower extremity. Prosthesis is used for granting an individual who has an amputated limb the opportunity to perform functional tasks, particularly ambulation (walking), which may be impossible to do without the limb .Ideally, a prosthesis must be comfortable to wear, easy to put on and to be remove, light weight, durable, and cosmetically pleasing. Furthermore, a prosthesis must function mechanically in a good way and requires reasonable maintenance only. The frequently used prosthetic largely depends on the motivation of the individual as none of the above characteristics matters if the patient does not wear the prosthesis. The basic components of the B-K lower limb prostheses are the foot-ankle assembly, shank, socket, and the adapter . The below-knee sockets are laminated by using composite materials (perlon,carbon fiber and acrylic resion) with different layers under the vacuum condition .

The gait cycle consists of the stance phase which takes about 62% of total gait cycle time and the swing phase which comprises about 38% of the total gait cycle time ,**Goldberg,et al.,2008.**The ground gait cycle of a person is normally comprised of the following steps : (Initial contact (heel strike) ,loading response (fully flat foot) in the stance phase, midstance, the terminal stance (heel off),Toe-off (pre swing in swing phase),initial swing, mid swing, and terminal swing) , **Jason, 2005,Goujon,2006, Kumar, 2005,Christopher, et al., 1999 .**

The impact occurs when two or more bodies collide. Among important characteristics of the impact is the generation of relatively large forces at points of contact for relatively short periods of time. Such forces are sometimes referred to as the impulse-type forces. Three general classes of impact which are considered in this work including : (1) the impact between spheres or other rigid bodies, where the body is considered to be rigid if its dimensions are large in comparison to the wavelengths of the elastic stress waves in the body; (2) the impact of the rigid body against a beam or plate that remains substantially elastic during the impact; and (3)the impact involving yielding of structures ,**Hoppmann**, 1961. As a result, when impacted, a metal structure typically deforms but does not actually fracture. In contrast, composites are relatively brittle.

The brittleness of the composite is reflected in its poor ability to tolerate stress concentrations. The characteristically brittle composite material has poor ability to resist the impact damage without extensive internal matrix fracturing,**Tuttle, 2004.**The deformation remains elastic if the impact V_O velocity does not exceed $V_E=\sqrt{(EI/\rho)}$ where KE is the elastic-limit curvature . When $V_O > V_E$ and the hardening is linear, different deformation patterns develop for $V_E < V_O < 2.087\ V_E$ and for $V_O > 2.087\ V_E$, **Jacob ,2008**.

Roger ,et al.1989. Concluded that at the lowest impact energy level, the composite is able to absorb the majority of the energy imparted to it. At increasing impact energy levels, the damage is seen to occur, i.e. the energy was absorbed elastically by the material is less than the energy imparted to the material. The energy that was absorbed elastically by the material is the difference of the maximum energy vs. time curve minus the energy at the end of the test.

L.S. Chocron,et al.,1997. Developed a new failure criterion that was based on the energy that crosses each yarn, to build a simple analytical model of impact in textiles. This rnodel had been checked with Dyneema armours and predicted accurately the residual velocity of the Fragment Simulating Projectiles. The model has been completed with a delamination equation taken from Beaumont in order to include the composite characteristics of delamination.

Serge,2007. Showed that composite structures are sometimes subjected to impacts in partial penetration or the complete perforation. Tests are conducted to determine the velocity required to achieve complete penetration for a given projectile, and a model is required for data reduction purposes in order to understand the effect of the various parameters and to extrapolate for other test conditions. Here, a systematic approach for developing engineering models for composite structures is presented and the models obtained are used to analyze the experimental results.

Mohd,2008. suggested a computational model to analyze the behavior of the composite material that was subjected to the impact load tensile load. A general purposed commercial finite element code was employed to develop the computational model. Fiber glass that reinforced composite, one of the commonly used structural composites, was chosen to be used as the test material. The computational model was constructed 2-D axissymmetric finite elements.

Alastair ,2008. described the recent progress on the materials modeling and numerical simulation of the impact and crash response of fiber reinforced composite structures. The work is based on the application of explicit finite element (FE) analysis codes to composite aircraft structures under both low velocity crash and high velocity impact conditions. The detailed results are presented for the crash response of the helicopter subfloor box structures using a strain based damage and failure criterion for fabric reinforced composites.

Thibaut,et al. ,2010. concluded that the dynamic fracture in shock-loaded materials is governed by the propagation, reflection ,and interactions of the stress waves. The post-shock analyses of the residual damage observed in samples recovered from laser shock experiments, less destructive than the more conventional techniques, can provide valuable insight into the key aspects of wave propagation prior to fracture, such as the effects of the structural anisotropy, the role of lateral waves associated to edge effects, or the influence of polymorphic phase transformations on the response to the shock loading.

The impact literatures and papers are concerned with the impact of the general composite materials .This mean that this paper deals with the impact problem in B-K prosthetic socket is very limited , therefore , this work is devoted to enrich this field of work and also stands as a benchmark for other investigators in the future .

2.EXPERIMENTAL WORK

2.1Material and Laminations

The materials of the B-K prosthetic socket chosen are randomly laminated. This means that the material is Isotropic . In this work, the material needed for socket are laminated using vacuum technique as it is shown in **Fig. 1 .** Perlon stockinet white, Carbon fiber sheet ,Lamination resin 80:20 polyurethane ,Hardening powder, and Polyvinyalcohol PVA bag are used in the B-K prosthetic socket lamination. All the lamination materials are tested using tensile and bending instruments by manufacturing tensile and bending specimens for each lamination according to ASTM D638 for tensile specimens and ASTM D790 for bending specimens. Three type of lamination materials are used in this work, namely (3Perlon+1 carbon fiber+3Perlon), (3Perlon+ 2 carbon fiber+3Perlon) and (4Perlon+2 carbon fiber+4Perlon) as shown in **Table1**.

2.2 Impact Testing

In this work all below- knee prosthetic socket lamination are tested using low velocity impact instrument ,**Nasser, 2011. Fig. 2** shows all parts of this instrument. All impact specimens are with dimension of (50*200)mm*mm and different thickness according to laminations layers to be suitable for the impact instrument requirements . All specimens are tested by a drop-weight low velocity impact tester with different high and different impact energy as it is shown in **Table 2.**

2.3The Interface Pressure Measurement

The interface pressure between the residual leg and prosthetic socket is measured by using piezoelectric sensor shown in **Fig. 3** The pole of the sensor is connected with multi-meter devise to obtain the magnitude of the voltage that resulted from the response of the sensor through the stance phase. The multi-meter and piezoelectric are interface with the computer and recording data as shown in **Fig. 4 .**The pressure is measured in the region between residual limb and B-K prosthetic socket in four lines (Interior, Lateral ,Posterior and medial).Each line is divided into three parts longitudinally as it is shown in **Fig. 5**. A male with age of 42 years, height of 164 cm, mass of 67 Kg, and stump length of 13 cm with a right transtibial amputation is chosen to achieve the above mentioned testing procedures. **Fig. 6** shows the amputee during IP test.

The program of multi-meter giving maximum and minimum value of voltage with time .This reading can be calibrated to the interface pressure against gait cycle time .

3 Theoretical Consideration

Process shown in **Fig. 2** in order to calculate the deflection, force, impact energy , and absorbed energy. The simulated model can be treated as a beam fixed to a supporting plate which in turn fixed to the base during which the impact ball hits the specimens at the midpoint. It is clear that deflection will result from bending and shear deformation but the beam is impacted by the impact ball with different impact energy .This means that the Castigliano's theorem must be used to estimate the total and dynamics deflection formula for all types of B-K prosthetic socket laminations materials. **Table 3**. lists the total and dynamics deflections formula for all types of laminations.

The total absorbed energy can be derived according to normal and shear by using the following general formula with the element length of d x.

Defor..energy= $\frac{1}{2}\left[\int_0^d \sigma_{xx\varepsilon_{xx}dV} + 2\int_0^d (\mathcal{T}_{xz}\gamma_{xz} + \mathcal{T}_{xy}\gamma_{xy})dv\right]$ (1)

Finally the absorbed energy also resulted due to momentum conversation using the general formula.

$$\left(mV_2 \;\; - mV_1 \;\;\right) = \int_{t1}^{t2} pdt \qquad (2)$$

$$E_{ab}A = \frac{1}{2}(mV_2^2 - mV_o^2) \qquad (3)$$

4. NUMERICAL ANALYSIS

The general analysis by using ANSYS has three distinct steps that:

- Building the geometry as a model.
- Applying the boundary conditions load and obtaining the solution.

- Reviewing the results.

In this work (below –knee)prosthetic sockets model was drawn by using CAD system (Auto CAD) which was processed according to an default pattern in three dimensions .The dimension was taken from the same B-K socket that done on it measurement of experimental part. The aim of drawing models by AUTOCAD is to use in ANSYS workbench program for modeling, meshing and defining boundary condition such as applied load. The models is illustrated in **Fig. 7**,this figure shows the FEM meshing model and loading boundary condition in a and b respectively .

5. RESULTS AND DISCUSSION

5.1 Mechanical Properties

The mechanical properties for each sample can be calculated by taking the average value of the mechanical properties (σ_y, σ_{ult}, E and G)according to the tensile and flexural test . The mechanical properties for all laminations are listed in **Table.4**.

5.2 Impact Results

The experimental impact test result can be divided into two groups. The first one is the force behavior of the specimen that includes oscillatory phenomena visible in the force–time trace .The second group is the deflection behavior according to the impact energy shown in **Table 2**. **Fig. 8** shows the force behavior for the first lamination(L1) which consists of three layers of perlon plus one layer of carbon fiber plus three layers of perlon . It is clear that the general behavior is near to the sinusoidal waves . **Fig. 8** shows the force behavior of the lamination materials according to three levels of impact energy, which are (8.82,18.12,and 36.12)) J for the impact load of (1)Kg with different impact height of (0.25,0,5 and 1)respectively .The figure shows that the maximum force is recorded at the mass 1 kg with height 1m In the same manner , it can be concluded that the maximum deflection recorded with the specimen subjected to 1kg with 1m height as it is shown in **Fig. 9.** The impact results for all lamination specimens are listed in **Table 5.**

The above table shows that the best behavior of absorbed energy is recorded for the below knee prosthetic socket which consists of three outer perlon layers plus one central carbon fiber layer plus three inner perlon layers .The ranges of the absorbed energy recorded for this lamination were between (74.8-89.40%) for all levels of the impact mass and height. While the second lamination which consists of(3perlon layer+2carbon fiber layers+3perlon layers)has the range of absorbed energy of(67.9-80)%. The third lamination which consists of(4perlon layer+2carbon fiber layers+4perlon layers)recorded the range of absorbed energy of(60.9-68.3)%.

5.3 Interface Pressure Results

The interface pressures results shows that the maximum value is recorded at socket interior region exactly at patella tendon with 202.6Kpa as it is shown in **Fig. 10** which shows the general IP behavior against gait cycle time during which two peaks are recorded at loading response , and toe off of gait cycle and small reduced will be noticeable at midstance of gait cycle. This behavior is the same for all measuring regions during which other maximum values IP are recorded at (popliteal depression, lateral tibia, medial gastrocnemius , and distal gastrocnemius) with values of (186.6,92.71,65.87, and 54.32) respectively as shown in **Table 6** .

5.4 Analytical Results

According to the loading boundary condition for the below – knee prosthetic socket of the testing amputee the Von –Mises stresses are shown in **Fig. 11** which shows that the stress distribution is a mirror of interface pressure distribution shown in **Fig. 7** and **Table 6 .** The Von- Mises stresses results shows that the maximum value is recorded at socket 5 interior region exactly at patella tendon with 0.8155 Mpa,while the values of stresses are recorded at (popliteal depression, lateral tibia, medial gastrocnemius and distal gastrocnemius) with values of (0.7212,0.5445,0.3954, and 0.2943) Mpa respectively .
Fig. 12 shows the stress distribution according to the interface pressure boundary condition and impact with impactor of 1 Kg of mass from 1 m height at the mid distance of socket interior length .It is clear that the values of stresses jump to the maximum value of 16.2 Mpa at impact contact point at center of anterior wall of prosthetic socket .**Table 7** shows all cases of the numerical solution for both inteterface pressure boundary condition and impact with different impact mass and impact height for all type of lamination .

6. CONCLUSION

1-The Maximum absorbed energy percent is recorded with B-K prosthetic socket lamination which consist of (3perlon +1 carbon fiber+3perlon) layers with 89.4%.
2- The maximum value of the interface pressure is recorded at socket interior region exactly at patella tendon with 202.6Kpa
3- The maximum value of the Von- Mises stress due to interface pressure boundary condition is recorded at B-K prosthetic socket at the interior region exactly at patella tendon with 0.8155 Mpa.
4- The maximum value of the Von- Mises stress due to interface pressure and impact boundary condition is recorded at B-K prosthetic socket lamination which consists of (3perlon +1 carbon fiber+3perlon) layers at the region of the impact contact in the center of anterior socket wall with 16.2 Mpa a0.8155 Mpa.
5- All types of B-K prosthetic socket lamination are safety used .
6- The suggested lamination which consists of (3perlon +1 carbon fiber+3perlon) is the best to be used due to its safety and because it reduces the cost and weight of the prosthetic socket.

7-References

Goldberg,J. E., Philip, S.R. and Eileen,G. F. ,2008, "***The Effects of Direct Measurement Versus Cadaver Estimates of Anthropometry in the Calculation of Joint Moments during Above –Knee Prosthetic Gait in Pediatrics"***, Journal of Biomechanics ,Vol.41,No.3. pp. 695-700

Jason,W.J., 2005***,"Preliminary Design Approach for Prosthetic Anke Joints using Compliant Mechanisms "***, Msc. Thesis ,mechanical engineering department ,Brigham young University

H. Goujon,2006 "***Analyse De La Marche del'Amputee Femoral"***, PhD. Thesis,biomechanical engineering department , Unversity of Ensam ..

Kumar, R.,T.,2005, ***"Task Oriented Stable Gait Synthesis in Biped Locomotion "***, Msc. thesis submitted to Indian institute of information technology .

Christopher, L.,V., Briant D.,S., and Jeremy C., C., 1999***,"Dynamics of Human Gait"***, Second edition , Kibiho publisher Cape town, South Africa.

Hoppmann, W.,H., 1961,*"Shock and Vibration Handbook"*,. McGraw-Hill Book Co., New York.

Tuttle, M.,E., 2004,*" Structural Analysis of Polymeric Composite Materials"*, Marcel Dekker Book, Inc
Jacob L.,R.,2008,*" Plasticity Theory"*, Dover Publications, University of California at Berkeley

Roger M., C., and Thomas ,D., J., January 1989 *" Instrumented Impact Testing of Composite Materials"*, Approved for public release; distribution unlimited, Bethesda, Maryland,Ship Materials Engineering Department .

Chocron, L,.S., Benloulo,R.,T., and etl, 1 997,*" A Simple Analytical Model for Ballistic Impact in Composites"*, Journal Dephysiqueiv, France .

Serge, A.,T., 2007,*" Ballistic Impact on Composites "*, 16Th International conference on composite Materials, Kyoto, Japan .

Mohd, A., S., 2008, *" The Study of Impact Response of Composite Materials "*, Report submitted to Faculty of Mechanical Engineering, University Malaysia Pahang.

Alastair ,F., J., 2008, " *Impact and Crash Modeling of Composites Structure* " , German Aerospace Center (DLR) ,Institute of Structures and Design, Stuttgart, Germany

Thibaut, D.,R., 2010 " *Wave Propagation and Dynamic Fracture in Laser Shock-Loaded Solid Materials"*, Edited by Andrey Petrin, CNRS,ENSMA,ParisTech,France.

Resan, K.,K., 2007 *"Analysis and Design Optimization of Prosthetic BK"*, Ph.D. thesis ,university of technology ,Baghdad,.

Jumaa ,S., C., 2009 *" Design and Optimization of the Above Knee Prosthetic Socket"*, PhD Thesis ,University of Technology ,Baghdad.

Nasserو N. J.و 2011*"Study of the Effect of Impact on Curved Composite Plates "*,Msc. Thesis ,Mech.Eng. Departments, Al-Mustansiriya Unversity,

NOMENCLATURE

Perlon= is a polyamide fibers Use in orthopedic technology as stockinette
B.K = below Knee
Vth= theoretical impactor velocity (m/s)
Vexp= experimental impactor velocity (m/s)
H= impactor height (m)
Abs.En.= absorbed energy (J)
Imp.En.= impact energy (J)
IP= interface pressure (Kpa)
Lam1= 3perlon+1carbon fiber+3perlon
Lam1= 3perlon+2carbon fiber+3perlon
Lam1= 4perlon+2carbon fiber+4perlon
Ms= impactor mass (Kg)
σ_Y = yield stress (Mpa)
σ_{Von} = Von –Mises stress(Mpa)

σ_{Ult} = ultimate stress (Mpa)
E,G= modulus of elasticity and rigidity (Gpa)
δ_T,δ_D= total and dynamics deflections (mm)

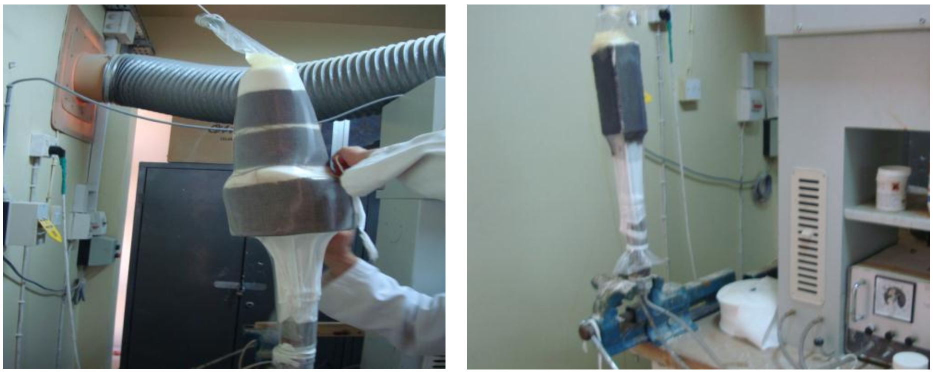

Figure 1. Vacuum technique for prosthetic socket lamination.

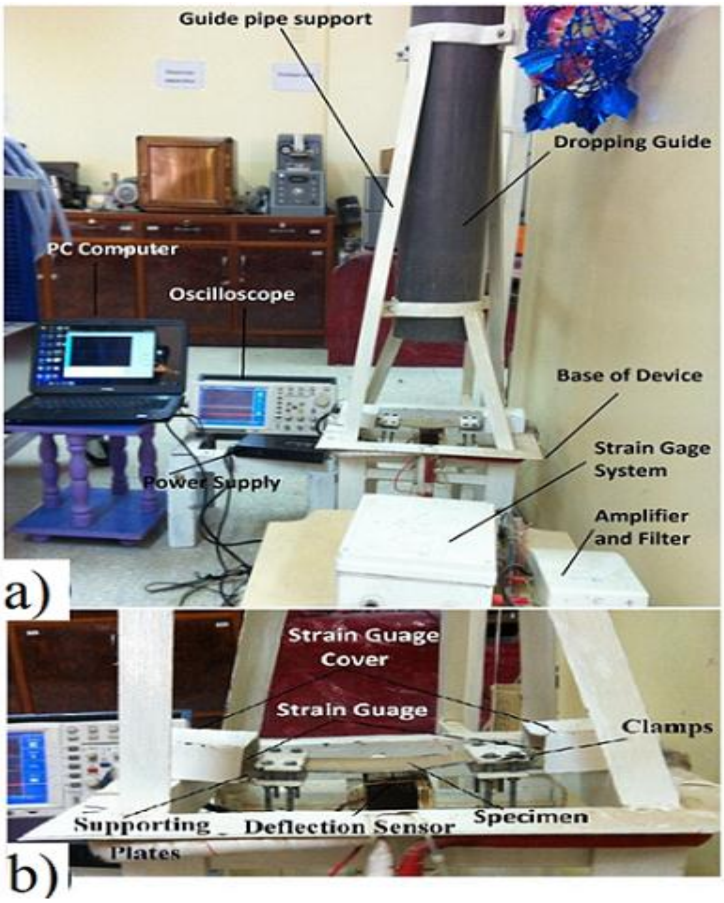

Figure 2. Impact instrument a)All parts b)Specimen region.

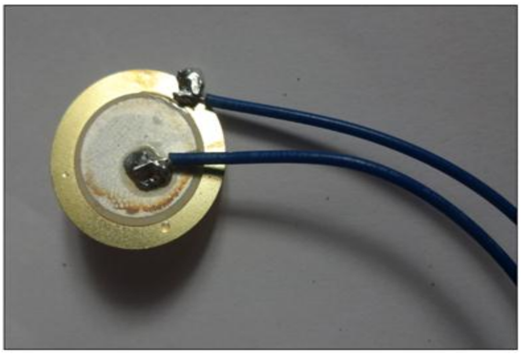

Figure 3. The piezoelectric sensor (Diameter = 15mm).

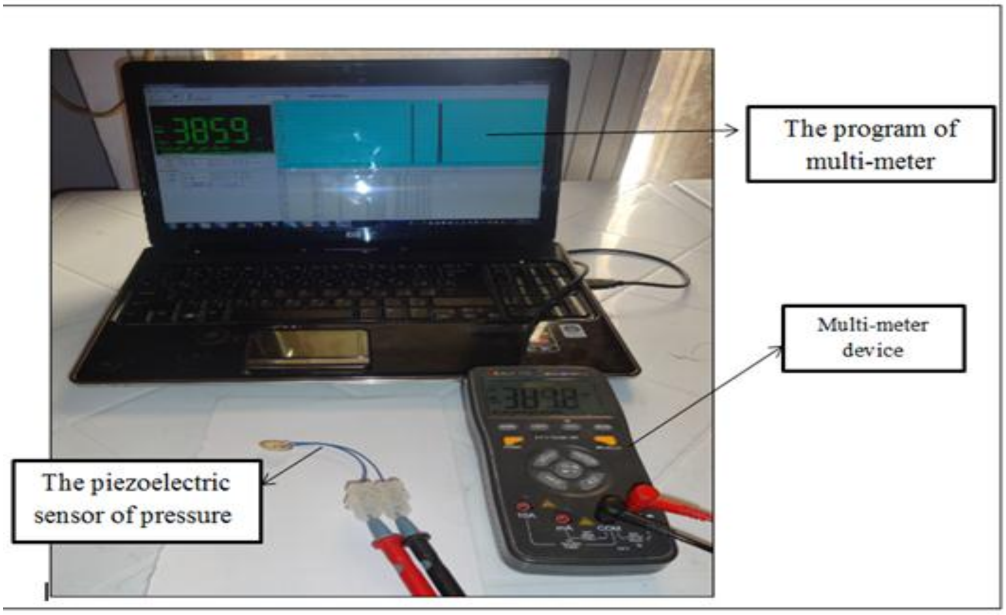

Figure 4. Multi-meter and sensor are interface with the computer.

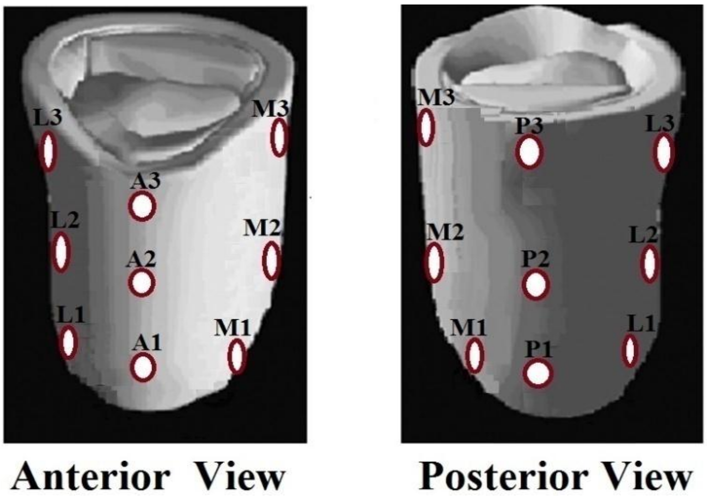

Figure 5. Piezoelectric sensor measuring position.

Figure 6. Transitibial amputee during IP test.

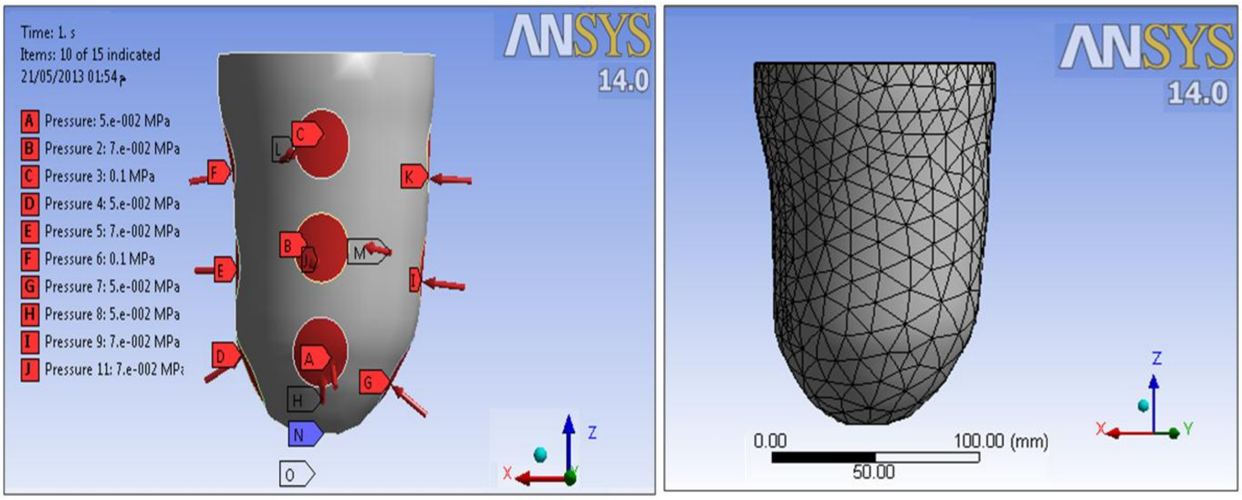

a) b)

Figure 7. FEM mesh(a) and boundary loading condition (b) of the B-K socket model.

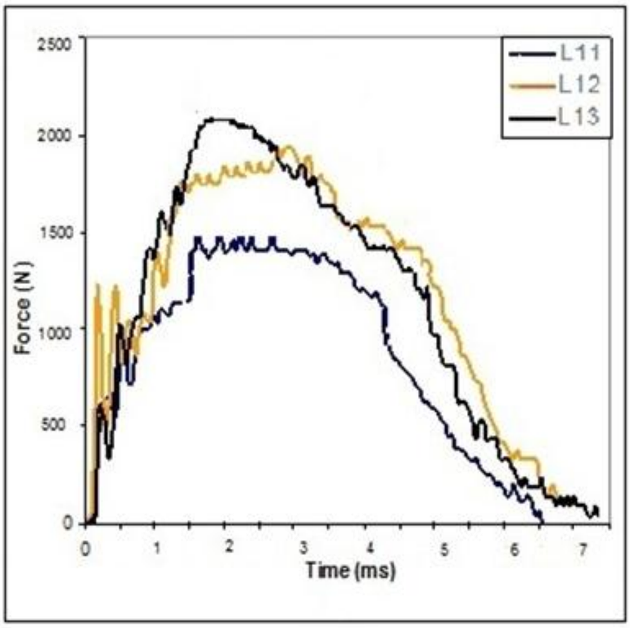

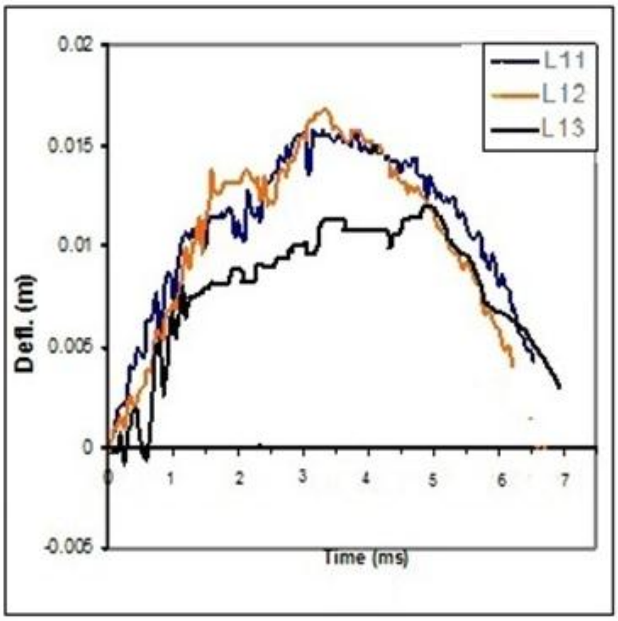

Figure 8. Force-Time curves for first lam.L1 **Figure 9.** Deflection-Time curves for first lam.L1.

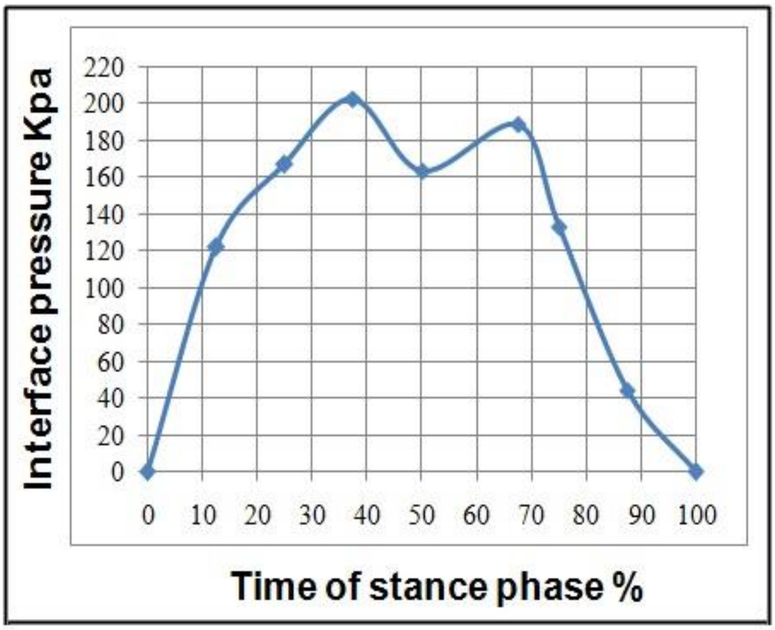

Figure 10. Interface pressure against gait cycle at Patella tendon.

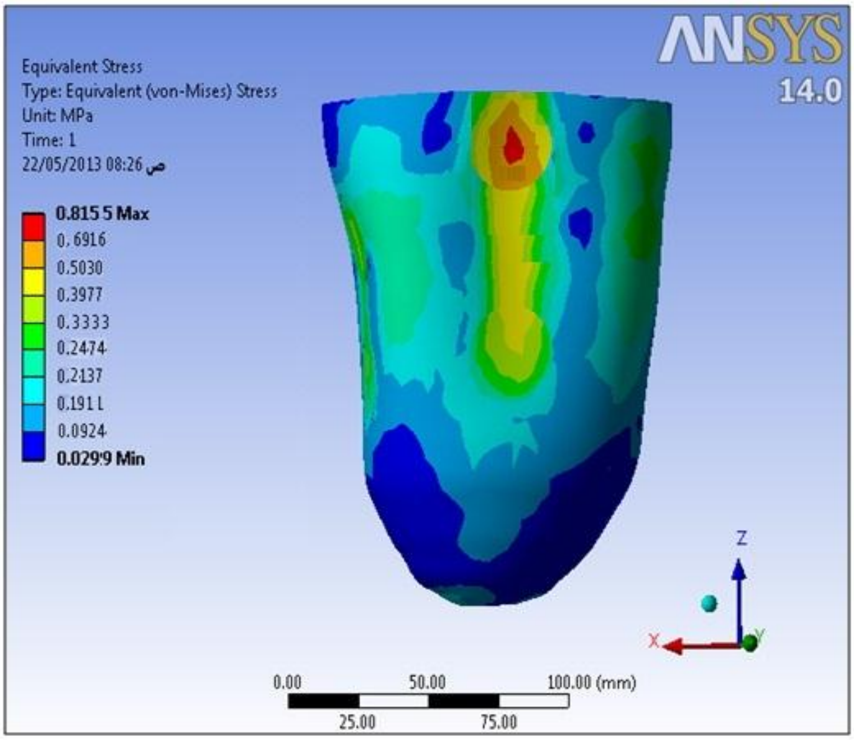

Figure 11. Von-Mises stress distribution according to the interface pressure boundary condition for B-K prosthetic socket lamination L1 (313).

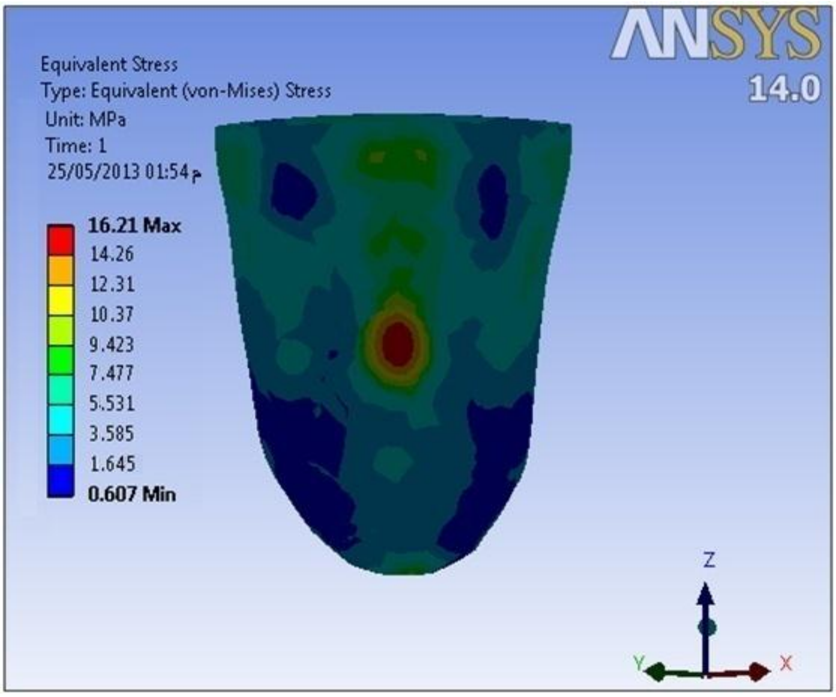

Figure12. Von-Mises stress distribution according to interface pressure boundary condition and impactor of 1 Kg with 1 m height at the center of the B-K prosthetic socket lamination L1 (313).

Table 1. All B-K prosthetic lamination material.

B-K Lam.	Total layers	Thick. mm	Lam. lay up procedures
Lam.1	7	2.8	3Perlon + 1 carbon fiber+3Perlon
Lam.2	8	2.9	3 Perlom + 2carbon fiber+ 3 Perlon
Lam.3	10	3.1	4 Perlon + 2carbon fiber+ 4 Perlon

Table 2. All impact specimens numbering with different impact energy.

Impact Mass Kg	Speci. Type	Speci. No.	Vth.	Vexp.	Imp. En. (J)	H (m)
0.25	L1	L11	2.2	2.1	0.55	0.25
		L12	3.1	3.01	1.13	0.5
		L13	4.4	4.25	2.25	1
	L2	L21	2.2	2.1	0.55	0.25
		L22	3.1	3.01	1.13	0.5
		L23	4.4	4.25	2.25	1
	L3	L31	2.2	2.1	0.55	0.25
		L32	3.1	3.01	1.13	0.5
		33	4.4	4.25	2.25	1
0.5	L1	L11	2.2	2.1	1.1	0.25
		L12	3.1	3.01	2.26	0.5
		L13	4.4	4.25	4.515	1
	L2	L21	2.2	2.1	1.1	0.25
		L22	3.1	3.01	2.26	0.5
		L23	4.4	4.25	4.515	1
	L3	L31	2.2	2.1	1.1	0.25

		L32	3.1	3.01	2.26	0.5
		33	4.4	4.25	4.515	1
1	L1	L11	2.2	2.1	2.205	0.25
		L12	3.1	3.01	4.53	0.5
		L13	4.4	4.25	9.031	1
	L2	L21	2.2	2.1	2.205	0.25
		L22	3.1	3.01	4.53	0.5
		L23	4.4	4.25	9.031	1
	L3	L31	2.2	2.1	2.205	0.25
		L32	3.1	3.01	4.53	0.5
		33	4.4	4.25	9.031	1

Table 3. Total and dynamics deflections formula for all type of below- knee prosthetic socket lamination material.

Lam. No.	δ_T	δ_D
L1	$\left(8.54 * 10^{-8} + \frac{98.39 * 10^{4}}{E}\right)P$	$\delta_T(1 + \frac{1+2h}{\delta_T})^2$
L2	$\left(8.54 * 10^{-8} + \frac{88.56 * 10^{4}}{E}\right)P$	$\delta_T(1 + \frac{1+2h}{\delta_T})^2$
L3	$\left(8.54 * 10^{-8} + \frac{80 * 10^{4}}{E}\right)P$	$\delta_T(1 + \frac{1+2h}{\delta_T})^2$

Table 4. Mech. properties of the tested specimens.

No. of Lam.	Lay up	σ_Y MPa	σ_{Ult} MPa	E GPa	G GPa
L 1	313	34.2	47	2.2	0.85
L 2	323	31	52.4	2	0.78
L3	424	32	54.7	1.9	0.73

Tabl1 5. Absorbed energy for all type of socket lamination materials with different of impact energy.

Impact Mass Kg	Spec. type	Spec. No.	Imp En. J	Abs. En. J	Percent of Abs. En.%
0.25	L1	L11	0.55	0.42	76.3
		L12	1.13	0.847	74.9
		L13	2.25	1.8	80
	L2	L21	0.55	0.38	69.1
		L22	1.13	0.768	67.9
		L23	2.25	1.63	72.4
	L3	L31	0.55	0.335	60.9
		L32	1.13	0.737	65.2
		33	2.25	1.456	64.57
0.5	L1	L11	1.1	0.898	81.6
		L12	2.26	1.919	84.9
		L13	4.515	3.652	80.9
	L2	L21	1.1	0.823	74.8
		L22	2.26	1.647	72.9
		L23	4.515	3.115	68.99
	L3	L31	1.1	0.725	65.9
		L32	2.26	1.46	64.6
		33	4.515	3.085	68.3
	L1	L11	2.205	1.942	88.1
		L12	4.53	4.047	89.4

1		L13	9.031	7.468	82.7
	L2	L21	2.205	1.552	70.4
		L22	4.53	3.474	76.7
		L23	9.031	7.225	80
	L3	L31	2.205	1.576	71.5
		L32	4.53	2.999	66.2
		33	9.031	5.735	63.5

Table 6. Maximum interface pressure recording at all measuring regions.

Socket Regions	Sensor Positions	Interface Pressure Kpa
Anterior	A1	45.76
	A2	77.87
	A3	202.6
Lateral	L1	50.4
	L2	86.7
	L3	52.5
Posterior	P1	54.32
	P2	62.7
	P3	186.6
Medial	M1	42.6
	M2	65.87
	M3	33.91

Table 7. Von-mises stress distribution according to IP and IP plus impact B.C. for all type of prosthetic socket lamination.

Impact Mass Kg	Spec. type	Spec. No.	Imp En. J	σ_{Von} Mpa, IP	σ_{Von}, Mpa IP+Impact
	L1	L11	0.55	0.8155	5.53
		L12	1.13		6.87

0.25		L13	2.25		8.96
	L2	L21	0.55	0.7152	4.95
		L22	1.13		5.65
		L23	2.25		7.76
	L3	L31	0.55	0.6189	3.99
		L32	1.13		4,92
		33	2.25		6.13
0.5	L1	L11	1.1	0.8155	7.45
		L12	2.26		9.87
		L13	4.515		11.87
	L2	L21	1.1	0.7152	6.23
		L22	2.26		8.87
		L23	4.515		10.12
	L3	L31	1.1	0.6189	6.14
		L32	2.26		7.98
		33	4.515		9,33
1	L1	L11	2.205	0.8155	8.44
		L12	4.53		12.4
		L13	9.031		16.21
	L2	L21	2.205	0.7152	8.14
		L22	4.53		10.77
		L23	9.031		14.54
	L3	L31	2.205	0.6189	7.77
		L32	4.53		9.54
		33	9.031		11.65

Mixed Convection in a Square Cavity Filled with Porous Medium with Bottom Wall Periodic Boundary Condition

Dr. Ihsan Y. Hussein
Professor
Department of Mechanical Engineering
College of Engineering - Baghdad University
E-mail: drihsan@uobaghdad.edu.iq

Dr. Luma F. Ali
Lecturer
Department of Mechanical Engineering
College of Engineering- Baghdad University
E-mail: luma.fadhil@yahoo.com

ABSTRACT

Transient mixed convection heat transfer in a confined porous medium heated at periodic sinusoidal heat flux is investigated numerically in the present paper. The Poisson-type pressure equation, resulted from the substituting of the momentum Darcy equation in the continuity equation, was discretized by using finite volume technique. The energy equation was solved by a fully implicit control volume-based finite difference formulation for the diffusion terms with the use of the quadratic upstream interpolation for convective kinetics scheme to discretize the convective terms and the temperature values at the control volume faces. The numerical study covers a range of the hydrostatic pressure head $\Delta h = 5\,mm$, $\Delta h = 10\,mm$, $\Delta h = 15\,mm$, $\Delta h = 20\,mm$, and $\Delta h = 30\,mm$), sinusoidal amplitude range of $250 \le q_w \le 1250\ W/m^2$ and time period values of $(30 - 120)s$. Numerical results show that the pressure contours lines are influenced by hydrostatic head variation and not affected with the sinusoidal amplitude and time period variation. It is found that the average Nusselt number decreases with time and pressure head increasing and decreases periodically with time and amplitude increasing. The time averaged Nusselt number decreases with imposed sinusoidal amplitude and cycle time period increasing.

Keywords: porous medium, mixed convection, square cavity, sinusoidal periodic heating, finite volume method.

الحمل المختلط في حيز مربع مملوء بوسط مسامي مع شروط حدية دورية على الجدار السفلي

الاستاذ الدكتور احسان يحيى حسين
قسم الهندسة الميكانيكية
كلية الهندسة/جامعة بغداد

المدرس لمى فاضل علي
قسم الهندسة الميكانيكية
كلية الهندسة/جامعة بغداد

الخلاصة

يقدم البحث الحالي دراسة نظرية لأنتقال الحرارة بالحمل المختلط العابر في حيز محدد وسط مسامي محصور و مشبع بالمائع و مسخن بفيض حراري دوري ذو دالة جيبية.تم حل معادلة بواسون للضغط, الناتجة من تعويض معادلة دارسي للزخم في معادلة حفظ الكتلة, بإستخدام تقنية الحجم المحدد. تم حل معادلة الطاقة بإستخدام الحجم المحكوم الضمني المبني على صيغة الفروق المحددة مع إستخدام نظام القانون التربيعي للأستكمال الداخلي لحركة الحمل الحراري لفك ارتباط الحدود المشتركة الحمل و قيم درجات الحرارة على حدود الحجم المحكوم. ان التحقق العددي قد غطى كل قيم الحمل المختلط ($\Delta h = 5$ ملم, $\Delta h = 10$ ملم, $\Delta h = 15$ ملم, $\Delta h = 20$ ملم, and $\Delta h = 30$ ملم) و التردد الجيبي ذو المدى ($250 \le q_w \le 1250$ واط/م^2) و قيم الفترة الزمنية $(120 - 30)$ثانية.لقد أظهرت النتائج النظرية ان توزيع الضغط يتاثر بتغير الارتفاع الستاتي و لا يتأثر بتغير مدى الموجة الجيبية و الفترة الزمنية للموجة. لقد وجد ان ان معدل قيم نسلت تنخفض بزيادة الزمن و ارتفاع الضغط تنخفض بشكل دوري بزيادة الزمن و مدى الدالة الجيبية. ان المعدل الزمني لقيم نسلت تنخفض بزيادة كل من المدى و الفترة الزمنية للدورة.

1. INTRODUCTION

The involvement of both natural and forced convection, referred as mixed convection, in porous media has been an important topic because of its wide range of applications in engineering and science. Some of these applications include oil extraction, energy storage units and ground water hydrology. Early studies on convection in porous media were largely devoted to buoyancy-induced flows and forced convection. The interaction mechanisms between these two modes of convection was given very little attention. For mixed convection in confined porous medium, the fluid velocity required for forced convection is occurred from either porous enclosures with lid-driven, vented openings, suction / injection ports, vibrational obstructed cavities, or others. In the present work, the mixed convection is achieved by providing a hydrostatic pressure head through an inlet port, accordingly a forced convection condition is imposed inside the porous enclosure. Besides, the buoyancy forces of natural convection are introduced due to the temperature gradient of the bottom heated wall. Mainly, the problems of mixed convection in confined porous medium can be classified into two categories, first the type of mixed convection in confined porous medium with uniform boundary conditions while the second category involves mixed convection with non-uniform boundary conditions.

The volume averaged equations governing unsteady, laminar, mixed convection flow in a top lid driven two-dimensional square enclosure filled with a Darcian fluid-saturated uniform porous media in the presence of internal heat generation was investigated numerically employing the finite-volume approach by **Khanafer,** and **Chamkha, 1999**. Then, the laminar transport processesin a lid-driven two-dimensional square cavity filled with a water-saturatedporous medium was conducted numerically utilizing the alternating direct implicit algorithm by **Al-Amiri, 2000** and **Kandaswamy, et. al., 2008**. Also, **Khanafer,** and **Vafai, 2002**, by using the finite volume numerical approach, analyzed the double-diffusive mixed convection in a lid-driven square enclosure filled with a non-Darcian fluid-saturated porous medium. The numerical investigation utilizing the finite volume method for two-dimensional steady state mixed convection flow in a square vented cavity filled with fluid-saturated porous medium with an isothermal left vertical surface and remaining three walls perfectly insulated was studied by **Mahmud,** and **Pop, 2006**. Later, **Oztop, 2006,** presented numerically the combined convection heat transfer and the fluid flow due to the position of heaters in a partially heated lid-driven square enclosure filled with homogeneous and isotropic porous material. The problem of mixed convection in a driven square cavity packed with homogeneous and isotropic porous medium was studied with the lattice Boltzmann method by **Chai, et. al., 2007**. Subsequently, the finite element numerical method carried out by **Barna, et. al., 2008,** examined and explained the two-dimensional steady mixed convection flow in a square vented cavity filled with fluid-saturated porous medium with all walls are isothermal at constant temperature. Besides, **Vishnuvardhanarao,** and **Das, 2008** and **Kumar, et. al., 2009** considered two-dimensional, mixed convection flow in a square enclosure filled with a Darcian fluid-saturated uniform porous medium. The first study of vibration and buoyancy induced transient mixed convection in an open-ended obstructed cavity filled with a fluid-saturated porous medium was investigated by **Chung,** and **Vafai, 2010**. Furthermore, **Kumar,** and **Murthy, 2010** focused their attention on a problem of steady non-Darcy mixed convection inside a vertical square enclosure filled with fluid-saturated porous medium with multiple fluid injections at the bottom wall and multiple suctions at the top wall. Thus, forced convection is imposed by this combination of suction/injection flow conditions and free convection is induced by the hot and isothermal left vertical wall. Afterwards, **Muthtamilselvan, 2011,** examined numerically, by employing the finite volume method, the steady state two-dimensional mixed convection flow and heat transfer in a two-sided lid-driven square cavity filled with heat generating porous medium. **Kumari,** and **Nath, 2011** carried out numerically the steady state two-dimensional mixed convection in a square cavity flow of a heat generating fluid in a lid-driven square cavity filled with a fluid-saturated non-Darcy porous medium. Mixed convection is also taken place because of the buoyancy- and shear-driven flow induced by a hot plate moving through the horizontal mid-plane of a rectangular enclosure filled with fluid-saturated porous medium. This problem governing equations were thereby solved numerically using the finite difference method by **Waheed, et. al., 2011**. Furthermore, **Oztop, et. al., 2012,** performed a numerical study to analyze the flow field and temperature distributions of steady state laminar mixed convection heat transfer in a square left vertical wall partially cooled lid-driven cavity filled with fluid-saturated porous medium.

For the second category of mixed convection with non-uniform boundary conditions, The numerical study to obtain combined convection field in an inclined lid-driven enclosures filled with fluid-saturated porous media and heated from one wall with a non-uniform heater was carried out by **Oztop,** and **Varol, 2009**. They assumed that the lid is moving at constant speed and temperature while the bottom wall of the cavity has sinusoidal temperature distribution and remaining walls are adiabatic. Thence, the characteristics of a two-sided lid-driven mixed convection flow in a steady state two-dimensional square cavity filled with heat generating porous medium was numerically inspected by **Muthtamilselvan, et. al., 2010**. The top wall is maintained at a constant temperature and the bottom wall is sustained at uniform or non-uniform temperatures (sinusoidal type), while the side vertical walls were considered to be adiabatic. Detailed analysis of mixed convection of fluid within square porous cavity with generalized boundary conditions involving linear and uniform heating of adjacent walls or uniform cooling of a side wall in presence of uniform motion of top adiabatic wall and uniform heating of the bottom cavity wall was carried numerically by **Basak, et. al., 2010**. Then, **Basak, et. al., 2011** performed a penalty finite element method to analyze the influence of various walls thermal boundary conditions on mixed convection lid-driven flows in a square cavity filled with fluid-saturated porous medium. Thereafter, the influence of uniform and non-uniform heating of the bottom wall on the flow and heat transfer characteristics due to lid-driven mixed convection flow within a square cavity filled with porous medium was studied numerically utilizing penalty finite element analysis by **Basak, et. al., 2012**. Furthermore, **Ramakrishna, et. al., 2012,** explored the numerical study that deals with lid-driven mixed convection within square cavity filled with porous media for various thermal boundary conditions based on thermal aspect ratio on bottom and side walls where the top wall is adiabatic and moves from left to right with uniform velocity. The influence of the non-uniform thermal boundary conditions on mixed convection flow and heat transfer in a lid-driven cavity filled with fluid-saturated porous medium was investigated numerically by **Sivasankaran,** and **Pan, 2012**.

In the present study, transient mixed convection in a two-dimensional square cavity subjected to static pressure head and filled with a Darcian fluid-saturated porous medium is investigated numerically. The two vertical walls of the confined porous medium are insulated while the bottom wall is heated periodically and the heat is lost by convection from the top wall which is exposed to the environment. Detailed numerical solutions are carried out by utilizing the finite volume method for a range of parameters, namely the pressure head, amplitude, time period of sinusoidal imposed heat flux. Numerical results are obtained for pressure, and temperature fields within the enclosure and are displayed using pressure contours lines and isotherms respectively. Also, the average and time averaged Nusselt number variations are depicted in the present paper.

2. MATHEMATICAL FORMULATION

The two-dimensional inclined cavity under investigation is filled with fluid-saturated porous medium and all the walls are impermeable except the upper wall. Glass beads with specified diameter is used as a porous media and distilled water is used as the incompressible fluid that saturates the porous medium. The schematic configuration of the problem is illustrated in **Fig. 1**, with L denoting the length of the square cavity. Furthermore, the porous medium is assumed to be in local thermal equilibrium with the fluid.

The two vertical left and right sidewalls are adiabatic, and a periodic sinusoidal heating is applied on the bottom wall while the top wall is exposed to the environment and losses heat by natural convection. Water is supplied to the cavity from an external tank with a static head from an opening inlet at the bottom left corner and there is a water outlet open at the upper right corner. The thermophysical properties of the fluid and the porous material are taken to be constant except for the density variation in the buoyancy force, which is treated by the Boussinesq approximation.

The Darcy equation formulation is adopted for modeling the fluid flow in the porous medium. The governing equations for mass, momentum, and energy in two-dimensional, Cartesian coordinates, laminar flow are as follows:

Continuity equation

$$\frac{\partial u}{\partial x}+\frac{\partial v}{\partial y}=0 \tag{1}$$

Momentum equation

$$u=-\frac{K}{\mu_f}\left[\frac{\partial p}{\partial x}+\rho_f g\sin\varphi\right] \tag{2}$$

$$v=-\frac{K}{\mu_f}\left[\frac{\partial p}{\partial y}+\rho_f g\cos\varphi\right] \tag{3}$$

Energy equation

$$\sigma\frac{\partial T}{\partial t}+\left[u\frac{\partial T}{\partial x}+v\frac{\partial T}{\partial y}\right]=\frac{k_{eff}}{(\rho C_p)_f}\left[\frac{\partial^2 T}{\partial x^2}+\frac{\partial^2 T}{\partial y^2}\right] \tag{4}$$

where u and v are the fluid velocities in x and y directions respectively, K is the porous medium permeability, μ_f is the fluid dynamic viscosity, p is fluid pressure, ρ_f is the fluid density, g is the acceleration due to gravity, φ is the inclination angle of the cavity, T is the fluid temperature, t is the time, and σ is the specific heat ratio which is given as:

$$\sigma=\frac{(\rho C_p)_m}{(\rho C_p)_f} \tag{5}$$

where C_p is the specific heat at constant pressure and the subscripts m and f denoted to effective value and fluid phase respectively, k_{eff} is effective thermal conductivity of porous medium and it is given by **Hadley, 1986**:

$$\frac{k_{eff}}{k_f} = (1-\alpha_o)\frac{\varepsilon f_o + \lambda(1-\varepsilon f_o)}{1-\varepsilon(1-f_o)+\lambda\varepsilon(1-f_o)} + \alpha_o \frac{2\lambda^2(1-\varepsilon)+(1+2\varepsilon)\lambda}{(2+\varepsilon)\lambda+1-\varepsilon} \tag{6}$$

where ε is the porosity of the porous medium and k_s and k_f are the thermal conductivity of the solid material and fluid phase of the porous medium respectively, $\lambda = k_s/k_f$ is the thermal conductivity ratio of solid and liquid phases, f_o is a parameter which is expected to be approximately constant for a contiguous solid, and α_o is an another parameter that is very sensitive to porosity changes and it is represented for different porosity ranges as, **Suresh, et. al., 2005**:

$$\log \alpha_o = -4.898\varepsilon \qquad 0 \le \varepsilon \le 0.0827 \tag{7a}$$

$$\log \alpha_o = -0.405 - 3.154(\varepsilon - 0.0827) \qquad 0.0827 \le \varepsilon \le 0.298 \tag{7b}$$

$$\log \alpha_o = -1.084 - 6.778(\varepsilon - 0.298) \qquad 0.298 \le \varepsilon \le 0.58 \tag{7c}$$

The equation of state under the Boussinesq approximation is assumed to be:

$$\rho = \rho_o[1-\beta(T-T_o)] \tag{8}$$

where ρ_o and T_o are respectively the density and the temperature in the reference state, β the coefficient of thermal expansion.
In accordance with the present problem, the above governing equations are subjected to the following initial and boundary conditions:

$$u = v = 0,\ T = T_o \qquad \text{at} \quad t = 0 \tag{9}$$

$$u = v = 0,\ \frac{\partial T}{\partial x} = 0 \qquad \text{at} \quad x = 0 \text{ and } x = L \tag{10}$$

$$u = 0, k_{eff}\frac{\partial T}{\partial y} = q_o + a\sin(2\pi t/\tau),\ p = \rho g(L+\Delta h) \qquad \text{at} \quad y = 0 \tag{11}$$

$$u = 0, k_{eff}\frac{\partial T}{\partial y} = h(T-T_o), p = 0 \qquad \text{at} \quad y = L \tag{12}$$

where q_o is the uniform heat flux, a is the sinusoidal amplitude, h is the natural heat convection coefficient.
After inserting the Boussinesq approximation in the momentum **Eqs. (2)** and **(3)**, and the resulting equations substituted in **Eq. (1)**, the following new pressure differential equation is obtained:

$$\frac{\partial^2 p}{\partial x^2} + \frac{\partial^2 p}{\partial y^2} = g\rho_o\beta\left[\sin\varphi\frac{\partial T}{\partial x} + \cos\varphi\frac{\partial T}{\partial y}\right] \tag{13}$$

Eqs. (4) and **(13)** are solved numerically with the applied initial and boundary conditions to simulate the mixed convection in the inclined square cavity. The average Nusselt number on the bottom hot wall is given as:

$$Nu = \frac{\int_0^L \frac{\partial T}{\partial y} dx}{(T_b - T_o)} \tag{14}$$

where T_b is the boom hot wall temperature.
The time averaged Nusselt number for specific time period τ is casted as;

$$Nu_{\tau av} = \frac{1}{\tau} \int_{(r-1)\tau}^{r\tau} \left[\frac{-\int_0^L \frac{\partial T}{\partial y}\Big|_{y=0} dx}{L(T_b - T_0)} \right] d\tau \tag{15}$$

where r is the number of time period.

3. NUMERICAL FORMULATION

The governing **Eqs. (4)** and **(13)** in the present problem of mixed convection in a cavity filled with porous medium are solved by using the finite volume method **Versteeg,** and **Malalasekera, 2007**. A fully implicit scheme is applied for discretizing the time derivatives. The convective fluxes at the cell interface are discretized by employing the Quadratic Upwind Interpolation for Convective Kinematics (QUICK) scheme and a second-order central difference scheme is used for the diffusion terms. The resulting algebraic equations are solved by the tri-diagonal matrix algorithm (TDMA). For convergence criteria, the relative variations of the temperature and pressure between two successive iterations are demanded to be smaller than the previously specified accuracy levels of 10^{-5}. The iterative procedure is initiated by the solution of the pressure equation followed by calculating the velocity field and then solving the energy equation until reaching a specific temperature. This specified temperature is the mean value of selected location temperatures near the bottom heated wall. In the present study, the desired temperature is taken as $90\ ℃$ which is the temperature at which the working water fluid changes to the two phase condition.
Before proceeding further, the grid independency tests are performed first. Numerical experiments were performed for various grid sizes viz. 12×12, 16×16, 20×20, 24×24, 28×28, and 32×32 to test and estimate the grid independent solutions. These numerical experiments were accomplished for a hydrostatic head $\Delta h = 10\ mm$ and constant heat flux $q = 500\ W/m^2$. It is observed that the average Nusselt number values at the bottom heated wall of the enclosure are very near to each other when the grid size is near 24×24. Therefore, a grid size of 24×24 is chosen for further computations because it consumed less computing time. The parameters of convergence are fixed to 10^{-5} for both pressure and temperature. Furthermore, a similar test was done for the time step value and it is found that $\Delta t = 0.05\ sec$ is very sufficient for the present problem.

4. RESULTS AND DISCUSSION

Published experimental data are not available for the cavity configuration and boundary conditions similar to that taken in the present study. Thus, the validation of the computations against suitable experimental data could not be performed. However, in order to validate the predictive capability and accuracy of the present code, three published works have been chosen. For validation purpose of mixed convection flow and heat transfer, a differentially heated square cavity of natural laminar heat transfer is considered. The left surface is heated isothermally and right surface is cooled to a lower temperature with top and the bottom walls maintained thermally insulated. Average Nusselt number is calculated and depicted in **Table 1** for $Ra = 100$ and compared with the earlier investigations **Saeid,** and **Pop, 2004**, **Baytas, 2000**, and **Walker,** and **Homsy, 1978**. From **Table 1**, it is clearly revealed that the agreement between the present and the previous results is very good indeed. So, these results provide great confidence to the accuracy of the present numerical method.

In the present investigation, Soda Lime glass beads saturated with distilled water is chosen as a porous media. Its permeability and porosity are taken as 1.57×10^{-9} and 0.418 respectively. The controlling parameters on the heat transfer and fluid flow for this investigation are the hydrostatic pressure head and sinusoidal amplitude and time period. The computations have been carried out for the pressure head of $\Delta h = 10$and $20mm$. The sinusoidal amplitude is varied in the range from 250 to $1250\ W/m^2$ while the time period range is 30–120 s.

The pressure field is indicated in **Fig. 2** for hydrostatic pressure head values of $\Delta h = 10\ mm$ and $\Delta h = 20\ mm$ and a fixed value of $a = 750\ W/m^2$ amplitude and $\tau = 60\ s$ sinusoidal time period. It is clear from this figure that the pressure values at specific nodal point increases as the pressure head difference. Also, the pressure distribution is not affected by the variation of the amplitude and the time period as seen in **Fig. 3**. This figure is plotted for different amplitudes and time period of $\tau = 30\ s$ and pressure head value of $\Delta h = 20\ mm$. The pressure is unaffected because the temperature gradient is small value that is deduced from the amplitude value and taken place in the right hand side of **Eq. (13)** compared with the pressure value on the bottom boundary wall.

The steady state response of the periodic sinusoidal boundary condition is performed when the absolute difference of time averaged Nusselt number between two successive periodic cycles is less than an estimated number of 0.35. When this state response is reached, the temperature contours line for eight time steps of the last cycle is demonstrated for specific amplitude value of $a = 500\ W/m^2$, cycle time period of $\tau = 60s$, and three hydrostatic pressure head values of $\Delta h = 10\ mm$ and $\Delta h = 20\ mm$, in **Figs. 4** and **5** respectively. It can be noticed that the first half of the cycle is almost devoted to the temperature increasing of the bottom wall and the nearby porous domain. While the second half of the cycle is adapted to the convection heat transfer to the downstream of the porous enclosure and the bottom temperature is approximately remaining constant during this half of the heating periodic cycle. In the second half of the cycle, the imposed heat flux becomes small and not sufficient to increase the bottom temperature but just to maintain its temperature almost constant. On the other hand, there is a temperature difference between the bottom region and the upper region of the confined porous medium which tends to a buoyancy effect inducing through the domain and hence natural convection currents are invoked in addition to the mixed convection and liquid velocity effect in transferring heat through the cavity. Also, it is clear that the mixed convection influence increases with the pressure head difference increase from $10\ mm$ to $20\ mm$ and results in a higher temperature values as shown in **Figs. 4** and **5** respectively.

Figs. 6 to **8** present the influence of the amplitude variation from $250\ W/m^2$ to $750\ W/m^2$on the temperature field within the eight time steps of the last cycle when a steady state response is reached for the case of $10mm$ pressure head and $30s$ time period. It can be easily seen that the increase of the amplitude tends to temperature increase especially for higher amplitude values that leads to vigorous increase in temperature distribution. The main reason behind this behavior is that the temperature difference in the porous domain increases when the imposed amplitude is increased and consequently the buoyancy force effect is increased. This tends to convection currents increasing and obtaining higher temperature values. Furthermore, the influence of time period on the temperature contours line is observed in **Figs. 9** and **10** for hydrostatic pressure head of $20mm$ and imposed heat flux amplitude of $250\,W/m^2$. These figures pronounce that the time period increase causes a temperature increasing near the bottom wall because the time of heating operation increases and thus more heat flux amplitude is imposed to the porous enclosure. Additionally a further time is given to transfer the heat of the bottom region to the entire porous domain region when the time period is increased and this leads to heating most of the domain by the superposition of forced and natural convection mechanism caused by pressure head difference and buoyancy force effects respectively.

The variation of the average Nusselt number is plotted with consumed time of sinusoidal imposed heating on the bottom wall of a non-inclined porous enclosure in **Figs. 11** and **12** for $\Delta h = 10\,mm$ and $\Delta h = 20\,mm$ hydrostatic pressure head difference respectively. This figure is displayed for various values of amplitude from $250\,W/m^2$to $750\,W/m^2$, time period of $60\,s$ and $30\,s$successively. It can be easily seen that the Nusselt number decreases periodically with heating time increasing. By referring to **Eq. (14)**, this decrease is mainly due to the fact that the Nusselt number is inversely proportional with the temperature difference between the bottom heated wall and the downstream liquid temperature. Therefore, as this temperature difference increases with time increasing, the Nusselt number is decreased and has a periodic behavior because of the periodicity of the imposed heat flux. Additionally, the average Nusselt number is not altered with the amplitude increasing at certain simulation time because the mixed convection currents accelerates the heating process and has vigorous effect on the heat transfer characteristics compared with the buoyancy force influence that is resulted from the temperature gradient related mainly to the imposed amplitude heat flux.

Moreover, the variation of average Nusselt number with periodic sinusoidal heating time along the enclosure bottom wall at different response time period is presented in **Figs. 13** and **14** for hydrostatic pressure head values of $10\,mm$ and $20\,mm$ respectively. From these two figures, it is indicated that the peak value of Nusselt number for each time period case decreases with time period increasing. The temperature difference between the heated wall and the top region of the enclosure increases with the time period increasing because there is sufficient time for heating process. This is thought to be the reason behind the reduction of the Nusselt number with increasing time period because of the contrary relation between the Nusselt number and the mentioned temperature difference. For the same reason mentioned previously for the average Nusselt number, the time averaged Nuselt number during the cycle of steady state response decreases with the increasing of both the imposed sinusoidal amplitude and the cycle time period as demonstrated in **Figs. 15** and **16** for hydrostatic pressure head values of $10\,mm$ and $20\,mm$ successively.

5. CONCLUSIONS

Convective flow and heat transfer in a square porous cavity with sinusoidal periodic heat flux at the bottom wall is investigated numerically. The following conclusions are made from this study.

- The pressure field and the velocity vector are increased with increasing hydrostatic pressure head.
- The first sinusoidal heating half cycle is devoted to the bottom wall and nearby porous domain temperature increasing while the second half of the cycle is adapted to convection heat transfer to the porous domain downstream.

- The amplitude increase causes temperature increase especially for higher amplitude values that leads to vigorous increase in temperature distribution and the sinusoidal time period heating increase causes a temperature increasing near the bottom wall.
- The average Nusselt number decreases periodically with sinusoidal heating time increasing for certain amplitude value and also decreases with amplitude increasing for specific simulation time when the pressure head is zero but it is not altered with amplitude increasing when the head pressure is greater than zero.
- The peak value of the average Nusselt number decreases with time increasing for each time period case.
- The time averaged Nusselt number decreases with the increasing of the imposed sinusoidal amplitude and the cycle time period.

REFERENCES

Al-Amiri, A. M., 2000, *Analysis of Momentum and Energy Transfer in a Lid-Driven Cavity Filled with a Porous Medium*, Int. J. Heat Mass Transfer, Vol. 43, pp. 3513–3527.

Basak, T., Krishna Pradeep, P. V., Roy, S., and Pop, I., 2011, *Finite Element Based Heat line Approach to Study Mixed Convection in a Porous Square Cavity with Various Wall Thermal Boundary Conditions*, Int. J. Heat Mass Transfer, Vol. 54, pp. 1706-1727.

Basak, T., Roy, S., and Chamkha, A. J., 2012, *A Peclet Number Based Analysis of Mixed Convection for Lid-Driven Porous Square Cavity with Various Heating of Bottom Wall*, Inter. Commun. Heat and Mass Transfer, Vol. 39, pp. 657-664.

Basak, T., Roy, S., Singh, S. K., and Pop, I., 2010, *Analysis of Mixed Convection in a Lid-Driven Porous Square Cavity with Linearly Heated Side Wall(s)*, Int. J. Heat Mass Transfer, Vol. 53, pp. 1819-1840.

Barna, S. F., Bhuiyan, A. A., Banna, M. H., and Sadrul Islam, A. K. M., 2008, *Effect of Inlet to Cavity Width Ratio on Mixed Convection in a Microstructure Filled Vented Cavity*, Proc. of the 4th BSME-ASME Int. Conf. on Thermal Engineering, Dhaka, Bangladesh, pp. 48-55.

Baytas, A. C., 2000, *Entropy Generation for Natural Convection in an Inclined Porous Cavity*, Int. J. Heat Mass Transfer, Vol. 43, pp. 2089–2099.

Chai, Z., Guo, Z., and Shi, B., 2007, *Lattice Boltzmann Simulation of Mixed Convection in a Driven Cavity Packed with Porous Medium*, Computational Science – ICCS 2007, Lecture Notes in Computer Science, Vol. 4487, pp. 802-809.

Chung, S., and Vafai, K., 2010, *Vibration Induced Mixed Convection in an Open-Ended Obstructed Cavity*, Int. J. Heat Mass Transfer, Vol. 53, pp. 2703-2714.

Hadley, G. R., 1986, *Thermal Conductivity of Packed Metal Powder*, Inter. J. Heat and Mass Transfer, Vol. 29, No. 6, pp. 909-920.

Kandaswamy, P., Muthtamilselvan, M., and Lee, J., 2008, *Prandtl Number Effects on Mixed Convection in a Lid-Driven Porous Cavity*, J. Porous Media Vol. 11, pp. 791–801.

Khanafer , K. M. and Chamkha , A. J., 1999, *Mixed Convection Flow in a Lid-Driven Enclosure Filled with a Fluid-Saturated Porous Medium*, Inter. J. Heat Mass Transfer, Vol. 42, pp. 2465–2481.

Khanafer, K., and Vafai, K., 2002, *Double-Diffusive Mixed Convection in a Lid-Driven Enclosure Filled with a Fluid-Saturated Porous Medium*, Numer. Heat Transfer, Part A, Vol. 42, pp. 465–486.

Kumar, B. V., and Murthy, S.V.S.S.N.V.G. K., 2010, *Mixed Convection in a Non-Darcian Fluid Saturated Square Porous Enclosure Under Multiple Suction Effect*, Int. J. Heat Mass Transfer, Vol. 53, pp. 5764–5773.

Kumar, D. S., Das, A. K., and Dewan, A., 2009, *Analysis of Non-Darcy Models for Mixed Convection in a Porous Cavity Using a Multigrid Approach*, Numer. Heat Transf. Part A, Vol. 56, pp. 685–708.

Kumari, M. and Nath, G., 2011, *Steady Mixed Convection Flow in a Lid-Driven Square Enclosure Filled with a Non-Darcy Fluid Saturated Porous Medium with Internal Heat Generation*, J. Porous Media, Vol. 14, No. 10, pp. 893 – 905.

Mahmud, S., and Pop, I., 2006, *Mixed Convection in a Square Vented Enclosure Filled with a Porous Medium*, Inter. J. Heat Mass Transfer, Vol. 49, pp. 2190–2206.

Muthtamilselvan, M., 2011, *Forced Convection in a Two-Sided Lid-Driven Cavity Filled with Volumetrically Heat-Generating Porous Medium*, Int. J. Appl. Math. And Mech., Vol. 7, No. 13, pp. 1–16.

Muthtamilselvan, M., Das, M. K., and Kandaswamy, P., 2010, *Convection in a Lid-Driven Heat-Generating Porous Cavity with Alternative Thermal Boundary Conditions*", Transp. Porous Med., Vol. 82, pp. 337–346.

Oztop, H. F., 2006, *Combined Convection Heat Transfer in a Porous Lid-Driven Enclosure Due to Heater with Finite Length*, Int. Community. Heat Mass Transf., Vol. 33**,** pp.772–779.

Oztop, H. F., and Varol, A., 2009, *Combined Convection in Inclined Porous Lid-Driven Enclosures with Sinusoidal Thermal Boundary Condition on One Wall*, Progress in Computational Fluid Dynamics, Vol. 9, No. 2, pp. 127–131.

Oztop, H. F., Varol, Y., Pop, I., and Al-Saleem, K., 2012, *Mixed Convection in Partially Cooled Lid-Driven Cavity with a Non-Darcy Porous Medium*, Progress in Computational Fluid Dynamics, Vol. 12, No. 1, pp. 46–55.

Ramakrishna, D., Basak, T., Roy, S., and Pop, I., 2012, *Numerical Study of Mixed Convection within Porous Square Cavities Using Bejan's Heatlines: Effects of Thermal Aspect Ratio and Thermal Boundary Conditions*", Inter. J. Heat and Mass Transfer, Vol. 55, pp. 5436–5448.

Sivasankaran, S., and Pan, K. L., 2012, *Numerical Simulation on Mixed Convection in a Porous Lid-Driven Cavity with Non-uniform Heating on Both Side Walls*", Numer. Heat Trans. Part A, Vol. 61, pp. 101–121.

Saeid, N. H., and Pop, I., 2004, *Transient Free Convection in a Square Cavity Filled with a Porous Medium*, Int. J. Heat Mass Transfer, Vol. 47, pp. 1917–1924.

Suresh, Ch. S. Y., VamseeKriskna, Y., Sundararajan, T., and Das, S. K., 2005, *Numerical Simulation of Three-Dimensional Natural Convection Inside a Heat Generating Anisotropic Porous Medium*, J. Heat Mass Transfer, Vol. 41, pp. 799–809.

Versteeg H. K., and Malalasekera, W., 2007, *An Introduction to Computational Fluid Dynamics: the Finite Volume Method*, 2nd Edition, Pearson Education Limited Prentice Hall, England.

Vishnuvardhanarao, E., and Das, M. K., 2008, *Laminar Mixed Convection in a Parallel Two-Sided Lid-Driven Differentially Heated Square Cavity Filled with Fluid-Saturated Porous Medium*, Numer. Heat Transf. Part A, Vol. 53, pp. 88–110.

Waheed, M. A., Odewole, G. A., and Alagbe, S. O., 2011, *Mixed Convective Heat Transfer in Rectangular Enclosures Filled with Porous Media*", ARPN J. of Eng. & Applied Sciences, Vol. 6, No. 8, pp. 47–60.

Walker, K. L., and Homsy, G. M., 1978, *Convection in a Porous Cavity*, J. Fluid Mech. Vol. 87, pp. 449–474.

Table 1. Comparison of average Nusselt number with previous workers for $Ra = 100$.

Authors	Nu
Saeid and Pop, 2004	3.002
Baytas, 2000	3.160
Walker and Homsy, 1978	3.097
Present result	3.076

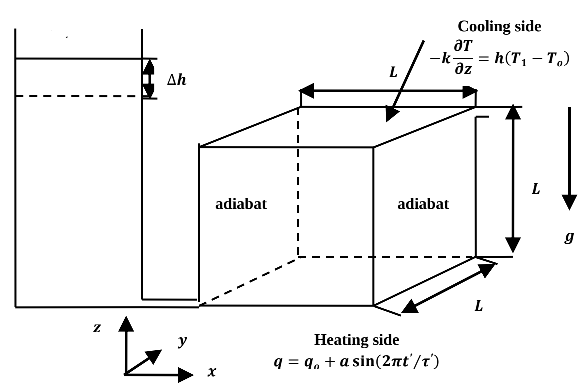

Figure 1. Schematic diagram of the physical problem and coordinates system.

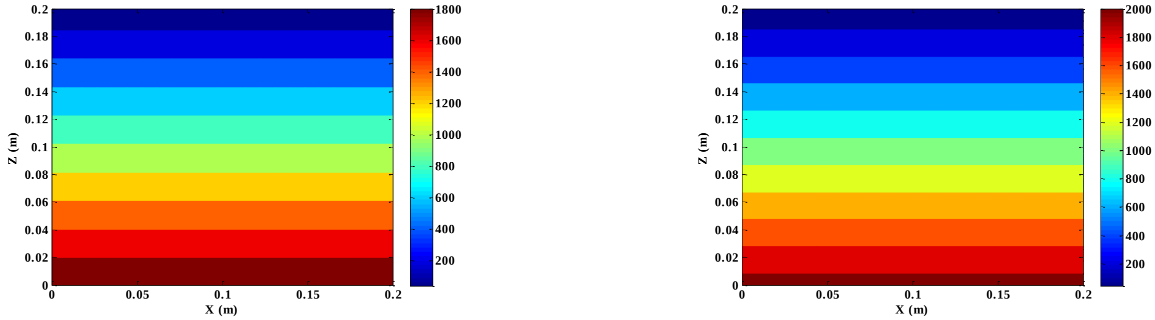

(a) (b)

Figure 2. Pressure field with $a = 750\, W/m^2$ and $\tau = 60s$: (a) $\Delta h = 10mm$, (b) $\Delta h = 20mm$.

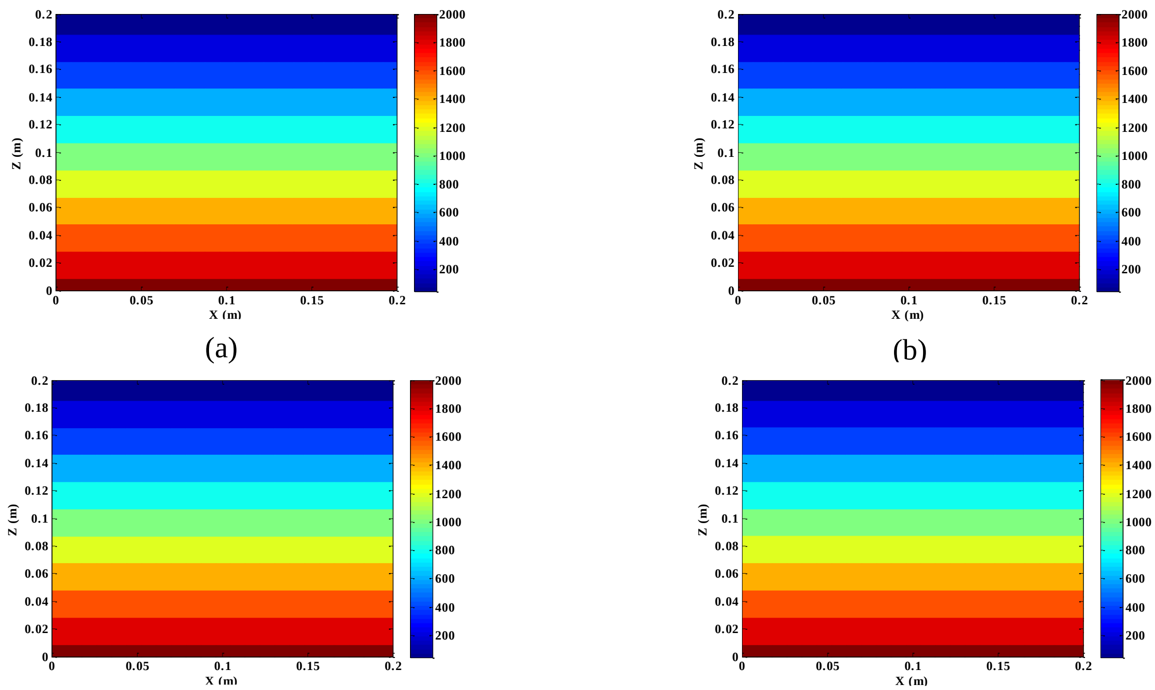

(a) (b) (c) (d)

Figure 3. Pressure contours line for different amplitude values with $\Delta h = 20\ mm$ and $\tau = 30\ s$: (a) $250\ W/m^2$, (b) $375\ W/m^2$, (c) $500\ W/m^2$, (d) $750\ W/m^2$.

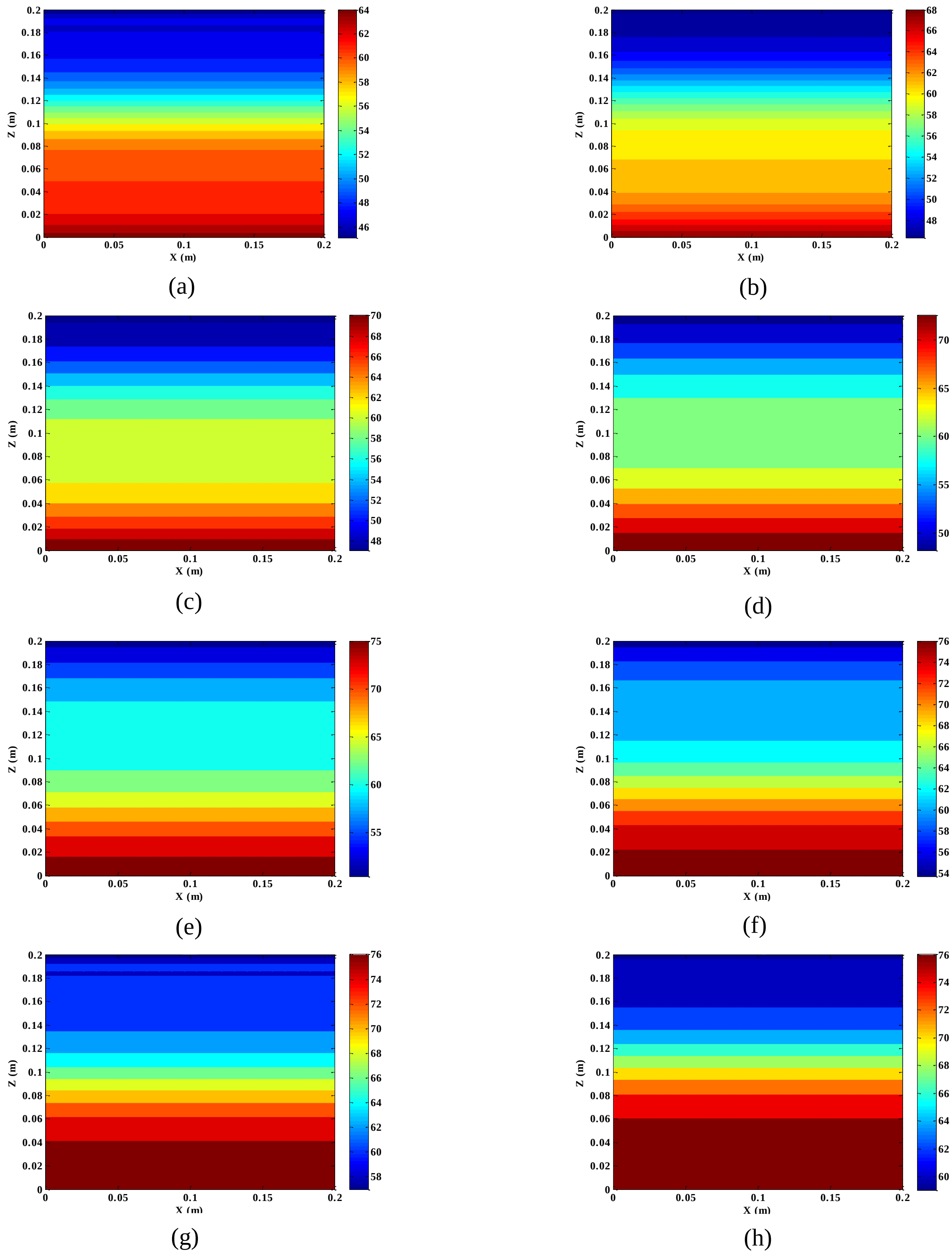

Figure 4. Temperature distribution for different time step when reaching steady state response with $a = 500\ W/m^2$, $\tau = 60s$, and $\Delta h = 10\ mm$: (a) $t = 0.125\ \tau$, (b) $t = 0.25\ \tau$, (c) $t = 0.375\ \tau$ (d) $t = 0.5\ \tau$, (e) $t = 0.625\ \tau$, (f) $t = 0.75\ \tau$, (g) $t = 0.875\ \tau$, (h) $t =\ \tau$.

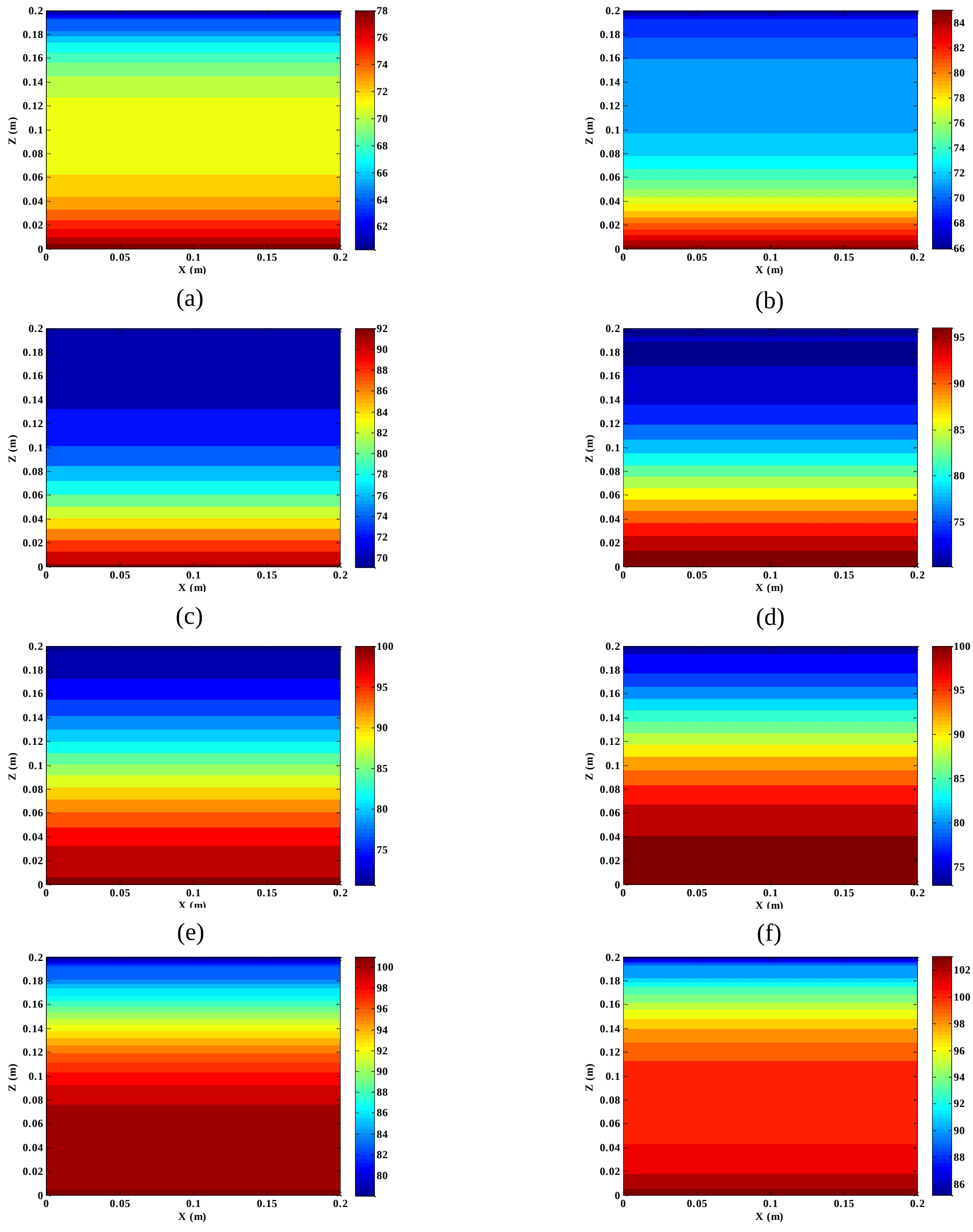

Figure 5. Temperature distribution for different time step when reaching steady state response with $a = 500\ W/m^2$, $\tau = 60s$, and $\Delta h = 20mm$: (a) $t = 0.125\ \tau$, (b) $t = 0.25\ \tau$, (c) $t = 0.375\ \tau$ (d) $t = 0.5\ \tau$, (e) $t = 0.625\ \tau$, (f) $t = 0.75\ \tau$, (g) $t = 0.875\ \tau$, (h) $t = \ \tau$.

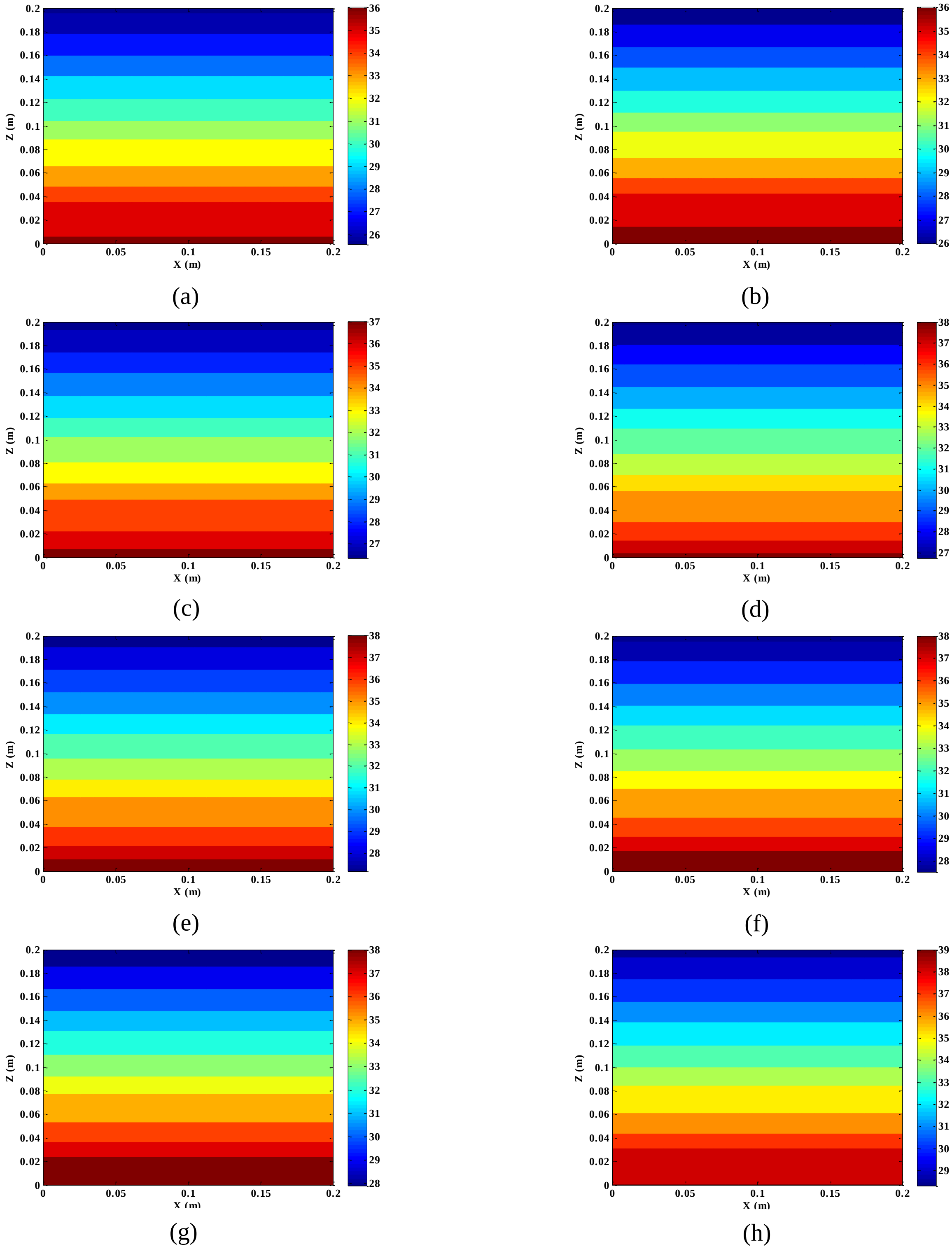

Figure 6. Temperature contours line for different time step when reaching steady state response with $a = 250\ W/m^2$, $\tau = 30s$, and $\Delta h = 10mm$: (a) $t = 0.125\tau$, (b) $t = 0.25\tau$, (c) $t = 0.375\tau$ (d) $t = 0.5\tau$, (e) $t = 0.625\tau$, (f) $t = 0.75\tau$, (g) $t = 0.875\tau$, (h) $t = \tau$.

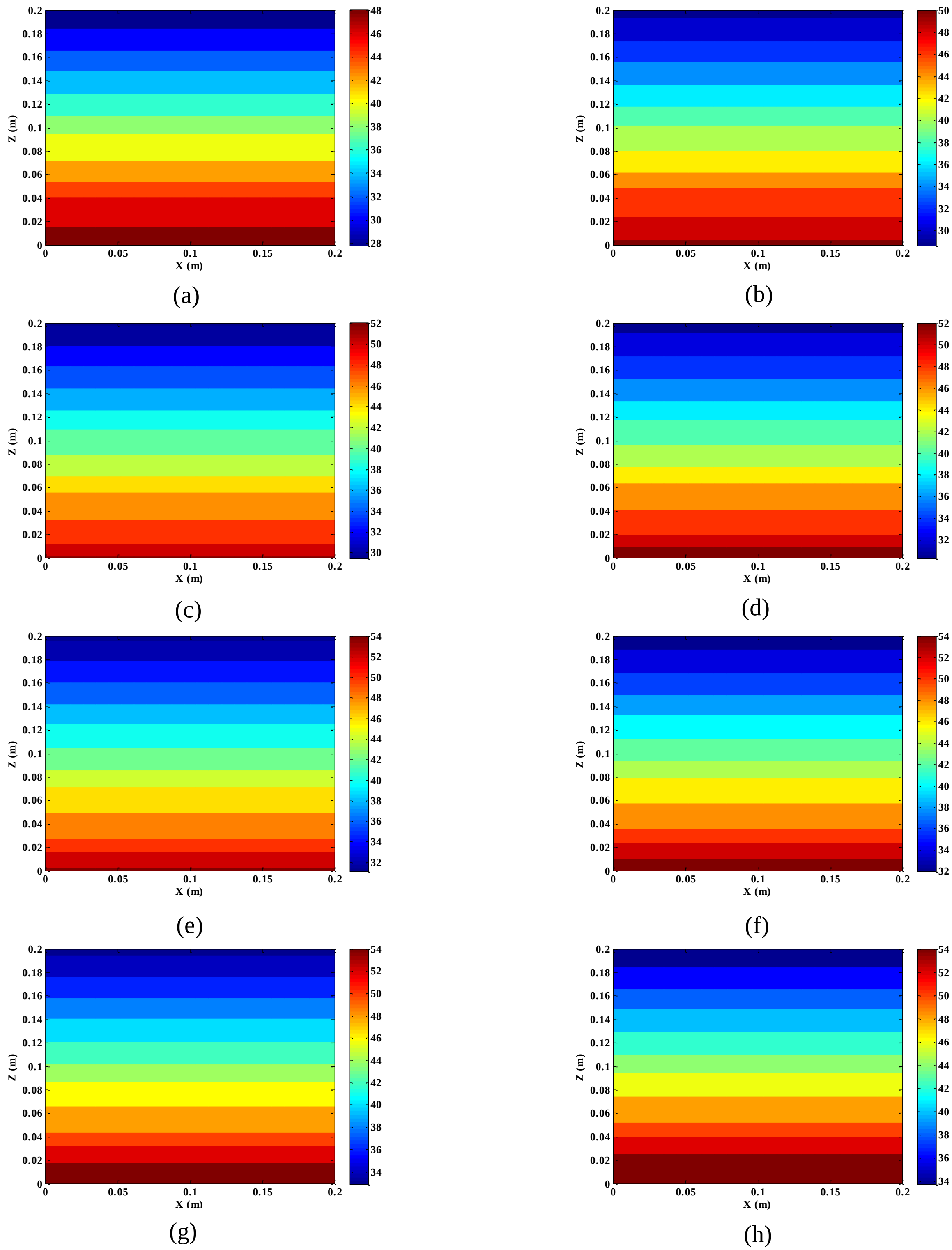

Figure 7. Temperature contours line for different time step when reaching steady state response with $a = 500\ W/m^2$, $\tau = 30s$, and $\Delta h = 10mm$: (a) $t = 0.125\tau$, (b) $t = 0.25\tau$, (c) $t = 0.375\tau$ (d) $t = 0.5\tau$, (e) $t = 0.625\tau$, (f) $t = 0.75\tau$, (g) $t = 0.875\tau$, (h) $t = \tau$.

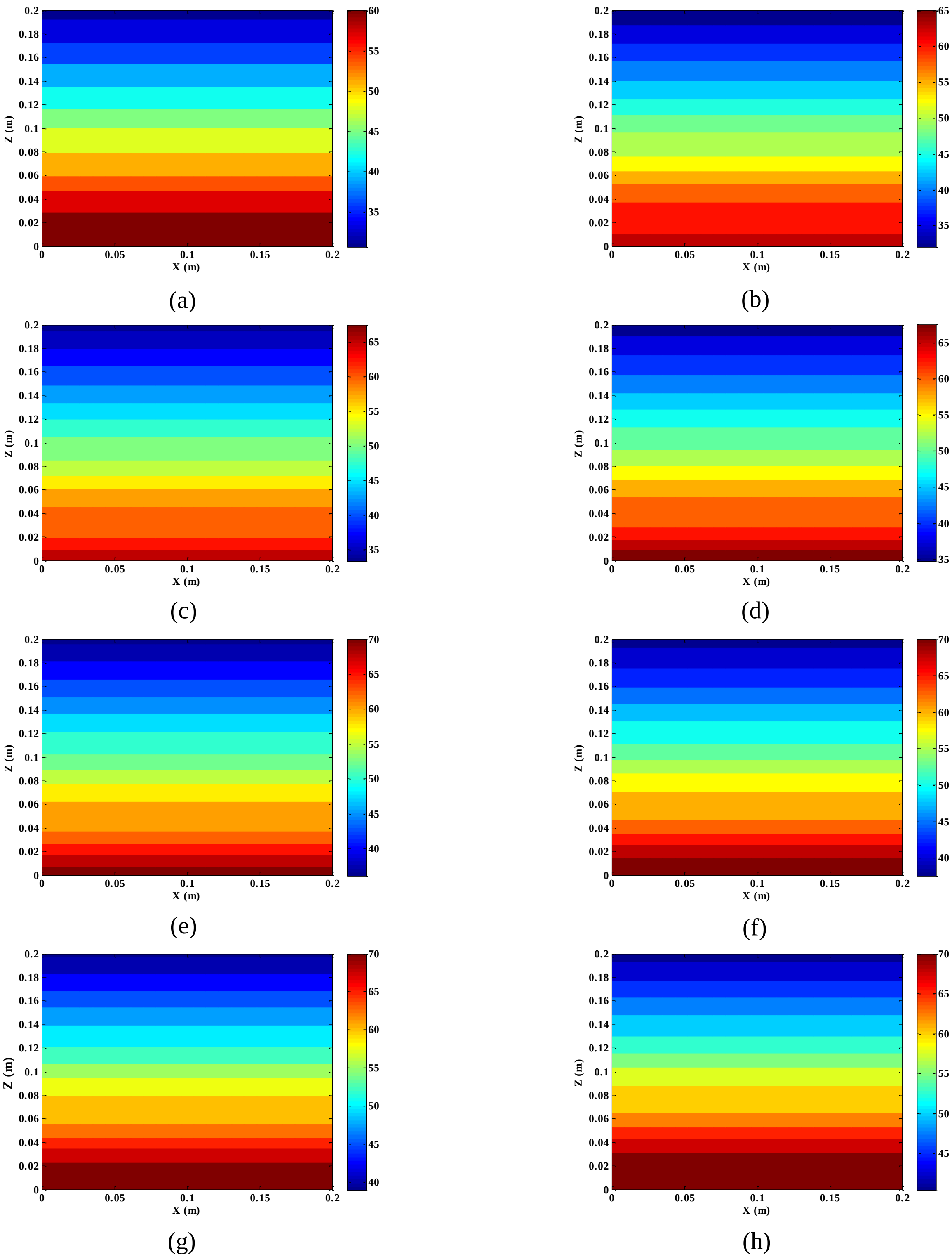

Figure 8. Temperature contours line for different time step when reaching steady state response with $a = 750\ W/m^2$, $\tau = 30s$, and$\Delta h = 10mm$: (a) $t = 0.125\tau$, (b) $t = 0.25\tau$, (c) $t = 0.375\tau$ (d) $t = 0.5\tau$, (e) $t = 0.625\tau$, (f) $t = 0.75\tau$, (g) $t = 0.875\tau$, (h) $t = \tau$.

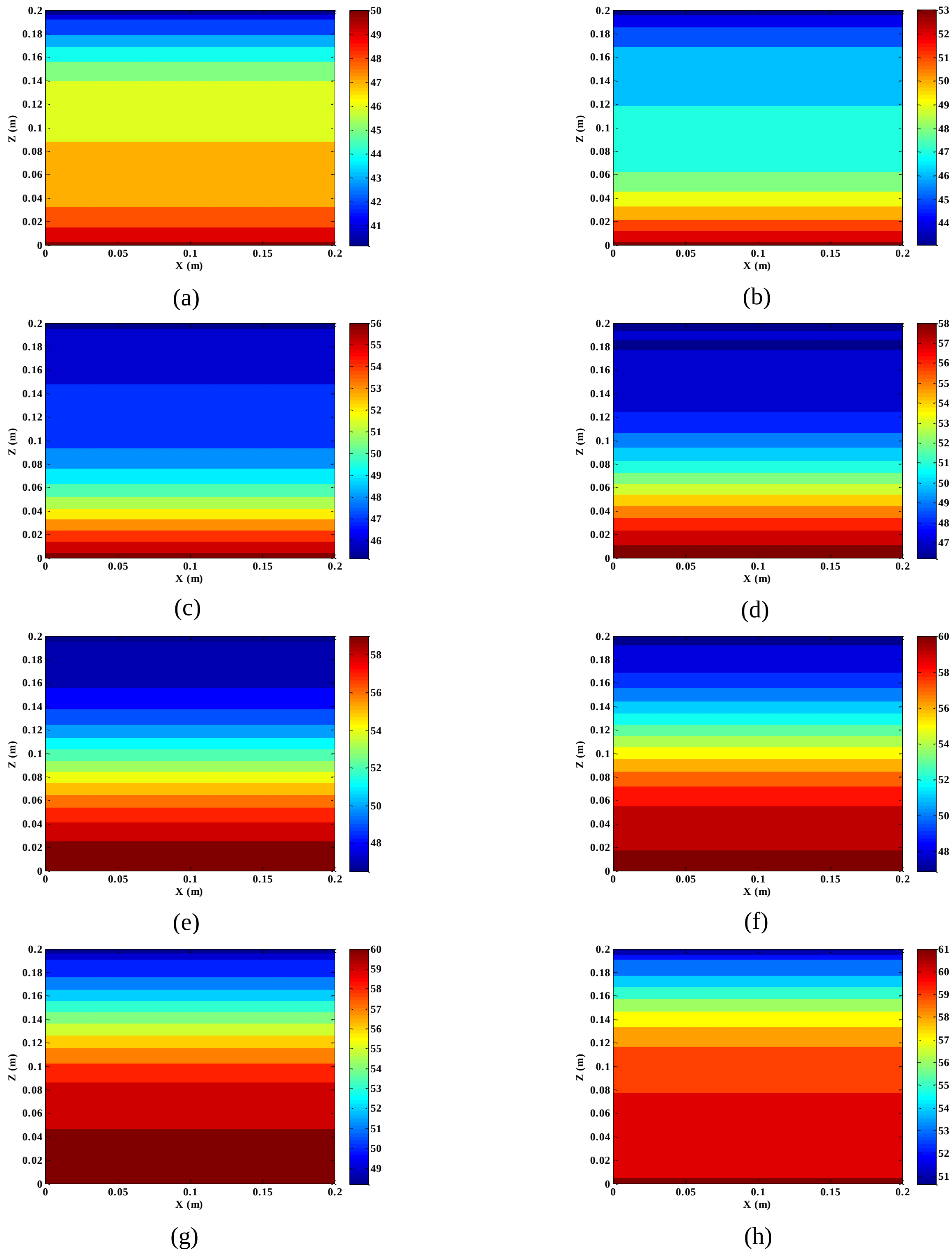

Figure 9. Temperature contours line for different time step when reaching steady state response with $a = 250\ W/m^2$, $\tau = 60s$, and $\Delta h = 20mm$: (a) $t = 0.125\tau$, (b) $t = 0.25\tau$, (c) $t = 0.375\tau$ (d) $t = 0.5\tau$, (e) $t = 0.625\tau$, (f) $t = 0.75\tau$, (g) $t = 0.875\tau$, (h) $t = \tau$.

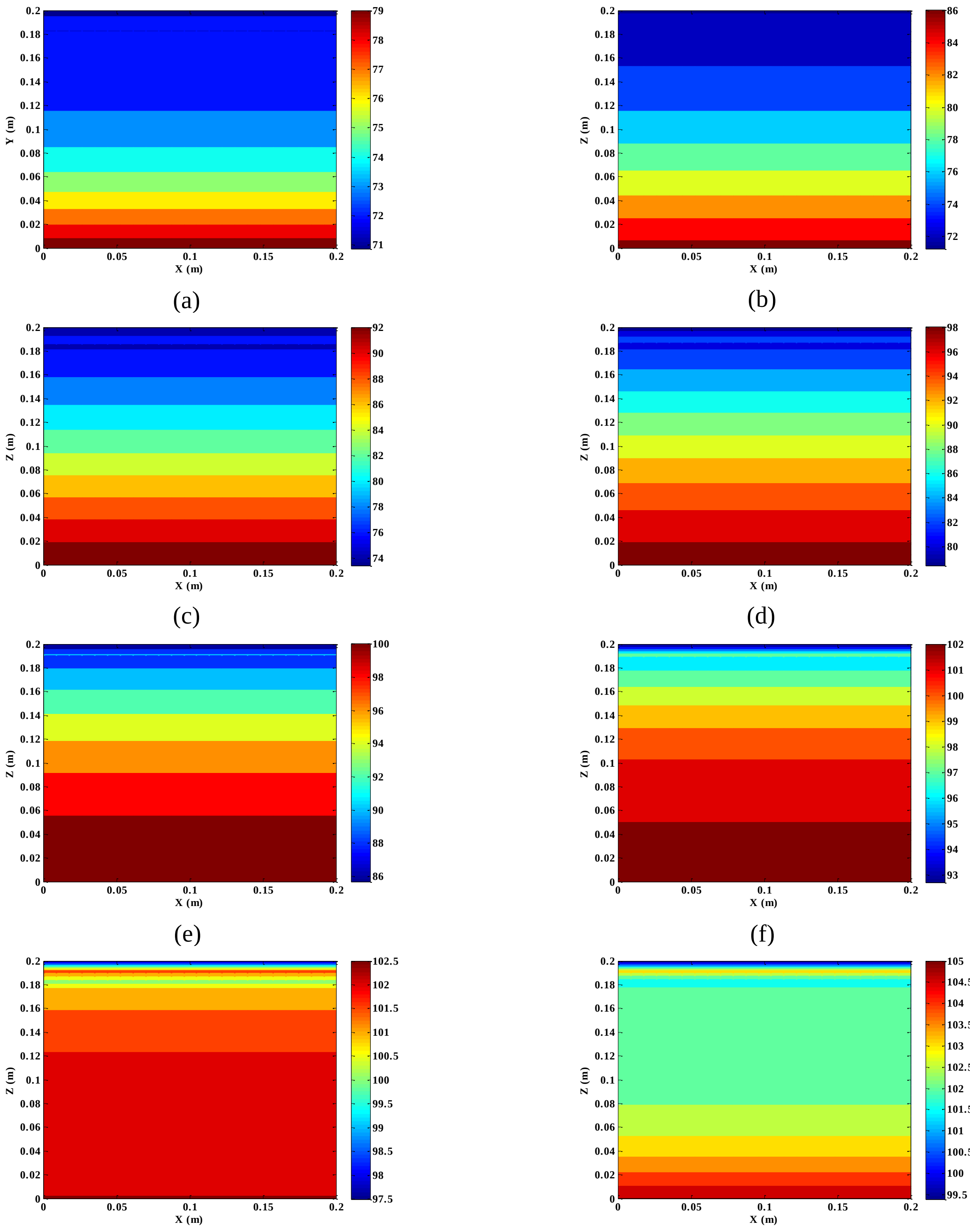

Figure 10. Temperature contours line for different time step when reaching steady state response with $a = 250\,W/m^2$, $\tau = 120s$, and $\Delta h = 20mm$: (a) $t = 0.125\tau$, (b) $t = 0.25\tau$, (c) $t = 0.375\tau$ (d) $t = 0.5\tau$, (e) $t = 0.625\tau$, (f) $t = 0.75\tau$, (g) $t = 0.875\tau$, (h) $t = \tau$.

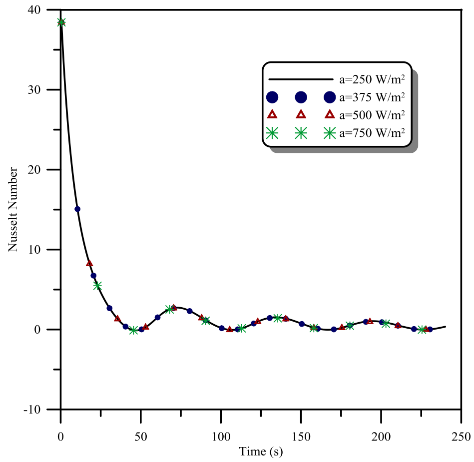

Figure 11. Average Nusselt number versus time for different amplitude, $\Delta h = 10\ mm$ and $\tau = 60\ s$.

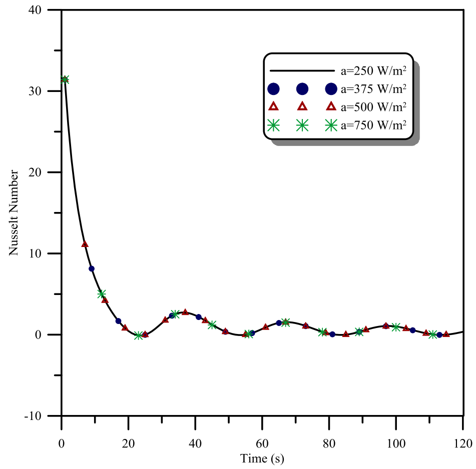

Figure 12. Average Nusselt number versus time for different amplitude, $\Delta h = 20\ mm$ and $\tau = 30\ s$.

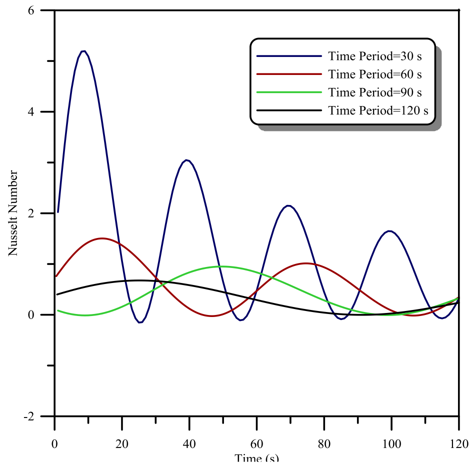

Figure 13. Average Nusselt number versus time at the last $120\ s, \Delta h = 10\ mm$ and $a = 375\ W/m^2$.

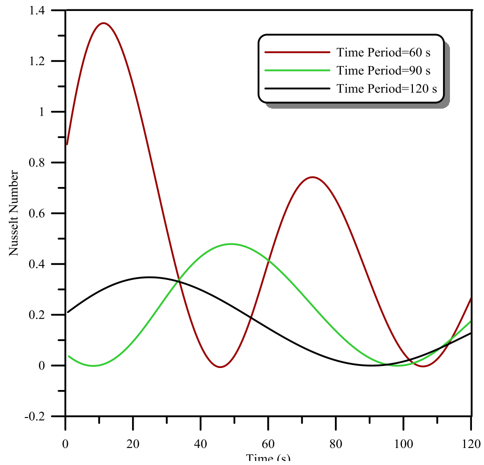

Figure 14. Average Nusselt number versus time at the last $120\ s$ for $\Delta h = 20\ mm$ and $a = 250\ W/m^2$.

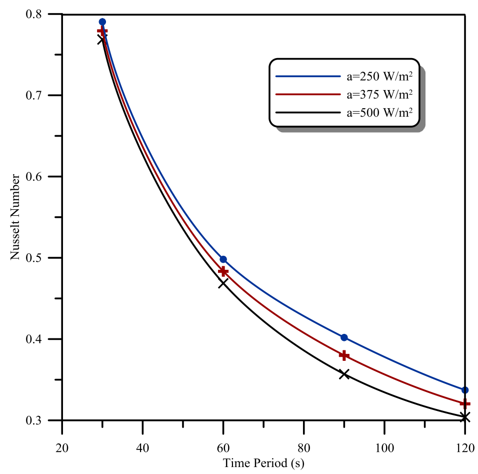

Figure 15. Time averaged Nusselt number variation with time period for different amplitude and $\Delta h = 10\ mm$.

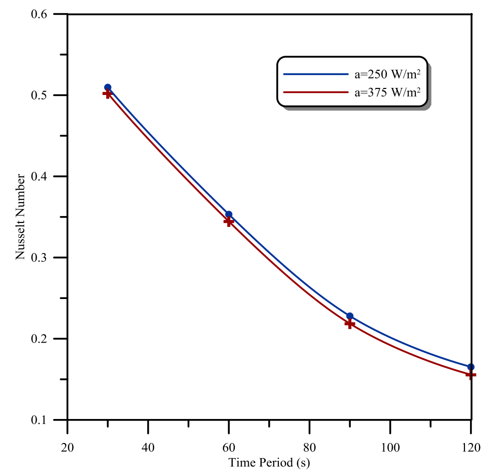

Figure 16. Time averaged Nusselt number variation with time period for different amplitude and $\Delta h = 20\ mm$.

Organic Solid Waste in Vessel Composting System

Dr. Jathwa Abdul Karime Ibrahim
Assistant Professor
Engineering College-Baghdad University
E-mail:jathwa58@yahoo.com

Al Taib Mohammed Abdul Majeed
Instructor
Engineering College-Baghdad University
E-mail : taib.asia@googlemail.com

ABSTRACT

Low-level microbial activity due to the production of organic acids is a recognized problem during the initial phase of food waste composting. Increasing such activity levels by adjusting the pH values during the initial composting phase is the primary objective to be investigated. In this study, sodium acetate (NaoAc) was introduced as an amendment to an in-vessel composting system. NaoAc was added when the pH of the compost mixture reached a low level (pH < 5), the addition increased pH to 5.8. This had a positive effect on the degradation of organic materials i.e. the formation of methane gas compared to the results without NaoAc addition.

The results also proved that anaerobic-aerobic in-vessel composting could reduce the large amounts of wastes by 33% -30%.

However the addition of NaoAc had no significant influence on temperature profile, bulk density, electric conductivity (EC), moisture contents, Nitrogen, phosphorus, potassium (NPK) and heavy metals (Cu, Cd, Ni, Pb) during the composting process, in fact heavy metals and (NPK) were below the maximum permissible levels of the Japanese organic farming and the USDA and US Compost Council standards .

To assess the performance of the composting process, two small-scale digesters were used with fixed temperature. Maximum methane content of 68±1% and 75±1% by volume of the generated biogas was achieved in the run without and with NaoAc respectively.

The germination index was 84.8 % which proved that the stabilized compost obtained in this research is of the “mature" kind and it is satisfactory for agricultural use according to the organic farming recommended by the Japanese Ministry of Agriculture, Forestry and Fisheries, and USDA and US Compost Council standards.

Keywords: compost, sodium acetate, biogas, mature compost, germination test, solid waste management.

تدبيل النفايات الصلبة العضوية باستخدام النظام المغلق

د.جذوة عبد الكريم ابراهيم
أستاذ مساعد
كلية الهندسة –جامعة بغداد

الطيب محمد عبد المجيد
باحث
كلية الهندسة-جامعة بغداد

الخلاصة

ان ظاهرة انخفاض الفعالية الميكروبية بسبب تولد الاحماض العضوية خلال المرحلة الاولية من عملية هضم المواد العضوية في الفضلات الصلبة سواء كانت هوائية اولاهوائية لهي ظاهرة شائعة ومعروفة ولطالما عانت منها التفاعلات اللاهوائية

للمادة العضوية . ولذلك كان الهدف الاساسي لهذا البحث زيادة الفعالية البكتيرية لهضم النفايات العضوية عن طريق ايجاد طريقة لضبط حامضية وسط التفاعل . فتم استعمال خلات الصوديوم كمادة معدلة الى وسط التفاعل، على ان يتم اضافتها بمجرد هبوط الحامضية لما دون 5 ومن ثم دراسة ما لهذه الاضافة من تاثير على الفعالية البكتيرية من خلال انتاج غاز الميثان ونوعية السماد العضوي الناتج . ادت اضافة خلات الصوديوم الى ارتفاع في درجة الحامضية الى 5.8 وقد كانت لهذه الزيادة اثرها الايجابي على تحلل المادة العضوية اي تولد كمية اضافية من غاز الميثان بكمية محسوسة قياسا الى تلك الكمية المنتجة بدون اضافة خلات الصوديوم.

كذلك اثبتت النتائج ان الهضم اللاهوائي –الهوائي في حيز محدود قادر على هضم كميات كبيرة من النفايات مختصرا حجمها الى 30-33% من حجمها الابتدائي. كما أثبتت النتائج ان اضافة خلات الصوديوم لم تكن ذات تاثير ملحوض على شكل مخطط الحرارة (Temperature Profile) ولا على الكثافة الكلية و التوصيلية الكهربائية ومحتوى الرطوبة وتراكيز النتروجين والفسفور والبوتاسيوم (NPK) والعناصر الثقيلة (Cu, Cd, Ni, Pb) اثناء عملية الهضم ، بل ان تراكيز العناصر الثقيلة وال (NPK) بقيت دون المحدادت الامريكية والبريطانية لمواصفات النوعية للسماد العضوي.

كذلك تم اعداد مفاعلات بايولوجية مصغرة وبحجم 1لتر في المختبر وبتثبيت الظروف المناسبة لتسهيل عملية التخمر لانتاج غاز الميثان . بلغت اعلى نسبة حجمية في انتاج غاز الميثان 68±1% و 75±1% للنمط بدون اضافة خلات الصوديوم كبفر وللنمط مع الاضافة على التوالي . واخيرا بلغت النسبة المئوية للانبات 84.8 مشيرة الى ان نوعية السماد العضوي المنتج في هذه الدراسة يمكن ان يصنف تحت الصنف الناضج "Mature" وهو مناسب للانبات والزراعة وحسب توصيات وزارةِ الزراعة والغابات والثروات السمكيةِ اليابانيةِ للزراعة العضوية وكذلك حسب معايير النوعية الأمريكية للسماد العضوي .

الكلمات الرئيسية

سماد عضوي ، خلات الصوديوم ، الغاز العضوي ، سماد عضوي ناضج ، اختبار الاستنبات، ادارة النفايات الصلبة .

1. INTRODUCTION

Food waste is the largest component of municipal waste streams after the recyclables are separated. It is associated with high disposal costs, **McDonnell, 1999**. Composting is a promising alternative treatment method for food waste that enables the valuable organic contents of food waste to be reused, **Kim et al., 2008**.

In recent years, composting has been presented as an environmental friendly and sustainable alternative to manage and recycle organic solid wastes, with the aim of obtaining a quality organic product, known as compost, to be used as organic amendment in agriculture. When mixed with soil, compost increases the organic matter content, improves the physical properties of the soil, and supplies essential nutrients, enhancing the soil's ability to support plant growth, **Iyengar, 2006.**

Compost can also be applied to the soil surface to conserve moisture, control weeds, reduce erosion, improve appearance, and keep the soil from gaining or losing heat too rapidly, **Swan, et al., 2002**.

Composting may be defined as a biological degradation of organic materials under controlled aerobic conditions. The process may be used to stabilize wastewater solids prior to their use as a soil amendment or mulch in landscaping, horticulture, and agriculture, **Lin et al., 2008**. To handle large volumes of municipal waste, the process of decomposition has to be speeded up. The microorganisms in the waste are given an environment, which allows them to grow rapidly and work at peak efficiency in breaking down the waste.

To do this, the microorganisms need air, water and nutrients, **Iyengar, 2006**.

When biodegradable organic solid waste is subjected to anaerobic decomposition, a gaseous mixture of Methane (CH_4) and Carbon dioxide (CO_2) known as biogas could be produced under favorable conditions. The decomposition of the waste materials is mainly done by the fermentation process, which is carried out by different group of microorganisms like bacteria, fungus, actinomycetes etc. **Swan, et al., 2002**.

Due to the presence of short-chain organic acids that are not only produced from raw materials, but also generated during the initial phase of batch composting pH will be lowered, inhibiting microbiological activity, **Nakasaki et al., 1993, Beck-Friis, et al., 2001, Reinhardt, 2002; Beck-Friis et al., 2003** and **Lin. et al., 2008**. Therefore, inhibiting the adverse effect of organic acids, i.e., controlling pH during the initial composting phase, is the primary issue to be resolved.

Anaerobic composting, while accepted elsewhere, has failed in our country due primarily to the odor nuisance, the time involved in producing a stable product and space requirements. While the aerobic process is characterized by a minimum odor nuisance and rapid decomposition when compared to the older anaerobic process. Still aerobic process has not yet been proven satisfactory and as of this date, there are no installations using this process, in operation in this country, except on an experimental or pilot plant basis.

In this research, an amendment material, sodium acetate (NaoAc), is introduced to the food waste composting process in order to resolve the difficulties noted above. NaoAc as a buffer salt combined with the acetic acids produced in the initial composting process can form NaoAc/HoAc a buffer solution in the composting reactor. Buffer solutions are potentially pH control amendments because of their capability to resist change in ambient pH and maintain it at a desired level, **Liang et al., 2006**.

However, few studies have examined the use of buffer salts for regulating the pH of the composting process. In addition, the effect of pH control amendments on the production of biogas has also been investigated. Therefore, the objective of this research is to examine the effect of NaoAc on the food waste composting process under controlled experimental conditions, quality of the final compost, as well as estimating the percentage of biogas generated due to organic solid waste degradation.

1.1 Compost Phases

The process starts with the oxidation of easily degradable organic matter; this first phase is called decomposition. The second phase, stabilization, includes not only the mineralization of slowly degradable molecules, but also includes more complex processes such as the humification of ligno-cellulosic compounds. From a technical point of view, the composting process is stopped at a phase in which the remaining organic matter present is relatively in large quantities (more than 50% of the starting amount); otherwise the process would continue, until all of the organic components are completely mineralized. The main product is called compost, which may be defined as the stabilized and sanitized product of composting, compatible, and beneficial to plant growth **Diaz et al., 2007.**

2. MATERIALS AND METHODS

2.1 Raw Sample

The Food Waste (FW) was collected from daily normal kitchen waste. FW was mainly food remaining in plates after lunch consisted of potatoes, carrots, beef, steamed rice, cooked soybean. Leaves were added as a bulking agent and as a source of nitrogen, while garden soil was added to provide more desired microorganisms, **Lin et al., 2008**.

2.2 In-vessel Composting Reactor

The composting system consisted of a cylindrical vessel metal tank (200 L) with an easy mechanism for turning the compost, as shown in **Fig.1**. A perforated steel screen was installed 10 cm above the reactor bottom, to recover leachate formed in the bottom section and through an opening valve.

A pressure gage was installed in the top of the reactor to measure the pressure of the gases produced while, temperature and humidity sensors with platinum probe were installed in the center inside the reactor. All the raw materials were minced into pieces of <5 mm in diameter using a food processor (Brown, China), and mixed well before the reaction began. To compare and analyze the effects of NaoAc on the composting processes, two experimental treatments were carried out in sequence. In Run B, NaoAc salt was added to the compost mixture; Run A was conducted as a control treatment without NaoAc addition. The detailed composition of raw materials for the compositing processes is summarized in Table 1.

The digesting process started in April until June; 2012. Day 1 is defined as April 22/ 2012. The digester cell was filled with 66.67 kg of different simulated food waste and 0.6 kg of sodium acetate as a buffer. The digester cell was operated anaerobically from day 1 to 5, and then air was introduced through day 6 to start the aerobic process.

For Run B, 600 g of NaoAc, was added to the compost mixture on day 4 immediately after sampling, when the pH had decreased to a relatively low level (pH < 5), **Giannis, et al., 2012**.

Temperature, pH, and moisture content were taken at regular intervals throughout the composting period. In addition, germination tests, NPK, and heavy metal analyses were carried out for examining the quality of the composted product for each run. Two replicates were conducted for each analysis.

Mixing was achieved by turning the arm of the screw by hand to ensure sufficient contact between bio-waste and the bacteria inside the digester, **Donovan et al., 2012**. Composting is essentially completed when mixing no longer produces heat in the pile, **Giannis, et al., 2012**.

At the end of each composting trial of 20-25 days, the formed product was collected from the bottom layer of the bioreactor and spread outside to form a pile. Six representative samples were collected from different points within the pile. The final sample was formed after mixing the six samples together to form a homogeneous material. From the homogeneous material two samples were selected from which a series of parameters were evaluated, **TMECC, 2002**.

2.3 Analytical Procedure

The standard methods followed for testing and evaluating compost and composting feedstock material were determined according to Test Methods for the Examination of Composting and Compost, **TMECC, 2002**.

Laboratory analyses included measurements of moisture content, pH, volatile solids, water soluble total Kjeldahl nitrogen (TKNW), NH_4^+, NH_3, phosphorous as P_2O_5 and PO_4^{-3}, potassium, electrical conductivity, heavy metals, and germination test.

Samples from the compost of about 50 g were collected and dried in an oven at 105 ^oC for 24 h; the loss of weight was taken as the moisture content. The oven-dried sample was further heated at 550 ^oC for 2h for the determination of volatile solids. pH of the clear supernatant was measured for the top clear liquid of the sample with a pH meter.

The water-soluble extract was prepared by mixing 10 g of sample with 100 ml of deionized water, then shaken for 2 h, and centrifuged at 3000 rpm. The supernatant was then filtered through a filter paper Whatman No. 1, **TMECC, 2002**. Nitrogen as total N, NH_3 NH_4^+, potassium and phosphorus as P_2O_5 and PO_4^{-3} were analyzed using Multi Direct Photometer for multi-parameter analyses. The electrical conductivity of the compost was analyzed once daily using EC meter.

Heavy metals of water-soluble extract samples were analyzed by Atomic Absorption Flame Emission Spectrophotometer (GBC scientific equipment Sens AA).

Germination test was performed for 48 h at 25^{o}C in the dark with 20 radish seeds placed on a 9 cm filter paper What man No. 1 soaked with 4 mL of compost extract and placed in a Petri dish, **Bertran et al., 2004**. Moreover, the germination test was repeated with deionized water as a control, and extract of commercial compost. The following equations were used to calculate the relative seed germination, relative root growth, and germination index (GI), **Zucconi et al., 1981** and **Tiquia et al., 1996.**

$$\textit{Relative Seed Germintation } \% = \frac{No.of\ seeds\ germinated\ in\ compost\ extract}{No.of\ seeds\ germinated\ in\ control\ extract}\ x100 \qquad (1)$$

$$\textit{Relative Root Growth } \% = \frac{Mean\ root\ length\ in\ compost\ extract}{\sqrt{Mean\ root\ length\ in\ control}}\ x\ 100 \qquad (2)$$

$$\textit{Germintation Index (GI)}\% = \frac{Relative\ Seed\ Germintation\ x\ Relative\ Root\ Growth}{100}\ x\ 100 \qquad (3)$$

Two plastic bottles one liter each were modified and used as digesters. The mouth of each was supplied with an airtight rubber stopper and an outlet to permit gas collection in a suitable glass bottle filled with 0.1 M of NaOH. Each digester was set up at several combinations of environmental conditions that play the main role in the efficiency of the anaerobic digestion process and biogas production. These conditions were temperature, starting pH and moisture content.

The temperature of the biodigesters was maintained at a constant value in a water bath (50^{o}C), thermostatically controlled as shown in **Fig. 2**.

Biogas formed was measured by "liquid displacement method". The schematic diagram of the experimental laboratory set up is shown in **Fig.3.**

Sampling proceeded until composting temperature was almost near ambient temperature and stand still **Gumaa, 2009**. Laboratory analyses included measurements of moisture content and temperature of the composted materials, which were recorded daily during the composting period. Composition of food samples used in the study is presented in **Table 2.**

The biogas is a mixture of carbon dioxide, methane, hydrogen sulphide and nitrogen, **Liang, et al, 2006**. The amount of hydrogen sulphide is less than 1%, **Kaparaju et al., 2008**. The amount of nitrogen is difficult to estimate although it can be measured with gas chromatography, (GC) **Juanga et al., 2005** and **Bonn, 2008**.

2.4 Laboratory Simulation

In order to study the influence of NaoAc addition on biogas production, two laboratory biodigesters in series was investigated spontaneously. In digester b, NaoAc salt was added to the mixture; digester a was conducted as a control treatment without NaoAc addition. The procedures held were as followed: the raw material mixture;

Composition of biogas was measured by taking a 50 ml of biogas sample in a large syringe and pushing the biogas slowly (over 10 minutes) through a 0.5L glass bottle liquid displacement system containing a strong solution of NaOH (4 g/l). As the biogas passes through this high pH solution, the CO_2 of the biogas is converted to carbonate and absorbed into the liquid, only the methane passes through the solution and an equivalent volume of alkaline solution is pushed out of the glass bottle as shown in **Fig. 3**.

The volume of alkaline solution that pours out of the bottle divided by the volume of biogas injected is equal to the fraction of methane in the biogas, **Juanga et al., 2005; Bonn, 2008** and **Gumaa, 2009.**

3. RESULT AND DISSCUSSION

Results are based on parameters used to assess the anaerobic-aerobic mixed solid waste conversion, NaoAc addition, and methane gas production.

3.1 Temperature Profiles

The temperature of the composting mixture in both runs rose soon after beginning the experiment and reached $63 \pm 2^{o}C$ within 20 to 25 days, corresponding to an average increase rate of 2°C/ day as shown in **Fig. 4.**

The temperature increased to the thermophylic level (above 50 °C) within 13, 7 days in Run A, Run B respectively, indicating that the indigenous microorganisms could easily utilize the organic materials in the amended food waste.

The thermophylic phase lasted more than 15days in Run A and 20 days in Run B, and then the temperature slowly dropped to a normal level. The duration of the thermophylic phase in Run B was relatively longer than that in Run A. The increase in temperature with time is consistent with previous reports of, **Benson et al., 2007**.

The overall average ambient temperature during this research was $40\pm3^{o}C$, indicating that exothermic reactions in the digester contributed considerable beneficial heating. For the batch digester the system was located in a water bath adjusted at 50 ^{o}C. This relatively high temperature would be expected to facilitate digestion. It also shows that the cell is capable of retaining heat that is generated during decomposition to withstand sudden electric cutoff.

It is clearly shown that composting proceeded more rapidly in the laboratory plastic biodigesters than in the large tank in both runs a and b due to the relatively optimal conditions i.e., under control and suitable surrounding environment. Temperature profiles for run a and run b are shown in **Fig. 5.**

3.2 The Changes of pH

The changes of pH are shown in **Fig. 6.** The pH had its lowest value at day 4 in all runs. The addition of NaoAc raised the pH value in Run A because NaoAc is an alkaline salt that forms a buffer solution through combining with acetic acids present in the composting material. This partially neutralized the acids and tended to maintain a relatively stable pH (5-5.8) level. However, maximum pH levels in the reactor with the addition of NaoAc were around 9.1, while in the control reactor was about 7.0.

3.3 Moisture Content

The moisture content tended to decrease due to the combination of high temperature levels and aeration during the thermophylic phase and was controlled by applying water (humidifying) the compost mass. The initial moisture content 63.5 % of the wet weight was reduced in all experiments to reach an average moisture content of 40±5% of the wet weight, remaining above the minimum moisture content of 40% suggested by **Liang et al., 2003** and Petric **Petric et al., 2009** for optimal composting conditions. After that, no significant changes in parameters have been observed.

3.4 Electric Conductivity

Fig. 7 shows the variation of electrical conductivity with time. The electrical conductivity slightly increased on day 1. Since decomposable compounds were easily released in the solution, the soluble ions in the water extract may increase slightly at the beginning of the composting process. The electrical conductivity was in the range of 2 to 3 dS/m during composting.

The initial EC increase could be caused by the release of mineral salts such as phosphates and ammonium ions through the decomposition of organic substances, **Fang and Wong, 2000**. As the composting process progressed, the volatilization of ammonia and the precipitation of mineral salts could be the possible reasons for the decrease of EC at the later phase of composting, **Beck et al., 2003.**

4. EVOLUTION OF COMPOST CHARACTERISTICS

4.1 Organic Matter Loss

Dry matter losses mainly occurred during the first 13 days **TMECC, 2002** but varied among composting runs, with a mean loss of dry matter of 32 ± 9% and a coefficient of variation of 15.6 %.

4.2 Compost Quality

The concentration of nitrogen was very low in the final compost suggesting that nitrogen was lost during composting upon opening the digesters. Losses of nitrogen in this composting process were governed mainly by volatilization of ammonia due to high pH (that is because of the addition of NaoAc) and high temperatures values of the substrate. Agitation and aeration rate may have also affected the rate of ammonia volatilization, **Beck et al., 2003**. However, as composting was developing nitrates concentration presented a significant increase which can be explained by the activity of autotrophic nitrobacteria which oxidize ammonium compounds into nitrates in the presence of oxygen-rich environment, **Benson, et al., 2007** and **Chroni et al., 2009**.

Nitrates reached 0.6 mg/l and 2.84 mg/l on the 40th day of the process, for Run A and B respectively, which can be considered as an indicator of a high degree of compost stabilization. Phosphorous as P_2O_5 reached 3.1 and 4.5 mg/kg on the 40th day of the process, for Run A and B respectively, which are higher than the recommended levels, while potassium as K_2O reached 3.12± 0.03 mg/kg for both runs. Results of Run A were expressed in **Table 3**.

4.3 Heavy Metals

Metal concentrations were below the maximum permissible levels of organic farming recommended by the Japanese Ministry of Agriculture. The maximum permissible levels for organic farming in Japan are 2 mg/kg mercury, 5 mg/kg cadmium, 50 mg/kg arsenic, 600 mg/kg copper, and 1800 mg/kg zinc, **Japanese Ministry of Environment, 2005**. As may be concluded, the quality of the current compost meets the requirements of USDA and US. Composting Council, **TMECC, 2002** as shown in **Table 3**.

4.4 Germination Test

Maturity of compost may be evaluated with the use of the cress seed germination bioassay, which is sensitive to excessive salinity or the presence of phytotoxic simple organic acids or phenol compounds, **Chroni, et al. 2009** and **Donovan, 2012**. One of the most significant germination tests is that reported by **Zucconi et al., 1981** and **Zucconi et al.1985**, and many later tests were developed from this.

The results of germination shows 86.5% relative seed germination and 98% root growth; the calculated value of germination index (GI) is 84.8% which is better than the suggested value of 60% for cress reported by Diaz **Diaz et al., 2007**. On the other hand, poor relative seed germination of 50.9%, root growth 16.4%, and GI 8.3% values were observed upon analyzing a commercial compost extract.

Table 5 gives values for very mature, mature and immature composts **TMECC, 2002**, which shows that the obtained compost can be classified as mature compost.

5. GAS PRODUCTION AND COMPOSITION

It was impossible to assess the impact of NaoAc addition on methane production in both runs A and B in the large tank; therefore, two-laboratory biodigesters of two liters each were used spontaneously as biodigesters (a and b). In digester b, NaoAc salt was added to the raw material mixture; digester a was conducted as a control treatment without NaoAc addition. Experiments were held in the Environmental Engineering Department laboratory in Baghdad University.

The largest fraction of gas probably had been lost from the compost by volatilization. The total volume of methane produced was 68±1% of the total gas produced with the absence of NaoAc, where the production reached 75±1%for the NaoAc-amended compost, indicating that the addition of NaoAc had effectively increased the extent of methane gas production due to effective material degradation.

Biogas production is very slow at both, the beginning and at the end period of observation. This is predicted due to the biogas production rate in the digester is directly corresponded to the specific growth rate of methanogenic bacteria in the biodigester, **Nopharatana et al., 2007**. After 27 days observation, biogas production tends to decrease due to the stationary phase of microbial growth.

The rate of methane gas produced agreed with other results of researchers, **Lo et al., 1984**, **Nopharatana et al., 2007** and **Kaparaju et al., 2008.**

6. CONCLUSIONS

The characteristics of the wastes composted and the temperature profiles obtained indicate that composting is a suitable technology to treat food wastes and to recycle them into stabilized and sanitized soil amendment. The final compost produced in this study was satisfactory for its agricultural application in terms of pH, electrical conductivity as a salt content index, germination test and heavy metal contents.

The main findings were:

1. In-vessel composting can process large amounts of waste without taking much space or cost as other solid waste management methods. In addition, it can accommodate virtually any type of

organic waste (e.g., meat, animal manure, bio solids, food scraps). The length of the composting process was 35 days in the vessel and two weeks of curing out of the vessel. The residuals after composting were about 33% of the original weight for run A and slightly less for run B 30%, i.e. the 66.6 kg turned to be 20.7 kg in the vessel B, indicating successful reduction. The bulk density of the composting materials was 750 kg/m^3 at day 1, and kept on decreasing after each mixing trial to reach 390 kg/m^3 of day 12. Almost equal for both runs.

2. The temperature of the composting mixture in both runs rose soon after beginning the experiment and reached 63 ± 2^{o}C within 20 to 25 days, corresponding to an average increase rate of 2 °C/ day. The duration of the thermophylic phase in Run B of 20 days was slightly longer than that in Run A of 15 days.
3. It was clearly shown that composting proceeded more rapidly in the laboratory plastic biodigesters than in the large vessel due to the relatively optimal conditions i.e., under control and suitable surrounding environment.
4. Final pH levels in reactors B was around 9.1, while the control reactor was about7.
5. Electrical conductivity slightly increased on day 1, as the composting process progressed, the volatilization of ammonia and the precipitation of mineral salts caused EC reduction at the later phase of composting. Overall, electrical conductivity was in the range of 2 to 3 dS/m for both runs.
6. The initial moisture content (63.5 % of wet weight) was reduced in all experiments to reach an average moisture content of 40±5 % of the wet weight.

6.1 Compost Maturity

Compost maturity was evaluated using certain indices; the levels of indices were relatively stable in the latter part of the composting period, and they remained constant.

1. Nitrates as ammonia reached 0.6 mg/l and 2.84 mg/l on the 40th day of the process, for Run A and B respectively, which can be considered as an indicator of a high degree of compost stabilization.

2. Phosphorous as P_2O_5 was 3.1 and 4.5 mg/l on the 40th day of the process, for Run A and B respectively, which are higher than the recommended levels. Potassium as K_2O reached 3.12 ± 0.03 mg/kg for both runs that is within the recommended level of the USA compost quality standard, **TMECC, 2002**.

3. The metal concentrations in this study were below the maximum permissible levels for organic farming recommended by the Japanese Ministry of Agriculture, **Japanese Ministry of Environment, 2005** and the recommended levels of the USDA and US Composting Council standards, **TMECC, 2002**.

6.2 Gas Production and Composition

In all cases, a peak in gas emissions was observed in coincidence with the thermophylic stage. In fact, gas emissions may be proposed as an indicator of the biological activity of composting materials, **Liang, et al., 2006**. Results showed:

1. Biogas production is very slow at the beginning and at the end period of observation.

2. The total volume of methane produced was 75±1% of the total gas produced in run a and 68±1% of the total gas produced in run b, indicating that the addition of NaoAc had effectively increased the extent of methane gas production due to effective material degradation.

6.3 Germination Test

The results showed that relative seed germination = 86.5%, relative root growth =98%, and GI=84.8%. The obtained compost can be classified as mature compost, **TMECC, 2002**. This stabilized compost can be finally considered very satisfactory for agricultural use.

REFERENCES

Beck-Friis, B., Smàrs, S., Jonsson, H., and Kirchmann, H., 2001. *Gaseous Emissions of Carbon Dioxide, Ammonia and Nitrous Oxide From Organic Household waste in a compost reactor under different temperature regimes*. Journal of Agricultural Engineering Research 78 (4), 423–430.

Beck-Friis, B., Smàrs, S., Jonsson, H., Eklind, Y., and Kirchmann, H., 2003. *Composting of Source-Separated Household Organics at Different Oxygen Levels: Gaining an Uderstanding of the Emission Dynamics*. Compost Science and Utilization 11 (1), 41–50.

Benson, C., Barlaz, M., Lane, D., and Rawe, J., 2007. *Practice Review of Five Bioreactor/ Recirculation Landfills*. Waste Management 27 (1), 13–29.

Bertran, E., Sort, X., Soliva, M. and Trillas, I., 2004. *Composting Winery Waste: Sludges and Grape Stalks.* Bioresource Technol. 95, 203–208.

Bonn, Jonas 2008. *Improved Techniques for Sampling and Sample Introduction in Gas Chromatography*," Royal Institute of Technology.

Chroni, C., Kyriacou, A., Manios, T., and Lasaridi, K.-E., 2009. *Investigation of the Microbial Community Structure and Activity as Indicators of Compost Stability and Composting Process Evolution. Process evolution.* Bio Resource Technology 34, 103–110.

Diaz, L.F. M. de Bertoldi, W. Bidlingmaier and E. Stentiford, 2007.*Compost Science and Technology*. Waste Management Series 8, British Library Cataloguing in Publication Data.

Donovan, Sally M. Donovan, Thomas Bateson, Jan R. Gronow and Nikolaos Voulvoulis, 2012. *Characterization of Compost-Like Outputs from Mechanical Biological Treatment of Municipal Solid Waste*. Centre for Environmental Policy, Imperial College London, United Kingdom.

Fang, M. and Wong, J.W.C., 2000. *Effects of Lime Addition on Sewage Sludge Composting Process.* Water Research 15, 3691–3698.

Giannis, A., Makripodis, G., Simantiraki, F., Somara, M., and Gidarakos, E., 2012. *Monitoring Operational and Leachate Characteristics of an Aerobic Simulated Landfill Bioreactor*. Waste Management 28 (8), 1346–1354.

Gumaa, Nadhem Haydar, 2009. *Effect of Some Factors on Anaerobic Biodegradation of Organic Solid Wastes and Biogas Production.* Proceeding of 3rd Scientific Conference of the College of Science, University of Baghdad 24 to 26 March 2009.

Iyengar, S.R., 2006. In-Vessel Composting of Household Wastes. Waste Management 26, 1070–1080.

Japanese Ministry of the Environment, 2005.Available at http://www.env.go.jp/recycle/waste_tech/ippan/h17/index.html

Juanga, J. P., Kuruparan, P. and Visvanathan, C., 2005, *Optimizing Combined Anaerobic Digestion Process of Organic Fraction of Municipal Solid Waste*. Environmental Engineering and Management, Asian Institute of Technology.

Kaparaju, P., Buendía, I., Ellegaard, L., and Angelidaki, I., 2008. *Effects of Mixing on Methane Production During Thermophilic Anaerobic Digestion of Manure: Labscale and Pilot-Scale Studies*. Bioresour. Technol. 99: 4919–4928.

Kim, J., Park, J., Byung-Hoon In, DaekeunKimd and Wan Namkoong,2008.*Evaluation of Pilot-Scale in-Vessel Composting for Food Wastetreatment*. BioCycle, 30(3):37-39.

Liang, C., Das, K.C., and McClendon, R.W., 2003. *The Influence of Temperature and Moisture Contents Regimes on the Aerobic Microbial Activity of a Biosolids Composting Blend. Bioresource.* Technology 86, 131–137.

Liang, Y., Leonard, J.J., Feddes, J.J.R., and McGill, W.B., 2006. Influence of Carbon and Buffer Amendment on Ammonia Volatilization in Composting. Bioresource Technology 97, 748–761.
Lin, Y.P., Huang, G.H., and Lu, H.W., 2008. *A Simulation-Aided Factorial Analysis Approach for Characterizing Interactive Effects of System Factors on Composting Processes.* Science of the Total Environment 402 (2-3), 268–277.

Lo, K.V., A. J. Whitehead, P. H. Liao, and N. R. Bulley, 1984. *Methane Production from Screened Dairy Manure Using a Fixed-Film Reactor.* Agricultural Wastes, 9(3): 175-188.

McDonnell, E.M., 1999. *Process Characterization, and Stability and Maturity Testing of Forced Air, Static Pile Processed Food Scrap and Wood Chip Compost*. Ph.D. Thesis, Cornell University, United States.
Nakasaki, K., Yaguchi, H., Sasaki, Y., and Kubota, H., 1993. *Effects of pH Control on Composting of Garbage.* Waste Management and Research 11 (2), 117.

Nopharatana, A., P. C. Pullammanappallil, and W. P. Clarke, 2007. *Kinetics and Dynamic Modeling of Batch Anaerobic Digestion of Municipal Solid Waste in a Stirred Reactor*, Waste Management, 27: 595–603

Petric, I., Sestan, A., and Sestan, I., 2009. *Influence of Initial Moisture Content on the Composting of Poultry Manure with Wheat Straw*. Biosystems Engineering 104, 125–134.
Reinhardt, T., 2002. *Organic Acids as a Decisive Limitation to Process Dynamics During Composting of Organic Matter.* Microbiology of Composting, 177–188.

Swan, J.R.M., Crook, B., and Gilbert, E.J., 2002. *Microbial Emissions from Composting Sites*.Issues Sci. Technol. 18, 73–101.

Tiquia, S.M., Tam, N.F.Y., and Hodgkis, I.J., 1996. *Effect of Composting on Phytotoxicity of Spent pig-Manure Sawdust Litter*. Environ. Pollut.93, 249.

TMECC, 2002.*Test Methods for the Examination of Composting and Compost*, USDA and US. Composting Council, Bethesda, MD.

Zucconi, F., Monaco, A., Forte, M., and de Bertoldi, M. 1985. *Phytotoxins During the Stabilization of Organic Matter. In: Composting of Agricultural and Otherwaste*, J.K.R. Gasser, Elsevier Applied Science, London, pp. 73–85.

Zucconi, F., Pera, M.A., Forte, M., and Bertoldi, M de. 1981. *Evaluating Toxicity of Immature Compost.* Biocycle., 22, 27–29.

Figure 1. In-vessel composting reactor.

Figure 2. Laboratory batch digesters of anaerobic digestion to estimate the generated biogas.

Figure3. Gas collection by displacement.

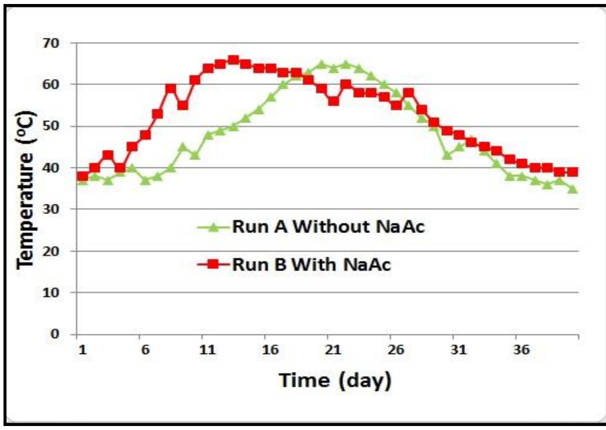

Figure 4. Temperature profiles through composting process.

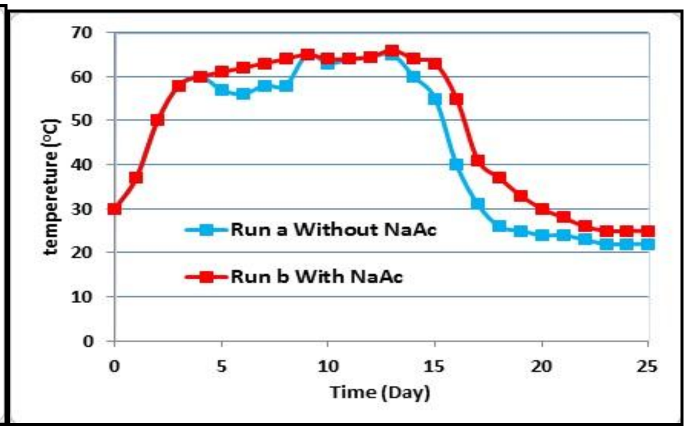

Figure5. Temperature profiles in simulated digester.

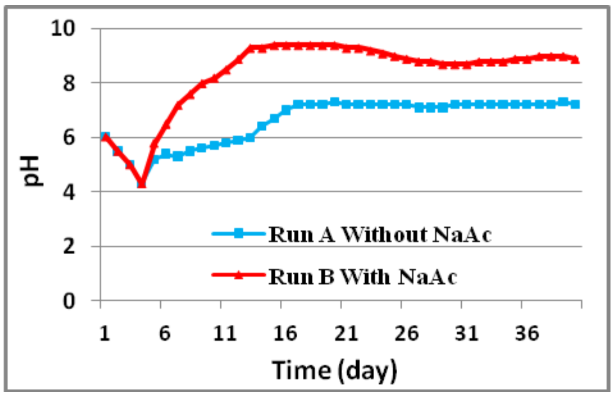

Figure 6. pH profiles of the composting processes.

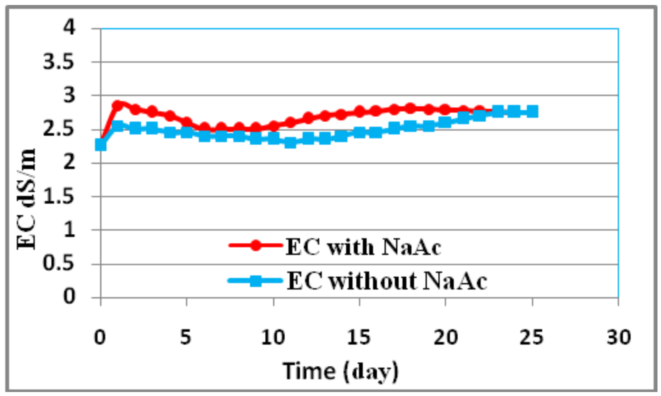

Figure 7. Variation of electrical conductivity during composting.

Table 1. Raw material for the compositing processes in the vessel.

Item (kg)	Run A	Run B
Potato	8.46	8.46
Carrot	13.06	13.06
Meat	2.34	2.34
Soybean	13.06	13.06
Steamed rice	13.34	13.34
Soil	13.34	13.34
Leaves	3.06	3.06
Water	4.66	4.66
NaoAc	0	0.60

Table 2. Raw materials for batch digesters lab-size.

Item (g)	Run a	Run b
Potato	74.1	74.1
Carrot	114.3	114.3
Beef	20.4	20.4
Soybean	114.3	114.3
Steamed rice	116.7	116.7
Soil	116.7	116.7
Leaves	26.8	26.8
Water	41	41
NaoAc	0	5.83

Table 3 Characteristics of run A compost and compost quality.

Heavy metal (mg/kg, dry weight)	**Run A compost**	**TMECC 2002 Max.**
Pb	110	150
Zn	--------	1400
Cu	28	750
Ni	35	210
Cd	0.54	2
Moisture content	40.2 %	30-60 %
Electrical conductivity (EC) dS/m	2.75	4.7
Available nutrients (NPK)mg/kg	1.1 N 3.1 P_2O_5 3.12 K_2O	1.6 N 2.57 P_2O_5 8 K_2O
C/N	20/ 25	20/30

Table 4. Outcomes of germination.

parameter	**Compost extract of in-vessel lab-scale reactor**	**Commercial compost extract**
Total seeds	75	75
Germinated seeds	45	33
Mean root length (cm)	0.98	0.85
%Relative seed germination	86.5	50.9
%Relative root growth	98	16.4
%Germination index	84.8	8.3

Table 5. Compost maturity Indices **TMECC, 2002.**

Method	Units Rating		
	Very Mature	Mature	Immature
NH4- : NO3-N Ratio	< 0.5	0.5 - 3.0	> 3
Total NH3-N ppm, dry basis	< 75	75 - 500	> 500
%Seed Germination	> 90	80 - 90	< 80
Plant Trials % of control	> 90	80 - 90	< 80

Modeling and Simulation of Cadmium Removal from the Groundwater by Permeable Reactive Barrier Technology

Dr. Ayad Abdulhamza Faisal
Assistant Professor
College of Engineering-University of Baghdad
e-mail: ayadabedalhamzafaisal@yahoo.com

Zaman Ageel Hmood
MSc. student
College of Engineering- University of Baghdad
e-mail: aube_z@yahoo.com

ABSTRACT

The removal of cadmium ions from simulated groundwater by zeolite permeable reactive barrier was investigated. Batch tests have been performed to characterize the equilibrium sorption properties of the zeolite in cadmium-containing aqueous solutions. Many operating parameters such as contact time, initial pH of solution, initial concentration, resin dosage and agitation speed were investigated. The best values of these parameters that will achieved removal efficiency of cadmium (=99.5%) were 60 min, 6.5, 50 mg/L, 0.25 g/100 ml and 270 rpm respectively. A 1D explicit finite difference model has been developed to describe pollutant transport within a groundwater taking the pollutant sorption on the permeable reactive barrier (PRB), which is performed by Langmuir equation, into account. Computer program written in MATLAB R2009b successfully predicted meaningful values for Cd^{+2} concentration profiles. Numerical results show that the PRB starts to saturate after a period of time (~120 h) due to reduce of the retardation factor, indicating a decrease in percentage of zeolite functionality. However, a reasonable agreement between model predictions and experimental results of the total concentration distribution of Cd^{2+} species across the soil bed in the presence of zeolite permeable reactive barrier was recognized.

Keywords: cadmium removal, sorption process, zeolite, permeable barrier, groundwater remediation.

نمذجة ومحاكاة معالجة المياه الجوفيه الملوثه بالكادميوم باستخدام تقنيه الحاجزالتفاعلي النفاذ

د.أياد عبد الحمزه
أستاذ مساعد
كلية الهندسة- جامعة بغداد

زمن عجيل حمود
طالبة ماجستير
كلية الهندسة-جامعة بغداد

الخلاصة

ازالة ايونات الكادميوم من المياه الجوفيه باستخدام حاجز تفاعلي نفاذ من الزيولايت تم التحري عنها بالدراسة الحالية. حيث اجريت العديد من فحوصات الدفعة لتوصيف خواص امتزاز ملوث الكادميوم من المحاليل المائية على مادة الزيولايت. تم دراسة تأثيرالعديد من المتغيرات التشغيليه مثل زمن التماس، الداله الحامضية الابتدائية للمحلول، التركيز الابتدائي للمعدن، كمية الماده المازة وسرعة الاهتزاز. ان افضل قيم لتلك المتغيرات والتي تحقق كفاءة ازالة لملوث الكادميوم تصل الى 99.5% كانت 60 دقيقه، 6.5، 50 ملغم/لتر،0.25 ملغم/100مليلتر و 270 دورة/دقيقه على التوالي.تم اعداد نموذج رياضي احادي البعد باستخدام طريقة الفروق المحددة والذي يأخذ الامتزاز الحاصل في منطقة الحاجز التفاعلي النفاذ بواسطة معادلة لانكمير بنظر الاعتبار. ومن ثم استخدام برنامج الماتلاب والذي استطاع ان يعبر بنجاح عن ذلك النموذج والذي يهدف الى رسم قيم تراكيز الكادميوم زمانيا ومكانيا. أظهرت النتائج العددية بدء عملية تشبع الحاجز الفعال النفاذ بعد فتره زمنية تصل الى (120ساعه) بفعل تناقص معامل الاحتجاز والذي يشير الى تناقص الاداء لذلك الحاجز. على العموم يوجد تطابق بين النتائج النظرية والنتائج المختبرية لتوزيع تراكيز الكادميوم على طول التربه الملوثه بوجود الزيولايت كحاجز تفاعلي نفاذ.

1. INTRODUCTION

The presence of toxic pollutants in groundwater brings about significant changes in the properties of water resources and has to be avoided in order to preserve the environmental quality. Heavy metals are among the most dangerous inorganic water pollutants, they can be related to many anthropogenic sources and their compounds are extremely toxic. Many heavy metals, such as mercury, chromium and cadmium, accumulate in the aquatic food web reaching human beings through the food chain, and causing several pathologies. The presence of heavy metals in groundwater is due to water exchange with contaminated rivers and lakes or to leaching from contaminated soils by rainfall infiltration.

Groundwater remediation techniques such as pump and treat are widely used but have proven that they are difficult, costly and ineffective most of the time in removing enough contamination to restore the groundwater to drinking water standards in acceptable time frames. The primary reason for the failure of pump and treat is the inability to extract contaminants from the subsurface due to hydro-geologic factors and trapped residual contaminant mass. Hence, the removal of these contaminants from groundwater is a major challenge for environmental engineering. One of the most promising technologies is the in-situ treatment of groundwater contaminants by means of permeable reactive or adsorbing barriers (PRBs)**, Di Natale, et al., 2008.**

The main advantage of a reactive barrier is the passive nature of the treatment: the contaminated groundwater moves under natural hydraulic gradient through the permeable reactive zone where the pollutant is degraded or immobilized. The use of reactive materials whose hydraulic conductivity is higher than that of the surrounding soils ensures that groundwater spontaneously flows through the barrier without any external energy input. This method is found to be more cost-effective than pump and treat and has been a demonstrated potential to diminish the spread of contaminants which have proven difficult and expensive to manage with other cleanup methods**, Puls, et al., 1998**.

Accordingly, PRBs are installed in the aquifer across the flow path of a contaminant plume. As the contaminated groundwater moves through these barriers due to the natural gradient, the contaminants are removed by physical, chemical and/or biological processes. Depending on what processes take place, the reactive barrier material can remain permanently in the subsurface, or replaceable units can be provided. As the reactions that occur in such systems are affected by many parameters, successful application of this technology requires a sufficient of contaminants characterization**, Stengele, and Kohler, 2001**.

2. THEORY

A general differential equation, describing the transport of a dissolved constituent, subject to physical and chemical transport processes. The mass conservation equation for control volume shown in **Fig. 1** may be expressed as**:**

(Rate of mass input) - (rate of mass output) ± (rate of mass production or consumption) = rate of mass accumulation (1)

This equation can be written mathematically as:

$$-\left[\frac{\partial J_x}{\partial x}+\frac{\partial J_y}{\partial y}+\frac{\partial J_z}{\partial z}\right] \pm r = \frac{\partial (nc)}{\partial t} \quad (2)$$

where J is the mass flux of solute per unit cross-sectional area transported in the direction indicated by the subscript x, y, or z; r is the rate of mass production/consumption given by the kinetic model of reaction, n is the porosity of the medium, and c is the solute concentration expressed as mass of solute per unit volume of solution.

The two mass transport processes of advection and dispersion govern J in **Eq. (2).** The transport of dissolved contaminants follows that of water via advection and is therefore related to the velocity of water flow. The direction of hydraulic gradients dictates to a large extent the direction of dissolved contaminant transport. If advection is the only mechanism of transport, the pore velocity (Darcy velocity divided by porosity) is an indicator of the transport of dissolved contaminants. In reality, however, there are other mechanisms incorporating with advection. The saturated soil possesses concentration gradients in addition to hydraulic gradients because of the localized presence of the dissolved chemical. These concentration gradients provide an additional mechanism of transport namely, diffusion. The effect of diffusion is represented by spread out of contaminant in all directions in response to concentration gradients. The relative contributions of advection and diffusion are therefore dependent on the magnitudes of velocity and the concentration gradients. The diffusion of chemicals in soils is typically grouped with another important transport mechanism known as mechanical dispersion. The mechanical dispersion is the effect of advective velocities which, when sufficiently high, cause a mixing of the chemical in the porous medium. Accordingly, the mass flux (J) due to advection and dispersion in the x direction may be expressed as**, Reddi, and Inyang, 2000**:

$$J_{advection} = V_x nc \quad \& \quad J_{dispersion} = -nD_x \frac{\partial c}{\partial x} \tag{3}$$

where V_x is pore velocity in the x direction. The D_x includes the two components of molecular diffusion and mechanical dispersion. Summing up the contributions from advection and dispersion, the mass fluxes are substituted into the **Eq. (2)** and the resultant will be:

$$-\left[\frac{\partial}{\partial x}\left(V_x nc - nD_x \frac{\partial c}{\partial x}\right)\right] - \left[\frac{\partial}{\partial y}\left(V_y nc - nD_y \frac{\partial c}{\partial y}\right)\right] - \left[\frac{\partial}{\partial z}\left(V_z nc - nD_z \frac{\partial c}{\partial z}\right)\right] \pm r = \frac{\partial (nc)}{\partial t} \tag{4}$$

By assuming that the velocities are steady and uniform, the dispersion coefficients do not vary in space, and the porosity of the medium is constant in time and space; one dimensional mass transport of solute in the saturated zone of the soil which well-known advection-dispersion equation (ADE) can be established as follows:

$$D_z \frac{\partial^2 c}{\partial z^2} - V_z \frac{\partial c}{\partial z} \pm \frac{r}{n} = \frac{\partial c}{\partial t} \tag{5}$$

The exact form of the ADE depends on the mass transfer processes accounted for in the term r. One of the dominant mass transfer mechanisms occurring during mass transport is sorption which represents the fundamental mechanism for the operation of the reactive permeable barriers. Incorporating sorption can be achieved by using Linear, Langmuir, or Freundlich isotherm. However, the simplest way for incorporation is the linear sorption isotherm as below:

$$S = K_d c \tag{6}$$

where S is the quantity of mass sorbed on the surface of solids and K_d is the distribution coefficient. The rate expression r is equal to the product of time derivative of S and dry mass density, ρ_b. Thus,

$$r = \rho_b \frac{\partial s}{\partial t} = K_d \rho_b \frac{\partial c}{\partial t} \tag{7}$$

Substituting **Eq. (7)** in the **Eq. (5)** and rearrangement of terms yields:

$$D_z \frac{\partial^2 c}{\partial z^2} - V_z \frac{\partial c}{\partial z} = R \frac{\partial c}{\partial t} \tag{8}$$

where R $(=1+\rho_b K_d/n)$ is known as the retardation factor since it has the effect of retarding the transport of adsorbed species relative to the advection front.

3. BOUNDARY VALUE PROBLEM

3.1 Governing Equations

The 1D model consists of the source area (where the aqueous-phase source is assumed to be perfectly mixed and the concentration, c_s, is assumed to be uniform) and two homogenous porous transport domains; the receiving aquifer and the permeable reactive barrier as shown in **Fig. 2.** Because the reactive barrier is permeable, flow velocity (V_B) in the barrier is evaluated as follows:

$$V_A n_A = V_B n_B \tag{9}$$

where n_A is the porosity of the aquifer; n_B is the porosity of the barrier; and V_A is the flow velocity in the aquifer. **Eq. (8)** can be re-written to describe the contaminant, i.e. Cd^{2+}, transport inside the barrier as follows:

$$D_{Bz} \frac{\partial^2 c_{CdB}}{\partial z^2} - V_{Bz} \frac{\partial c_{CdB}}{\partial z} = R_B \frac{\partial c_{CdB}}{\partial t} \tag{10}$$

where c_{CdB} is the cadmium concentration in the permeable reactive barrier for $L_A \le z \le L_A+L_B$; D_{Bz} is the reactive barrier molecular dispersion coefficient in the direction of flow and R_B is the retardation factor in the barrier. In the same manner, solute transport in the aquifer can be written as:

$$D_{Az} \frac{\partial^2 c_{CdA}}{\partial z^2} - V_{Az} \frac{\partial c_{CdA}}{\partial z} = R_A \frac{\partial c_{CdA}}{\partial t} \tag{11}$$

where c_{CdA} is the cadmium concentration in the aquifer for $0 \le z \le L_A$ and $L_A+L_B \le z \le L$; D_{Az} is the hydrodynamic dispersion coefficient and R_A is the retardation factor in the aquifer. However, the value of R_A is assumed equal to 1 in the present study. Also, continuity is assumed at the reactive barrier- aquifer interface.

3.2 Initial and Boundary Conditions

The mathematical model consists of the three governing differential equations describing cadmium transport in the aquifer upstream of the barrier, in the barrier, and in the aquifer downstream of the barrier **Eqs. (10)** and **(11**). Each equation in each domain must have one initial and two boundary conditions to generate the required solution describing the contaminant distribution as function of distance and time. The initial conditions:

$$c_{CdA}(z,0) = 0 \quad \text{for } 0 \le z \le L_A \text{ and } L_A+L_B \le z \le L \tag{12a}$$
$$c_{CdB}(z,0) = 0 \quad L_A \le z \le L_A+L_B \tag{12b}$$

Also, two boundary conditions and four intermediate conditions at the interface between the barrier and the aquifer are selected to complete the solution process as follows:

$c_{CdA}(0,t)=c_s$ (13a)

$$\frac{\partial c_{cdA}}{\partial z}=0 \qquad @\ (L,t) \tag{13b}$$

$c_{CdA}(L_A,t)=c_{CdB}(L_A,t)$ (13c)

$c_{CdA}(L_A+L_B,t)=c_{CdB}(L_A+L_B,t)$ (13d)

$$-D_{Bz}n_B\frac{\partial c_{CdB}}{\partial z}+V_{Bz}n_Bc_{CdB}=-D_{Az}n_A\frac{\partial c_{CdA}}{\partial z}+V_{Az}n_Ac_{CdA} \qquad @\ (L_A\ ,\ t) \tag{13e}$$

$$-D_Bn_B\frac{\partial c_B}{\partial x}+V_Bn_BC_B=-D_An_A\frac{\partial c_A}{\partial x}+V_An_AC_A \qquad @\ (L_A+L_B,\ t) \tag{13f}$$

where L_A is the distance from source of contaminant to the reactive barrier and L_B is the thickness of the reactive barrier.

An explicit method among finite difference methods was applied to the PDE describing the transport of contaminant through saturated zone of the soil. **Eq. (10)** was formulated with the following producer: for time, forward difference was used; for space, backward difference was used for simple partial difference; and center difference was used for quadratic partial difference:

$$c^{n+1}_{CdB_i}=c^{n}_{CdB_i}+\left(\frac{\Delta t}{R_B}\right)(D_{Bz})\left(\frac{c^{n}_{CdB_{i-1}}-2c^{n}_{CdB_i}+c^{n}_{CdB_{i+1}}}{(\Delta z)^2}\right)-\left(\frac{\Delta t}{R_B}\right)(V_{Bz})\left(\frac{c^{n}_{CdB_i}-c^{n}_{CdB_{i-1}}}{\Delta z}\right) \tag{14}$$

This equation can be re-written as a following simple form:

$$c^{n+1}_{CdB_i}=e_ic^{n}_{CdB_{i-1}}+a_ic^{n}_{HCdB_i}+b_ic^{n}_{CdB_{i+1}} \tag{15}$$

$$e_i=\left[\frac{D_{Bz}(\Delta t)}{R_B(\Delta z)^2}+\frac{V_{Bz}(\Delta t)}{R_B(\Delta z)}\right]$$

$$a_i=\left[1-2\frac{D_{Bz}(\Delta t)}{R_B(\Delta z)^2}-\frac{V_{Bz}(\Delta t)}{R_B(\Delta z)}\right]$$

$$b_i=\left[\frac{D_{Bz}(\Delta t)}{R_B(\Delta z)^2}\right]$$

where e_i a_i, and b_i are the coefficients associated with $c^{n}_{Cd_{i-1}}$,$c^{n}_{Cd_i}$&$c^{n}_{Cd_{i+1}}$, respectively. The superscript n+1 and n are the next and present time step, respectively; $\Delta t=t^{n+1}-t^{n}$ is the time step size, and *i*, *i*+1, *i*-1 are the grid identification **Fig. 3.**

Similar to **Eq. (10),** the migration of Cd^{2+} through the aquifer domain described by **Eq. (11)** can be formulated in the same procedure. The formulation of discretized algebraic equations was followed by development of computer program for its implementation. This program was written in MATLAB R2009b.

4. EXPERIMENTAL METHODOLOGY

4.1 Materials

Naturally Iraqi soil was used as porous medium in the experiments conducted in the present study. **Table 1** summaries the composition and properties of this soil. It was cleaning and well-sorted which needed to an additional sieving to achieve satisfactory uniformity. The proper characterization and preparation of the soil was important in order to ensure high accuracy in the experimental procedure.

A commercially zeolite pellets with diameter (35.96 mm) manufactured by (Dwax company for synthetic zeolite) were used as reactive materials. The resins were washed with 1M of NaOH and 1M of HCl in order to remove possible organic impurities, and then they washed with distilled water to remove all excess and basic. Finally the resins were dried for 24 hours. **Table 2** shows the composition and reported physico-chemical properties of the zeolite used in the present study.

Cadmium was selected as a representative of heavy metal contaminants. To simulate the water's cadmium contamination, a solution of $Cd(NO_3)_2.2H_2O$ (manufactured by E. MERCK, Denmark) was prepared and added to the specimen to obtain representative concentration.

4.2 Batch Experiments

Batch equilibrium tests are carried out to specify the best conditions of contact time, pH, initial concentration, resin dosage and agitation speed. This means that these tests are suited to identify the activity of the reactive material and the sorption isotherm. Series of 250 ml flasks are employed. Each flask is filled with 100 ml of cadmium solution which has initial concentration of 50 mg/l. About 0.25 g of adsorbent was added into different flasks. The solution in the each flask was kept stirred in the high-speed orbital shaker at 270 rpm for 3 hours. A fixed volume (20ml) of the solution was withdrawn from each flask. This withdrawn solution was filtered to separate the adsorbent and a fixed volume (10 ml) of the clear solution was pipetted out for the determination of the amount of unsorbed metal ion still present in solution. The measurements were carried out using atomic absorption spectrophotometer (AAS). These measurements were repeated for two times and average value has been taken. However, the adsorbed concentration of metal ion on the resin was obtained by a mass balance.

Kinetic studies were investigated with different values of pH (2, 4, 6.5, and 8), different values of initial concentration of Cd^{2+} (50, 100, 150, 200 and 250 mg/l), five amounts of adsorbent dosage (0.15, 0.25, 0.5, 1 and 2 g) and finally two values of shaking speed (200 and 270 rpm).

4.3 Column Test Setup

Fig. 4 shows the schematic diagram of the reactor setup used in the present study. This setup is constructed of Perspex cylinder having height and diameter equal to 70 and 5 cm, respectively; the column is equipped with seven sampling ports at the distance of 10 (port 1), 20 (port 2), 30 (port 3), 40 (port 4), 50 (port 5), 60 (port 6), 65 cm (port 7) from the bottom. These ports along the length of the column should be constructed of stainless steel fittings which blocked with Viton stoppers. Sampling was carried out at specified periods from sampling ports using needle to be inserted into the center axis of the column.

At the beginning of each test, the column was packed with 45 cm depth of soil specimen measured from the bottom of this column. Then, zeolite with depth of 5 cm was placed at the top surface of the packed soil. Again, 15 cm of the soil was added above the layer of the zeolite. The column was then filled with distilled water that was fed slowly into the bottom of the column and forced upward through the medium. The up flow column test was performed at constant temperature, 25±1 ºC.

The contaminated solution with Cd^{2+}, which simulated the contaminated groundwater, was introduced into the column from certain reservoir. The flow from this reservoir, which is placed at the elevation higher than the level of column outlet, was controlled by valve 1, flow meter and valve 2. The elevation of water in the reservoir was changed to form the required hydraulic gradient across the specimen and, consequently, this was determining a flow rate within the column. However, three values of flow rate (5, 10, and 15 ml/min) are selected here with corresponding velocities equal to (3.978, 7.958, and 11.937 m/day) respectively. About 11–15 l of artificial contaminated water was flushed the column for each experiment.

Monitoring of Cd^{2+} concentration along the length of the column in the effluent from sampling ports was conducted for a period of 15 hrs. Water samples were taken regularly (after 5, 10, and 15 hours) from these ports. For sampling the ports, three needles were connected to the three ends of Viton stoppers covered port 2, port 4, and port 6 in each test. However, these selected sampling locations may be changed periodically to comprise the ports (1, 3, and 5) during the same test. In addition to specify three locations only for sampling, the column effluent line was closed and a small amount of water (1-1.5 ml) was withdrawn from these ports. In this way, the samples were taken at the flow rate of the column and this minimized disruption of flow within the column. The samples were immediately introduced in poly-ethylene vials and analyzed by AAS.

The filling material in the column was assumed to be homogeneous and incompressible, and constant over time for water-filled porosity. The volumetric water discharge through the column cross section was constant over time and set as the experimental values. The pollutant inlet concentration was set constant. All tubing and fitting for the influent and effluent lines should be composed of an inert material. Information from the column study can be used along with the site characterization and modeling to help in designs the field-scale PRB.

4.4 Hydraulic Parameters Determination

The porosity, *n*, of column was estimated from the weight of the sand soil, M, and the volume of the column, V, according to the following formula:

$$n = 1 - \frac{\rho_b}{\rho_s} \qquad \& \qquad \rho_b = \frac{M}{V} \tag{16}$$

where ρ_b is the bulk density of the soil column and ρ_s is its mass density.

A tracer experiment was performed to determine the effective dispersion coefficient for the system. A sand soil was packed into the column in a dry condition for a depth of 45 cm. The column was then filled with distilled water that was fed slowly into the bottom of the column and forced upward through the medium, pushing the air in front of it. As a result of this procedure, no difficulties with entrapped air were encountered. A solution of 1 g/l NaCl in distilled water as a tracer was continuously fed into the column, at a rate of 0.3 l/hr. Electrical conductivity was measured with time, as a representative of concentration, by using conductivity meter at port 7 (z_o=65 cm). In this case, the value of D_L is given by the following formula**, Ujfaludi, 1986**.

$$D_L = \frac{1}{8}\left[\frac{(z_o - V t_{0.16})}{(t_{0.16})^{0.5}} - \frac{(z_o - V t_{0.84})}{(t_{0.84})^{0.5}}\right]^2 \tag{17}$$

where D_L is the longitudinal dispersion coefficient, V is the mean pore velocity of seepage (volume rate of flow per unit cross sectional area of voids), $t_{0.16}$ and $t_{0.84}$ are the arrival times of c/c_o = 0.16 and 0.84 relative concentration values, respectively.

In order to establish the relationship between the D_L and V, the experiment described above was repeated with another two values of flow rate. These values were 0.6 and 0.9 l/hr. However, the same procedure can be adopted to develop the same relationship between the D_L and V when the porous medium will be a zeolite.

.

5. RESULTS AND DISCUSSION

5.1 Batch Experiments

5.1.1 Equilibrium time

Fig. 5 shows the effect of contact time on cadmium exchange using 0.25 g of zeolite added to 100 ml of metal solution for batch tests at 25±1ºC. Equilibrium for the purposes of this study was taken as having been reached when the cadmium removal efficiency values plateau. This occurred at a reaction time of approximately 1 h. This value can be subsequently used for all batch tests.

It is clear from figure mentioned above that the percentage of metal ion sorbed (i.e., adsorption rate) was very fast initially and it's increased with increasing of contact time until reached the equilibrium time. This may be a result to decrease mass transfer coefficient of the diffusion controlled reaction between resins and metal ions**, Zaiter, 2006**. Also this may be due to the presence of large number of resin sites available for the adsorption of metal ions. As the remaining vacant surfaces decreasing, the adsorption rate slowed down due to formation of replusive forces between the metals on the solid surfaces and in the liquid phase**, El-Sayed, et al., 2010.** However, further increase in contact time had no significant effect on cadmium removal. The maximum removal efficiency of cadmium using zeolite achieved in the present study was 99.8%.

5.1.2 Initial pH of the solution

Fig. 6 shows that the sorption behavior of metal ions is more sensitive to pH changes. A general increase in cadmium sorption with increasing pH of the solution has been observed up to pH equal to 6.5. There are no hydroxo complexes in the solution at pH less than 6.5; only dissociated aqua-ion-forming Cd(II) ions are present. Accordingly, the increase in the metal removal as the pH increases (i.e., as the solution becomes more basic) can be explained on the basis of a decrease in competition between proton and metal species for the surface sites, and by the decrease in positive surface charge, which results in a lower columbic repulsion of the sorbing metal. However, further increase in pH values would cause a decreasing in removal efficiency. This may be attributed to the formation of negative cadmium hydroxides $Cd(OH)_2^-$ which are precipitated from the solution making true sorption studies impossible. In addition, at low pH values an excess of protons can compete effectively with the Cd(II) ions for binding sites on zeolite surface.

5.1.3 Initial cadmium concentration

To study the effect of initial concentration of cadmium on the removal efficiency, the operating conditions were set as follows: volumes of solutions used were 100 ml, concentration of cadmium ranging between 50 and 250 mg/l, were shaken with 0.25 g/100 ml of zeolite for 1 h with initial pH of the solution is 6.5.

Fig.7 illustrates the removal of Cd^{2+} ions by zeolite as a function of initial metal ion concentration. The results show that there was a higher removal of the metal in the first values of initial concentration. This removal was decrease with increasing of initial concentration up to 200 mg/l and beyond this value, there is not a significant change at the amount of adsorbed metal ions. This plateau represents saturation of the active sites available on the zeolite samples for interaction with metal ions. It can be concluded that the amount of metal ions adsorbed into unit mass of the zeolite at equilibrium (the adsorption capacity) rapidly decreases at the low initial metal ions concentration and then it begins to a slight decrease with increasing metal concentration in aqueous solutions in the length between 200 and 250 mg/l. These results indicate that energetically less favorable sites become involved with increasing metal concentrations in the aqueous solution**, Buasri, et al., 2008.**

5.1.4 Resin dose

The dependence of Cd(II) sorption on adsorbent dosage was studied by varying the amount of zeolite from 0.15 to 2 g added to 100 ml of metal solution for batch tests at 25±1ºC, while keeping other parameters as follows; c_o=50 mg/l, pH=6.5, shaking speed=270 rpm and contact time=1 hour. **Fig. 8** presents the Cd(II) removal efficiency as a function of different amounts of zeolite. It can be observed that removal efficiency of the zeolite improved with increasing adsorbent dosage from 0.15 g to 0.25 g for a fixed initial metal concentration. This was expected due to the fact that the higher dose of adsorbents in the solution, the greater availability of exchangeable sites. This also suggests that after a certain dose of adsorbent (0.25 g), the maximum adsorption sets in and hence the amount of Cd(II) bound to the adsorbent and the amount of Cd(II) in solution remains constant even with further addition of the dose of adsorbent.

5.1.5 Agitation speed

Fig. 9 shows that about 77% of the cadmium ions were removed at shaking speed equal to 200 rpm when the contact time at equilibrium and that Cd removal increases with the increase in shaking speed. There was gradual increase in metal ions removal when agitation speed was increased from 200 to 270 rpm at which about 99.5% of Cd ions have been removed at equilibrium time. These results can be associated to the fact that the increase in the agitation speed improves the diffusion of metal ions towards the surface of the adsorbent. Thus, proper contact is developed between metal ions in solution and the binding sites, which promotes effective transfer of sorbate ions to the sorbent sites. **Fig. 9** also shows that optimum equilibrium was reached at the agitation speed of 270 rpm. Therefore, higher uptake of metal ions could be possible at this speed of agitation as it will assure that all the sites are made readily available for metal ions uptake. However, greater availability of functional groups on the surface of adsorbent, which is required for interaction adsorbent and Cd(II), significantly improved the binding capacity and the process proceeded rapidly. This result is important, as the agitation speed and, consequently, the equilibrium time is one of the important parameters for an economical contaminated water treatment system.

5.2 Sorption Isotherms

The Batch Equilibrium Technique (BET) is often used to determine the adsorption characteristics of various materials such as zeolite by plotting their adsorption isotherms. From the experimental results in **Table 3**, the amount of cadmium removed from the solution per gram of zeolite sample (mg/g) can be calculated as follows:

$$q_e = (c_o - c_e)\frac{V}{m} \tag{18}$$

The adsorption isotherms were produced by plotting the amount of heavy metal removed (adsorbed) from the heavy metal solution (q_e in mg/g) against the equilibrium concentration of heavy metal in the solution (c_e in mg/l) at constant temperature. The present data in Table 4 are fitted with linearized form of Langmuir model and the empirical coefficients a and b may be obtained by plotting c_e/q_e as a function of c_e **Fig. 10**. Also the same data are fitted with linearized form of Freundlich model and the values of K_F and n were determined from the slope and intercept of the linear plot of ln q_e versus ln c_e **Fig. 11**.

This means that the values of empirical constant (a) and the saturation coefficient (b) are 49.5mg/g and 0.29 l/mg respectively. The value of (a) is represented the amount of adsorbate adsorbed to form a monolayer coverage on the solid particles which related to the retention capacity of the adsorbent. On the other hand, the value of (b) is represented the Langmuir adsorption equilibrium constant. It is related to the binding energy between the adsorbent and the adsorbate. Hence, The Langmuir isotherm equation will be;

$$q_e = \frac{14.355 C_e}{1+0.29 C_e} \tag{19}$$

Also, the values of Freundlich sorption coefficient (K_F) and an empirical constant (1/n) are 26.168 mg/g and 0.13349 respectively. Hence, the Freundlich isotherm equation will be;

$$q_e = 26.168 c_e^{0.13349} \tag{20}$$

The relationship between the adsorbed and the aqueous concentrations at equilibrium has been described by Langmuir and Freundlich isotherms models **Eqs. (19)** and **(20).** The comparison of the experimental values with the values of q_e obtained by these models is shown in **Fig. 12**. As seen from this figure, the fitness between the experimental values and the predicted values using these models were generally very good for all two parameter isotherm models. However, it is clear that the Langmuir isotherm model provided the best correlation (coefficient of determination (R^2) = 0.9887) in compared with Freundlich isotherm model (R^2 = 0.9033) for cadmium adsorption on the zeolite. Accordingly, the Langmuir isotherm model was used to describe the sorption of solute on solid in the partial differential equation governed the transport of a solute undergoing equilibrium sorption through permeable reactive barrier in the continuous mode.

The essential feature of the equation can be expressed in terms of dimensionless separation factor, S_f, defined as:

$$S_f = \frac{1}{1+bC_o} \tag{21}$$

The value of S_f indicates the shape of the isotherm to be unfavorable for S_f >1, linear for S_f =1, favorable for 0< S_f <1, or irreversible for S_f =0**, Bulut, et al., 2008; Hadjmohammadi, et al., 2011**and **Plamondon, et al., 2011.** The variation of S_f with the initial cadmium concentration of the solution is shown in **Fig. 13**.

5.3 Longitudinal Dispersion Coefficient

Results of the experimental runs concerned the measurement of longitudinal dispersion coefficient (D_L) of soil and zeolite are summarized in **Table 4**. Measured values of D_L versus mean pore velocity (V) obtained with soil particles are shown in **Fig. 14**. While **Fig. 15** shows the relationship between D_L and V for zeolite particles. It is clear that the curves inclined with the horizontal axis. This suggests a linear relationship between the values of D_L and V for sand soil and zeolite as follows:

For soil, $D_L = 9.96678\,V + 0.395667$ R^2=0.993 (22)

For zeolite, $D_L = 17.0019\,V + 0.0033$ R^2=0.9393 (23)

Eqs. (21) and **(22)** are taken the general form of longitudinal hydrodynamic dispersion coefficient as follows:

$$D_L = \alpha_L V + \tau D_o \tag{24}$$

where α_L is the longitudinal dispersivity (cm), τ is the tortuosity and D_o is the molecular diffusion coefficient (cm^2/s). For high velocities the first part dominates, which is the common situation in groundwater, although flow in aquifers is still rather slow compared to fluxes in other hydrological compartments. The proportionality factor between dispersion and velocity along a flow path line is given by the parameter α_L, which has the physical dimension of [length]. One may also use the term dispersion length or longitudinal dispersivity. The subscript 'L' refers to longitudinal, as it is valid only in the direction of the flow. Tortuosity is a measure of the effect of the shape of the flow path followed by water molecules in a porous medium. It is calculated depended on the porosity of the medium (n) as follows:

$$\tau = n^{m-1} \tag{25}$$

Archie (1942) reports values of m; 1.8–2 for consolidated sandstones, 1.3 for unconsolidated sand in a laboratory experiment, and 1.3–2 for partly consolidated sand. For theoretical or conceptual work the value m = 2 is considered, which may be justified if there is no further information as cited by**, Holzbecher, 2007**. The longitudinal dispersivity and the molecular diffusion coefficient can be calculated for sand soil and zeolite ,**Table 5**.

5.4 Cadmium Transport and Adsorption Equations

The equation describes the transport of cadmium through reactive permeable barrier undergoing equilibrium sorption **Eq. (10)** can be re-written as:

$$D_{Bz}\frac{\partial^2 C_{CdB}}{\partial z^2} - V_{Bz}\frac{\partial C_{CdB}}{\partial z} = \frac{\partial C_{cdB}}{\partial t} + \frac{\rho_b}{n_B}\frac{\partial q_e}{\partial t} \tag{26}$$

where c and q_e are the solute concentrations in aqueous and on solid phases, t is the travel time, D is the hydrodynamic dispersion coefficient, V is the mean pore velocity, and z is the travel distance. The sorption of solute on solid is governed by Langmuir sorption isotherm. Combination of these two equations can be explained as:

$$D_{Bz}\frac{\partial^2 C_{CdB}}{\partial z^2} - V_{Bz}\frac{\partial C_{CdB}}{\partial z} = \frac{\partial C_{cdB}}{\partial t} + \frac{\rho_b}{n_B}\frac{\partial\left(\frac{ab\,C_{cdB}}{1+bC_{cdB}}\right)}{\partial t} \tag{27}$$

This equation can be simplified as:

$$D_{Bz}\frac{\partial^2 C_{CdB}}{\partial z^2} - V_{Bz}\frac{\partial C_{CdB}}{\partial z} = \left(1 + \frac{\rho_b}{n_B}\left(\frac{ab}{(1+bC_{cdB})^2}\right)\right)\frac{\partial C_{cdB}}{\partial t} \quad (28)$$

The effect of sorption is to retard the flow of this contaminant. The retardation factor for the Langmuir sorption isotherm, R_L, is expressed in **Eq.(29),** where ρ_b is the bulk density of the adsorbent (g/cm^3), n_B is the porosity of the barrier (=0.34), b (=K_L=0.29) the Langmuir adsorption constant related to the binding energy (l/mg) and a (=q_{max}=49.5) is the maximum amount of solute absorbed by the solid during the batch test (mg/g). Retardation is linked to the adsorption constant; a high value of R_L will give a long retardation and an efficient barrier design. The retardation factor is often calculated to compare the relative migration in contaminant transport and PRB design:

$$R_L = 1 + \frac{\rho_b}{n_B}\left(\frac{ba}{(1+bC_{cdB})^2}\right) \quad (29)$$

The results in **Table 6** showed that retardation reduced with the increase in initial metal concentration, which is often found for other pollutants and adsorbents. A similar trend was found in field tests when studying lithium in a heterogeneous aquifer**, Plamondon, et al., 2011.**

5.5 Model Verification

Parameters and constants related to the sand soil and zeolite adopted for verification of model were evaluated, either through laboratory tests or through approximation using literature data **Table 7**. Porosity and bulk density were experimentally determined. The tortuosity factor (τ) for sand soil modeled was not determined experimentally, but a value of 0.51 for soil and 0.34 for zeolite were used in this study.

Fig. 16 reports the concentration lines of cadmium in the aquifer at different values of contaminated groundwater flow rate after the time interval equal to 0.5 hr. without using PRB. It is clear from this figure that the propagation of contaminated plume is very fast and the time required for reaching the concentration of cadmium in the outlet of column to the constant concentration applied to the lower boundary (i.e., 50 mg/l) is not exceeded 1 h. Also, it seems that the increased value of flow rate will increase the velocity of flow for same cross sectional area of soil specimen and, consequently, this will increase the velocity of cadmium plume propagation. The concentration of the contaminated plume reaching the outlet may attain concentration levels higher than 20 mg/l and largely above the 0.005 mg/l quality limit prescribed for surface waters or drinking water**, Di Natale, et al., 2008.**

After the introduction of the PAB **Fig. 17**, the contaminant plume is hindered by the zeolite and the cadmium concentration level reaching the outlet is around zero after 24 hour for different values of contaminated groundwater flow rate (i.e., 5, 10 and 15 cm^3/min). It is clear from this figure in comparison with **Fig. 16** the important role of zeolite barrier in restriction the propagation of contaminant plume. However, the barrier starts to saturate with increasing the travel time as shown in the **Fig. 18**. This means that the cadmium retardation factor was reduced, indicating a decrease in percentage of zeolite functionality for cadmium retardation. This explains the increase of effluent concentration of cadmium from RPB with increased the travel time.

Many values of zeolite depths such as 10 and 15 cm are applied using numerical model developed here. For column configuration adopted in the present study, the results proved that the depth of zeolite not have any significant effect on distribution of contaminant concentration through the barrier for a given value of flow rate. This means that the equilibrium state was achieved during short period in spite of the optimum contact time calculated from batch tests was 60 min. Accordingly, the zeolite depth applied in the continuous tests was 5 cm.

Comparisons between the predicted and experimental results for cadmium concentration during the migration of the contaminant plume for simulated problem adopted here at different time intervals for specified flow rate are depicted in **Fig. 19**. A reasonable agreement between these results can be observed. These concentrations seem to be almost identical however they are slightly different. The highest percentage of difference encountered between the predicted and experimental concentrations was not exceeded ±20%. However, any variation between the model predictions and experimental results could be attributed to the many causes such as neglecting the salts (such as calcite or carbonate…etc.) adsorption and their adsorption competition with the cadmium over the solid surface (soil and zeolite). The retardation factor of the contaminant on the soil particles assumed equal to 1, i.e. there is no adsorption, in the present study. Also, the competition between the dissolved salts in the groundwater from soil and cadmium are not considered in the present mathematical modeling.

6. CONCLUSIONS

1) The interactions between cadmium ions and zeolite have been investigated. The batch results indicated that several factors such as adsorption or equilibrium time, initial pH of the solution, initial metal ion concentration, resin dose and agitation speed affect the adsorption process. However, the optimum values of these factors will achieve the maximum removal efficiency of Cd^{+2} were 1 hr., 6.5, 50 mg/l, 0.25 g/100 ml, and 270 rpm respectively.

2) The adsorbed amount of cadmium ions can be:

- Increased with increasing pH of the solution up to pH equal to 6.5. However, further increase in pH values would cause a decreasing in removal efficiency. This may be attributed to the formation of negative cadmium hydroxides $Cd(OH)_2^-$ which are precipitated from the solution making true sorption studies impossible.
- Decreased with increasing of initial concentration up to 200 mg/l and beyond this value, there is not a significant change at the amount of adsorbed metal ions. This plateau represents saturation of the active sites available on the zeolite samples for interaction with metal ions.
- Increased with increasing adsorbent dosage from 0.15 g to 0.25 g for a fixed initial metal concentration. This was expected due to the fact that the higher dose of adsorbents in the solution, the greater availability of exchangeable sites.
- Increased with increasing agitation speed from 200 to 270 rpm at which about 99.5% of Cd ions have been removed at equilibrium time. These results can be associated to the fact that the increase in the agitation speed improves the diffusion of metal ions towards the surface of the adsorbent. Thus, proper contact is developed between metal ions in solution and the binding sites, which promotes effective transfer of sorbate ions to the sorbent sites.

3) The experimental equilibrium data obtained were applied to the Langmuir and Freundlich isotherm equations to test the fitness of these equations. The experimental data for cadmium sorption on the zeolite were correlated reasonably well by the Langmuir adsorption isotherm with coefficient of determination (R^2) equal to 0.9887 in compared with Freundlich isotherm model (R^2 = 0.9033). Consequently, the isotherm parameters (q_{max} and K_L) have been calculated and they are equal to 49.5 mg/g and 0.29 l/mg respectively.

4) The dimensionless separation factor (S_f) showed that ion exchange of cadmium ions on zeolite is favorable. The values of S_f are decreased with increasing of initial cadmium concentration. This indicates that ion exchange is more favorable for the higher initial concentration in compared with lower concentration.

5) A 1D numerical model is used to describe pollutant transport within groundwater and the pollutant adsorption on the PRB. The model is applied to a given problem where a PRB is used to restrict the migration of pollutant dissolved in an inflowing groundwater contaminated by the mobilization of Cd(II). Numerical results showed that the PRB starts to saturate after a period of time (~120 hr) due to reduce of the retardation factor, indicating a decrease in percentage of zeolite functionality. However, a reasonable agreement between model predictions and experimental results of the total concentration distribution of Cd^{2+} species across the soil bed was recognized.

REFERENCES

Buasri, A., Yongbut, P., Chaiyut, N., and Phattarasirichot, K., 2008, *Adsorption Equilibrium of Zinc Ions from Aqueous Solution by Using Modified Clinoptilolite*, Chiang Mai J. Sci., Vol. 35, No. 1, PP. 56-62.

Bulut, E., Ozacar, M., and Sengil, I. A., 2008, *Equilibrium and Kinetic Data and Process Design for Adsorption of Congo Red on to Bentonite*, Journal of Hazardous Materials, Vol. 154, PP. 613-622.

Di Natale, F., Di Natale, M., Greco, R., Lancia, A., Laudante, C., and Musmarra, D., 2008, *Groundwater Protection from Cadmium Contamination by Permeable Reactive Barriers*, Journal of Hazardous Materials, Vol. 160, PP. 428–434.

El-Sayed, G. O., Dessouki, H. A., and Ibrahim, S. S., 2010, *Bio-sorption of Ni(II) and Cd(II) Ions from Aqueous Solutions onto Rice Straw*, Chemical Science Journal, CSJ-9.

Faisal, A. A., 2006, *Numerical Modeling of Light Non-aqueous Phase Liquid Spill Transport in an Unsaturated-saturated Zone of the Soil*, Ph.D Thesis, Baghdad University, College of Engineering.

Hadjmohammadi, M. R., Salary, M., and Biparva, P., 2011, *Removal of Cr(vi) from Aqueous Solution using Pine Needles Powder as a Bio-sorbent*, Journal of Applied Sciences in Environmental Sanitation, Vol. 6, No. 1, PP. 1-13.

Holzbecher, E., 2007, *Environmental Modeling Using MATLAB*, Springer Berlin Heidelberg New, ISBN: 978-3-540-72936-5.

Plamondon, C. O., Lynch, R., and Al-Tabbaa, A., 2011, *Metal Retention Experiments for the Design of Soil-Mix Technology Permeable Reactive Barriers*, Clean – Soil, Air, Water, Vol. 39, No. 9, PP. 844–852.

Puls, R. W., Powell, R. M., Blowes, D. W., Vogan, J. L., Gillham, R. W., Powell, P.D., Landi, R., Sivavec, T., and Schwltz, D., 1998, *Permeable Reactive Barrier Technologies for Contaminant Remediation*, EPA, 600, (R-98), 125.

Reddi, L. I., and Inyang, H. I., 2000, *Geo-environmental Engineering: Principles and Applications*, Marcel Dekker, Inc, ISBN: 0-8247-0045-7.

Stengele, R. H., and Kohler, S., 2001, *Permeable Reactive Barrier Systems for Groundwater Clean-up*, Geological Survey of Finland, Special paper (32), PP. 175–182.

Ujfaludi, L., 1986, *Longitudinal Dispersion Tests in Non-uniform Porous Media*, Hydrological sciences Journal, Vol. 31, No. 4, PP. 467-474.

Zaiter, M. J., 2006, *Treatment of Low-and Intermediate-Level Radioactive Liquid Waste from Altwath Site using Iraqi Zeolite*, M.Sc. Thesis, Baghdad University.

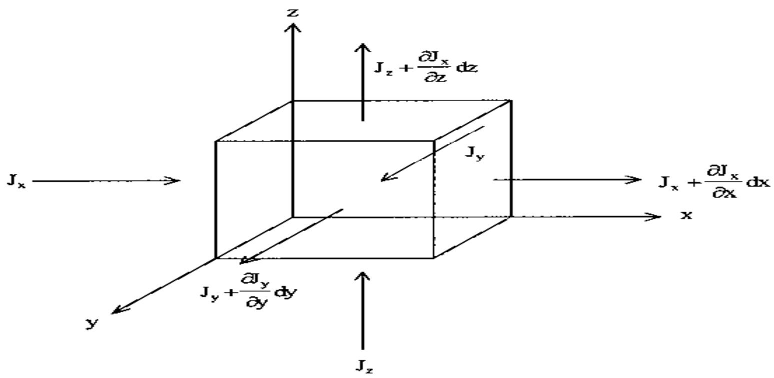

Figure 1. Elemental control volume for mass flux**, Reddi and Inyang, 2000**.

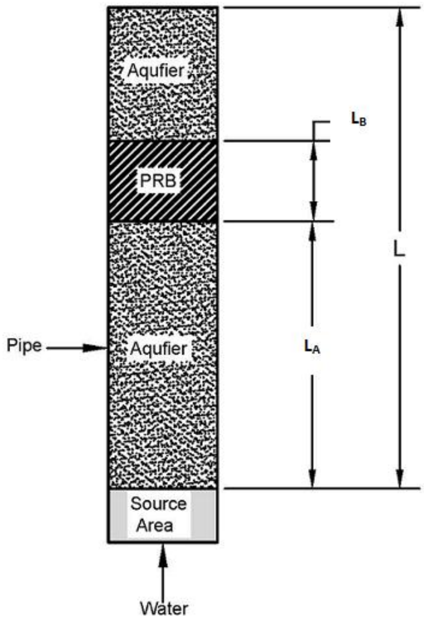

Figure 2. Conceptual model of a contaminant plume passing through a permeable reactive barrier.

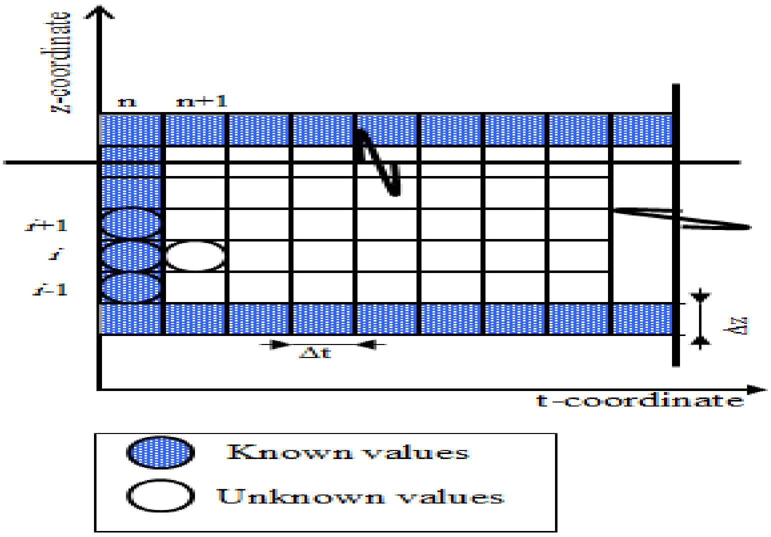

Figure 3. Scheme of spatial and temporal discretization**, Faisal, 2006**.

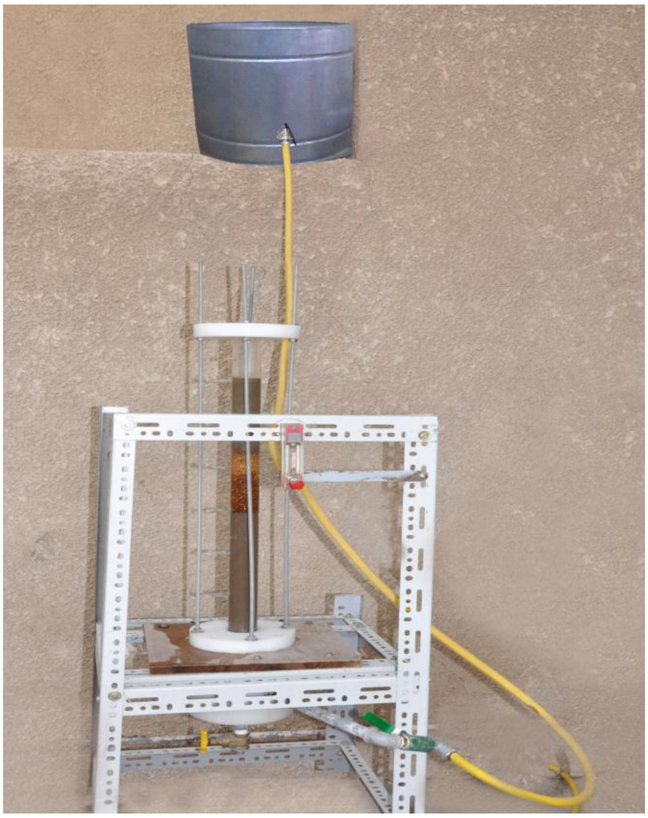

Figure 4. Experimental set-up of column test used in the present study**.**

Table 1. Composition and properties of the soil used in the present study.

Property	Value
Particle size distribution (ASTM D 422) Sand (%) Silt (%) Clay (%)	 90 10 -
Hydraulic conductivity (or coefficient of permeability) (cm s^{-1})	1.54×10^{-4}
Cation exchange capacity (meq/100 g)	1.56
pH	7.5
Organic content (ASTM D 2974) (%)	0.26
Bulk density (g/cm^3)	1.29
Porosity (n_A)	0.51
Soil classification	Sand

Table 2. Composition and physico-chemical properties of zeolite.

Property	Percentage (%)
SiO_2	34.48
Al_2O_3	29.94
L.O.I	15.05
Na_2O	13.40
CaO	2.52
TiO_2	1.70
Bulk density (g/cm^3)	0.58
Particle density (g/cm^3)	1.2
Porosity (n_B)	0.34
Surface area (m^2/g)	1000
Cation exchange capacity (meq/100 g)	1.8

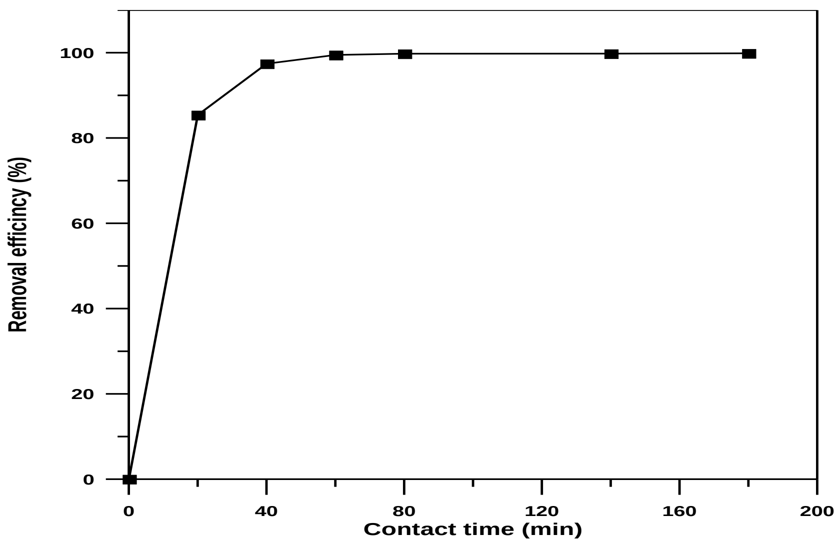

Figure 5. Removal efficiency of cadmium on zeolite as a function of contact time (pH= 6.5; c_o= 50 mg/l; dose=0.25 g; speed= 270 rpm; T= 25±1^oC).

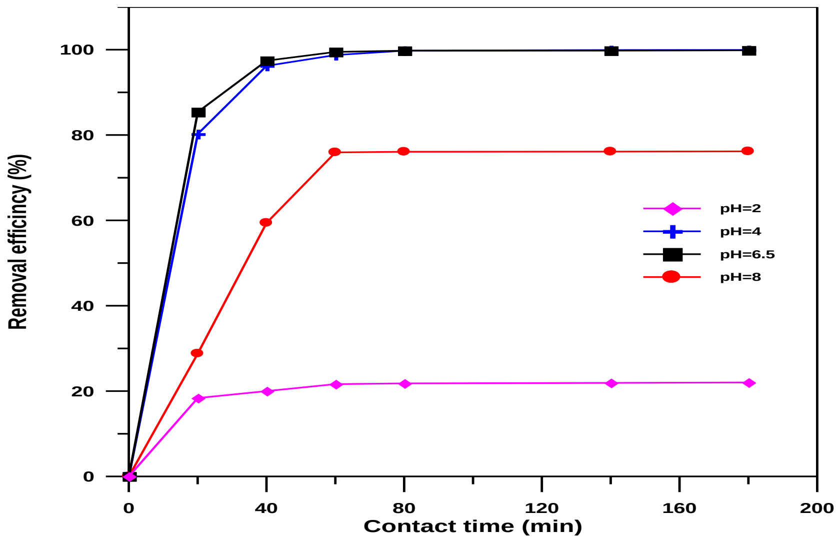

Figure 6. Effect of initial pH on removal efficiency of cadmium on zeolite as a function of contact time (c_o= 50 mg/l; dose=0.25 g; speed= 270 rpm; T= 25±1^{o}C).

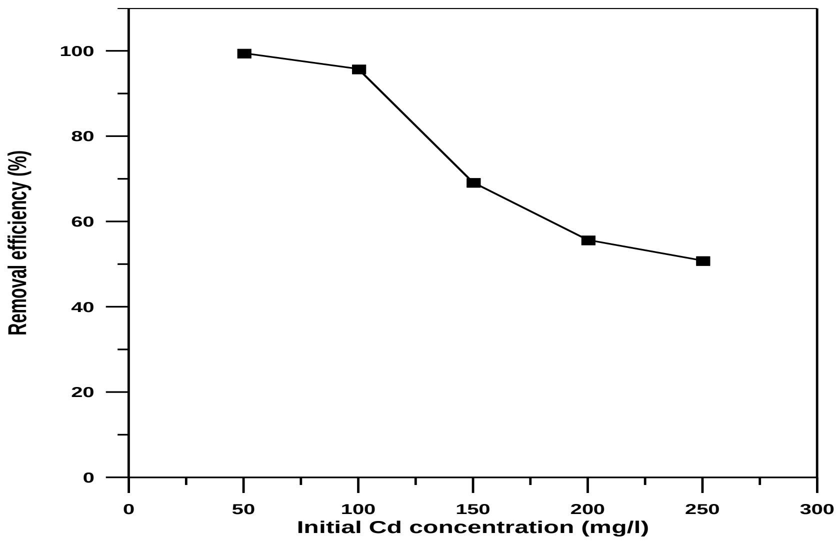

Figure 7. Effect of initial concentration on removal efficiency of cadmium on zeolite (pH=6.5; dose=0.25 g; speed= 270 rpm; contact time=1 h; T= 25±1^{o}C).

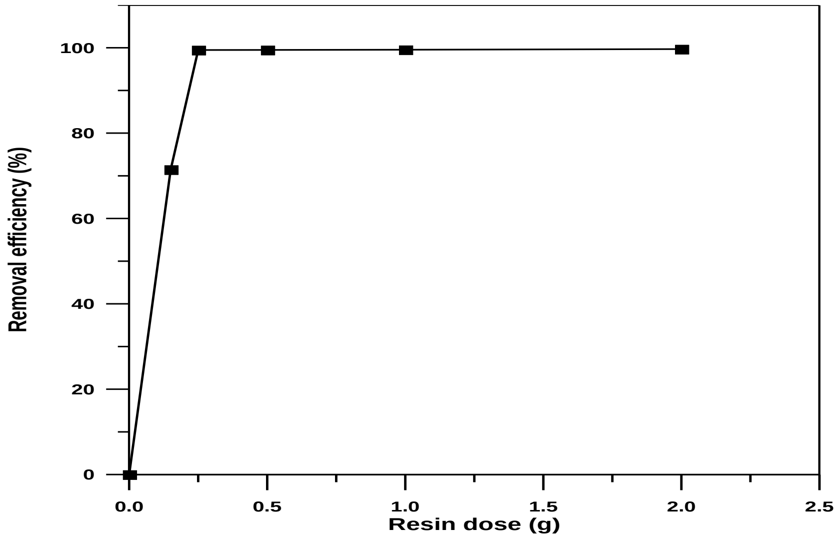

Figure 8. Effect of resin dosage on removal efficiency of cadmium (c_o=50 mg/l; pH=6.5; speed= 270 rpm; contact time=1 h; T= 25±1°C)

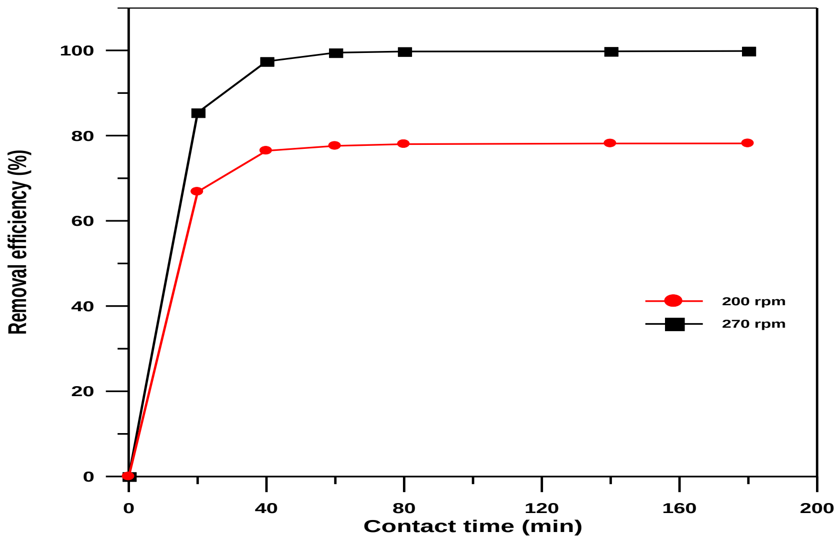

Figure 9. Effect of agitation speed on removal efficiency of cadmium as a function of contact time (c_o=50 mg/l; pH=6.5; resin dose= 0.25 g/100 ml; T= 25±1°C)

Table 3. Experimental equilibrium data of cadmium on zeolite resin (pH=6.5; resin dose= 0.25 g/100 ml; agitation speed= 270 rpm; contact time=1 h; T= 25±1°C).

Initial Con. (c_o) (mg/l)	**Equilibrium Con. (c_e) (mg/l)**	**Sorbed Con. (q_e) (mg/g)**
50	0.255	19.9
100	4.22	38.3
150	46.26	41.5
200	88.66	44.5
250	122.93	50.8

Table 4. Measured values of the longitudinal dispersion coefficient for used mediums as a function of mean pore velocity.

Sand Soil	V (cm/s)	0.00903	0.01806	0.02709
	D_L (cm^2/s)	0.490	0.567	0.670
Zeolite	V (cm/s)	0.0135	0.0270	0.0406
	D_L (cm^2/s)	0.199	0.53	0.66

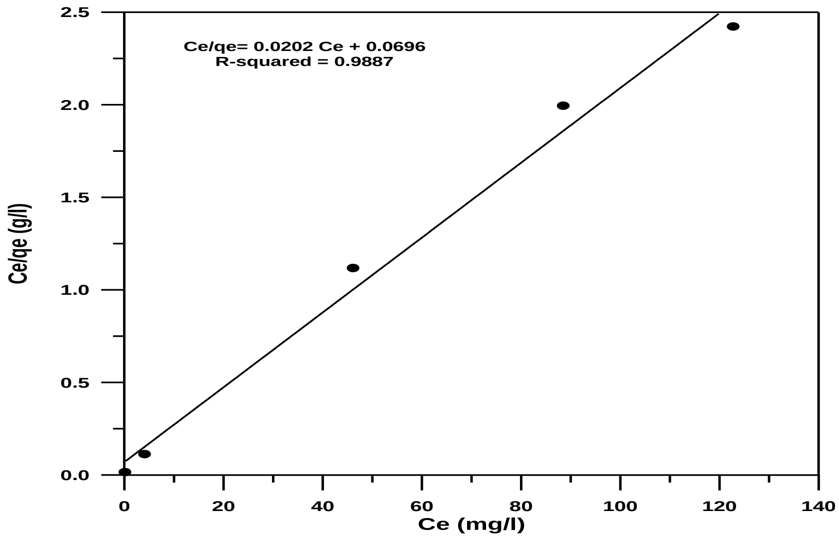

Figure 10. Langmuir isotherm for ion exchange of cadmium on zeolite (pH=6.5; resin dose= 0.25 g/100 ml; agitation speed= 270 rpm; contact time=1 h; T= 25±1^{o}C).

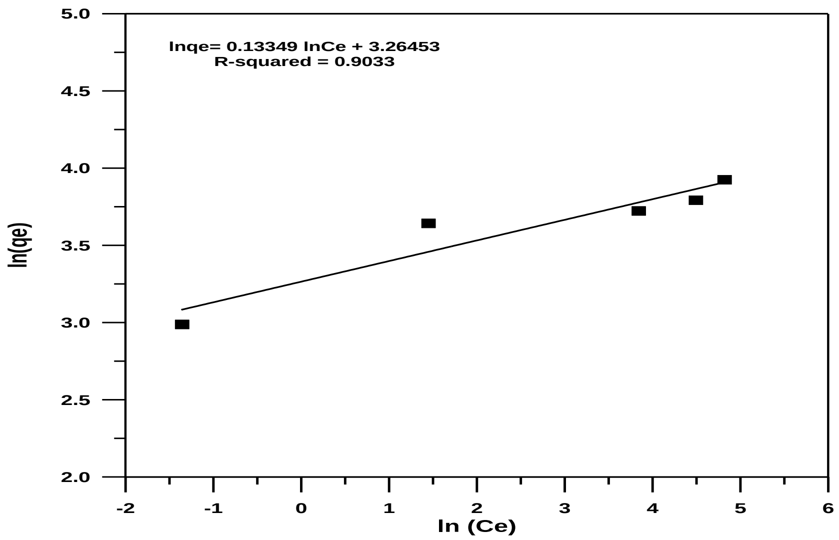

Figure 11. Freundlich isotherm for ion exchange of cadmium on zeolite (pH=6.5; resin dose= 0.25 g/100 ml; agitation speed= 270 rpm; contact time=1 h; T= 25±1^{o}C).

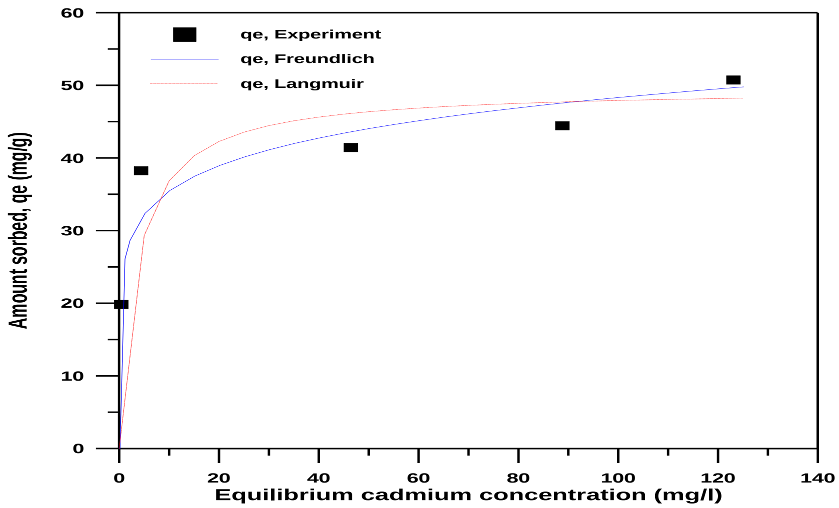

Figure 12. Comparison of the experimental results with the q_e values obtained by two isotherm models for Cd^{2+} removal by zeolite.

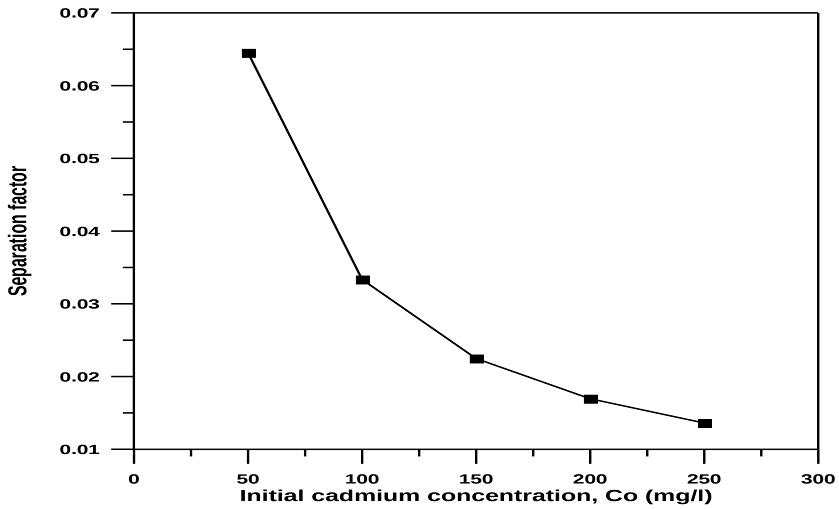

Figure 13. Variation of adsorption intensity with initial cadmium concentration on zeolite resin**.**

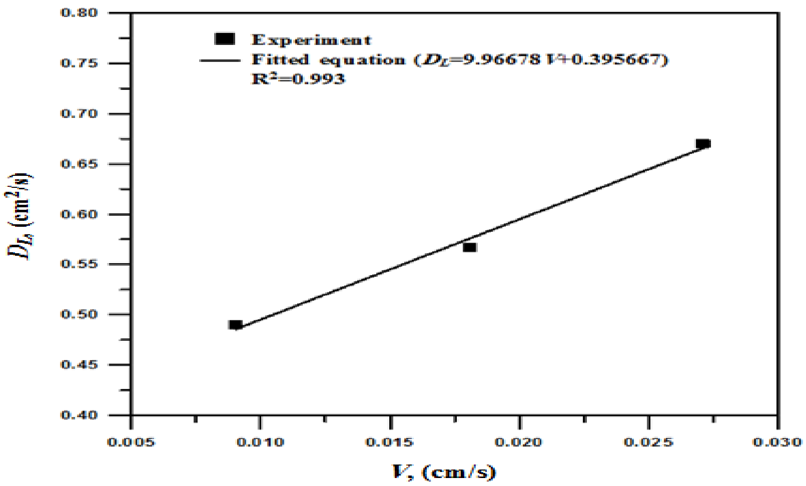

Figure 14. Longitudinal dispersion coefficient versus mean pore velocity relation for sand soil.

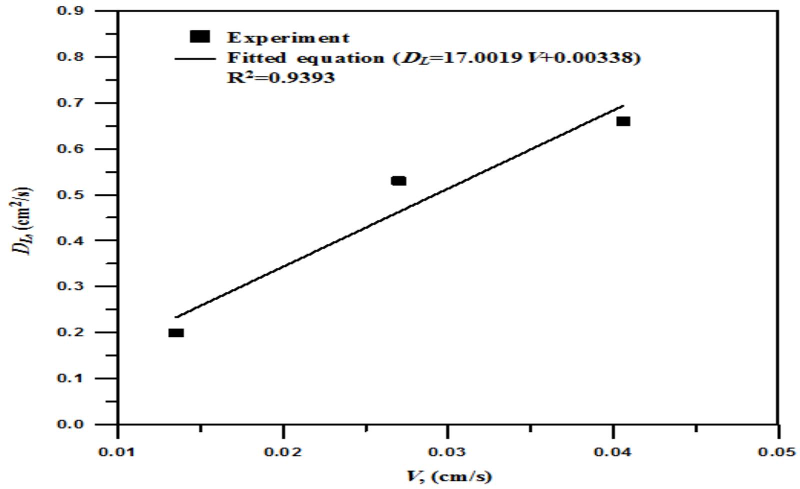

Figure 15. Longitudinal dispersion coefficient versus mean pore velocity relation for zeolite resin.

Table 5. Calculated values of the longitudinal dispersivity and molecular diffusion coefficient for used mediums as a function of mean pore velocity.

Sand Soil	V (cm/s)	0.00903	0.01806	0.02709
	α_L (cm)	9.96678	9.96678	9.96678
Zeolite	V (cm/s)	0.0135	0.0270	0.0406
	α_L (cm)	17.0019	17.0019	17.0019

Table 6. Calculated values of retardation factor dependent on Langmuir sorption isotherm.

Initial Con. (c_o) (mg/l)	**Equilibrium Con. (c_e=c_{cdB}) (mg/l)**	R_L
50	0.255	13883
100	4.22	3238
150	46.26	78
200	88.66	23
250	122.93	13

Table 7. Summary of PRB application example parameters.

Item	Parameter	Value or description
Aquifer characteristics	Aquifer bed depth before barrier (cm)	45
	Aquifer bed depth after barrier (cm)	15
	Porosity of aquifer (n_A)	0.51
	Longitudinal dispersivity (α_L, cm)	9.96678
	Bulk density (g/cm^3)	1.29
	Particle density (g/cm^3)	2.65
PRB characteristics	Adsorbing medium	zeolite
	Barrier bed depth (cm)	5
	Porosity of barrier (n_B)	0.34
	Longitudinal dispersivity (α_L, cm)	17.0019
	Bulk density (g/cm^3)	0.58
	Particle density (g/cm^3)	1.2
Numerical model parameters	Number of nodes	65
	Time step size (min)	0.001
	Initial concentration of Cd^{+2} (mg/l)	zero
Boundary conditions	Concentration of Cd^{+2} @ z=0 (mg/l)	50
	$\frac{\partial c_{cd}}{\partial z}$ at $z_{0=65\ cm}$	zero

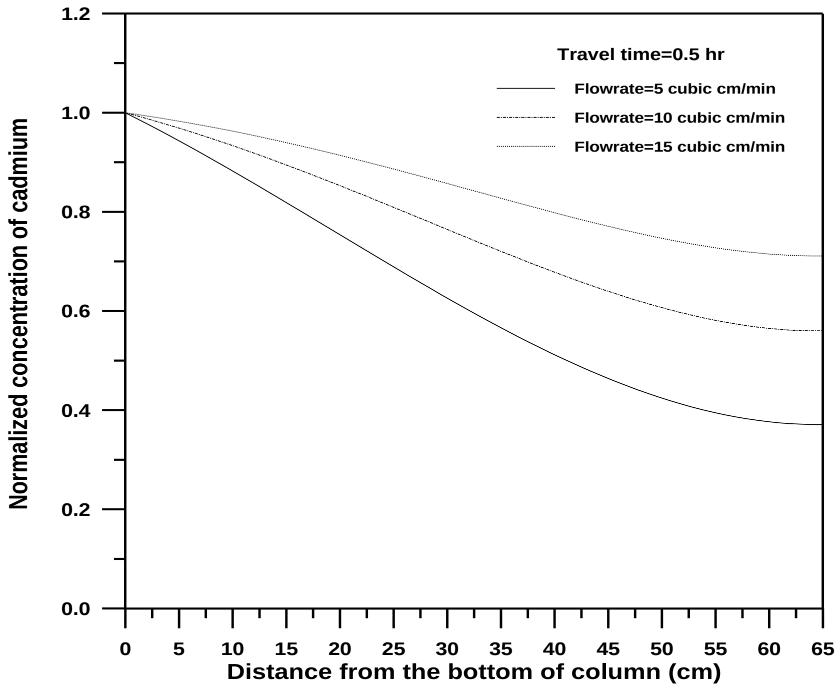

Figure 16. Cadmium concentration distribution in the groundwater along the length of the soil column without using PRB after 0.5 hr.

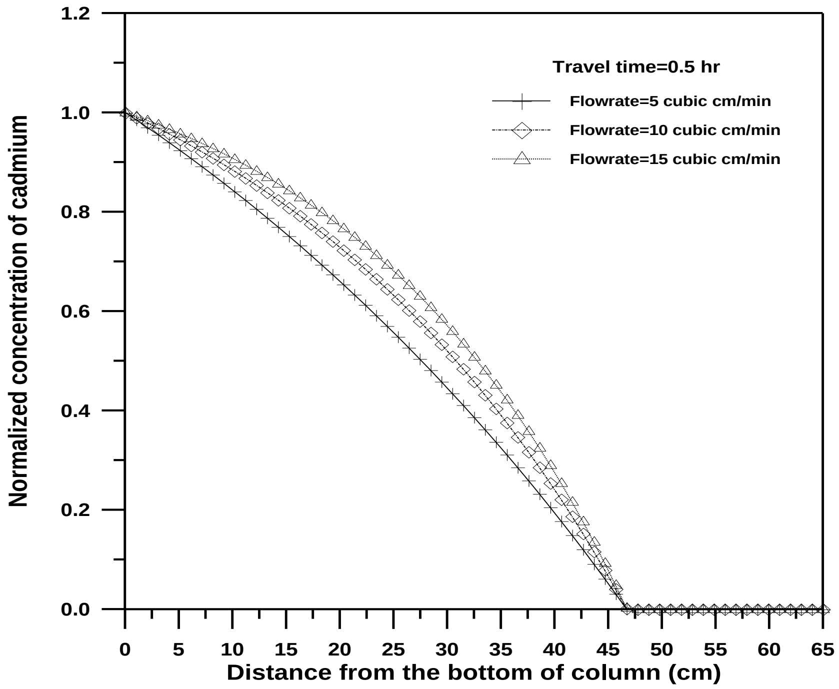

Figure 17. Cadmium concentration distribution in the groundwater along the length of the soil column with using PRB after 0.5 hr.

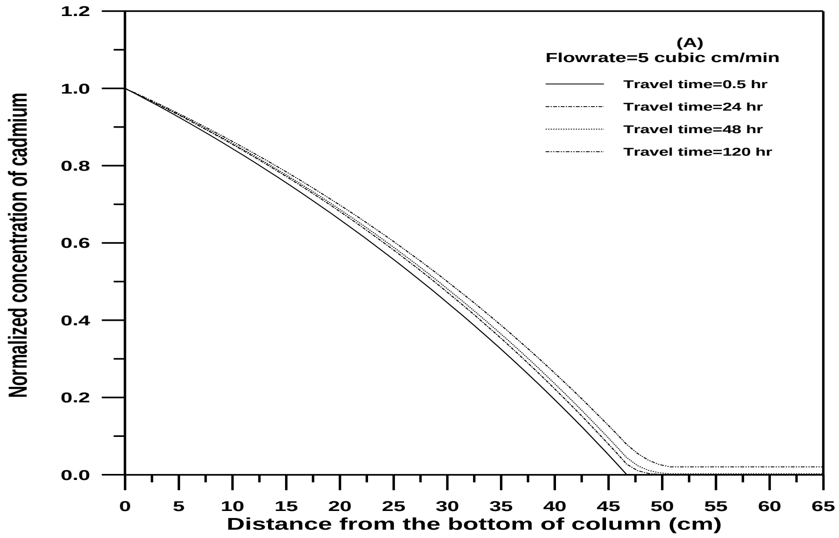

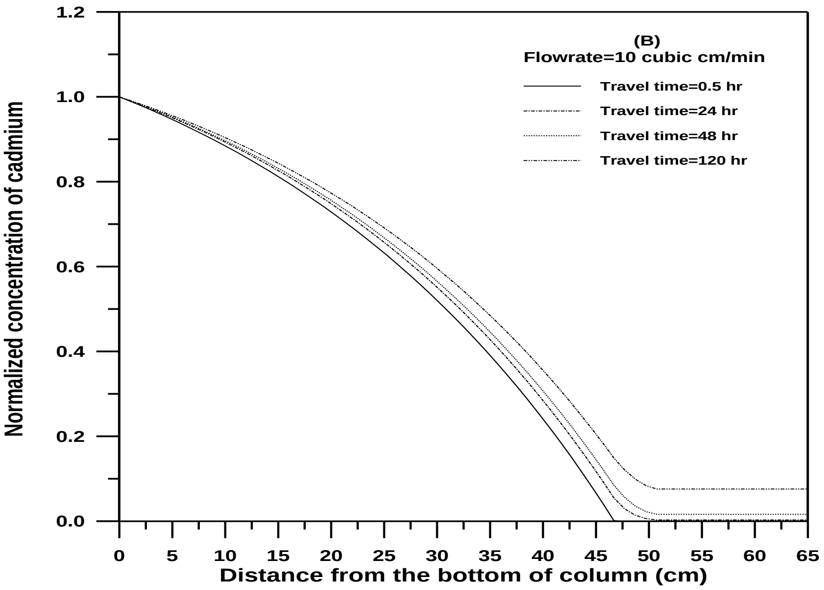

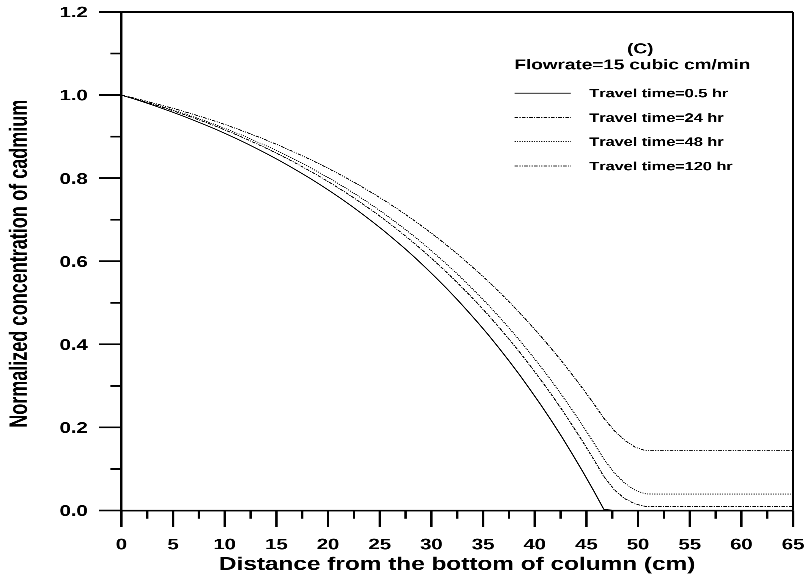

Figure 18. Cadmium concentration distribution in the groundwater along the length of the soil column with using PRB at different time intervals for flow rate equal to (A) 5, (B) 10, (C) 15

cm^3/min.

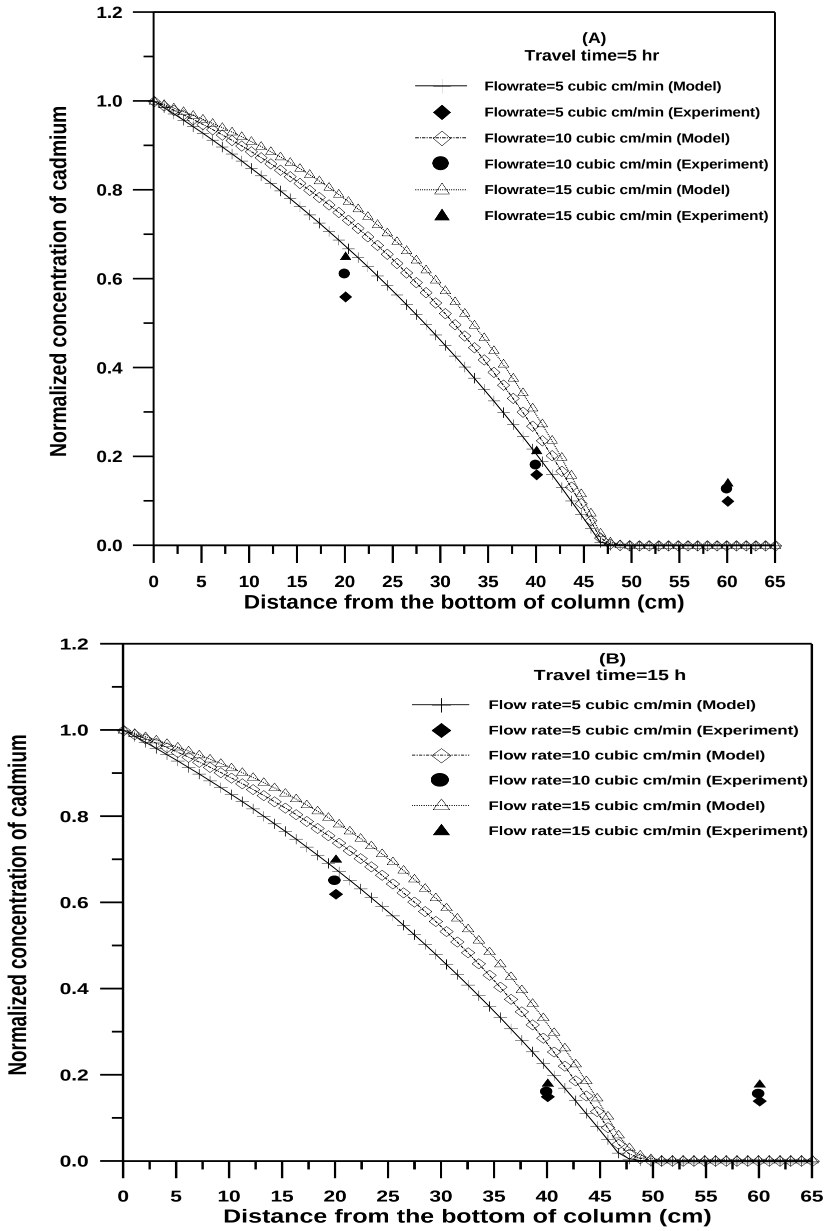

Figure 19. Comparison between model predictions and experimental results for Cd^{+2} concentrations in groundwater for travel time equal to (A) 5 hr and (B) 15 hr.

Manufacturing an Organic Solar Cell and Comparing with Different Dyes

Lect. Ghassan Luay Yusif

Mechanical Department, University of Baghdad

ghassanalani65@gmail.com

ABSTRACT

A solar cell was manufactured from local materials and was dyed using dyes extracted from different organic plants. The solar cell glass slides were coated with a nano-porous layer of Titanium Oxide and infused with two types of acids, Nitric acid and Acetic acid. The organic dyes were extracted from Pomegranate, Hibiscus, Blackberry and Blue Flowers. They were then tested and a comparison was made for the amount of voltage they generate when exposed to sunlight. Hibiscus sabdariffa extract had the best performance parameters; also Different plants give different levels of voltage.

Keywords: photovoltaic, photo cell, organic cells, organic photo dyes, renewable energy

تصنيع خلية شمسية عضوية مع مقارنة اصباغ عضوية مختلفة

غسان لؤي يوسف
جامعة بغداد/ كلية الهندسة / قسم الميكانيك

الخلاصة

تم تصنيع الخلايا الشمسية من مواد محلية وقد تم طلائهم باصباغ مستخرجة من النباتات العضوية المختلفة. وقد تم طلاء الشرائح الزجاجية الخلايا الشمسية مع طبقة نانو المسامية بأوكسيد التيتانيوم والتي تم مزجها مع نوعين من الأحماض، وحمض النيتريك وحمض الخليك. تم استخراج الأصباغ العضوية من الرمان، الكركديه، و التوت البري والزهور الزرقاء. ثم تم اختبارها مع إجراء مقارنة لكمية فرق الجهد التي تولدها عن تعرضها لاشعة الشمس. النباتات المختلفة لهم كفاءات مختلفة و افضل اداء كان لنبات الكركديه الحاوي على صبغة "سابداريفا"

الكلمات الرئسية : الخلايا العضوية الشمسية , الخلايا العضوية , الخلايا الشمسية , الخلايا الفلطائية ,الطاقة المتجددة

1. INTRODUCTION

A solar cell is an electronic device that produces electricity when light falls on it. The light is absorbed and the cell produces dc voltage and current. The device has a positive and a negative contact between which the voltage is generated and through which the current can flow.

L.u.Okoli et. al.2011, performed a study on the performance of the Anthocyanin dye which is an extract from hibiscus sabdariffa which is an edible plant called zobo by Nigerians. He found that the photo conversion efficiency of the cell fabricated with the local dye is not poor when compared with the result of the Ruthenium-stained cell and other existing results.

Jill Johnsen 2006, used Blackberry juice Titanium oxide (TiO_2) as a light absorber and the oxidization of water (to produce oxygen, hydrogen, and electrons) replaces the I-/I_3 - cycle, replenishing the electrons released from chlorophyll. Ultimately, carbon dioxide acts as an electron acceptor, resulting in the fixing of carbon dioxide.

Khwanchit Wongcharee et.al 2006, fabricated solar cells by using natural dyes extracted from rosella, blue pea and a mixture of the extracts. The light absorption spectrum of the mixed extract contained peaks corresponding to the contributions from both rosella and blue pea extracts. However, the mixed extract adsorbed on TiO2 does not show synergistic light absorption and photosensitization compared to the individual extracts. The Dye-Sensitized Solar Cells (DSSCs) efficiency that used ethanol as an extracting solvent was found to be diminished after being exposed to the simulated sunlight for a short period.

Brian A. Gregga et al 2003, compared between organic and inorganic photovoltiacs.he concluded that The photoinduced generation of a free electron and hole in OPV cells is simultaneous with, and identical to, the initial separation of the electron from the hole across the interface. This is a fundamental mechanistic difference relative to conventional solar cells, in which generation and separation are two spatially and temporally distinct processes

For a PV cell to function, light must be absorbed and converted to electrons. This feat is accomplished by the anthocyanin, which has a molecular structure that acts like a photon antenna. As light is collected, the molecule enters an excited state whereby it dumps an electron wherever it can to relieve this “excitement”. The electron is harnessed by attaching the anthocyanin to a semiconductor, titanium dioxide. Titanium dioxide, also known as titania, is one of the most common oxide compounds on Earth. Anthocyanins, as well as other inorganic compounds, attach themselves very well to titania due to a number of hydroxyl (-OH) bonds on both the titania and the dye. When electrons are produced by the dye, they conduct themselves through the molecule and into the titania. As long as the titania film is bound to a conductive surface, these electrons can be harnessed to do useful work, such as power a light bulb. As the adage goes, however, something cannot be got for nothing. The dye molecule cannot produce an endless supply of electrons and they must be regenerated. By using an electron donor, or redox electrolyte, the electrons are supplied back to the dye. Of course, this electrolyte does not have an unlimited supply of electrons either. The electrolyte receives its electrons from the return of the dye-generated electrons that were sent through the circuit. This cycle is important- electrons are never “used up” or destroyed, the power is just used to do some amount of work. This whole device: dye, titania, and electron donor complex creates what is known as a dye-sensitized solar cell, or DSSC. This type of cell was “invented” and published by Michael, **Grätzel in the journal Nature in 1991,** but nature itself has been performing this same process for millennia in plants by using chlorophyll. Smestad, G. P et.al

2.EXPERIMENTAL WORK

The **Fig. 1** shows how an organic solar cell works and in order to manufacture one the following steps are taken:

2.1 Preparing the ITO Slides

1. The ITO glass strips(5 x 4)cm were extracted from used mobile phones since their screens are manufactured from ITO glass i.e. that one side is electrically conductive.
2. Identify the conducting side of a tin oxide-coated piece of glass by using a MultiMate to measure resistance.
3. The conducting side will have a resistance of 20-30 ohms.
4. With the conducting side up, tape the glass on three sides using one thickness of tape. Wipe off any fingerprints or oils using a tissue wet with ethanol

2.2 Preparing the TiO_2 Paste

Grind about 0.5 gram of nanocrystalline titanium dioxide (TiO_2) in a mortar and pestle with a few drops of very dilute nitric acid. Alternate grinding and addition of a few drops of very dilute nitric acid until you obtain a colloidal suspension with a smooth consistency, somewhat like latex paint or cake icing, as shown in **Fig 2**.

2.3 Applying the Film

1. Add a small amount of titanium dioxide paste and quickly spread by pushing with a microscope slide before the paste dries. The tape serves as a 40-50 micrometer spacer to control the thickness of the titanium dioxide layer as show in **Fig 3**.

2. Wait couple of minutes for the coat to dry. Carefully remove the Scotch tape border.
3. Heat the coated glass strip gently until the wet paste dry’s off and then gradually cool it off; So that it does not crack

2.4 Preparing the Dye

1. Prepare a couple of grams of blackberries and crush the in a glass container. The crushed juice slurry is then filtered with a filter funnel.
2. Put the coated face of the ITO glass strip on the blackberry juice that was just prepared and leave it for a couple of minutes so that it can soak up the juice, as shown in **Fig 4**.
3. After 10-15 minutes, gently rinse the coated ITO glass strip with distilled water followed by alcohol. This will represent the Anode electrode.

2.5 Preparing the Cathode Electrode

Light a candle, and tip the conductive side of the second piece of ITO glass strip at an angle so that it can collect soot from the candle as shown in **Fig 5.** The graphite from the soot functions as a cathode then an electrolyte is injected to the assembly.

2.6 Assembling the Solar Cell

Place the cathode with the soot face up on the table. Place a couple of drops of Iodine (electrolyte) on the anode and the place the anode electrode on top of it, as shown in **Fig 6**. And hold the two pieces of glass strips together with a rubber band or clamps.
The photovoltaic cell is now functional and all it needs to produce electricity is to be exposed to sunlight as shown in **Fig.7**.

The same procedure was performed in making the solar cells for all the other dyes that were used in this research and they were: Hibiscus, Pomegranate, Black berry and the blue flower. Then another type of solar cell as made similar to the first except instead of using Nitric acid with the $TiO_{2,}$ Acetic acid was used. Then their voltages were measured that was produced under two types of acid used and the types of dyes for each of the two sets of cells.

3. DISCUSSION and CONCLUSION

The highest voltage was generated by hibiscus it reached its peak after 15 minutes; **Table 1**; and then started to descend in voltage. The reason is owed to the probability that some of the dye and electrolyte evaporated due to the sunlight heat this is one of the drawbacks and disadvantages of open organic cells.

The lowest value was generated by the pomegranate; **Table 1**; this is due to that is was slightly more diluted than the rest of the dyes. All the dyes started at a low value and started to build up between 9 and 21 minutes. From **Table 2** find the pomegranate dye together with the blackberry dye produce more voltage than when nitric acid as used.

The voltage generated in the photovoltaic is due to that all of the extracted organic dyes have a compound known as “Anthocyanins “which is considered as a photo sensitizer. NEHA M. **NATARAJ et. al. 2012.**

Hibiscus sabdariffa extract has the best performance parameters, it corresponds to anthocyanins, because the chemical adsorption of these dyes occurs due to the condensation of alcoholic-bound protons with the hydroxyl groups on the surface of nanostructure TiO2 .**Jude O. Ozuomba1 et. al. 2013**. The reason behind the fact that the different dyes gave different levels of voltages is that they have different Ph concentration levels and thus the higher the acidity (the lower the Ph) the higher absorption of thelight wave length will be and thus a higher photo voltage will result. From this research it can be concluded the following:

1. It is possible to generate voltage from organic dyes.
2. Different plants give different levels of voltage

REFERENCES

Chasteen .S and Johnsen.J , 2006, *Make Your Own Blackberry Juice Solar Cell,* Exploratorium Teacher Institute.

Chavadejb.S ,khwanchit.W and), vissanu meeyooa, March 2007, *Dye-sensitized Solar Cell using natural dyes extracted from rosella and blue pea flowers,* Department of Chemical Engineering, Mahanakorn University of Technology, Nong Chok, Bangkok 10530, Thailand

Gregga. B. A and. Hanna.C.M, March 2003, *Comparing organic to inorganic photovoltaic cells: Theory, Experiment and Simulation*, Journal of Applied Physics Volume 93, No.6 15.

. Nataraj.N,2012, *A Comparative Study of the Photovoltaic (PV) Response of Anthocyanin Dyes from Different Natural Sources*, US Army Research Laboratory Composites and Hybrid Materials Branch,Materials Division

Okoli.L.U, Ekpunobi A. J.and, Ozuomba J. O,2011, *A Comparative Study of The Performance of Dye –Sanitized Solar Cells Based on Antocyanin Local Dye Ruthenium* Dye, Digest Journal of Nanomaterials and Biostructures Vol. 6, No 4, October-December 2011, p. 1929-1934

OzuombaO.J, OkoliU.L and Ekpunobi.J.A,2013, *The Performance and Stability of Anthocyanin Local dye as a Photosensitizer for DSSCs*, Advances in Applied Science research, 2013, 4(2):60-69.

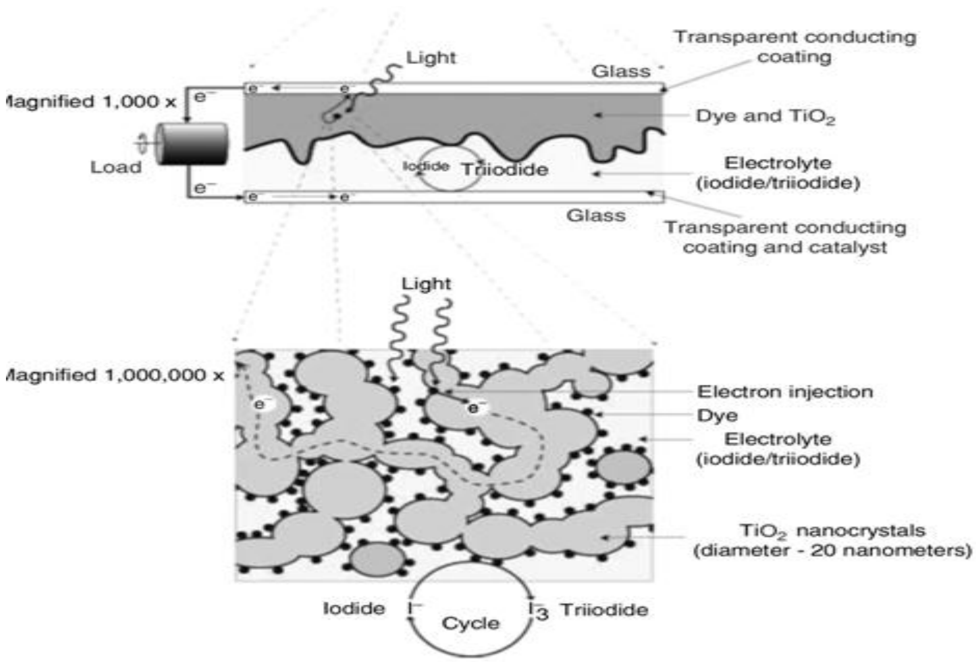

Figure.1 How a photochemical solar cell works Gavin D.J.Harper 200.

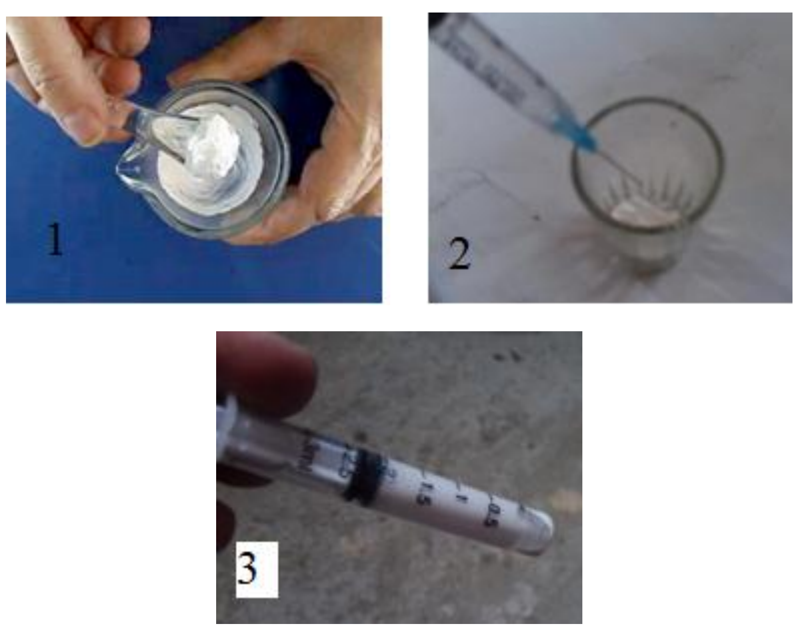

Figure 2. Preparing the TiO_2 paste.

Figure3. Applying the film of TiO2 to the ITO glass.

Figure 4: Applying the dye to the TiO_2. **Figure 5.** Applying the soot to the 2nd ITO slide.

Figure 6. Applying the Iodine Electrolyte. **Figure 7.** The solar cell subjected to a light source.

Table 1. Different organic dyed solar cells in which nitric acid 10% was mixed with the TiO_2.

Blue Flower mV	Hibiscus mV	Black berry mV	Pomegranate mV	Time(min)
125	130	74	2	0
117	120	66	40	3
126	148	52	35	6
137	155	47	29	9
136	153	42	18	12
134	147	35	19	15
137	141	32	18	18
138	130	30	16	21
136	129	26	10	24
138	127	26	9	27
135	123	25	6	30

Table 2. Different organic dyed solar cells in which acetic acid 4-6 % was mixed with the Ti.

Blue Flower	Hibiscus	Blackberry	Pomegranate	Time min
147	145	103	212	0
110	88	114	182	3
88	58	124	180	6
106	39	125	162	9
98	49	117	152	12
92	48	123	139	15
86	56	110	127	18
78	29	114	115	21
81	35	120	116	24
75	41	127	112	27
71	47	125	105	30

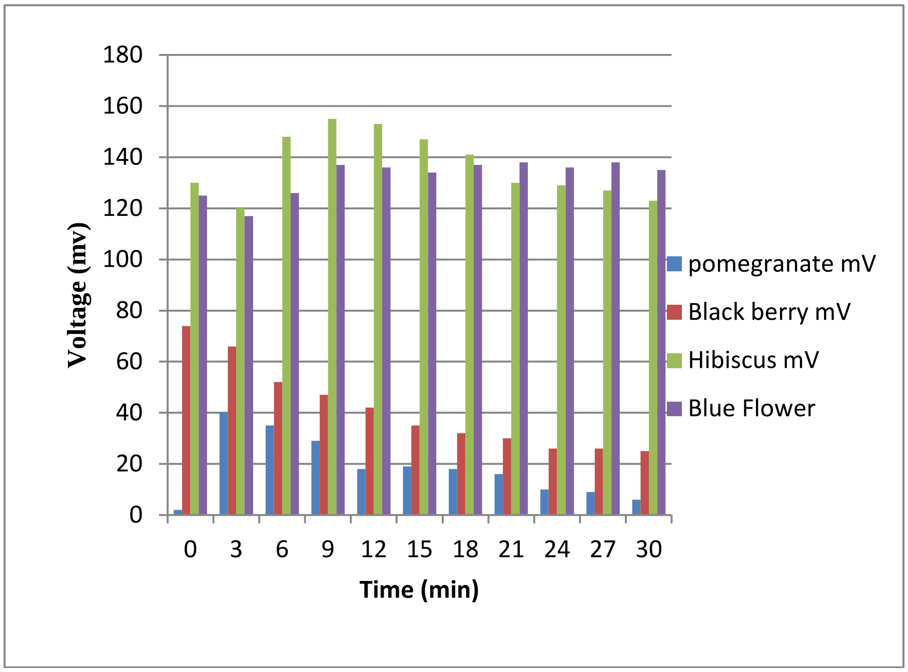

Figure 8. The different voltages generated in a time span of 30 minutes using in which Nitric acid was mixed with the TiO_2.

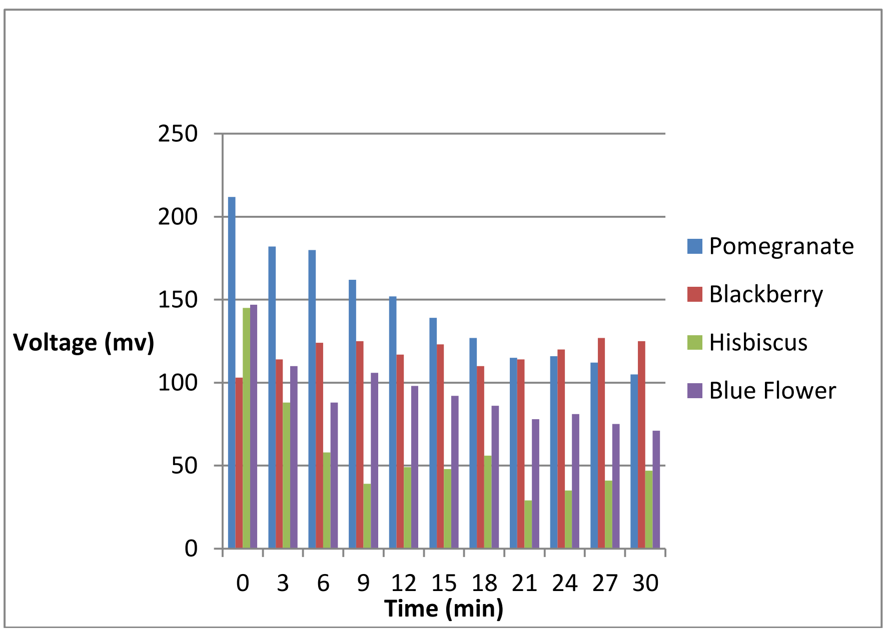

Figure 9. The different voltages generated in a time span of 30 minutes using in which acetic acid 4-6 % was mixed with the TiO_2.

Active Carbon from Date Stones for Phenol Oxidation in Trickle Bed Reactor, Experimental and Kinetic Study

Wadood T. Mohammed
Assistant Professor
Engineering College - Baghdad University
E-mail: dr.wadood@yahoo.com

ABSTRACT

The catalytic wet air oxidation (CWAO) of phenol has been studied in a trickle bed reactor using active carbon prepared from date stones as catalyst by ferric and zinc chloride activation (FAC and ZAC). The activated carbons were characterized by measuring their surface area and adsorption capacity besides conventional properties, and then checked for CWAO using a trickle bed reactor operating at different conditions (i.e. pH, gas flow rate, LHSV, temperature and oxygen partial pressure). The results showed that the active carbon (FAC and ZAC), without any active metal supported, gives the highest phenol conversion.

The reaction network proposed accounts for all detected intermediate products of phenol oxidation that composed by several consecutive and parallel reactions. The parameters of the model estimated using experimental data obtained from a continuous trickle bed reactor at different temperatures (120-160 °C) and oxygen partial pressures (8-12 bar). Simple power law as well as Langmuir-Hinshelwood (L-H) expressions accounting for the adsorption effects were checked in the modeling of the reaction network. A non-linear multi-parameter estimation approach was used to simultaneously evaluate the high number of model parameters. Approach by simple power law only succeeds in fitting phenol disappearance. Instead, when L-H expressions are incorporated for the intermediate reaction steps, the model accurately describes all the experimental concentration profiles, giving mean deviations below 10%.

Key words: oxidation, trickle bed, phenol, wastewater, catalytic wet air oxidation.

اكسدة الفينول في مفاعل سيحي باستخدام الكاربون المنشط المحضر من نوى التمر: دراسة عملية وحركية

أ.م.د. ودود طاهر محمد
كلية الهندسة – جامعة بغداد

الخلاصة

تم استخدام الاكسدة الرطبة بوجود العامل المساعد في اكسدة الفينول في مفاعل سيحي باستخدام الكاربون المنشط كعامل مساعد والذي تم تحضيره من نوى التمر باستخدام كلوريد الحديد والزنك كمنشطات (ZAC, FAC).

تم اجراء عدة فحوصات على الكاربون المنشط المحضر منها المساحة السطحية وسعة الامتزاز بالاضافة الى الفحوصات التقليدية. ثم تم اختبار العامل المساعد في تقنية الاكسدة الرطبة للفينول تحت ظروف مختلفة (منها درجة الحامضية pH ومعدل جريان الغاز ومعدل جريان السائل ودرجة الحرارة وضغط الاوكسجين الجزيئي). اظهرت النتائج ان الكاربون المنشط (ZAC, FAC) وبدون اي مادة منشطة اضافية اعطت نسبة تحول للفينول كبيرة جداً.

شبكة التفاعلات المقترحة من خلال المركبات الوسطية الناتجة من اكسدة الفينول تضمنت بعض التفاعلات المتتالية والتي جرت آنياً. تم ايجاد معاملات الموديل باستخدام البيانات العملية التي تم الحصول عليها من المفاعل السيحي المستمر تحت ظروف درجة حرارة (120-160 °C) وضغط الاوكسجين الجزيئي (8-12 bar). قانون الاس البسيط وعلاقة

Lanymuir-Hinshelwood قد استخدمت في ايجاد تأثير الامتزاز على شبكة التفاعلات. تقنية التخمين غير الخطية لعدة متغيرات قد استخدمت لايجاد العديد من المتغيرات آنياً. وقد وجد ان قانون الاس البسيط نجح في وصف تحول الفينول بينما علاقة (L-H) مع قانون الاس وصفت التفاعلات الوسطية بنجاح ومعدل انحراف اقل من 10%.

1. INTRODUCTION

Recently, increasingly stringent regulations require ever more treatment of industrial effluents to generate better quality product waters that can be more easily reused or disposed of without negative effects to the environment.

A wide range of treatment technologies is being developed and optimized for many applications in different industries. In the last few years, catalytic wet air oxidation (CWAO) represents an interesting technique to treat wastewater pollution. CWAO uses molecular oxygen as oxidizing agent and operates commonly at temperatures of 403-523 K and pressures of 10-50 atm [**Santiago, et al., 2005, Quintanilla, et al., 2007**].

Trickle bed reactors (TBR), which are catalytic packed fixed-bed tubular devices traversed vertically downwards by a gas-liquid stream, are used in different industrially important three-phase catalytic reactions such as in wastewater treatment, in petroleum (hydrodesulfurization, hydro-denitrogenation, etc.), and different chemical areas (hydrogenation, reactive animation, liquid phase oxidation, etc.), in biochemical, and electrochemical processing [**Nigam, et al., 2002**].

In view of the importance of the gas-liquid mass transfer resistance, Tukac, et al., 2001, have experimentally studied the effect of catalyst wetting for phenol CWAO and concluded that incomplete wetting facilitates oxygen transfer through direct contact between gas and solid. Their results are, however, in contrast with simulations of **Larachi, et al., 2001**, and **Iliuata and Larachi, 2001**, showing that complete wetting is more advantageous. This discrepancy is caused by the fact that typical CWAO operating conditions fall in the transition region between gas-limited and liquid-limited reactant. Besides catalyst wetting, internal diffusion limitations can also significantly affect reactor performance.

Because of its unique properties, activated carbon (AC) has been extensively used not only as an adsorbent but also as a catalyst support or even a direct catalyst [**Rodriguez-Reinoso, 1998**]. In particular, AC has often been used as a support for active metals dedicated to CWAO [**Hu, et al., 1999, Trawczynski, 2003, and Gomes, et al., 2003**]. It is also well known that AC alone can perform as true catalyst for several reactions [Coughlin, 1969, Pereira, et al., 2000]. However, the potential of AC, in the absence of an active metal, as direct catalytic material for CWAO has only been recently proved for the destruction of phenol and other bioxenotic organic compounds [**Fortuny, et al., 1998, Sautos, et al., 2002**]. It is noticeable that it performs better than other supported catalysts based on transition metals [**Matatov-Meytal, and Sheintuch, 1998**]. This better performance could be due to the phenol adsorption capacity of the AC that may enhance the oxidation environment conditions. Nevertheless, the performance of different ACs can be significantly different [**Fortuny, et al., 1999**], which strongly suggests that not only adsorption but also other specific characteristics of the ACs affect their behavior in CWAO. In all the above studies using AC, the only compound tested was phenol and less attention was devoted to other reluctant organic compounds, even using metal supported catalyst [**Suarez-Ojeda, 2005**].

Kinetic studies of CWAO over AC are very scarce in the literature [**Eftaxias, et al., 2005**]. Some oxidation tests have been carried out in batch reactors with its characteristically high liquid to solid (catalyst) ratio. In the case of phenol and phenolic compounds that exhibit a high polymerization potential, fast catalyst deactivation occurred in batch oxidation. This was most likely due to the formation of condensation products in the liquid phase and their subsequent desorption on the AC surface [**Stuber, et al., 2001**]. Fixed bed reactors (FBR), and particularly trickle bed reactors, providing a low liquid-to-solid ratio have therefore been adopted as a suitable solution [**Maugans and Akgerman, 2003**]. However, kinetics obtained in batch systems cannot be successfully used for TBR design and almost no information is available for the latter operation regime.

Hence, to properly design and operate industrial CWAO units, the kinetics and catalytic performance of AC need to be found in continuous reactor system.

The aim of this work was to prepare activated carbon from date stones by ferric chloride activation (FAC) and zinc chloride activation (ZAC) and examine them as catalysts for oxidation of phenol in small-scale TBR at different operating conditions (i.e. feed solution pH, gas flow rate, LHSV, temperature and oxygen partial pressure). It was an aim also to develop a realistic kinetic model to meet the process in a wide range of oxygen partial pressure and temperature.

2. KINETIC MODELING

2.1 Reactor Mass Balance

The small-scale TBR used for the kinetic study was modeled according to the following assumptions:

- Absence of mass transfer limitations.
- Isothermal and isobaric operation.
- Constant oxygen partial pressure throughout the reactor.
- Ideal plug flow to describe TBR behavior [**Froment, et al., 1999**].

Then, the one-dimensional model can be written in terms of space-time in the following way:

$$\frac{dC}{d\tau} = R\rho_1 \qquad (1)$$

Where C is the concentration vector, τ the space-time (τ = catalyst mass / liquid mass flow rate), R the net production rate vector and ρ_1 is the liquid density, supposed to be constant during the experiment. Each component of R corresponds to the net production rates of the respective species.

2.2 Kinetics Equations

2.2.1 Power law expressions

Fortuny et al., 1999, described phenol destruction from the same experimental data set using a simple power law expression. Therefore, it seemed reasonable to extend the kinetic modeling to the rest of the reaction network in terms of power law kinetics. The kinetic expression employed was

$$r = K_{ap} C_{ph} \tag{2}$$

With

$$K_{ap} = K'_o \, exp\left(-\frac{E_a}{RT}\right) P_{O_2}^{\beta} \tag{3}$$

β being the reaction order with respect to oxygen.
The above expression for K_{ap} was modified to incorporate the oxygen mole fraction in the liquid phase, x_{o2}^{β}, instead of the partial pressure, leading to

$$K_{ap} = K''_o \, exp\left(-\frac{E_a}{RT}\right) x_{O_2}^{\beta} \tag{4}$$

This was done because the reactions actually take place in the liquid phase. Thus, the solubility of oxygen characterizes the oxygen contribution to the kinetic expression rather than the oxygen partial pressure. Furthermore, the oxygen solubility is not only a function of pressure but also of temperature. Therefore, the oxygen mole fraction in the liquid phase was considered to be more representative. This mole fraction was calculated using Henry law [**Himmelblau, 1960**], this is given by equation,

$$P_{O_2} = H_{O_2} x_{O_2} \tag{5}$$

The rate form expressed by Eq. (4) was extended to the rest of the reactions in the network.

2.2.2 Langmuir-Hinshelwood (L-H) kinetics

The use of L-H expressions was also considered, as they are based on a more realistic description of a heterogeneous catalytic reaction mechanism. The expressions derived assume competitive adsorption of organic species on the same active sites of the catalyst. Then, the rate equation becomes

$$r_i = K_{ap,i} \frac{K_i C_i}{1 + \sum_j K_j C_j} \tag{6}$$

With j running over the adsorbed species. Obviously, the adsorption constant K_i in the nominator corresponds to the reacting compound. The rate parameter K_{ap} is of the same form as in the power law, Eq. (4), whereas the adsorption constant K presents the form

$$K_j = K_{oj} \, exp\left(-\frac{\Delta H_j}{RT}\right) \tag{7}$$

ΔH being the heat of adsorption. This type of L-H expressions is similar with that used in study for CWAO modeling [**Eftaxias, et al., 2001**]. We considered a model where phenol destruction follows simple power law kinetics and the rest of the reactions are better represented by L-H expressions.
In order to fit the model to the experimental data, a non-linear multiparameter estimation approach was followed. Thus, all parameter (i.e. frequency factors, activation energies, reaction orders with respect to oxygen, heat of adsorption and adsorption pre exponential factors) were evaluated simultaneously. The algorithm used in this study is described by **Goffe, et al., 1994**.

3. EXPERIMENTAL WORK

3.1 Materials

Date stones were used as the precursor for the preparation of activated carbon. The date stones were first washed with deionized water to get rid of impurities, dried at 100 °C for 24 h, crushed using disk mill, and sieved to get a function with average particle size of 2 mm. Ferric chloride and zinc chloride have been purchased from Aldrich with purities of 99.9% were used as chemical reagents for activation of date stones.
Analytical grade phenol has been purchased from Aldrich and used without further purification for the preparation of feed solution.

3.2 Preparation of Activated Carbon

Dried stones was well mixed with solution of $ZnCl_2$ or $FeCl_3$ at an impregnation ratio of 0.5 and 1.5 (weight of activator/weight of dried stones) respectively, for 24 h at room temperature. The impregnated samples were next dried at 110 °C until completely dried and stores in a desiccator. For the carbonization of dried impregnated samples, a stainless steel reactor was used. The reactor was sealed at one end and the other end had a removable cover with a hole at the center to allow for the escape of the pyrolysis gases. The reactor was placed in a furnace and heated at constant rate of 10 °C/min and held at carbonization temperature of 710 °C and 75, 30 min for $FeCl_3$ and $ZnCl_2$ carbonization time respectively. Then they were withdrawn from the furnace and allowed to cool. Samples were soaked with 0.1 M HCl solution such that the liquid to solid ratio is 10 ml/g. The mixtures were left overnight at room temperature, and then filtered. The samples were repeatedly washed with distilled water until the pH of filtrate reached 6.5 – 7. Then the samples were dried at 110 °C for 24 h. Finally the samples were stored [**Samar, and Muthanna, 2012, Hameed et al., 2009**].

3.3 Characterization of Activated Carbon

The prepared activated carbons were characterized by selected physical properties including bulk density, surface area (BET) and SEM. Chemical properties including ash and moisture contents, thermogravimetric analysis (TGA) and adsorption capacity. [**ASTM (2000), Adekola and Adegoke, 2005**]

3.3.1 Adsorption capacity test

The maximum adsorption capacity of prepared carbons at optimum conditions were determined by performing adsorption tests in a set of 250 ml Erlenmeyer flasks where 100 ml of phenol solutions with initial concentrations of 100-500 mg/l were placed in these flasks, which contain 0.05 g of prepared activated carbon. Other operating parameters are kept constants from the previous studies that carried out for the same purpose (i.e. agitation speed, temperature, particle size). The amount of phenol adsorbed at equilibrium, q_e (mg/g) was calculated using equation

$$q_e = \frac{(C_o - C_e)V}{W} \tag{8}$$

Where C_o and C_e are initial and equilibrium concentration of phenol (mg/l), respectively, V is the volume of the aqueous phenol solution (l), and W is the weight of activated carbon used (g). The experimental data obtained were fitted to the Langmuir isotherm model, which can be written as

$$q_e = \frac{q_m B C_e}{1 + B C_e} \tag{9}$$

Where q_m is the maximum amount of phenol adsorbed per unit mass of activated carbon (mg/g), C_e is the equilibrium concentration of the phenol (mg/l), and B is the Langmuir constant (l/mg).

3.4 CWAO Experimental Set-up and Procedure

CWAO experiments were carried out in a trickle bed reaction system in co-current gas-liquid down flow. The reactor containing the activated carbon packed bed consists of a stainless steel tube (80 cm long and 1.9 cm inner diameter) and controlled automatically by four sections of 15 cm height steel-jacket heaters. Typically, about 20 – 30 cm height of the activated carbon enclosed between two layers of inert material and the liquid flow rate was then calculated to give a space time of 0.33 – 1 h, i.e. LHSV of 1 to 3 h^{-1}. The air oxidant comes from a high pressure cylinder equipped with a pressure controller to maintain the operating pressure of 8–12 bar. All the experiments were run between 120-160 °C. Stoichiometric excess of gas flow rate was 60% to 100%, initial phenol concentration was 5 g/l.
The phenol and intermediates compounds of the exited samples were determined by HPLC following an analytical procedure described elsewhere [**Fortuny, et al., 1999**]. A complete scheme of the experimental apparatus was shown in **Fig. 1**.

4. RESULTS AND DISCUSSION

4.1 Catalyst

4.1.1. Activated carbon capacity
The maximum phenol uptakes of both FAC and ZAC prepared at optimum conditions have been determined by fitting experimental equilibrium data, calculated from Eq. 8, to the Langmuir isotherm model, Eq. 9, and presented in **Fig. 4**. These results show

that the maximum phenol uptakes of FAC was 290.5 mg/g while 210.0 mg/g for ZAC, this may due to the ability of ferric chloride to produce carbon structure with high portion of micropores content (approximately 10 °A) as compared to that obtained using zinc chloride, due to their smaller ionic radius of the Fe^{+3} ions (55 pm) compared to Zn^{+2} ions (74 pm) as explained by [**Rufford, et al., 2010**].

4.1.2. Activated carbon characterization

The characteristics of FAC and ZAC prepared at optimum conditions mentioned previously were determine and summarized in Table 1. The results of this table show that the surface area of FAC and ZAC are 773.2 and 1049.1 m^2/g respectively. These results are in agreement with those reported by **Samar, and Muthanna, 2012**.
Figures 2 and 3 show the SEM image and the weight loss for both types activated carbon during the TGA carried out between 100 and 900 °C. TGA interpretation is conducted in accordance with that by **Figueriredo et al., 1999**. Which assigns each temperature zone to the desorption of a particular surface group or groups.
The evolution of FAC and ZAC is similar. There is almost no significant loss up to nearly 500 °C. Then there is a zone with marked drop in weight.

4.2 Catalytic Activity Tests
The activated carbons were checked as catalytic matter for the CWAO of phenol for 6 h operation periods. The performance of the activated carbons will be discussed in terms of phenol conversion, x_{ph}, as a measure of the phenol destruction ability as defined by equation

$$x_{ph} = 100 \cdot \frac{C_{ph}^{o} - C_{ph}}{C_{ph}^{o}} \tag{10}$$

Where C_{ph} is the actual measured phenol concentration in the sample and C_{ph}^{o} is the initial phenol concentration. To discuss the depth of oxidation, intermediate compounds measurements will also be used in terms of reduction as described in Eq. (10).

4.2.1 Determination of the most active type

In the first set of experiments, the reaction was carried out at feed solution pH of 7.2, S.E of 80%, LHSV of 1 h^{-1}, temperature of 160 °C, P_{O_2}=12 bar, and initial phenol concentration of 5 g/l.
Figure 5 presents a comparison of the activities of FAC and ZAC catalysts. Both show similar behavior. As found, three different zones can be identified in both cases. In the first zone, from starting up to 1 h, adsorption predominates. This results in an apparent total phenol conversion. Note that for the given liquid flow rate and feed phenol concentration, the length of the adsorption zone at 140 °C is roughly in agreement with the adsorption capacities for FAC and ZAC at 25 °C. This is rather unexpected as the adsorption of phenol on activated carbon is known to be exothermic and the capacity should decrease as the temperature increase. However, further adsorption tests with FAC and ZAC carried out at oxic conditions and temperature of

25, 120 and 160 °C reveal, albeit small, decrease in adsorption capacity at 120 °C. Later, at 160 °C, the adsorption capacity is even restored to that at 25 °C.
Oxidation coupling of phenol can provide a satisfactory explanation of the enhanced adsorption exhibited by FAC and ZAC in CWAO at 140 °C. It is known [**Cooney**, **and Xiz, 1994, Grant, and King, 1990**] that AC catalysts, albeit slowly at room temperature, the formation of phenol dimers that are subsequently irreversibly adsorbed on the AC surface, thus increasing the AC adsorption capacity. Higher temperature and partial oxygen pressure should significantly enhance the rate of oxidative coupling, which could result in an enlargement of the initial adsorption zone during CWAO experiments. Also, HPLC analysis detected low oxidation intermediates during the adsorption period of apparent 100% conversion, which supports the oxidative coupling hypothesis.
Once the adsorption step has reached a pseudo equilibrium state, phenol conversion drops rapidly to achieve an almost constant phenol conversion, which is then maintained to the experiments end. This drop in phenol conversion also marks the starting point for the occurrence of partial oxidation compounds.

4.2.2 Effect of pH
Another factor that could influence the adsorption capacity is the pH. **Fig. 6** shows the pH profiles throughout the test. At the start the pH is about 7.2, close to neutrality, which confirms the absence of any compounds in the effluent. Then the pH began to decrease during the transient state and reached a steady state value. This decrease is caused by the formation of organic acids as oxidation by-products.
The adsorption period occurs at pHs above 6 and a decrease in adsorption capacity has been reported above this pH for several substituted phenols. These compounds can be in undissociated and ionized forms, above a pH of 6 and it is well known that ionized forms of species adsorb less effectively onto AC than their undissociated forms do [Cooney, and xi, 1994]. However, as shown in **Table 1**, the pH in the point of zero charge (pH_{pzc}) of these ACs are 8.0, therefore the AC surface is positively charged during the adsorption period and during the rest of the test; therefore, the ACs surface would exhibit a high affinity for anions or ionized forms of parent compounds.

4.2.3 Effect of gas flow rate
This set of experiments was carried out over FAC catalyst at different gas flow rate, i.e. stoichiometric oxygen excess of (60-100)%, keeping other variables constant at LHSV=1 h^{-1}, temperature=160 °C, oxygen partial pressure=12 bar, and phenol concentration=5 g/l.
Figure 7 illustrates that the higher phenol conversion achieved at 80% S.E as mentioned previously, beyond that decreased with further increasing.
The results above show that an increasing gas flow rate to 80% S.E. causing decreasing in the liquid hold up and liquid film thickness covered catalyst surface, and enhancing oxygen transfer to the liquid phase, and from the liquid phase to the catalyst surface, therefore, leading to high conversion. But increasing S.E. to 100% causes decreasing phenol conversion because of decreasing in the spreading of the liquid film over catalyst, hence, wetting decrease.

4.2.4 Effect of LHSV

Figure 8 presents that the liquid flow rate has a large effect on phenol conversion. As clear from this figure phenol conversion of 87.16% and 82.5% were achieved at LHSV of 2 and 3 h^{-1}. This is due to reduction in the space time of reactant in the reactor (i.e. reducing the time required for phenol reaction with oxygen over the catalyst). Moreover, higher liquid flow rates give greater liquid hold up which evidently decreases the contact of liquid and gas reactants at the catalyst active site, by increasing the film thickness. While at low liquid flow rate with other conditions, the process undergoes more conversion.

4.2.5 Effect of temperature

The influence of temperature on phenol conversion was studied at 120, 140, and 160 °C. **Fig. 9** shows that to about 1 h and at 160 °C, phenol conversion is 100%, while at 140 °C and 120 °C, phenol conversion are 92.7% and 88.6% respectively, after that phenol conversion decrease gradually. The general behavior is, higher conversion is achieved at higher temperature due to the fact that at higher temperature, kinetic constant (rate constant) is favorably affected resulting in increasing in phenol conversion, according to Arrehenius equation:

$$k = A exp\left(\frac{-E_a}{RT}\right) \tag{11}$$

In addition, at high temperature in aqueous solutions, the form in which oxygen participates in chemical reactions is complex. The necessary elevated temperatures can lead to the formation of oxygen radicals, $O^{\cdot}$, which in turn can react with water and oxygen to form peroxide, H_2O_2, and ozone, O_3, so that these four species $O^{\cdot}$, O_2, O_3, and H_2O_2 are all capable of participating in the phenol oxidation.

4.2.6 Effect of oxygen partial pressure

Compared to temperature, oxygen partial pressure has less influence on the phenol conversion. It can be seen from **Fig. 10**. Increasing oxygen partial pressure from 8 bar to 12 bar resulted in an increasing in phenol conversion from 94.1% to 100%.
In general, elevated pressure is required in such process, increasing pressure increases the density of gas and it's solubility in the aqueous solution. To add, an increasing in gas partial pressure provide a lateral push force for the reactants to cover as much surface area over catalyst possible.

4.3 Reaction Pathway

The oxidation routes of the compounds have been established with the help of our experimental data and the classical phenol oxidation pathway of **Eftaxiax, et al., 2006, Santos, et al., 2005, and Quintanilla, et al., 2005**. From previous studies, it can be concluded that phenol is necessary for the formation of 4-HBA. Eventually, phenol can interact with carboxylic acid surface groups to form 4-HBA. The appearance of both 4-HBA and p-benzoquinone in the liquid samples suggests that phenol undergoes two parallel reactions to yield 4-HBA and p-benzoquinone via hydroquinone. This assumption has been tested in terms of kinetic modeling by comparing the prediction of the parallel phenol degradation route with two consecutive schemes as shown

Scheme 1: $C_6H_5OH \rightarrow C_6H_4O_2 \rightarrow C_7H_6O_3$ (12)

Scheme 2: $C_6H_5OH \rightarrow C_7H_6O_3 \rightarrow C_6H_4O_2$ (13)

Scheme 3: $\begin{array}{l} C_6H_5OH \rightarrow C_7H_6O_3 \\ C_6H_5OH \rightarrow C_6H_4O_2 \end{array}$ (14)

Simplified pathway with seven reactions proposed for the catalytic wet air oxidation of phenol over FAC shown in **Fig. 11**. It postulates that maleic acid is mainly coming from the ring opening of 4-HBA, whereas p-benzoquinone break down to formic acid and acetic acid has to follow routes that by pass maleic acid formation. Experimental support comes from a close inspection of the intermediate profiles (Figs. 9b-9g, 10b-10g). The profiles for 160 °C and 12 bar indicate that the maximum of p-benzoquinone and formic acid occur at early space times compared to those of 4-HBA and maleic acid appearing significantly later. Thus the formation of formic acid and maleic acid must be mainly related to the destruction of p-benzoquinone and 4-HBA, respectively. A direct path from p-benzoquinone to formic acid by passing the formation of maleic acid is consistent with the Devlin and Harris mechanism [**Devlin, Harris, 1984**]. However, acetic acid formation via the decomposition route of maleic acid alone could not account for the high amounts of refractory acetic acid observed. The build-in of a reaction from p-benzoquinone to acetic acid has been necessary to improve the prediction of acetic acid profiles.
The corresponding reaction equations of the reaction network developed here are listed below:

$$C_6H_5OH + CO_2 \xrightarrow{r_1} C_7H_6O_3 \quad (15)$$

$$C_6H_5OH + O_2 \xrightarrow{r_2} C_6H_4O_2 + H_2O \quad (16)$$

$$C_7H_6O_3 + 4O_2 \xrightarrow{r_3} C_4H_4O_4 + 3CO_2 + H_2O \quad (17)$$

$$C_6H_4O_2 + 5O_2 + H_2O \xrightarrow{r_4} CH_2O_2 + C_2H_4O_2 + 3CO_2 \quad (18)$$

$$C_6H_4O_2 + 5O_2 + 2H_2O \xrightarrow{r_5} 4CH_2O_2 + 2CO_2 \quad (19)$$

$$CH_2O_2 + \frac{1}{2}O_2 \xrightarrow{r_6} CO_2 + H_2O \quad (20)$$

$$C_4H_4O_4 + O_2 \xrightarrow{r_7} C_2H_4O_2 + 2CO_2 \quad (21)$$

$$C_4H_4O_4 + O_2 \overset{r_7}{\rightarrow} C_2H_4O_2 + 2CO_2$$

The net destruction or production rates R_j of the involved compounds can then be determined as

$$R_{phenol} = -r_1 - r_2 \qquad (22)$$

$$R_{4-HBAl} = r_1 - r_3 \qquad (23)$$

$$R_{p-benzo.} = r_2 - r_4 - r_5 \qquad (24)$$

$$R_{maleic.} = r_3 - r_7 \qquad (25)$$

$$R_{acetic.} = r_4 + r_7 \qquad (26)$$

$$R_{formic.} = r_4 + 4r_5 - r_6 \qquad (27)$$

4.4 Model Prediction

In this study, the unknown parameters have been optimized by a non-linear regression technique. The reactor equation, Eq. (1), has been numerically solved with a fourth-order Runge-Kutta method to calculate the theoretical outlet phenol and intermediate concentrations ($C^{cal.}$) of the objective function. Testing of different objective functions has shown that the best balanced criterion is to compare experimental and calculated concentrations in terms of absolute errors as given

$$\phi = \sum_{i,n,k} \left| C_{i,n,k}^{exp} - C_{i,n,k}^{cal} \right| \qquad (28)$$

Where the indexes i, n, k run over the component, the experiment and the space time, respectively.

Rate model includes testing the influence of phenol adsorption, a series of optimization runs has been done with the rate model cancelling the contribution of phenol adsorption in the denominator of L-H equations for reaction (3)-(7). With this model, the best data fit has been performed, the objective function progressing significantly to 71 mmol/l. Finally, the block adsorption of either carboxylic acids or only aromatic intermediates has been checked, but in both cases the fit equality deteriorates to that obtained with the simple power law model. Thus, only the best results obtained with the simplified reaction network and rate model are presented that, **Figs. 9a3 – 9g and 10a3 – 10g** compared the model predictions and the experimental phenol and intermediate concentrations. As can be seen in **Fig. 8a3**, calculated phenol shows good agreement with experimental data leading to a very small mean error. The prediction of intermediates is less accurate, but still satisfactory given the complexity of the reaction system studied. Overall, the proposed model matches all data with an acceptable global error.

The parameters optimized are listed in **Tables 2 and 3**. The oxidation reactions of phenol to 4-HBA and p-benzoquinone have activation energies of 80.7 and 70.1 KJ/mol, which lie in the range 65-85 kJ/mol [**Eftaxias, et al., 2005**] observed for kinetically controlled CWAO of phenol over different supported catalysts. For the ring opening reactions of 4-HBA to maleic acid and p-benzoquinone to formic acid, respective value of 78.2 and 53.8 kJ/mol have been obtained. These also close to other reported data over another catalyst.

5. CONCLUSIONS

Ferric chloride and zinc chloride have been used to prepare activated carbons from date stones for removal of phenol from aqueous solutions in a TBR. The maximum phenol uptake of carbons prepared by ferric chloride and zinc chloride activations, as calculated from Langmuir isotherm model, were 290.5 and 210.0 mg/g respectively.
The catalytic performance of a prepared active carbon (FAC and ZAC) and its reaction kinetics (on FAC) were assessed for the CWAO of phenol in a TBR operated under different conditions of temperature and oxygen partial pressure. A temperature of 160 °C, 12 bar of O_2 and space times of about 1 h resulted in phenol destruction about 100%. The main intermediates detected were 4-hydrobenzoic acid, benzoquinone, maleic, formic and acetic acids. The prepared activated carbon (FAC and ZAC) showed a similar or even better catalytic performance than many of the noble metal or transition metal oxide-based catalysts recently developed for the CWAO of phenol.
Although the adsorption of phenol on the active carbon was seen to take place, kinetic analysis showed that both the simple power law model and more mechanistic Langmuir-Hinshelwood models can accurately predict the entire experimental results. The oxidation reactions of phenol to 4-HBA and p-benzoquinone have activation energies of 80.7 and 70.1 kJ/mol.

6. REFERENCES

Adekola, F. A., Adegoke, H. I., 2005, Adsorption *of blue dye on activated carbons produced from rice husk, coconut shell, and coconut coirpith*, lfe Journal of science 7, 151-157.

ASTM standard, 2000, *Standard test method for total ash content of activated carbon*. Designation D2866-94.

Cooney Do, Xiz, 1994, *Activated carbon catalyzes reactions of phenolic during liquid-phase adsorption*. AIChE J., 40 (2), 361-4.

Coughlin, R. W., 1969, *Carbon as Adsorbent and Catalyst*, Ind. Eng. Chem. Prod. Res. Dev. 8, 12.

Devlin H. R., Harris J., 1984, *Mechanism of the oxidation of aqueous phenol with dissolved oxygen*, Ind. Eng. Chem. Res. 23, 387.

Eftaxias A., Font J., Fortuny A., Fabregat A., and Stubar F., 2006, *Catalytic wet air oxidation of phenol over active carbon catalyst Global kinetic modeling using simulated annealing*, Applied Catalysis B: Environmental 67, 12-23.

Eftaxias A., Font, J., Fortuny, A., Fabregat, A., Stuber, F., 2005, *Kinetics of phenol oxidation in a trickle bed reactor over active carbon catalyst*, J. Chem. Technol. Biotechnol. 80, 677-687.

Eftaxias, A., Font, J., fortuny, A., Giralt, J., Fabregat, A., Stuber, F., 2001, *Kinetic modeling of catalytic wet air oxidation of phenol by simulated annealing*, Applied Catalysis B: Environmental 33, 175-190.

Fortuny, A., Bengoa, C., Font, J., Castells, F., Fabregat, A., 1999, *Water pollution abatement by catalytic wet air oxidation in a trickle bed reactor*, Catal. Today 53, 107.

Fortuny, A., Font, J., Fabregat, A., 1998, *Wet air oxidation of phenol using active carbon as catalyst*, Applied Catalysis B: 19, 165.

Fortuny, A., Miro, C., Font, J., Fabregat, A., 1999, *Three phase reactors for environmental remediation: catalytic wet oxidation of phenol using active carbon*, Catal. Today 48, 323.

Froment, G. F., Bischoff, K. B., 1990, *Chemical Reactor Analysis and Design*, Wiley, New York, USA, 403.

Goffe, W. L., Ferrier, G. D., Rogers, J., 1994, *Global optimization of statistical functions with simulated annealing*, Econometrics 60, 65.

Gomes, H. T., Figueiredo, J. L., Faria, J. L., 2003, *Metallic Oxides: Filling the Gap between Catalysis and Surface Science*, Catal. Today 75, 23.

Grant T. M., King C. J., 1990, *Mechanism of irreversible adsorption of phenolic compounds by activated carbons*, Ind Eng. Chem. Res., 29, 264-71.

Hameed, B. H., Salman, S. M., Ahmad, A. L., 2009, *Adsorption isotherm and kinetic modeling of 2, 4-D-Pesticide on activated carbon derived from date stones*, Journal of Hazardous Materials 163,121-126.

Himmelblau, D. M., 1960, *solubilities of inert gases in water*, J. Chem. Eng. Data 5, 10.

Hu, X., Lei, L., Chu, H. P., Yue, P. L., 1999, *Copper/activated carbon as catalyst for organic wastewater treatment*, Carbon 37, 631.

Larachi, F., lliuta, I., Belkacemi, I., 2001, *Catalytic wet air oxidation with Deactivating catalyst Analysis of Fixed and sparged Three phase Reactors*, Catalysis Today 64, 309-320.

Larachi, F., lliuta, I., Belkacemi, I., 2001, *Wet Air Oxidation Solid Catalysis Analysis of Fixed and Sparged Three Phase Reactors*, Chem. Eng. Process. 40, 175-185.

Matatov-Meytal, Y., Sheintuch, M., 1998, *Catalytic Abatement of Water Pollutants*, Ind. Eng. Chem. Res. 37, 309.

Maugans, C. B., and Akgerman A., 2003, *Catalytic wet oxidation of phenol in a trickle bed reactor over a Pt/Tio_2 catalyst*. Wat. Res. 37: 319-328.

Muthanna J., and Samar K., 2013, *Adsorption of P-Chlorophenol onto microporous activated carbon from Albizia lebbeck seed pods by one-step microwave assisted activation*, Journal of Analytical and Applied Pyrolysis 100, 253-260.

Nigam, K. D. P., Iliuta, I., Larachi, F., 2002, *Liquid back-mixing and mass transfer effects in trickle-bed reactors filled with porous catalyst particles*, Chemical Engineering and Processing 41, 365-371.

Pereira, M. F. R., Orfao, J. J. M., Figueiredo, J. L., 2000, *Oxidative dehydrogenation of ethylbenzene on activated carbon catalysts 2.Kinetic modelling*, Appl. Catal. A, 19, 643.

Quintanilla A., Casas J. A., Zazo J. A., Mohedano A. F., Rodriguez J. J., 2006, *Wet air oxidation of phenol at mild conditions with a Fe/activated carbon catalyst*, Appl. Catal. B: Environ. 62, 115.

Quintanilla, A., Casas, J. A., Rodriguez, J. J., 2007, *Catalytic wet air oxidation of phenol with modified activated carbons and Fe/activated carbon catalysts*. Applied catalysis B: Environmental 76, 135-145.

Rodriguez-Reinoso, F., 1998, *The role of carbon materials in heterogeneous catalysis*, Carbon 36, 159.
Rufford, T. E., Hulicova-Jurcakova, D.,

Zhu, Z., Lu, G. Q., 2010, *A comparative study of chemical treatment by FeCl3, MgCl2, and ZnCl2 on microstructure, surface chemistry, and double-layer capacitance of carbons from waste biomass*, Journal of materials Research 25, 1451-1459.

Samar K., Muthanna J., 2012, *Optimization of preparation conditions for activated carbons from date stones using response surface methodology*. Powder technology 224, 101-108.

Santiago, M., Stuber, F., Fortuny, A., Fabregat, A., Font, J., 2005, *Modified activated carbons for catalytic wet air oxidation of phenol*, Carbon 43, 2134-2145.

Santos A., Yustos P., Cordero T., Gomis S., Rodriguez S., Garcia-Ochoa F., 2005, *Catalytic wet oxidation of phenol on active carbon: stability, phenol conversion and mineralization*, Catal. Today 102-103, 213.

Santos, A., Yustos, P., Gomis, S., Garcia-Ochoa, F., 2002, Proceedings of the Ninth Mediterranean Conference of Chemical Engineering, Barcelona, November, 91.

Stuber F., Polaert I., Delmas H., Font J., Fortuny A., and Fabregat A., 2001, *Catalytic wet air oxidation of phenol using active carbon*, J. Chem. Technol. Biotechnol, 76, 743-751.

Suarez-Ojeda, M., Stuber, F., Fortuny, A., Fabregat, A., Carrera, M., Font, J., 2005, *Catalytic wet air oxidation of substituted phenols using activated carbon as catalyst*, Applied catalysis B: Environment 58, 105-114.

Trawczynski, J., 2003, *Noble metals supported on carbon black composites as catalysts for the wet-air oxidation of phenol*, Carbon 41, 1515.

Tukac, V., Vokal, J., and Hanika, J., 2001, *Mass Transfer limited wet oxidation of phenol*, J. Chem. Techn. Biotechnol. 76, 506-510.

NOMENCLATURE

A = Preexponential factor, h^{-1}
B = Langmuir constant, L/mg
C = Compounds concentration, mol/L
C_e = Equilibrium concentration of phenol, mg/L
C_o = Initial concentration of phenol, mg/L
E_a = Activation energy, J/mol
H = Enthalpy of adsorption, J/mol
K = Adsorption preexponential factor, L/mol
k = Reaction rate constant, h^{-1}
K_{ap}= Rate parameter, reaction dependent unit
K_o' = Preexponential factor, reaction dependent unit
K_o'' = Preexponential factor, reaction dependent unit
P = Oxygen partial pressure, bar
q_e = Amount of phenol adsorbed per unit mass of activated carbon at equilibrium, mg/g
q_m = Maximum amount of phenol adsorbed per unit mass of activated carbon, mg/g
R = Net reaction rate, mol /kg_{cat} h
r = Reaction rate, $mol\, kg_{cat}^{-1}$ h^{-1}
R = Universal gas constant (8.314 J/mol K)
T = Temperature, ^oC
V = Volume of aqueous solution, L
W = Weight of activated carbon, g
x = Molar fraction of dissolved oxygen, dimensionless
β = Oxygen order of reaction, dimensionless
ρ_1 = liquid density, kg/L
τ = Space-time, (kg_{cat} /kg_L) *h*

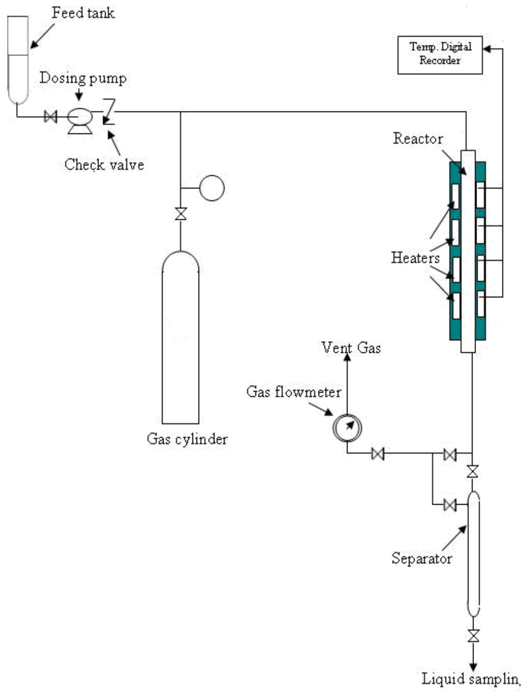

Figure 1 Experimental Apparatus

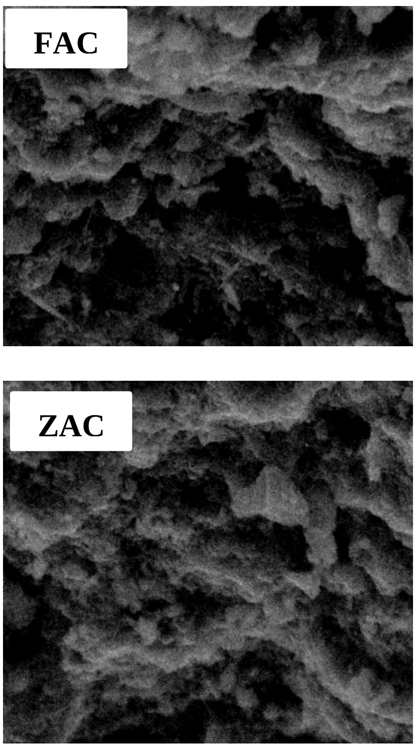

Figure 2. SEM Image

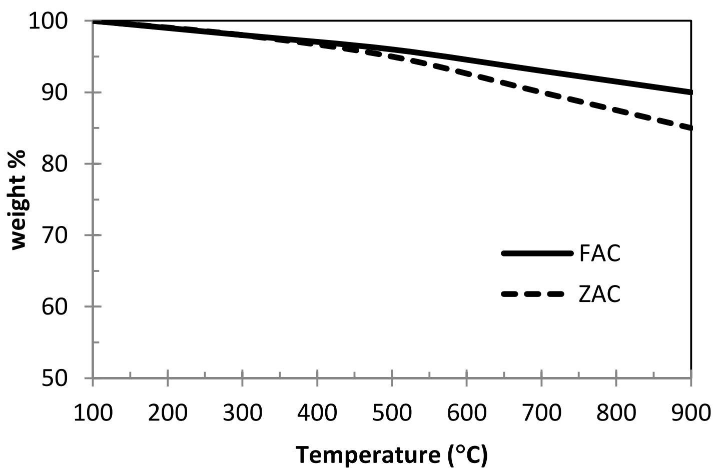

Figure 3. TGA Profiles of the Activated Carbon Samples

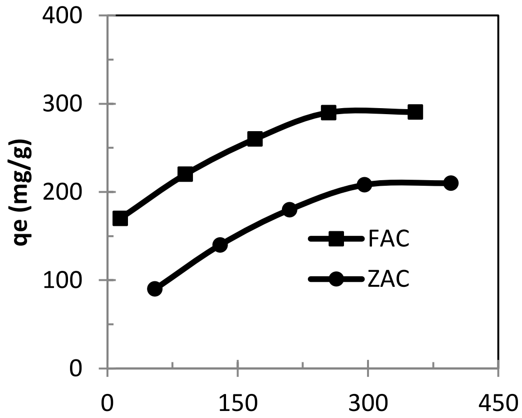

Figure 4 Equilibrium isotherm of phenol adsorption on activated carbon samples correlated with Langmuir equation

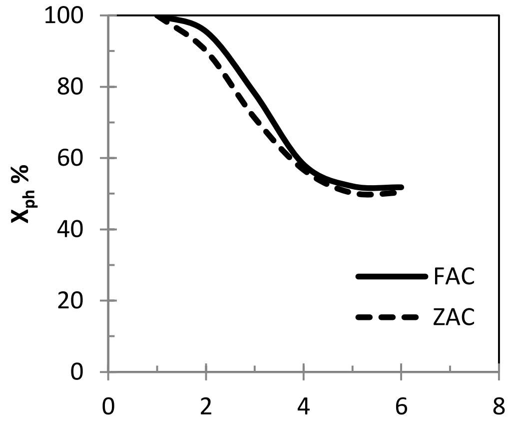

Figure 5 Evolution of phenol conversion during CWAO using FAC and ZAC

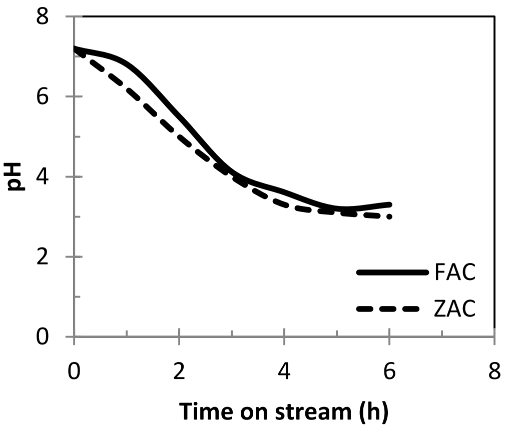

Figure 6 Evolution of process pH during CWAO using FAC and ZAC

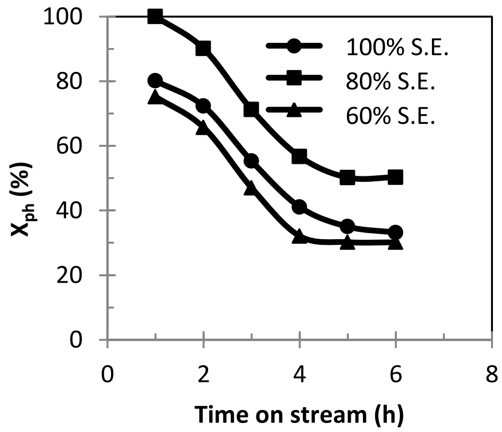

Figure 7 Evolution of phenol conversion during CWAO using FAC catalyst at different gas flow rate (pH=7.2, LHSV= $1h^{-1}$, T= 160°C, P_{O_2}= 12 bar).

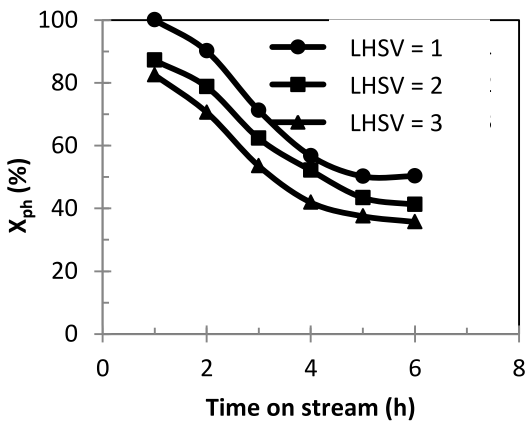

Figure 8 Evolution of phenol conversion during CWAO using FAC catalyst at different LHSV (pH=7.2, S.E.= 80%, T= 160°C, P_{O_2}= 12 bar

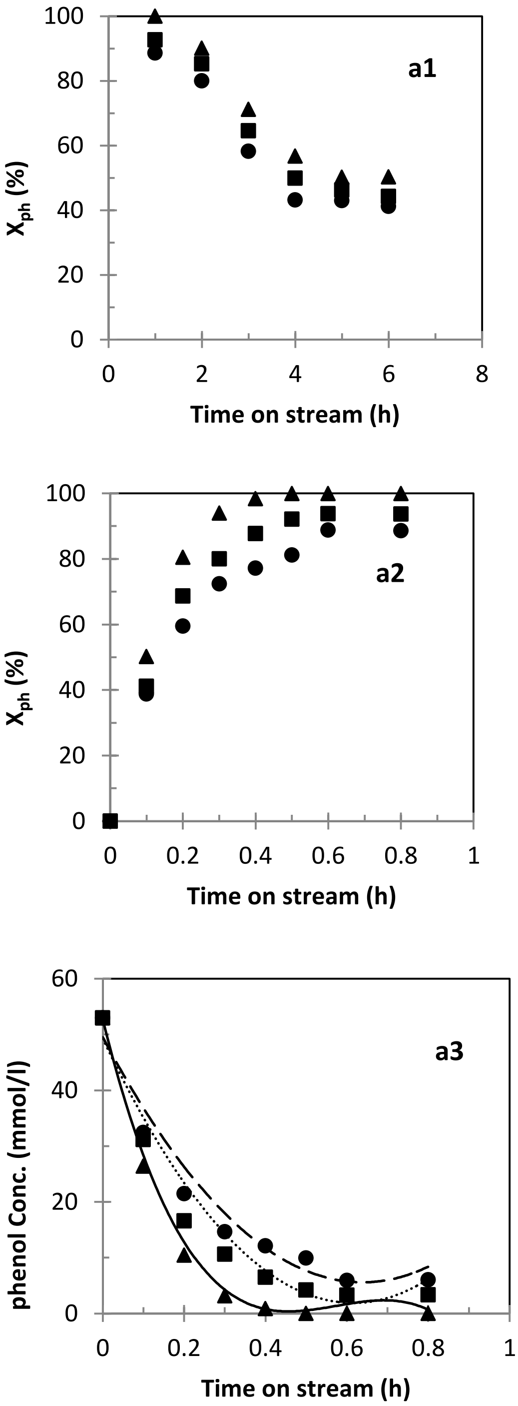

Figure 9a. Effect of temperature on phenol oxidation (FAC, pH=7.2, S.E.= 80%, LHSV= 1 h^{-1}, P_{O_2}= 12 bar, C_{ph}=5 g/l) Experimental Data ●120 **°C,** ■ 140 **°C,** ▲ 160 **°C**; Solid Line predictions Rate Model

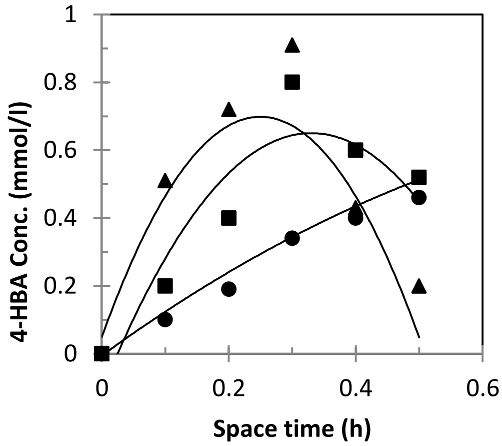

Figure 9b Concentration profiles of 4-Hydroxybenzoic acid (4-HBA)(FAC, pH=7.2, S.E.= 80%, LHSV= 1 h^{-1}, P_{O_2}= 12 bar, C_{ph}=5 g/l), Experimental Data ●120 **°C,** ■ 140 **°C,** ▲ 160 **°C**; Solid Line predictions Rate Model

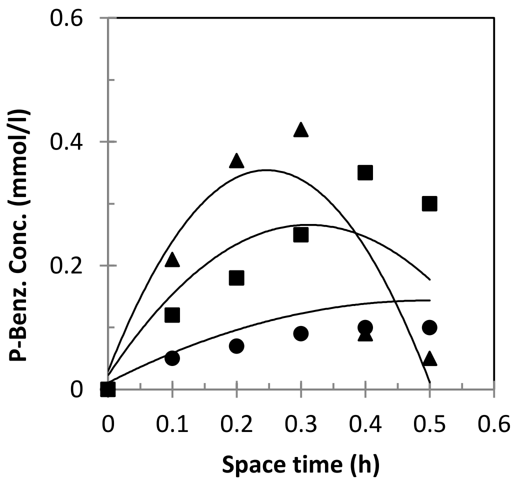

Figure 9c Concentration profiles of P-Benzoquinone (FAC, pH=7.2, S.E.= 80%, LHSV= 1 h^{-1}, P_{O_2}= 12 bar, C_{ph}=5 g/l), Experimental Data ●120 °C, ■ 140 °C, ▲ 160 °C; Solid Line predictions Rate Model

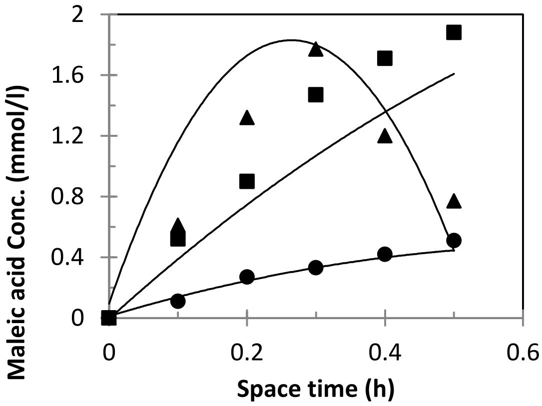

Figure 9d Concentration profiles of maleic acid, (FAC, pH=7.2, S.E.= 80%, LHSV= 1 h^{-1}, P_{O_2}= 12 bar, C_{ph}=5 g/l) , Experimental Data ●120 °C, ■ 140 °C, ▲ 160 °C; Solid Line predictions Rate Model

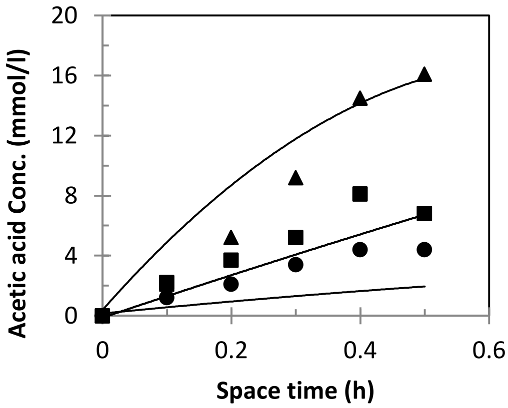

Figure 9e Concentration profiles of acetic acid (FAC, pH=7.2, S.E.= 80%, LHSV= 1 h^{-1}, P_{O_2}= 12 bar, C_{ph}=5 g/l), Experimental Data ●120 °C, ■ 140 °C, ▲ 160 °C; Solid Line predictions Rate

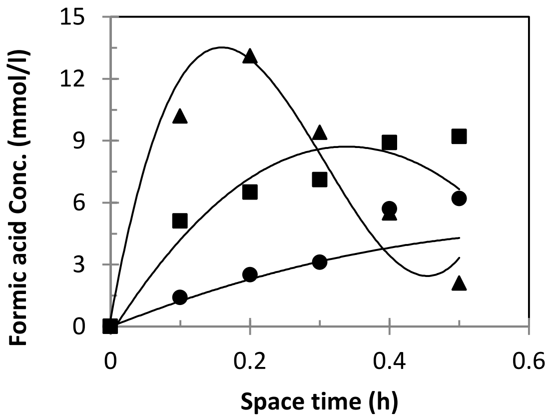

Figure 9g Concentration profiles of formic acid (FAC, pH=7.2, S.E.= 80%, LHSV= 1 h^{-1}, P_{O_2}= 12 bar, C_{ph}=5 g/l), Experimental Data ●120 °C, ■ 140 °C, ▲ 160 °C; Solid Line predictions Rate

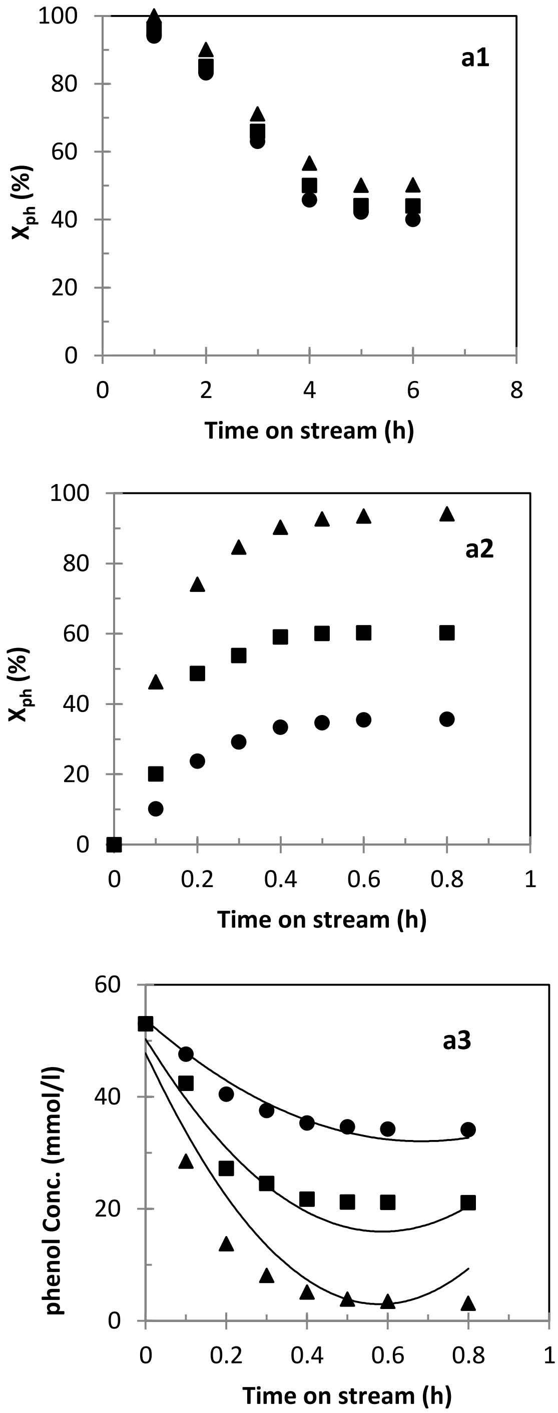

Figure 10a Effect of oxygen partial pressure on phenol oxidation, (FAC, pH=7.2, S.E.= 80%, LHSV= 1 h^{-1}, T=160 °C, C_{ph}=5 g/l), Experimental Data ●8 bar, ■ 10 bar, ▲ 12 bar; Solid Line predictions Rate Model

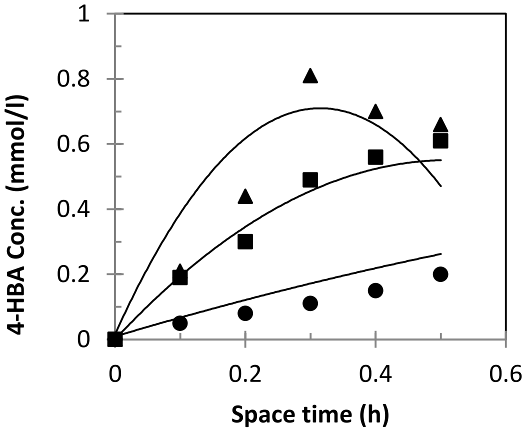

Figure 10b Concentration profiles of 4-Hydroxybenzoic acid (4-HBA), (FAC, pH=7.2, S.E.= 80%, LHSV= 1 h^{-1}, T=160 °C, C_{ph}=5 g/l), Experimental Data ●8 bar, ■ 10 bar, ▲ 12 bar; Solid Line predictions Rate Model

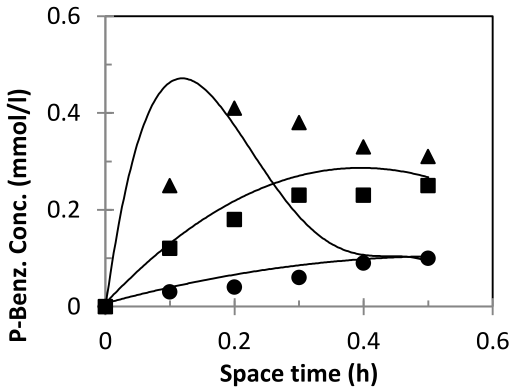

Figure 10c Concentration profiles of P Benzoquinone, (FAC, pH=7.2, S.E.= 80%, LHSV= 1 h-1, T=160 °C, Cph=5 g/l), Experimental Data ●8 bar, ■ 10 bar, ▲ 12 bar; Solid Line predictions Rate Model

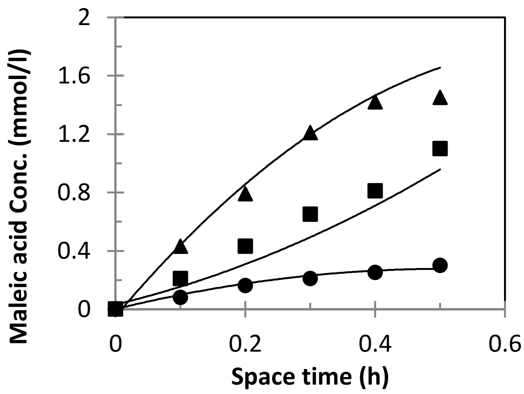

Figure 10d Concentration profiles of maleic acid (FAC, pH=7.2, S.E.= 80%, LHSV= 1 h^{-1}, T=160 °C, C_{ph}=5 g/l), Experimental Data ●8 bar, ■ 10 bar, ▲ 12 bar; Solid Line predictions Rate Model

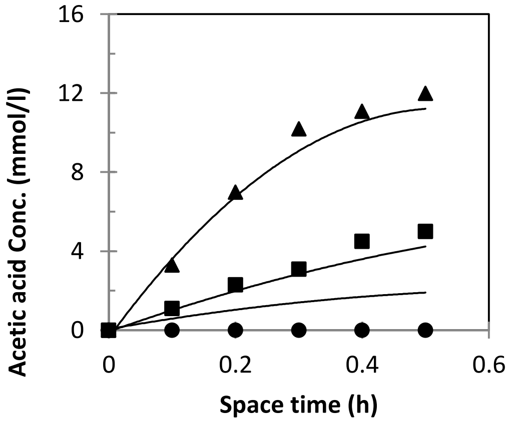

Figure 10e Concentration profiles of acetic acid, (FAC, pH=7.2, S.E.= 80%, LHSV= 1 h^{-1}, T=160 °C, C_{ph}=5 g/l), Experimental Data ●8 bar, ■ 10 bar, ▲ 12 bar; Solid Line predictions Rate Model

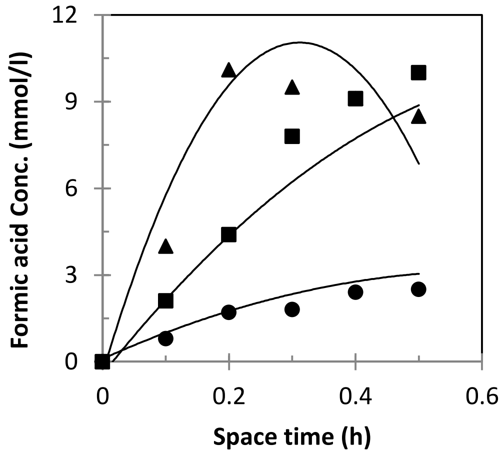

Figure 10g Concentration profiles of formic acid, (FAC, pH=7.2, S.E.= 80%, LHSV= 1 h^{-1}, T=160 °C, C_{ph}=5 g/l), Experimental Data ●8 bar, ■ 10 bar, ▲ 12 bar; Solid Line predictions Rate Model

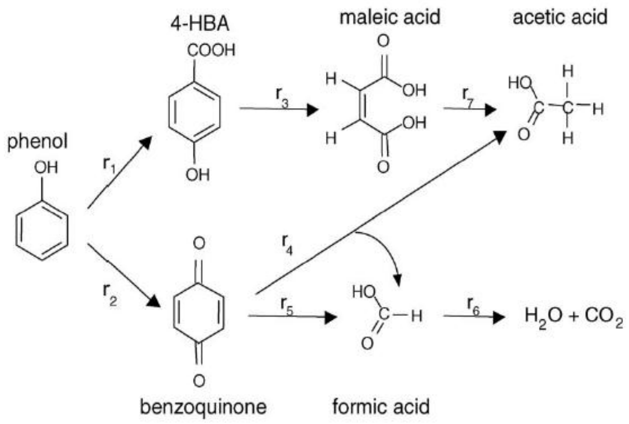

Figure 11 Proposed Reactions Pathway for the CWAO of Phenol over FAC [**Eftaxiax, et al., 2006**]

Table 1 Characteristic of Activated Carbon Samples

Characteristic	**FAC**	**ZAC**
Bulk density g/ml	0.28	0.33
Ash content (%)	6.34	1.85
Moisture content (%)	11.51	9.17
Activated carbon capacity (mg/g)	290.5	210.0
Surface area (m^2/g)	773.2	1049.1
pH_{PZC}	8.0	8.0

Table 2 Frequency factors, activation energies and reaction order obtained with the model and reaction scheme

Rate	**log K_o**	**E_a (KJ/mol)**	**β**
r_1	13.9 ± 0.1	80.7 ± 1	1.00 ± 0.03
r_2	13.2 ± 0.1	70.1 ± 0.8	0.9 ± 0.02
r_3	16.5 ± 0.4	82.0 ± 1	0.91 ± 0.1
r_4	20.1 ± 0.7	115 ± 3	0.62 ± 0.2
r_5	13.2 ± 0.3	55.9 ± 2	0.73 ± 0.1
r_6	15.6 ± 0.4	64.7 ± 2	0.76 ± 0.1
r_7	13.9 ± 0.1	56.7 ± 3	0.64 ± 0.1

Table 3 Adsorption parameters for intermediates compounds

Compound adsorbed	**log K_o (L/mmol)**	**ΔH (KJ/mol)**
4-HBA	0.15 ± 0.02	-1.81 ± 0.4
P-Benzoquinone	1.52 ± 0.1	-1.85 ± 0.2
Maleic acid	-1.51 ± 0.1	-2.58 ± 0.5
Acetic acid	1.58 ± 0.1	-0.81 ± 0.5
Formic acid	0.92 ± 0.05	-3.1 ± 0.4

قائمة المحتويات

القسم العربي:

أثر المنظومة الخدمية في تطورات الشكل المعماري

أ.د. بهجت رشاد شاهين
قسم الهندسة المعمارية
جامعة بغداد/ كلية الهندسة
bahjatsha@yahoo.com

أ.م. د. علي مجبل العذاري
قسم الهندسة المعمارية
الجامعة التكنولوجية
ali_ethari@yahoo.com

م. د. أسامة عبد المنعم خريبط
قسم الهندسة المعمارية
جامعة بغداد/ كلية الهندسة
eng_usama_oat@yahoo.com

مستخلص البحث

تشكّل العمارة خلاصات فكرية ومنظومات متعددة تتغير مكنوناتها وهذا ما يميزها عن باقي العلوم. إذ تعد العمارة طريقة للحياة والقيم عبر نتاجاتها التعبيرية التي تظهرها منظوماتها المرتكزة على خصائصها التكوينية والتكنولوجية في الشكل والمنشأ والخدمات والمواد فضلاً عن أشكالها المعنوية، وكل ذلك مقرون بوسائل وتقنيات بشكل لا يجعل من العمارة مجرد وسيلة لتحقيق هدف ما. وإذ تؤسس الأشكال نظاماً متكاملاً حيث لا تنطلق عملية الخلق والإبداع المعماري من فراغ بل تتبع قاعدة تصورية تنبثق منها حالة جديدة لنتاج معماري جديد. وتركزّت مشكلة البحث العامة في قلة الدراسات الفكرية والتطبيقية الشاملة والموجهة نحو تأثير المنظومات الخدمية في تكوين وتعبيرية لبنية الشكل المعماري بشكل عام. فضلاً عن عدم وجود تصور واضح عن الطبيعة التعبيرية المتحققة في نمط معالجة المنظومات الخدمية للشكل المعماري.

بالتالي يهدف البحث بشكل عام إلى تشخيص تأثير المنظومات الخدمية كمتغير أساس في إظهار الإبداع الشكلي، وتحديد مفردات هذا التأثير في العمارة وبما يخص تحقيقه من خلال نمط معالجة العناصر الخدمية للشكل المعماري. حيث يفترض البحث إلى وجود أثر مباشر للمنظومة الخدمية في النتاج المعماري بحيث تحمل تلك المنظومة وظيفتيّن أساسيتين تكمن الأول في توفير الجانب العملي والأدائي بينما تتركز الثانية بتوفير الإمكانيات التعبيرية للشكل المعماري الناتج، وتلك العلاقة كان لها الأثر البالغ في صياغة نمط العمارة على المدار الزمني.

الخصائص التكوينية، التكامل المنظوماتي، المنظومات الخدمية، الإبداع الشكلي، الوسائل والتقنيات المعمارية، الإمكانيات التعبيرية.

The Effect of Services system in Architectural form developments

Prof. Dr. Bahjat Rashad Shaheen
Architectural department
Baghdad University/college of engineering
bahjatsha@yahoo.com

Ass. Prof. Dr. Ali Mejbel Al-Ethari
Architectural department
University of Technology
ali_ethari@yahoo.com

Lec. Usama Abdul-Mun'emt
Architectural department
Baghdad University/ college of engineering
eng_usama_oat@yahoo.com

Abstract

Architecture forms theoretical summaries and multi systems that have the essence of change, and that what distinguishes Architecture from other sciences and their systems.

Architecture means way of life via its expressional products and that appears through its systems. These systems are based on formative and technological properties in form, structure, services and materials as well as their moral forms.

All these are associated with techniques and facilities in order to establish integrated system. Architectural creation does not come from void but it depends on a conception base to create a new condition for creative architectural product.

The general problem of the research concentrated on limited theoretical and practical studies, related to the effect of the technological systems integration on the expressional sides of architectural form in general. Besides, the absence of clear concept about the expressional aim in treatment type of technological systems of architectural form.

Therefore, the research, in general, aimed to diagnose the effect of technology as a main factor to reveal the formal expression and creation, and to define items of architectural expression, and correlation with its implementation by mechanical treatment for architectural form.

So, the research assumes the presence of direct expressional effects in structural and mechanical systems on the architectural form. Each of these systems has two functions: the first one is supplying the practical role, while the second function concentrated on the implementation of the expressional possibilities of architectural product form.

Formative properties, integrated system, Service system, formative creation, Architectural techniques and means, expressional possibilities.

المقدمة

يمثل التطور التكنولوجي المؤثر الأبرز في التصميم المعماري والركن الأساسي من أركان تطور المجتمعات، حيث يعد ارتباط التصميم المعماري بالتطورات المتلاحقة للتكنولوجيا من أبرز سمات عصرنا بكل ما تحمله تلك المؤثرات من تعدد في مرتكزاتها ومنظوماتها. حيث أضحت منظومات المبنى (المنشئية، الخدمية، الداخلية،...الخ) عنصراً محورياً ضمن عملية الإبداع للعمارة والذي ينعكس على تبلور التشكيل المعماري لدى إفرازه لتلك المنظومات المتداخلة، فيكتسب التشكيل المعماري عندها أفكاراً إبداعية من شأنها تلبية الاحتياجات المختلفة لكل من الأدائية الوظيفية والمتطلبات التعبيرية. ومن هنا تبرز أهمية المنظومة الخدمية باعتبارها واحدة من تلك المنظومات الرئيسة والتي يفترض مراعاة عناصرها تعبيرياً خاصةً مع إمكانيات إظهار تلك العناصر، وقد اعتاد الأنسان تزيين وسائل حياته وأدواته. إذ تأثر التصميم المعماري بالتطور التكنولوجي الكبير لعناصر المنظومة الخدمية، حيث عمد المصممون المعماريون ومهندسو الخدمات إلى استعمال أحدث التقنيات المتوفرة في تصميم وتنفيذ النتاج المعماري، التي تعتمد أساساً على التكنولوجيا في كافة جوانبها الشكلية والمنشئية والمعلوماتية لذلك إمتلكت التكنولوجيا الخدماتية أهمية كبيرة في إقرار سمات النتاج المعماري.

1: المنظومات في العمارة:

تعد العمارة أم الفنون فهي التعبير الإبداعي لأبنية تتوفر فيها "ثلاثية فيتروفيوس" وهي عناصر المنفعة والمتانة والجمال، وتلبي حاجات الأنسان المادية والروحية بأوسع المديات وافضل الوسائل المتوفرة في كل زمان بكل إمكانياته المادية والفكرية، وعلى هذا الأساس فقد ارتبطت العمارة بجملة من المنظومات المترابطة بعلاقات تأثيرية متبادلة فيما بينها. [Ackoff,1974,p:13]. حيث يمثل المبنى مجموعة من المكونات التي تمتلك كلاً كاملاً من عدة صفات (بصرية، فضائية، صوتية،...الخ) وكلها يتم تصميمها لكي تعمل بصورة معينة بغية تحقيق الأهداف المرجوة وتخدم مجموعة من الفعاليات، وتلك العمليات والفعاليات تستعيد هويتها عندما يدخل الأنسان والطاقة كمدخلات (Inputs) مع استمرار التغيرات بالمواقع بينهما وهذه الشمولية (Totality) تنظم المتغيرات التي تحدث حولها وبالمقابل تتأثر بوجودها وعملياتها. فيمثل المبنى منظومة تمتلك الصفات التي تساعده على إدامة عملياته بفاعلية اذا تم اعتباره تكوين فيزياوي يحمل الحيوية التي تمكنه من الانطلاق من الكل إلى جميع الأجزاء ويتفاعل معها ومع البيئة المحيطة وهي اهم ما يميز أي منظومة. [Handler,1970,p:23]. وبالتالي يمكن اعتبار المبنى "ككل" يتكون من مجموعة من المنظومات "الأجزاء" والتي تتفاعل مع بعضها بعلاقات حيوية تسعى لتحقيق تكوين متكامل. ويذكر (Bachman)(1)، [Bachman,2003,p:17]. إلى ان الخصائص المشتركة للعناصر المنشئية والميكانيكية والعناصر الأخرى تشير إلى كلمة منظومة بشكل مختلف عن معناها العلمي في تمييز وتصنيف مجموعات العناصر احدهما عن الآخر، فالمنظومة المنشئية على سبيل المثال تشتمل على الجسور والأعمدة والتي من خلالها تعمل على مقاومة القوى والإجهادات ونقل الأحمال من خلال الشبكة المنشئية إلى الأسس وتبقي البناية في حالة من الاستقرار.

أما منظومة الشكل المعماري فتعمل على العزل الوظيفي والبيئي بينما المنظومات الخدمية فهي تحاول إبقاء الشاغلين في حالة من الراحة. بالتالي المنظومة في العمارة تشير إلى المكونات المتشكلة كمجموعة مترابطة من المادة والقوى في المبنى.

وأشارت دراسة (Rush) إلى وجود أربعة منظومات رئيسة للمبنى بشكل عام والتي تشير بوضوح إلى الوظائف الأساسية للمبنى، حيث تشكل تلك المنظومات المبنى ككل [Rush, 1986, p:8]. وهي:

- **منظومة الشكل المعماري.**

---

(1) (**Leonard R. Bachman**): معماري وباحث ألماني متخصص بشؤون المنظومات المعمارية وتكاملاتها، ومن ابرز مؤلفاته (Integrated Buildings) 2003.

- منظومة الشكل المنشئي.
- منظومة الفضاء الداخلي.
- منظومة الخدمات.

ويتم التركيز هنا على منظومتي الشكل المعماري والخدمات بعدها ابرز مكونات المبنى الرئيسية والتي أثرت وبشكل كبير في صياغة نمط ولغة العمارة على مدار تطوراتها.

2: منظومة الشكل المعماري Architectural Form system:

الشكل عموماً هو ترتيب ملائم للعناصر والمفردات المفصولة عن بعضها البعض بمسافات زمانية أو مكانية محددة متخذة هيئة ظاهرة معينة، وبالتالي يتكون هذا الشكل من عناصر فيزياوية "الكتلة" تحيط بعناصر غير فيزياوية "الفضاء"، وهذه الكتلة تكون مسؤولة عن صياغة وتنظيم الفضاء الذي يحيط ويحتضن الوجود الإنساني فيتحرك فيه متحسساً الإيعازات من العالم الخارجي والذي تعتمد أبعاده، مقاييسه، نوعيته، فضلاً عن إضاءته على خصائص ما يحيط به من تكوينات كتلية. [هوشيار قادر،2003، ص:30].

وللشكل في العمارة مرجعية منطقية يتعلق بهدف وظروف صنعه ومجال إدراكه وان الشكل ذا الجمال المستقل أو الذاتي يفرز إدراكاً حسياً مباشراً ووقتياً مما يختزل العمارة إلي مجرد انطباعات شكلية تتعارض مع جوهرها الحقيقي ذي الإبعاد الفكرية والوجدانية والزمنية [سوسن أحمد حلمي،1997].

وعليه يُعد الشكل تمثيلاً مادياً بصرياً ناتج عن تفاعل جملة من المتطلبات الاجتماعية والتكنولوجية لتأسيس مادة قابلة للإدراك تمتاز عن غيرها بكونها أماكن للإيواء الإنساني، فالشكل المعماري لم يكون أبداً البنية الظاهرة وإنما هو البنية المدركة المتميزة بارتباطاتها الفكرية والتكنولوجية.

3: منظومة الخدمات Services System:

تُعد منظومة الخدمات من اكثر أنظمة المبنى تغيراً بتقدم الزمن بسبب التطورات المتسارعة للتكنولوجيا، فقد كان لدخول المنظومات الخدمية وبهذا الحجم والكلفة الأثر البالغ على التصميم المعماري بصورة عامة وعلى منظومة الشكل المعماري على وجه الخصوص. وتشتمل نظم الخدمات على عدة نظم فرعية متنوعة في وظائفها، ورغم ان الجوانب البيئية تستحوذ على نسبة كبيرة من المنظومة الخدمية والتي تتداخل مع أجزاء لا يمكن اعتبارها ضمن الفكرة الأساسية للخدمات كالمعالجات الصوتية وكاسرات الشمس وغيرها. [Burberry,1979,p:122]. وقد جمع (Banham)(2) بين منظومة الخدمات والمنظومة المنشئية والذين عدهما ينجزان مهمة الحركة والاتصال بين شاغلي المبنى. بينما تتجاوز اغلب المصادر التعريف المطلق للمنظومة الخدمية حيث تنتقل بين أجزاءه انطلاقاً من تعريف المنظومة ذاتها باعتبارها مجموعة من الأجزاء والأدوات المكونة لها، وتشكل فيه العوامل المشتركة والعلاقات بين تلك الأجزاء الجانب المهم.

وتشترك جميع مكونات منظومة الخدمات بصفتين أساسيتين، الأولى بكونها تتعامل مع الطاقة وتعمل بها، أي إنها أما ناقلة للطاقة أو مستهلكة لها، أما الثانية هي صفة الحركة إذ ان منظومة الخدمات أما أن تكون مكونات متحركة أو تتولى هي نقل الأشياء التي تعمل بها كالماء (للتبريد) عبر الأنابيب، والهواء (للتبريد والتدفئة والتهوية) عبر مجاري الهواء (Ducts) والطاقة الكهربائية عبر الأسلاك فضلاً عن الأشخاص والبضائع عبر المصاعد. [Banham,1969,p:11].

3-1: المكونات الأساسية لمنظومة الخدمات:

تتميز المنظومة الخدمية عن سواها من منظومات المبنى بالتطورات والتغيرات المتلاحقة وعلى هذا الأساس فمكوناتها تتزايد بمرور الوقت لتشمل أجزاء لم تكن موجودة سلفاً كنظام المعلومات على سبيل المثال. وبالتالي فالمكونات الفرعية لمنظومة

---

(2) (Banham): يعد من ابرز نقاد العمارة الذين تناولوا موضوع الخدمات في العمارة، وناقش العديد من الحركات التي مزجت بين الماكنة والعمارة مثل البروتالزم والبوب ارت الاركيكرام وما لها من اثر كبير على مسار الخدمات في الجانب المعماري.

الخدمات تمتاز بالتغيير المستمر سواء بالزيادة أو النقصان في ضوء التغييرات التكنولوجية المتلاحقة. [Mason,1986,p:21]. وبالنسبة للكثير من الدراسات تم تصنيف منظومة الخدمات إلى مجموعة من المنظومات الفرعية وابرزها:

- منظومة التكييف والتدفئة والتهوية Heating, Ventilation, Air-condition system (HVAC).
- منظومة خدمات الغاز Gas services system.
- منظومة المياه والمجاري Water and Plumbing
- منظومة الكهرباء والإضاءة Electrical and Lighting system.
- منظومة الاتصالات والمعلومات Communication and Information system.
- المصاعد والسلالم الكهربائية Elevator and Escalator.
- منظومة الحماية من الحريق Fire protection system.
- منظومة الأمن Security system.
- المنظومات الخاصة الأخرى والتي يتطلب وجودها برنامج المبنى وطبيعته. [Mason,1986,p:21].

3–2: تصميم منظومات الخدمات:

يعد هذا الجانب جزءاً أساسياً من كامل العملية التصميمية كونها تشكل نسبة كبيرة من حجم المبنى خصوصاً في المنشآت الكبيرة والصناعية، ويُعد توزيعها عاملاً مهماً في تحديد إدائيتها ومرونتها، لذا يجب ان يكون تنظيم المنظومة الخدمية في المراحل الأولية للتصميم بغية الوصول للتكامل التصميمي الأمر الذي يعطي المرونة لإعادة توقيع الفعاليات والمعدات. وهذا يتطلب بالضرورة مشاركة المعماري مع مهندسيّ الخدمات في المراحل المختلفة للتصميم لتجنب فقدان السيطرة على تنظيم الفضاءات وبالتالي فقدان المرونة في المبنى.[Barton,1983,p:13].

وعليه يجب ان يكون هنالك تحديد نوع وطبيعة الخدمات مع المنشأ والإنهاءات.

3–3: العوامل المؤثرة على تصميم منظومة الخدمات:

هنالك مجموعة من العوامل التي تؤثر بدرجة كبيرة في الإمكانيات التصميمية للمنظومات الخدمية أهمها:

أ) نوع المبنى: يؤثر نوع وطبيعة المبنى على شكله الظاهر وارتفاعه وتخطيطه، وبالتالي فان التمريرات الخدمية العمودية والأفقية تختلف أيضاً فالمباني المكتبية العالية تتطلب تمريرات عمودية اكثر من الأفقية بينما تحتاج الأبنية التعليمية الأفقية الممتدة على مساحة أفقية كبيرة إلى تمريرات أفقية اكثر.

شكل (1).

ب) الكلفة: هنالك علاقة وثيقة بين نوع المبنى والكلفة، إذ تختلف الكلفة باختلاف نوع المبنى وتتناسب طردياً مع درجة التعقيد حيث نلاحظ في إحصائيات جرت في المملكة المتحدة بأن كلفة الخدمات في المستشفيات شكلت حوالي 50% من الكلفة الكلية في حين إنها شكلت 18% من كلفة المصانع و12% من كلفة المنازل تقريباً [Maver,1971,p:11]. وتجدر الإشارة هنا بأن كلفة المنظومات الخدمية لا تقتصر على كلفة إنشائها وإنما تتعداها لتشمل كلفة الطاقة التي تستهلكها. وهذا يطرح إمكانية زيادة كلفة إنشاء الخدمات من اجل تقليل كلفة استهلاك الطاقة.

ج) حجم وشكل المبنى: يعد هذا الجانب عاملاً مهماً في التأثير على تصميم منظومة الخدمات من حيث تكاملها وتوزيعها خاصة فيما يتعلق بطبيعة تمريرات الخدمات سواءاً العمودية منها أم الأفقية، كما ان المتطلبات الخدمية للمبنى المتعدد الطوابق تختلف في أهميتها قياساً بالمبنى المنخفض، إذ تشكل الحركة العمودية والمناور الخدمية جوهر التصميم الخدمي.

فضلاً عن مساهمة الشكل المناخي الجيد والتوجيه السليم للمبنى وفتحاته في تقليل الجهد على منظومة الخدمات بطريقة تقلل الاعتماد عليها فضلاً عن تقليل حجم الأجهزة والفضاءات التابعة لها. [Barton,1983,p:8].

د) نمط الأنشاء: ويبرز هذا العامل من خلال المواد المستخدمة وخصائصها المنشئية والفيزياوية وما تؤثر به من خلالها على منظومة الخدمات وهذا الجانب طرحته الكثير من الدراسات والبحوث التي عنت بالانتقال الحراري عبر الجدران والسقوف حيث

تشكل سهولة تمرير الخدمات من خلال المنظومة المنشئية واحدة من اهم العوامل الأساسية التي تحكم العلاقة بين منظومات المبنى [Maver,1971,p:9]. كما وتؤثر أنماط معينة من الأساليب المنشئية في سهولة التعامل مع المنظومة الخدمية كالمنشأ المستند على مجمع الخدمات (Core) والذي يسهل التمريرات الخدمية [Barton,1983,p:8]. شكل (2).

3-4: الأنماط الشكلية لمنظومة الخدمات:

تتعامل العمارة بشكل جوهري مع منظومات الخدمات من النواحي المظهرية والتعبيرية بطريقتين:

3-4-1:: منظومة الخدمات المخفية:

تمثل جوانب الإخفاء بالنسبة لمنظومة الخدمات الصفة الغالبة في العمارة المعاصرة ولكن بشكل لا يلغي التأثيرات التعبيرية لها على منظومة الشكل المعماري، ولكن هو نوع من التأثير الذي يمتلك متطلباته الخاصة. ويلجا الكثير من المعماريين إلى جانب الإخفاء لعدة أسباب منها عدم رغبتهم في التعامل مع المنتجات الحديثة أو كما سماها (Banham) بـ"البدع التقنية"، حيث كان ينظر إلى التكنولوجيا باعتبارها وسيلة وليست غاية لذلك وجد اغلب المعماريون طرقاً مختلفة لدمج منظومات الخدمات المعقدة والضخمة داخل نسيج المبنى. وقد يكون الإخفاء لأسباب أيديولوجية تتعلق بتوجهات المرحلة، فنجد حركة "العمارة الحديثة" مثلاً ومن خلال أسلوبها الدولي (International style) عمدت إلى نقاء الشكل والبساطة المطلقة في حين حاول معماريو "ما بعد الحداثة" استعمال الأشكال التقليدية في مبانيهم، بالتالي سعى معظمهم إلى إخفاء الجانب الخدمي باعتباره منتجاً جديداً وينافي روح الماضي المنشودة. وقد حاول بعض هؤلاء المعماريين الملاءمة بين الأشكال الكلاسيكية والخدمات، [Banham,1969,p:245]. وهذا ما نلحظه في مبنى (مرسيليا) للمعمار (Le Corbusier)، شكل (3).

أما في بيت (فرانس وورث) للمعمار (Mies van der Rohe)، شكل (4)، والبيت الزجاجي للمعمار (Philip Johnson)، شكل رقم (5)، نلاحظ تميّز البيتين بالبساطة والشفافية وتشكيل فضاء مستمر لا تخترقه سوى الأعمدة المنشئية الرقيقة فضلاً عن كتلة مصمتة تمثل الفضاءات الخدمية (كالحمامات والمطبخ والمدخنة) ليكون نظام الخدمات هنا ذا سمة شكلية مميزة خاصة في الليل عند الإنارة وانسياب الفضاء الخارجي إلى الداخل. بالتالي لا يمكن إخفاء الأثر الشكلي لمنظومة الخدمات بالرغم من عدم ظهورها بشكل جلي، حيث أتاحت المنظومة الخدمية إمكانية التنوع المطلق والاختيار الواسع للأشكال مثلما جعلت أي مبنى مقبولاً وظيفياً وأدائياً [Banham,1969,p:239]. لذلك يعد تأثير الإنارة الصناعية في المبنى العامل البارز في التأثير الشكلي غير المباشر لمنظومة الخدمات، إذ يرى الفيلسوف (Lewis Mumford)(3) ان استخدام عناصر الإنارة أدى إلى زيادة الإحساس بوجود السطوح الداخلية للفضاء، ليتاح الإدراك الأكثر وضوحاً لميزات المحيط الداخلي،[رغد نعمة،1997، ص:71]. ومن ابرز الحركات المعمارية التي عمدت إلى الإفادة من دخول بعض عناصر المنظومة الخدمية إلى المجال المعماري وخاصة ما تعلق منها بعناصر الإنارة الداخلية هي حركة (الفن الجديد-الآرت نوفو)(4). شكل (6).

3-4-2:: منظومة الخدمات الظاهرة:

شكّل الجانب الجمالي هنا العامل البارز، فعمارة الإظهار كان عليها ان تنتظر إلى حين حدوث تغيير في الأفضليات الجمالية فضلاً عن انتظارها نمو الصعوبات التي تنجم عن تعقيد عملية إخفاء الخدمات فالمسألة الجوهرية هنا وفقاً لرأي (Banham) هي جمالية وتكنولوجية على حدٍ سواء. [Banham,1969,p:237]. وقد بدأت عناصر منظومات الخدمات تأخذ تعبيراتها بعد

(3) (**Lewis Mumford**): كان ناقداً اجتماعيًا وفيلسوفًا ومؤرخًا أمريكيًا. تركزت أفكاره في العلاقة بين مجتمع العصر الحديث والبيئة المحيطة بهم. ويختص عديد منها بتخطيط المدن.

(4) (**حركة الفن الجديد**) "الآرت نوفو" هي حركة معمارية اهتمت بشدة بالفضاء الداخلي ومفرداته عبر توجهات جمالية جديدة واعتمدت على الدرجات المتعددة للون الواحد والخطوط الدقيقة في رسوم الجدران وإنهاءات الأرضيات مع التأكيد على استخدام الألوان والمعالجات التزيينية الصغيرة. [Banham,1969,p:44].

الحرب العالمية الثانية ولم يكن ظهور الخدمات على نمط واحد وإنما تنوّع وتغّير حسب الفكر التصميمي متنقلة بين مجرد السماح لها بالظهور إلى إبرازها بشكل نصبي أو حتى كشفها بصورة كاملة أمام الناظر [Hawkes,1986,p:64].

فقد تظهر الخدمات بطريقة مبسطة كما فعل المعمار الأمريكي (Harson)، "مصمم مبنى الأمم المتحدة مع (Oscar Niemeyer)"، عندما ترك الخدمات مكشوفة وملونة في سقف المبنى مع ترك مجاري الهواء ووحدات دفع الهواء (A.H.U) مرئية بصورة كاملة على كل السقف. [Banham,1969,p:235].

كما يمثل مبنى (مختبرات ريتشارد) في "فيلادلفيا" للمعمار (Luis Kahn) العلامة الفارقة في تاريخ إظهار الخدمات، حيث برزت بشكل نصبي مميز الأمر الذي دفع بنقاد العمارة إلى الحديث لأول مرة عن جماليات المنظومة الخدمية بهذا القدر. إذ كانت لفكرة تقسيم المبنى إلى فضاء خادم وآخر مخدوم أثراً كبيراً على مجموعة كبيرة من المعماريين بالرغم من كون (Kahn) لم يكن مؤمناً بعملية إظهار الخدمات إلا

عندما تُفرض عليه من قبل الوظيفة، في حين اذا لم يتطلب المبنى خدمات كثيرة فانه يسعى إلى إخفائها كما فعل في تصميمه لمركز (Yale University Art Gallery)، [Hawkes,1986,p:65]. فعملية إظهار عناصر منظومة الخدمات هنا في الواقع ما هي إلا عملية إبعاد لها عن التأثير على المبنى "المخدوم" الذي تمت فيه تغطية الخدمات وإخفاؤها بواسطة السقوف الثانوية.

فأضحت بعض العناصر الشكلية التي استخدمها (Kahn) مثل "أبراج الخدمة" بشكلها النصبي شكلاً مغرياً للمعماريين وبدأت تدخل التصاميم المعمارية بكثرة لتمثل وجهاً من أوجه إظهار المنظومات الخدمية، ووصلت عملية إظهار الخدمات إلى ذروتها على يد المعماري (Richard Rogers) الذي قدم مبنى (اللويدز بنك)، كما اشترك مع (Renzo Piano) في تصميم مبنى (بومبيدو سنتر). وتلك الأبنية أظهرت الوجه الحقيقي لتأثير المنظومة الخدمية في الشكل العام للمبنى.

ومن التوجهات الشائعة في توقيع فضاءات المكائن الخدمية في المباني العمودية من خلال وضعها في منتصف المبنى. وهذا له أسبابه المتعددة منها:

- سبب وظيفي: لغرض التوزيع المتساوي للخدمات فضلاً عن ضمان اقصر طريق للتمريرات الخدمية التي تصل لطوابق المبنى المختلفة.
- سبب منشئي: وهذا مرده وجود المعدات الثقيلة وذات الاهتزازات الكبيرة أثناء التشغيل مما يعكس خطر كبير على المبنى من جراء تلك الاهتزازات. خاصة عند توقيعها في سطح المبنى.
- سبب تعبيري: وهذا الجانب يرتبط بغاية كسر التكرار والرتابة لطوابق المبنى خاصة في المباني المتعددة الطوابق. والمثال البارز على ذلك المنحى هو برج جامعة بغداد. حيث تتركز فضاءات المكائن ففي منتصف المبنى تقريباً. شكل (7).

<u>4: العلاقة التكاملية بين منظومة الشكل المعماري ومنظومة الخدمات:</u>

يعمل الجمع بين المنظومتين على الحماية البيئية والسيطرة على قوى الطبيعة وتقديم الراحة البيئية.

وهذه المنظومات ذات أهمية كبيرة، فمنظومة الشكل توفر الحماية الفيزياوية من القوى الخارجية بينما تعمل منظومة الخدمات على إكمال ذلك لتوفير الراحة في الداخل، الحاجة إلى منافذ خارجية للهواء، الماء، الطاقة، مما يعني ان منظومة الشكل عادةً ما يُخترق بالخدمات. والكلام عن تأثير الخدمات على منظومة الشكل المعماري لا يعني كونها المؤثر الوحيد، إذ تعد العمارة فعالية معقدة مرتبطة بمجالات متنوعة منها التقني ومنها الإنساني، منها ما يشكل جزءاً من تكوينها ومنها ما هو خارج عنها إلا انه مؤثر فيها، بالتالي نلحظ ان المؤثرات على الشكل كثيرة ومتنوعة ومن جملتها منظومة الخدمات حيث اصبح هنالك إمكانية طرح تبعية الشكل المعماري للمنظومة الخدمية أو ان الخدمات تتبع الشكل. حيث يرى (Banham) ان الخدمات ممكن ان تؤثر على الشكل بطريقتين: **الأولى:** من خلال الفضاءات والمعدات اللازمة للخدمات، **والثانية:** من خلال تحرير المنشأ من عبء الظروف البيئية التي كان يتحملها. [Banham,1969,p:71].

وشهدت عمارة القرن العشرين دخول فضاءات ومعدات لم تعهدها من قبل كان معظمها ناتج من تطورات المنظومة الخدمية ومتطلباتها. ويرى المختصون ان تأثير هذه المعدات جاء عن طريقين: <u>الأول</u> يتمثل في وجود فضاء كبير لاحتواء المكائن

والخدمات الهندسية وأهمية توقيع هذا الفضاء في المكان الملائم، والثاني يتمثل بالحاجة لوضع نظام التوزيع بصورة صحيحة ليؤدي الغرض منه بكفاءة، مع مراعاة سهولة الوصول إليه وصيانته كلما اقتضت الحاجة. [Burberry,1986,p:63]. كما ساد في مرحلة العمارة الحديثة تميّز قاعة المكائن في الطوابق العليا لناطحات السحاب، فعلى الرغم من ان وجود مثل هذه القاعات في قمة المبنى يكون محدداً تقنياً إلا ان المعماريين جعلوه طريقة لخلق التنويع في الواجهات خصوصاً ان هذه الواجهات كانت عادة ما تتميز بالتشابه والتكرار في مفرداتها، مع ملاءمته لفكرة التمييز الوظيفي لعناصر المبنى، كما في مبنى "سيكرام" للمعمار (Mies Van der Rohe)، شكل (8)، بالرغم من تأثيرها الشكلي المحدود خصوصاً إنها اكتفت غالباً بتغيير لون الزجاج أو تركيبة الفتحات "اللوفرات" وبما يحافظ على الشكل النقي للمبنى. [Ibid,p:228]. فالقرار التصميمي باحتواء أجهزة الخدمات داخل فضاء مغلق أو كشفها إلى الفضاء المفتوح ينبع من فكرة المصمم عن إبراز أو إخفاء الخدمات، وقد تظهر هذه المنظومة الخدمية بشكل مخفي داخل المبنى أو قد تكون بشكل بارز إلى الخارج كما هو الحال في مبنى "اللويدز" للمعمار (Richard Rogers)، شكل (9). حيث سمى المصمم هذه المجموعة الخدمية بأسم التوابع "Satellites" وهي ذات منشأ مستقل عن بقية أجزاء المبنى وتشكل ابرز سمات التشكيل الخارجي له. [Davies,1986,p:76-80].

ويرى (Banham) بأن المعماريين كانوا بحاجة إلى عناصر معمارية عمودية كالأبراج التي استخدمها (Le Corbusier) في مبنى "رونشامب" والتي كانت مستغلة للحركة العمودية فقط وأتى المعماريون من بعده بنفس الأبراج وبرروها وظيفياً بإدخال جانب الخدمات ونظام التوزيع العمودي إليها. [Banham,1969,p:239]. كما ساهم استخدام (Louis Kahn) للخدمات العمودية بشكلها البارز في مختبرات "ريتشارد" في فيلادلفيا، في إزالة العوائق الأخيرة أمام إبراز نظام التوزيع العمودي في المباني، معطياً الخدمات تعبيريتها المباشرة وفق المبدأ المعروف لـ(Kahn) "الفضاء الخادم والمخدوم". [Hawkes,1986,p:64].

5: جوانب الإبداع في منظومة الخدمات والفضاءات النفعية:

كانت العلاقة التقليدية التي تربط بين عناصر الخدمة وعناصر الانتفاع داخل المبنى تقوم على أساس المزج بين فضاءات كل منهما في المبنى الواحد حيث كانت تقع في قلب المبنى "في أغلب الأحيان" ومتصلة بالفضاءات الانتفاعية، إلا أنه في عام 1904 ولدت فكرة جديدة للفصل المتصل بين فضاءات الخدمات الفضاءات الانتفاعية، حيث صمم (Frank Lloyd Wright) مبنى "شركة لاركن" على أساس وضع الخدمات في كتلة مستقلة بعيدًا عن فضاءات الموظفين، كما دفع بالسلالم إلى الأركان خارج كتلة المبنى الرئيسية، الشكل (10)، وبذلك يكون (Wright) قد وضع البذرة الأولى لفكرة الفضاءات الخادمة والفضاءات المخدومة (Servant Spaces and Service Spaces) والتي كانت من المقومات المهمة في تطور الفكر التصميمي في القرن العشرين، ومنها استقى بعض المعماريين محاولات أخرى لتطوير هذا المبدأ التصميمي. فظهرت بشكل متطور وأكثر وضوحًا في أعمال (Louis Kahn) في تصميم "مبنى المعامل الطبية" بجامعة فيلاديلفيا (Medical Laboratory Building) 1964، حيث قام وضع عناصر الحركة من سلالم ومصاعد وفضاءات تكييف أو غيرها من الشبكات والتوصيلات الصحية والكهربائية في أبراج رأسية بعيدًا عن وسط الفضاءات، حتى لا تعيق الاستخدامات وتعمل على توفير المرونة الكافية لعمل أي تعديلات مستقبلية. وبشيء أكثر تطورًا ظهرت هذه الفكرة في هيئة جديدة في أعمال معماريّ اتجاه "التكنولوجيا العالية" (Hi-Tech)، [محمد محمود عويضة،1984، ص:54].

ومن جانب آخر أخذت العلاقة بين الفضاءات الانتفاعية وفضاءات الخدمة شكلاً آخراً من الأشكال المبتكرة التي ظهرت في الفكر المعماري المعاصر، فقد استطاع (Wright) أن يقدم هذه الفكرة في صورة أخرى من خلال برج المعامل لمبنى شركة جونسون (Johnson Wax Company) 1947 شكل (11)، حيث ابتكر فكرة القلب الخرساني، لوضع الخدمات وعناصر الحركة في قلب المبنى الإنشائي ويترك الحيز من حولها حراً يمكن تقسيمه أو استخدامه بأي شكل وحسب الحاجة.

6: مفردات الاطار النظري:

وبعد مناقشة ابرز المفردات البحثية واستخلاص مستويات العلاقات الرابطة المختلفة بينها تبرز لدينا مجموعة من المحاور الرئيسية التي مثلت مفردات الاطار النظري للبحث.

حيث تجسّد القيم الممكنة الخصائص المستخلصة والصفات المميزة لكل مفردة من مفردات الاطار النظري وفق كل ما تم طرحه من أفكار ومفاهيم خلال متن البحث. وصولاً لتحديد الصفات المميزة لكل مفردة بغية تشخيص اثر عناصر المنظومات الداخلة في العملية التصميمية على النتاج وتحديد اهم مؤشرات ذلك التأثير وتجلياته في نتاج أي عمارة، وعليه تمثلت مفردات الاطار النظري بثلاث محاور أساسية وهي:

6-1: منظومات المبنى:

يناقش هذا الجانب المنظومات المتعددة الداخلة في العملية التصميمية بكل أبعادها والذي جاء بثلاث محاور ثانوية، مثّل كل محور منظومة من المنظومات الأساسية (منظومة الشكل المعماري، منظومة الخدمات)، وابرز سماتها. واندرج ضمن كل منظومة منها مجموعة من الخصائص والمميزات وكما يأتي:

أ- منظومة الشكل المعماري: جاء هذا المحور بمجموعة من الخصائص التي ميّزت النتاج ومنها ما تعلق بطبيعة الشكل الظاهر وخصائصه وما يمكن ان يأتي من تميز على مستوى الشكل، ومدى ارتباط هذا الشكل بطرز معمارية أو حركات فكرية أثرت في ذلك النتاج، فضلاً عن مستويات الذاتية والتفرد التصميمي والمقياس العام لذلك الشكل.

ب- منظومة الخدمات: احتوى هذا الجانب على مجموعة مفردات ارتبطت بعناصر المنظومات الخدمية. منها ارتباط تلك المنظومة بنوع المبنى والأثر الوظيفي عليها، والمستوى التكنولوجي لمنظومة الخدمات، وكذلك المؤثرات البيئية فيها، درجة الاقتصادية، فضلاً عن جوانب متعددة أخرى منها تأثير توزيع عناصر الخدمات بالحركات الفكرية المعمارية ومدى ارتباط الخدمات بالمواد المستخدمة والأثر المتبادل بينهما.

6-2: تكامل العلاقات المنظوماتية:

يناقش هذا الجانب ابرز مستويات العلاقة التأثيرية الرابطة، والمتبادلة بين مكونات العملية التصميمية وخاصة ما يتعلق منها بالمنظومات والعلاقة بينها، حيث جاء هذا الجانب بمحورين أساسيين هما:

أ- **خصائص العلاقة الرابطة بين المنظومات:** وهنا يتم التركيز على طبيعة ومميزات العلاقات الرابطة بين منظومات المبنى الأساسية وتوضيح طبيعة العلاقة الرابطة بين منظومتي الخدمات والشكل وتأثير عناصر منظومة الخدمات في الشكل المعماري الظاهر. ومميزات طبيعة العلاقة بين منظومة الشكل ومنظومة العناصر الخدمية.

ب- مستويات تكامل العلاقة المنظوماتية: يتم فيه التركيز على موضوع التكامل وما يمثله من جانب يحكم طبيعة العلاقة الرابطة بين منظومات المبنى الرئيسية والتي اتسمت بمستويات ودرجات مختلفة.

6-3: تعبيرية وأدائية النتاج المعماري:

يعكس هذا المحور خصائص مهمة تتعلق بالجانب الظاهراتي في النتاج المعماري، حيث هدف إلى توضيح السمات المادية والتعبيرية التي يتمتع بها الشكل المعماري على عدة مستويات. حيث جاء ضمن محوري أساسيين:

أ- مستويات تعبيرية النتاج: هنا يتم التركيز على توضيح مستويات الخصائص التعبيرية والجمالية التي حملها النتاج المعماري.

ب- الأدائية المنظوماتية: حمل هذا الجانب مجموعة من الموضوعات التي ارتبطت بالجانب الأدائي والوظيفي لكل منظومة من المنظومات المؤثرة في المبنى ومن ابرزها ي مستويات أدائية عناصر منظومة الشكل المعماري، فضلاً عن أدائية العناصر الخدمية.

7: الأمثلة التطبيقية للبحث:

المشروع الأول: مركز بومبيدو في باريس، فرنسا 1972-1975.(CENTRE GEORGES POMPIDOU)

تصميم/ ريتشارد روجرز، رينزو بيانو (Renzo Piano - Richard Rogers)

أ- الوصف العام للمشروع:

وصلت عملية الإظهار وتعبيرية كل من المنشأ والخدمات ذروتها على يد المعماري (Richard Rogers) عندما قدّم مبنى (بومبيدو سنتر) مع (Renzo Piano). ويعد مركز "بومبيدو" (Pompidou) متحفاً ومركزاً ثقافياً يقع وسط باريس في ميدان الخمسة هكتار بين "اللوفر ونوتردام"، في الموقع المعروف (Plateau Beabourg) الذي أعطى للمجمع اسمه الأصلي. ويعد نقّاد العمارة مركز "بومبيدو" بأنه مبنى يستعرض التقنية العالية بطريقة واضحة، وهذا الهدف خلق مرونة وحرية واسعة لمنظومة الفضاءات الداخلية بصورة حركّت عناصر البنى التحتية والخدمية إلى الخارج لترك الفضاءات الداخلية غير معرقَلة.

ب- مستوى منظومة الشكل المعماري:

انطلق معماريو المبنى من فكرة خلق وإبداع فضاءات عرض حرة وفسيحة في آن واحد، موظفين أطروحة (Mies Van der Rohe) الخاصة بتنظيم الفضاءات الشاملة، فشكل المبنى المتوازي الأضلاع الذي يمتلك 50 متراً عرضاً و170 متراً طولاً، تم تسقيف طوابقه الستة عبر منظومة من المساند المتشابكة المثبتة خارج المبنى [Reising,2010] شكل(12)

وساهمت معالجات واجهات المبنى الحضور الكثيف لعناصر الأنشاء والتراكيب البنائية الطولية والمحورية والمتصالبة التي غطت بعناصرها مفردات الواجهة وأكسبتها انطباع العفوية، ومما زاد في خلق حالة تعبيرية المنظومات كشف مجاري وأنابيب الخدمات الهندسية نحو الخارج؛ هذا عدا اللجوء لتوظيفات عنصر اللون وتشغيله تكوينياً للقيام بوظائف جديدة لم تكن معتادة سابقاً في العمارة المدنية. إذ حرص المصممون ان يكون لعنصر اللون دوراً مؤثراً في صياغة المنظومة التكوينية لواجهات المبنى، حيث تم توظيف عنصر اللون بصبغاته المختلفة على أجزاء مختارة من الواجهة المتشكلة من عناصر مختلفة، فلونت مجاري التهوية بالأخضر وأنابيب الماء بالأزرق وقنوات الأسلاك الكهربائية بالأصفر، في حين لونت عناصر الانتقال والحركة مثل المصاعد والسلالم المتحركة (Escalators) بالأحمر. وفي النتيجة فان قرار كشف ونقل جميع المنظومات المنشئية والحركية إلى واجهات المبنى أوحى إلى نزعة واضحة نحو استغلال تلك العناصر في تعبيرية المبنى الظاهرة. بالتالي خلق المبنى ظاهرة معمارية جديدة حُظيت بانتشار واسع في مجمل الممارسة التصميمية العالمية اللاحقة.

ج- مستوى منظومة الخدمات:

تم وضع كل معدات الخدمات الثقيلة والسخانات وأجهزة التكييف المركزية للمبنى في السرداب مع خزانات الماء ومنظومة التوزيع الكهربائي الرئيسية فضلاً عن أجهزة معالجة المياه. وتوزعت كل تلك الخدمات ضمن منشأ الجدار الشرقي، فالمعدات تكون في المستوى السفلي منه بينما أجهزة تكييف المبنى تكون بمستوى السقف. [Reising,2010]. شكل (13). ضمن كل طابق هنالك خدمات مكشوفة تحت السقف تشتمل على عناصر التوزيع الهوائي والإضاءة، بينما توضع في المستوى العلوي للأرضية عناصر التوزع والربط السلكي والأنابيب الصغيرة. وهذا يتم من خلال رفع الأرضية الثانوية التي تستند إلى الأرضية المنشئية الخرسانية. كما ان كل بحر منشئي في الفضاء الداخلي يعد منطقة حرارية مستقلة تتسلم الهواء من عناصر التوزيع الهوائي السقفية. فهنالك (26) عنصر توزيع هوائي عالي السرعة متعدد الأحجام عند السقف، وكل منها يجهز الهواء المكيف إلى الأسفل ويعود من احدى البحور المنشئية الـ(13) من كل طابق، ولغرض تقليل ارتفاع السقف يُقسم كل عنصر توزيع هوائي إلى عدة أجزاء مكونّة (كالمرشحات الهوائية، المراوح، المحركات والمنافذ الهوائية)، وتكون منافذ النفخ الهوائية واضحة جداً من الشرفات الجانبية الشرقية، وبالتالي واضحة للعيان من جهة الميدان المقابل للمبنى. [Simon,2009]

تكون الفكرة الرئيسية للخدمات هنا هي فكرة القشرة الخادمة حيث يصف (Piano) المبنى بانه "مركبة فضائية لا تطير" مفتخراً في كون المركز حقق اهم أهدافه المتمثلة في تغيير صورة المتاحف والمراكز الثقافية من أبنية جامدة ومعزولة عن العامة إلى مبانٍ متفاعلة مع الجمهور. كما شكّل النجاح الذي لقيه مركز "بومبيدو" نقطة انطلاق لنوع جديد من التعبيرية التي برزت فيها عناصر الخدمات بشكلها الظاهر، وأنابيبها ومجاري الهواء، والسلالم الكهربائية وغرف المكائن المكشوفة، وقد وصف النقاد طريقة إظهار الخدمات في المركز بانها "إثارة الخدمات". في حين صنّف المنظّر المعماري (Charles Jencks) مبنى "بومبيدو" ضمن

حركة التقنيات العالية (Hi-Tech) التي يعدها امتداداً للعمارة الحديثة، واصفاً إياه بانه **احتفال النظام التكنولوجي.** بينما جعل أخرون المبنى امتداداً للعمارة الفيكتوري وحركتي (الاركغرام والمستقبلية). [Jencks,1987,p:110].

وقد برر المعماريان عملية الإظهار الخدماتي من خلال البحث عن أشكال جديدة قادرة على توفير المرونة الكافية لاستيعاب وظائف ومتطلبات متغيرة.

المشروع الثاني:

مركز سنسبري للفنون البصرية/ في إنكلترا 1976–1977: (SAINSBURY CENTRE FOR VISUAL ARTS)

تصميم/ نورمان فوستر ومشاركوه. (NORMAN FOSTER & PARTNERS)

أ– الوصف العام للمشروع:

يمثل مركز "سنسبري" الاستخدام البارز الأول لمبنى عام من الواح الأكساء الخارجية (Cladding) المعزولة حيث حمل هذا المبنى الشكل الكفوء وتبنّي المواد المنشئية الصناعية الكفوءة، وامتاز المبنى بكونه ذي حجم وفضاء واحد يحوي مجموعة الوظائف الفنية ومدرسة الفنون الجميلة فضلاً عن مجموعة من الاستخدامات العامة.[Bachman,2003,p:361]. ويعد وضع كل فضاءات المبنى تحت سقف واحد مصدراً لتحديات متعددة منها: الفصل بين الوظائف، مشكلات الآمن والخصوصية، المشكلات الصوتية. الأمر الذي ولّد صعوبة في توزيع وفصل الفعاليات المتعددة ضمن الحجم الواحد، وكان اختيار (Foster) للمخطط المفتوح الكبير متسق مع مجموعة من الأهداف، منها محاولة تخفيض الطاقة اللازمة للتكيف من خلال التخلّي عن التبريد الميكانيكي قدر الإمكان الأمر الذي شكّل تحدّياً لـ(Foster) حيث تعمل الرطوبة العالية ومستويات درجة الحرارة العالية تأثيراً سلبياً للعناصر الفنية كما تلعب تلك العوامل أيضاً في التأثير على مواد اللوحات. [مجد عمر،2009،ص:1].

ب– مستوى منظومة الشكل المعماري:

يؤطر هيكل النظام المنشئي الأنبوبي غلاف الطبقة المزدوجة للجدران الطويلة وسقف المبنى، فالجانب الخارجي مكسو بمنظومة قابلة للتمدد من الألواح ذات الأبعاد (2.4×1.2 م) من الألمنيوم الصلب والألياف الزجاجية، فضلاً عن وجود الواح منها متحركة تكون مركبة بسارية مستمرة ومثبتة ببراغي.

وبالرغم من أن كل الألواح قابلة للحركة إلا ان التخطيط العام يعرض أربعة صفوف طويلة فقط من نوافذ الإضاءة السقفية المستمرة تكون اسفل المحور الطويل للسقف. ويكون الإفريز البارز والمقوّس شفافاً ليجاري نمط الإضاءة السقفية ويستعمل الواح الألياف الزجاجية الشفافة للإعلان عن المداخل الأرضية. ويتضمن الأكساء (Cladding) الداخلي أيضاً الواح ألمنيوم متحركة، كما أن الألواح السقفية تتحرك آلياً لتنظيم دخول ضوء الشمس، حيث أن اغلب تلك الألواح مدعومة بغطاء سمعي ليفي للسيطرة على الضوضاء والانعكاسات. [المصدر السابق،ص:1].

وتوجد منطقة عناصر الخدمات بين الطبقتين الخارجية والداخلية ضمن السمك المنشئي للهيكل العام. حيث تحوي منطقة الجدار "التي تكون بعمق (2.1 م)" على الحمامات والمخازن الصغيرة وبعض المكاتب فضلاً عن عناصر المنظومة الخدمية عند مستويات الطابق الأرضي والوسطي، بينما عند المستويات الأعلى توجد المخازن الكبيرة. أما منطقة السقف فتُستخدَم عناصرها للتعديل الضوئي حيث يتم نشر ضوء الشمس من خلال الألواح المتحركة المدارة من قبل المتحسسات الضوئية تحت النوافذ السقفية خلال الهيكل المنشئي. شكل (14). [المصدر السابق ،ص:1].

ج– مستوى عناصر منظومة الخدمات:

تأتي المساهمة المتميزة تكنولوجياً لمركز "سنسبري" من خلال شكل الجدار كتطبيق متجدد لمبدأ فضاءات الخادم والمخدوم، والبيئة الخارجية والداخلية، بدلاً من استعمال الجدار الرقيق، حيث استخدم (Foster) سطوح التغليف على جانبيّ الجدار ذي العمق الكبير من الهيكل المنشئي ويتم استغلال ذلك السمك بفضاءات الخادم والخدمات الميكانيكية، ووحدات التهوية، والمكاتب والحمامات، شكل (15). فضلاً عن كل الوظائف التي لا تنتمي للاستعمالات العامة للمعرض. وهذا الأمر ساهم في

تحرير الفضاء المركزي الكبير بوجود حركة مفتوحة وإضاءة نهارية وحجم مشترك. فالهيكل المنشئي هنا يكون مستغلاً في هذا المخطط. وتخدم المستويات الأرضية للفضاءات حاجات المستخدمين الخاصة بينما يمثل السقف مصدراً للإضاءة سواءً الطبيعية أم الصناعية. [Bachman,2003,p:370].

كما أن ستراتيجية الغلاف الخارجي تم توجيهها نحو التقليل قدر الإمكان من أحمال التبريد وأنظمة التكييف (HVAC). أما الحرارة فتوزع على المبنى من خلال مجمع الخدمات المركزي على شكل ماء بدرجة حرارة عالية بينما يتم دفع الهواء مباشرة من الألواح المثبتة على الغلاف الخارجي. وإجمالاً هنالك (40) وحدة مروحية مثبتة في ثلاثة مستويات عليا من مستويات الجدار الجنوبي. شكل (15).

جدول رقم (1) تطبيق مفردات الإطار النظري للبحث على مشروع بومبيدو سنتر في باريس 1972-1975

	المفردات الرئيسية	المفردات الفرعية	القيم الممكنة	الخواص
أولاً	منظومة الشكل المعماري	طبيعة الشكل الظاهر والتميّز الشكلي	غير تقليدي، تكرار في عناصر التكوين، تعقيد عالي في التشكيل	الاعتماد على أشكال جديدة في التشكيل الخارجي
منظومات المبنى		ارتباط التكوين بطرز معمارية	ارتباطه بعمارة الـ(High-tech)	الاعتماد على توجهات عمارة التقنيات العالية في المعالجة
		مستوى الذاتية في التصميم	ذاتية عالية في اختيار الكثير من المعالجات	الخروج عن المألوف في معالجاته للواجهة
		المقياس العام للشكل	مقياس لا أنساني	الاعتماد على مقاييس الالة في العناصر
		مستوى ارتباط الشكل بالجانب التكنولوجي	تأثر كبير بالتطورات التكنولوجية في مجال العمارة والخدمات	الاعتماد على التقنيات الحديثة من نواحي المواد والمعالجات
		التأثير الوظيفي على الشكل الظاهر	عدم بروز الأثر الوظيفي في الشكل	لا يوجد ارتباط بين الشكل والوظيفة
		خصوصية المكان والمحيط وتأثيره الشكلي	تفرد عالي في المعالجات والتشكيل العام للمبنى	الخروج عن المألوف والسياق العام للموقع
		مستوى المواد البنائية	استخدام المواد المصنعة الحديثة	المواد المستخدمة كان لها الأثر الشكلي الكبير في النتاج
	منظومة الخدمات	ارتباط الخدمات بنوع المبنى والأثر الوظيفي	توافق عناصر الخدمات مع التقسيم الوظيفي	ارتباط الوظيفة الداخلية مع عناصر الخدمة الظاهرة في الفضاء
		المستوى التكنولوجي لمنظومة الخدمات	مستوى تكنولوجي وتقني عالي في خدمات المبنى	ترتبط عناصر الخدمة ومعالجاتها بالتطورات التكنولوجية بشكل وثيق
		المؤثرات البيئية في منظومة الخدمات	ترتبط المعالجات الخدمية بالمؤثرات البيئية بشكل كبير	تنطبق عناصر الخدمة حسب الحاجة البيئية
		درجة الاقتصادية في المنظومة الخدمية	لا توجد اقتصادية عالية في المنظومة الخدمية	الاعتماد على مستوى عالي من التقنية في المواد والمعالجات
		تأثر توزيع عناصر الخدمات بالحركات الفكرية المعمارية	ارتباطه بتوجهات عمارة الـ(High-tech)	الاعتماد على توجهات عمارة التقنيات العالية في العناصر والمعالجات الخدمية
ثانياً	خصائص العلاقة بين المنظومات	طبيعة العلاقة بين الخدمات والشكل	علاقة التشابك وتكون جزء مكمل للتشكيل	الاعتماد على عناصر الخدمات في الواجهات
تكامل العلاقات المنظوماتية		تأثير الخدمات على المنظومة الشكلية	اثر كبير على التشكيل العام للواجهة	بروز عناصر الخدمة على الواجهات
		طبيعة العلاقة بين المنشأ والخدمات	علاقة الاتصال وعلاقة	يوفر المنشأ الهيكل

بهجت رشاد شاهين
علي مجبل العذاري
أسامة عبد المنعم خريبط

				تشابك في وقت واحد	السائد للمنظومة الخدمية
	مستويات تكامل العلاقة المنظوماتية	تكامل العلاقة بين منظومتي المنشأ والخدمات	مستوى التكامل	تكامل فيزيائي	يشتركان بنفس الحيز
			درجة التكامل	علاقة اتصال وتشابك	يوفره المنشأ الإسناد للنظم الخدمية
		تكامل العلاقة بين منظومتي الشكل والخدمات	مستوى التكامل	تكامل فيزيائي	تظهر عناصر الخدمات بنفس الواجهات
			درجة التكامل	علاقة تشابك	تنطبق فيها المنظومتان احدهما على الأخرى وتشتركان بالمتطلبات الفضائية
ثالثاً	مستويات تعبيرية النتاج	النمط التعبيري للعناصر الخدمية		تعبيرية عالية	إظهار عناصر الخدمات داخلياً وخارجياً
تعبيرية وأدائية النتاج المعماري		درجة التكتونية في النتاج		تكتونية عالية	الإظهار العالي للمنشأ والتمفصل
		درجة تعبيرية المادة البنائية		تعبيرية واضحة للمواد	الأثر التعبيري للمواد المستخدمة
	الأدائية المنظوماتية	مستويات أدائية عناصر المنظومة الشكلية	الإداء الشكلي	أداء تشكيلي عالي	استخدام تشكيلات جديدة
			الإداء الإنشائي	وجود أداء منشئي	وجود وظيفة مشتركة لعناصر المنشأ
			الإداء الخدمي	أداء خدمي عالي	توفير العزل البيئي اللازم
		مستويات أدائية عناصر المنظومة الخدمية	الإداء الشكلي	أداء تشكيلي عالي	إظهار العناصر الخدمية على الواجهات الخارجية للمبنى
			الإداء الإنشائي	لا يوجد	
			الإداء الخدمي	كفاءة أدائية عالية	استثمار التقنيات الخدمية العالية في المبنى

جدول رقم (2) تطبيق مفردات الإطار النظري للبحث على مشروع مركز سنسبري في إنكلترا 1976–1977

	المفردات الرئيسية	المفردات الفرعية	القيم الممكنة	الخواص
أولاً				
منظومات المبنى	منظومة الشكل المعماري	طبيعة الشكل الظاهر والتميّز الشكلي	بساطة ظاهرة، وتوازن تكويني وتكرار في العناصر المستخدمة	الاعتماد على بساطة في التشكيل الخارجي
		ارتباط التكوين بطرز معمارية	ارتباطه بعمارة الـ(High-tech)، مع تفرّد محدود	الاعتماد على توجهات التقنيات العالية في العديد من المعالجات
		مستوى الذاتية في التصميم	موضوعية عالية في اختيار الكثير من المعالجات الشكلية	عدم الخروج عن المألوف في كثير من تفاصيل الواجهة
		المقياس العام للشكل	مقياس أنساني واضح	الاعتماد على مقاييس الأنسان
		مستوى ارتباط الشكل بالجانب التكنولوجي	تأثر كبير بالتطورات التكنولوجية في مجال المواد البنائية	استغلال التقنيات الحديثة في علوم المواد البنائية من خلال استخدام المواد الحديثة
		التأثير الوظيفي على الشكل الظاهر	بروز الأثر الوظيفي في الشكل الظاهر	وجود ارتباط نسبي بين الشكل الخارجي والوظيفة
		خصوصية المكان والمحيط وتأثيره الشكلي	تفرد عالي في المعالجات والتشكيل العام للمبنى	محاولة الخروج عن المألوف والسياق العام للموقع
		مستوى المواد البنائية	استخدام المواد المصنعة الحديثة	المواد المستخدمة كان لها الأثر الشكلي الكبير في النتاج الظاهر
	منظومة الخدمات	ارتباط الخدمات بنوع المبنى والأثر الوظيفي	توافق عناصر الخدمات مع التقسيم	ارتباط الوظيفة الداخلية مع عناصر

				الوظيفي	الخدمة الظاهرة في الفضاء
		المستوى التكنولوجي لمنظومة الخدمات		مستوى تكنولوجي عالي في خدمات المبنى	ترتبط عناصر الخدمة ومعالجاتها بالتطورات التكنولوجية بشكل وثيق
		المؤثرات البيئية في منظومة الخدمات		توافق المعالجات الخدمية بالمؤثرات البيئية بشكل كبير	تنطيق عناصر الخدمة حسب الحاجة البيئية
		درجة الاقتصادية في المنظومة الخدمية		لا توجد اقتصادية عالية في المنظومة الخدمية	الاعتماد على مستوى عالي من التقنية في المواد والمعالجات
		تأثر توزيع عناصر الخدمات بالحركات الفكرية المعمارية		ارتباطه بتوجهات عمارة الـ(High-tech)	الاعتماد على توجهات عمارة التقنيات العالية في العناصر والمعالجات الخدمية
ثانياً					
تكامل العلاقات المنظوماتية	خصائص العلاقة بين المنظومات	طبيعة العلاقة بين الخدمات والشكل		علاقة الاتصال فيما بينهما	لا يوجد تأثير لعناصر الخدمات في الواجهات الخارجية
		تأثير الخدمات على المنظومة الشكلية		لا يوجد اثر كبير على التشكيل العام للواجهة	عدم بروز عناصر الخدمة على الواجهات
		طبيعة العلاقة بين المنشأ والخدمات		علاقة التشابك بين المنظومتين وتتداخلان فيما بينهما	يوفر المنشأ الحيز والهيكل الساند للمنظومة الخدمية
	مستويات تكامل العلاقة المنظوماتية	تكامل العلاقة بين منظومتي المنشأ والخدمات	مستوى التكامل	تكامل فيزيائي وإدائي	يشتركان بنفس الحيز والوظيفة
			درجة التكامل	علاقة اتصال وتشابك	يوفر المنشأ الإسناد والحيز للمنظومة الخدمية
		تكامل العلاقة بين منظومتي الشكل والخدمات	مستوى التكامل	تكامل أدائي	تؤدي عناصر الشكل الخارجي بعض واجبات المنظومة الخدمية
			درجة التكامل	علاقة التشابك	تنطبق فيها المنظومتان احدهما على الأخرى وتشتركان بالمتطلبات الفضائية
ثالثاً					
تعبيرية وأدائية النتاج المعماري	مستويات تعبيرية النتاج	النمط التعبيري للعناصر الخدمية		لا وجود لتعبيرية العناصر الخدمية	لا يوجد إظهار لعناصر الخدمات في تشكيلات المبنى
		درجة التكتونية في النتاج		تكتونية غير عالية	الإظهار المحدود للمنشأ
		درجة تعبيرية المادة البنائية		تعبيرية واضحة للمواد	الأثر التعبيري للمواد المستخدمة
	الأدائية المنظوماتية	مستويات أدائية عناصر المنظومة الشكلية	الإداء الشكلي	أداء تشكيلي عالي	استخدام تشكيلات ومواد جديدة
			الإداء الإنشائي	لا يوجد	
			الإداء الخدمي	أداء خدمي جيد	توفير العزل البيئي اللازم
		مستويات أدائية عناصر المنظومة الخدمية	الإداء الشكلي	أداء تشكيلي محدود	عدم إظهار العناصر الخدمية على الواجهات الخارجية للمبنى
			الإداء الإنشائي	لا يوجد	
			الإداء الخدمي	كفاءة أدائية عالية	استثمار التقنيات الخدمية العالية

8: الاستنتاجات والتوصيات.

- يجب ان يكون هنالك تحديد نوع وطبيعة الخدمات المطلوبة بالاعتماد على نوع المبنى ودرجة تعقيده وهذا يفرض إقرار كيفية تكامل منظومات الخدمات مع المنشأ وعناصر البناء المختلفة وكيف ستظهر ودرجة المرونة في المنظومات.
- يمكن عد المنظومات في أي مبنى هي منتجات إنسانية تسعى لتحقيق الأهداف الإنسانية المعرفة، وموجهة نحو الوصول إلى حلول للمكونات الشخصية بمقدار تأثيرها على المنظومة ككل من خلال تحقيق الأهداف بربط أدائية المنظومات مع الكل، وبالتالي يمكن اعتبار المبنى "ككل" يتكون من مجموعة من المنظومات "الأجزاء" والتي تتفاعل مع بعضها بعلاقات حيوية تسعى لتحقيق تكوين متكامل.
- تعد منظومة الخدمات ابرز مكونات المبنى الرئيسية والتي أثرت وبشكل أو بآخر في صياغة نمط ولغة العمارة على مدار تطوراتها. حيث تُعد منظومة الخدمات من اكثر أنظمة المبنى تغايراً بتقدم الزمن بسبب التطورات المتسارعة للتكنولوجيا. بسبب الارتباط الوثيق والمتبادل بين التكنولوجيا ومنظومة الخدمات.

- ان لتكامل منظومات المبنى العديد من الفوائد التي تكمن في كونه يؤثر إيجاباً على الزمن المستغرق للتصميم والأنشاء وعلى كمية المواد المستخدمة، وهذا يتكامل مع إمكانية الحصول على فضاءات موظفة بشكل جيد موفرة المرونة وإمكانية التوسع المستقبلي.
- تأثير المنظومة الخدمية على جانب الشكل المعماري اخذ يتزايد لسببين أساسيين، الأول يتمثل بظهور مبانٍ تستخدم الخدمات كتشكيل واضح يضاف إلى العمارة، أما السبب الثاني فيكمن بالدور المتعاظم للخدمات من حيث الكلفة التي قد تصل إلى 30% من الكلفة الإجمالية للمبنى.
- علاقة المنظومات مع بعضها هي علاقة تكاملية اذا أخذت بنظر الاعتبار "الكل" وتختلف المنظومة عن العلاقة باعتبار ان العلاقة هي بين عنصرين فقط. ولا تتيح دراسة العلاقة بينهما بمعرفة ارتباطهما بالكل، أما المنظومة فتدرس علاقة المكونات والأجزاء المتعددة بالمنظومة وتتيح معرفة تلك الأجزاء ضمن الكل.
- التركيز على الفكر التجزيئي في حل المشكلات وتقسيمها إلى مناطق متخصصة يجعلنا بازدياد نهمل الموضوع الواسع والذي يعطي للأشياء وحدتها، وبالحقيقة ان هذه النظرة قد تعدّت العلم والتكنولوجيا لتشمل مجال كافة علوم الحياة.
- ارتباط المنظومة الخدمية عبر تطوراتها بمفاهيم الماكنة، خاصة ما تعلق منها بالجوانب التعبيرية حيث ان التعامل مع الخدمات يفرض على المصمم الكثير من السياقات العملية والوظيفية البحتة الخاضعة بدورها للمحددات المنطقية والعلمية التي يمثلها منطق الماكنة. فمنظومة الخدمات (وما ارتبط بها من مفاهيم الماكنة) ليست مجرد تكوين مادي لها بل تشتمل أيضاً على قيماً ميتافيزيقية وتعبيرية متزايدة بصورة أثرت في الكثير من الأفكار المعمارية المعاصرة.
- أصبحت جماليات العناصر الخدمية جزءاً من الفنون ولم يعد هنالك تحرّج من قبول تلك الجماليات الجديدة التي دعت إليها الكثير من الحركات والتي بدت عند طرحها لأول وهلة غريبة عن السياق الفني والمعماري. فكانت فكرة (عمارة الماكنة) لا تهدف إلى إنتاج ماكنة بقدر ما انصب جل اهتمامها على إنتاج عمارة تعبر عن الماكنة.
- من الضرورات التصميمية مراعاة العناصر الخدمية تعبيرياً خاصةً مع إمكانيات ودعوات إظهار تلك العناصر.

المصادر والمراجع

المصادر العربية:

- رغد نعمة الله حمد الله، **التكنولوجيا والشكل: اثر التكنولوجيا الحديثة في شكل المسكن**، رسالة ماجستير غير منشورة، كلية الهندسة، جامعة بغداد، 1997.
- سوسن احمد حلمي، **منطق العمارة استطلاع فلسفي نظري لمناطق آليات الإدراك والحكم في العمارة**، مجلة جمعية المهندسين، المصرية، آذار،1997.
- مجد عمر حافظ، **العمارة الفائقة التكنولوجيا**، مقال منشور، موقع ملتقى المهندسين العرب، الشبكة الدولية، 2009.
http://www.arab eng.org/vb/showthread.php?t=103751&page=22#ixzz1n6MHAjOG
- محمد محمود عويضة، **تطور الفكر المعماري في القرن العشرين**، دار النهضة العربية، بيروت، لبنان، 1984.
- هوشيار قادر رسول، **العمارة والتكنولوجيا: دراسة تحليلية للفعل التكنولوجي في العمارة**، أطروحة دكتوراه غير منشورة، كلية الهندسة، جامعة بغداد، 2003.

المصادر الاجنبية:

- Ackoff, Russell L., Redesigning the Future: **A system Approach to Societal problems**, A wily- Interscience publication, John Wiley and Sons, New york, 1974.
- Bachman , Leonard R., **Integrated Buildings The Systems Basis Of Architecture**, Published by John Wiley & Sons, Inc., Hoboken, New Jersey, 2003.
- Banham, Reyner, **The Architecture of the Well-tempered Environment**, Architectural Press, London, 1969.
- Barton. Paul K., **Building Services Integration**, E & F. N. Spon, London, 1983.
- Burberry, Peter, **Distribution and Sizing**, in space for services. AJ, 5 March 1986. Architectural Press.
- Burberry, Peter, **Environment and Services**, Michel's Building Series, Halsted Press, New York, 1979.
- Davis, Colin, Lloyd's, **The Omniplatz, The Architectural Review**, No.1076, October, Architectural Press, 1986.
- Groak, Steven, **The Idea of Building**, E & F. N. Spon, London, 1992.

- Handler, Benjamin, **Systems Approach to Architecture**, American Elsevier publishing company, New York, 1970.
- Harbison, Robert, **Thirteen Ways.. Theoretical Investigation in Architecture**, MIT, press, Cambridge, 1997.
- Hawkes, Dean, **The Architectural Dimension, in Space for Services**, AJ, 26 February, Architectural Press. 1986.
- Jencks, Charles, **The Language of Post-Modern Architecture**, Fifth Edition, Academy Editions, London, 1987.
- Mason, John and Venning. Bob, **Structure and Services, Demands/options, in space for Services**, AJ, 12 March, Architectural Press. 1986.
- Maver , Thomas, **Building Service Design**, RIBA Press, London, 1971.
- Reising, Natasha, **Centre Georges Pompidou**, Internet Research, 2010. http://www.daapspace.daap.uc.edu%2F~larsongr%2FLarsonline%2FRogers_files%2FPiano-Pompid.pdf
- Rush, R.D., **The Building Integration handbook**, The American Institute of Architects, 1986.
- Simon, Herb, **Complexity of architecture in complex city**. Internet article, 2009. http://www.edge.architects.com/complex_city.htm

بهجت رشاد شاهين
علي مجبل العذاري
أسامة عبد المنعم خريبط

شكل (1) اتجاهات التمريرات الخدمية بشقيها العمودي والأفقي والتي تعتمد بشكل أساسي على نوع وطبيعة المبنى

المصدر: http://www3.hku.hk/mech/sbe/case_study/case/hk/hku-bsb/bsb-index.html

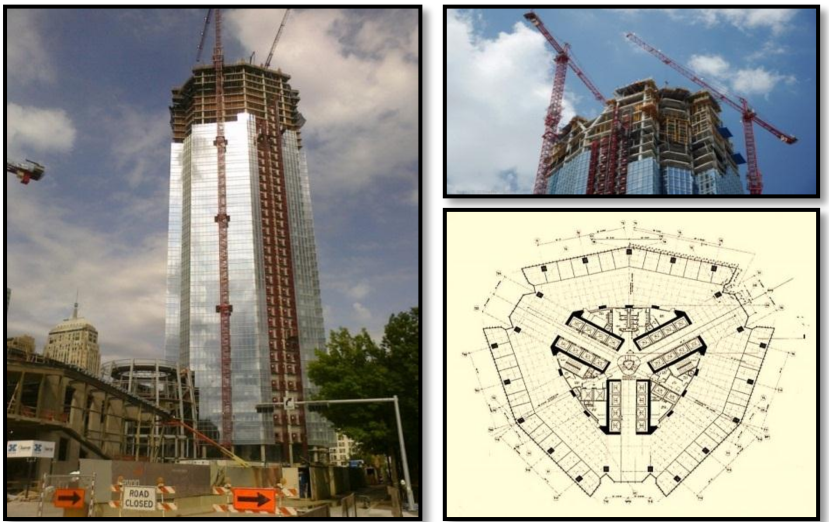

شكل (2) أهمية الـ(Core) في تسهيل التمريرات الخدمية في مبنى (Devon Tower) حيث تؤثر أنماط معينة من الأساليب المنشئية في سهولة التعامل مع المنظومة الخدمية

المصدر: http://media.photobucket.com/image/structural%20core%20building/gandjdunlap/DevonFloor.jpg

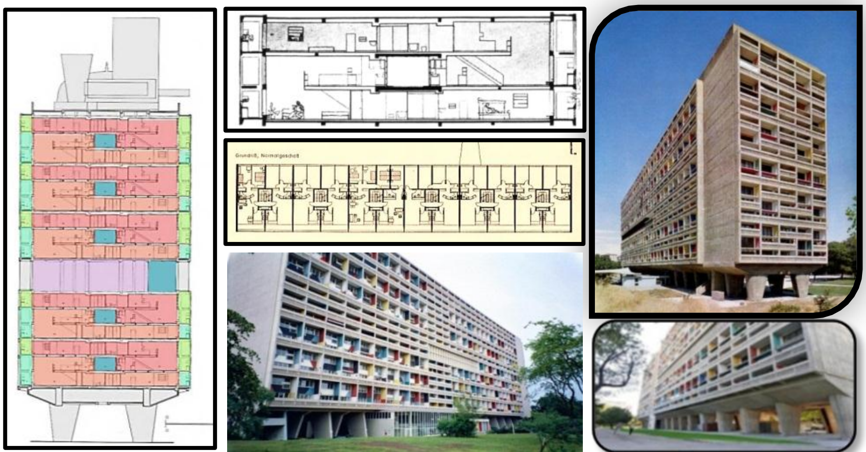

شكل (3) مبنى مرسيليا للمعمار (Le Corbusier)، حيث ان أجزاء من المنظومة الخدمية كانت دائماً تظهر

المصدر: http://ardourofthelayman.blogspot.com/2010_10_01_archive.htm

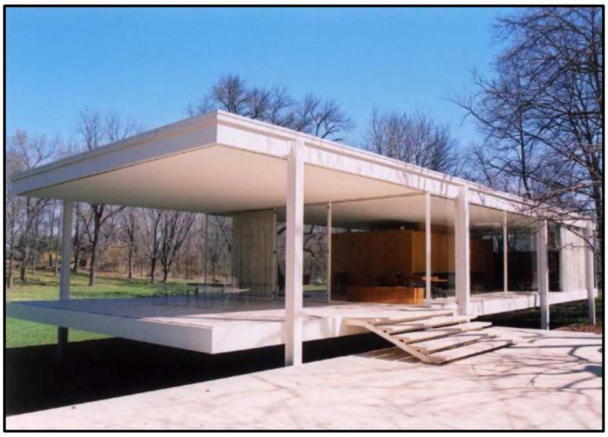

شكل (4) بيت Farnsworth للمعمار (Mies van der Rohe) الذي تميّز بالبساطة والشفافية وتشكيل فضاء مستمر لا تخترقه سوى الأعمدة المنشئية فضلاً عن كتلة مصممة تمثل الفضاءات الخدمية

المصدر: http://www.e-architect.co.uk/chicago/farnsworth_house.htm

شكل (5) تصميم البيت الزجاجي (glass house) للمعمار (philip johnson) ومدى اتسامه بالشفافية العالية والاختراق البصري

المصدر: http://www.ichalcarper.com/outdoor-design/philip-johnsons-glass-house

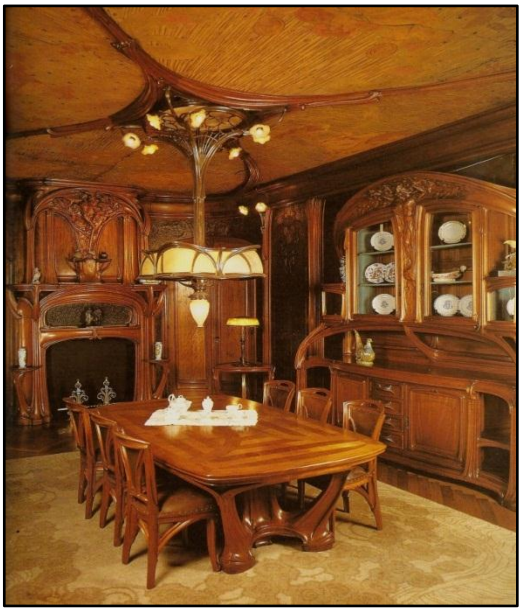

شكل (6) دخول عناصر الإنارة الصناعية إلى المجال المعماري في حركة (الفن الجديد–Art Nouveau) الذي يعد العامل البارز في التأثير الشكلي غير المباشر لمنظومة الخدمات

المصدر http://www.myajade.com/light-it-up/art-nouveau-lighting/

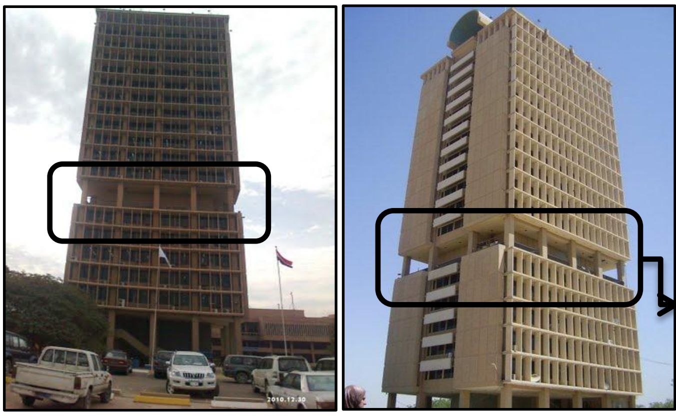

شكل (7) برج جامعة بغداد للمعمار (Walter Gropius) الذي يمثل التوجهات الشائعة في توقيع فضاءات المكائن الخدمية في المباني العمودية

يتبين وجود طابق خاص للخدمات. وذلك للأسباب الوظيفية والمنشئية والتعبيرية

المصدر: الباحث

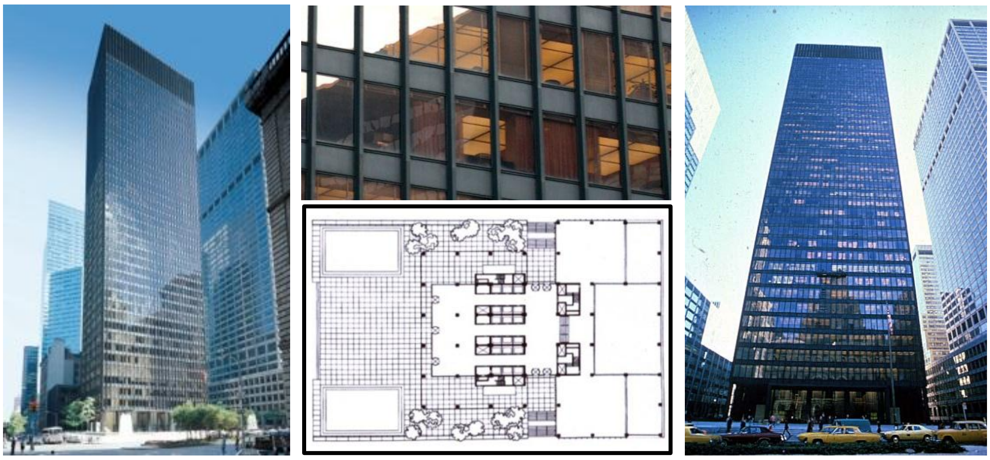

شكل (8) مبنى "سيكرام" للمعمار (Mies Van der Rohe) حيث كان السعي نحو تمييز فضاءات الخدمات عن السياق مع الملاءمة مع فكرة التمييز الوظيفي لعناصر المبنى

المصدر http://www.skyscraper.org/EXHIBITIONS/FAVORITES/fav_seagram.htm

شكل (9) منظومة الخدمات لمبنى اللويدز في لندن للمعمار (Richard Rogers)

المصدر: http://www.walklondon.com/london-attractions/lloyds-of-london.htm


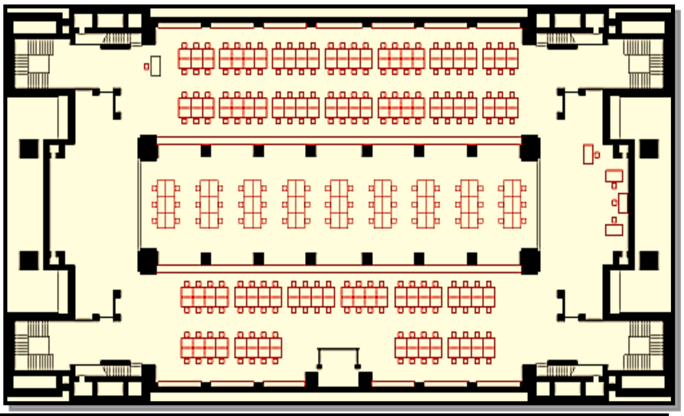

شكل (10) مبنى "شركة لاركن" للمعمار (Frank Lloyd Wright). وضع الخدمات في كتلة مستقلة بعيدًا عن فضاءات الموظفين

المصدر: http://www.carusostjohn.com/media/artscouncil/history/taylorist/index_02.html


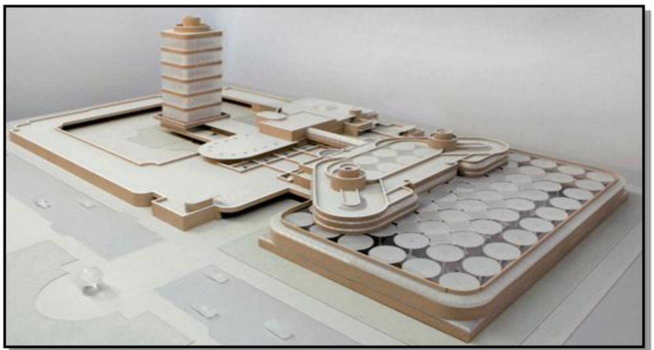

شكل (11) مبنى شركة جونسون للمعمار (Frank Lloyd Wright) 1947 وفكرة القلب الخرساني لوضع الخدمات وعناصر الحركة في قلب المبنى وترك الفضاء حوله حراً يمكن تقسيمه بأي شكل

المصدر:http://www.greatbuildings.com/cgi-bin/gbi.cgi/Johnson_Wax_Building.html/cid_johnson_wax_002.gbi

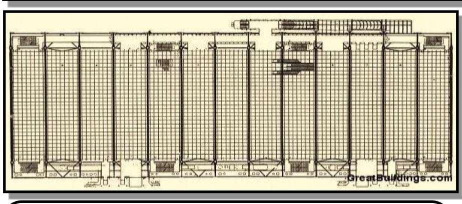

شكل (12) مبنى بومبيدو سنتر في باريس للمعماريّن (Richard Rogers) و (Renzo Piano)

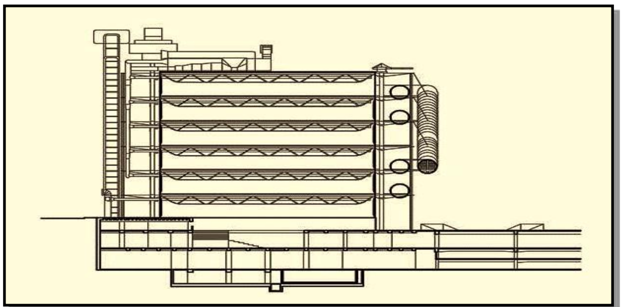

المصدر:http://web.france.com/places/centre_georges_pompidou_paris

شكل (13) منظومة الخدمات لمبنى بومبيدو سنتر في باريس للمعماريين (Richard Rogers) و(Renzo Piano)

المصدر: http://www.placesinparis.com/centre-pompidou/

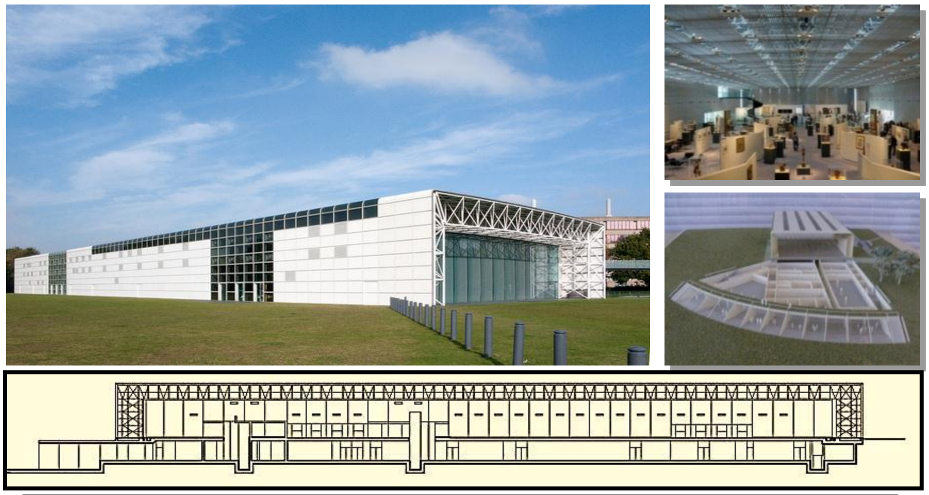

شكل (14) منظومة الشكل المعماري لمركز سنسبري للفنون البصرية/ في إنكلترا للمعمار (Norman Foster)

المصدر: http://www.flickr.com/photos/martinrp/323106894/sizes/z/in/photostream/

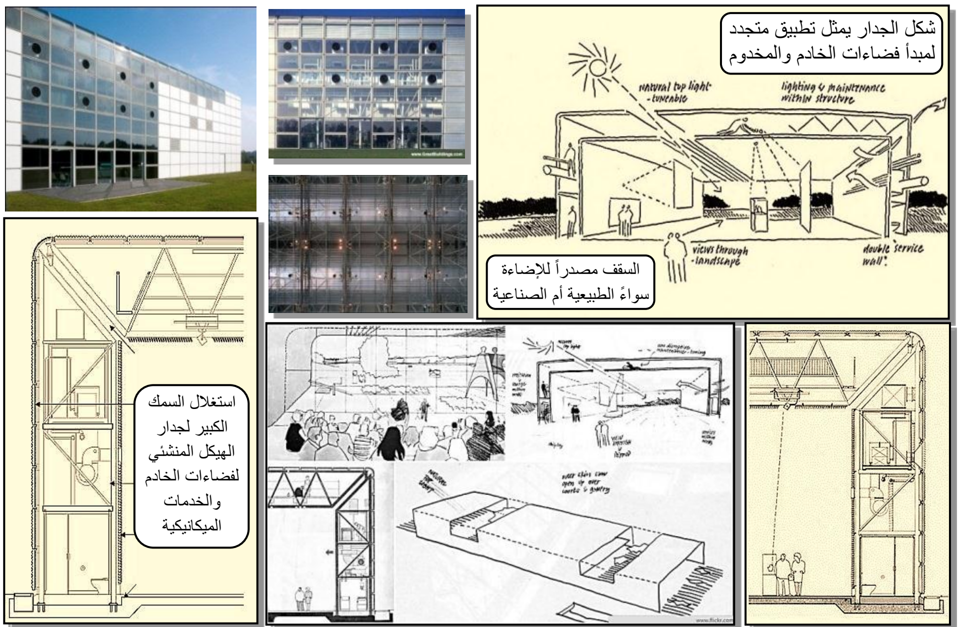

شكل (15) منظومة الخدمات لمركز سنسبري للفنون البصرية/ في إنكلترا للمعمار (Norman Foster)

المصدر: http://en.wikiarquitectura.com/index.php/Sainsbury_Center_for_Visual_Arts

تصنيع ودراسة اداء الاسطح الانتقائية المستخدمة في اللاقطات الشمسية المسطحة

د. طالب كشاش مرتضى
استاذ مساعد
قسم هندسة المكائن والمعدات
الجامعة التكنولوجية

د. قصي جهاد عبد الغفور
استاذ مساعد
قسم هندسة المكائن والمعدات
الجامعة التكنولوجية

زينب بهجة كريم

الخلاصة

في هذا البحث تم إجراء دراسة عملية لإختبار الأداء الحراري لأسطح إنتقائية تستخدم في المجمعات الشمسية لأساس من الحديد والحديد المغلون والألمنيوم المتوفر تجارياً، حيث تم عملياً طلاء العينات بطريقتين هما الطلاء الكهربائي والرش الكيميائي الحراري. وتمت مقارنة الأداء الحراري لهذه العينات مع عينة بدون طلاء وعينة أخرى مطلية بطلاء أسود و غير لامع متوفر تجاريا. بالنسبة لعينات الطلاء الكهربائي تم دراسة الأداء بتغيير عدة محددات وهي زمن التغطيس بحوض الطلاء، البعد بين القطبين, كثافة التيار الكهربائي ونسبة مساحة وجه واحد للعينة (الوجه الكبير للعينة) الى مساحة وجه واحد للقطب (الوجه الكبير لقطب النيكل). أما عينات الرش الكيميائي الحراري فقد تم طلائها بتغيير زمن الطلاء، ضغط غاز الترذيذ، البعد بين فتحة المرذذ وسطح العينة وكمية الجريان للمحلول المستخدم. بينت النتائج إن أفضل أداء ضمن عينات الحديد يعود للعينة التي تم طلاؤها بطبقتي طلاء, الأولى هي طبقة من الزنك بطلاءً كهربائياً حيث كان زمن الطلاء دقيقتين والثانية طبقة من النيكل الأسود وبزمن طلاء قدره (20) دقيقة وببعد بين القطبين (6 cm) وكثافة تيار ($0.15\ A/dm^2$) ونسبة مساحة وجه واحد للعينة الى مساحة وجه واحد للقطب تساوي (1). إذ بلغت نسبة الزيادة في الخزن الحراري لعينة الطلاء الكهربائي إلى عينة الحديد المغلون بدون طلاء عند بداية فحص اداء العينات (58.23%) وعند نهاية فحصها (44.97%).. بالنسبة لعينات الألمنيوم كان أفضل أداء (كمية الحرارة المخزونة) يعود لعينتين أحداهما عينة بطلاء كهربائي والاخرى عينة برش كيميائي حراري، حيث إن عينة الطلاء الكهربائي قد تم طلاؤها بالنيكل الأسود لمدة (20) دقيقة وبإستخدام تيار ذو كثافة ($0.15\ A/dm^2$) والبعد بين القطبين (6 cm) ونسبة مساحة وجه واحد للعينة الى مساحة وجه واحد للقطب تساوي (1). أما عينة الرش الكيميائي الحراري فقد تم طلاؤها بطبقة من النيكل الأسود عندما كان زمن الطلاء (16) ثانية، والبعد بين فتحة الخزان وسطح العينة (27 cm) و كمية الجريان (4.8 ml/min.) و ضغط غاز الترذيذ (1 bar) و درجة حرارة سطح العينة ($290\ ^0C$).

Manufacturing and Study the performance of Selective Surfaces that used in flat plate Solar Collectors

Talib k. murtadha
Asst. prof. dr.
University of Technology
Mechanical Engineering Department
talib_km@yahoo.com

Qussay jihad abdul ghafour
Asst. prof. dr.
University of Technology
Mechanical Engineering Department
kaisyqj@yahoo.com

Zainab bahjat kareem
zbahjat@yahoo.com

ABSTRACT

In this research an experimental study has done for testing the thermal performance of selective surfaces used in solar collectors for substrate of iron, galvanized iron and aluminum which are commercially available. The coating process for the samples has done in two ways, the electroplating and the chemical spray pyrolysis. The results of the thermal performance test of these samples are comparing with the thermal performance of a sample without paint and other paint with black paint without shines commercially available. For the electroplated samples, the performance study has done for different immersion time in plating bath, the distance between electrical poles, the current density, and area ratio of the sample plated area to the nickel pole face area. The chemical sprayed pyrolysis samples, study has done for different coating times, atomizing gas pressures, distance between the aperture of atomizer and the sample and the paint mass flow rate. The results showed that the best performance of the iron's samples is the sample which is coated with two layers. The first layer is of zinc done by electroplating where the time of plating is (2 min.) and the second layer is of black nickel done by electroplating, where the time is (20 min.), the distance between the poles is (6 cm), the current density is (0.15 A/dm^2) and area ratio of the sample plated area to the nickel pole face area is equal to (1). The percentage of the increasing in heat storage of electroplating sample to galvanized iron sample without paint at the beginning of testing the performance of samples and at the end were (58.23%& 44.97%) respectively. For aluminum samples, the best performance was regarded for two samples electroplating sample and chemical spray pyrolysis sample. The best electroplating sample was coated with a layer of black nickel where the time of plating is (20 min.), the distance between the poles is (6 cm), the current density is (0.15 A/dm^2) and area ratio of the sample plated area to the nickel pole face area is equal to (1). While the best chemical spray pyrolysis sample has been coated with a layer of black nickel where the time of plating is (16 sec.) and the distance between the aperture of the reservoir and the surface of the sample is (27 cm), the amount of flow is (4.8 ml / min.), the atomizing gas pressure is (1 bar) and temperature of the sample surface is (290 ^{0}C).

الكلمات الرئيسية:- المجمعات الشمسية، اللاقط المسطح، الاسطح الانتقائية، الطلاء الكهربائي، الرش الكيميائي الحراري.

المقدمة

تم إستخدام الطاقة الشمسية في مجالات شتى من ضمنها السخانات الشمسية ذات الأسطح المستوية التي هي عبارة عن مجمعات شمسية حرارية تقوم بتحويل الطاقة الشمسية الى طاقة حرارية، وهذه المجمعات إقتصادية وبسيطة في تصميمها ومتطلبات صيانتها، وإن الجزء الاهم لهذه المجمعات هو السطح المستوي الماص الذي يقوم بإمتصاص الأشعة الشمسية وتحويلها الى حرارة ونقلها الى مائع العمل. من أجل ذلك تم التوجه الى صناعة الأسطح الانتقائية والتي هي عبارة عن أسطح ماصة للأشعة الشمسية تكون قيمة الإمتصاصية (α) لها أعلى ما يمكن وقيمة الانبعاثية (ε) اقل ما يمكن.

عمد العديد من الباحثين الى تحسين اداء المجمعات الشمسية بطرق عديدة منها :-

1- طلاء السطح الماص بطرق مختلفة منها الطلاء الكهربائي والرش الكيميائي الحراري وغيرهما، ومن المهم مراعاة التصاقية الطلاء بالعينة ومدى مقاومته للظروف الجوية المختلفة.

2- تغيير شكل السطح الماص.

أجرى الباحثان **[Gogna & Chopra, 1979]** دراسة مفصلة عن التركيب والخواص البصرية والحرارية لسطح انتقائي من النيكل الاسود على اساس من الحديد المغلون وذلك باستخدام طريقة الطلاء الكهربائي وكانت محتويات الحوض ملح النيكل وملح الزنك وايونات الامونيوم وايونات الثايوسيانات. تم تغيير محددات الترسيب والتي تشمل الحامضية (ph = 4.5 – 6) ودرجة حرارة الحوض (Solution Temperature =(30-60)°C) وكثافة تيار (Current Density =(0.5-8) mA\cm^2) وذلك في محاولة لتحسين الخواص البصرية. الشكل (1) يوضح تغير الامتصاصية (α) والانبعاثية (ε) مع زمن التغطيس بالحوض وسمك الطلاء حيث نلاحظ ان بزيادة سمك الطلاء تزداد الامتصاصية بسرعة الى ان تصل الى قيمة التشبع (Saturation Value) وهي (α=0.95) والانبعاثية تزداد بصورة بطيئة لسمك يصل الى (0.41μm) وبعده تكون الزيادة سريعة، وتم الحصول على امتصاصية مقدارها (α=0.94) وانبعاثية قيمتها (ε=0.09) عندما كانت درجة حرارة الحوض (40°C) وحامضية المحلول (5.8) وكثافة التيار (3.5 mA\cm^2).

أجرى الباحثان **[Madhusudan & Sehgal, 1982]** دراسة عملية مفصلة عن التركيب والخواص البصرية والحرارية لسطح إنتقائي من النيكل الأسود على أساس من الحديد المغلون والألمنيوم المتوفرين تجاريا بإستخدام طريقة بسيطة وغير مكلفة هي طريقة الرش الكيميائي الحراري، وكانت مكونات محلول الرش هي الثايوريا ونترات النيكل. تم تغيير عدة محددات هي درجة حرارة سطح المسخن الكهربائي، وكمية الجريان، ونسبة الخلط للمحلول، وتم رسم الإمتصاصية (α) والإنبعاثية (ε) ونسبة الإمتصاصية الى الإنبعاثية (α/ε) بوصفها دالة مع سمك الطلاء كما هو موضح في الشكل (2). بينت النتائج أن أفضل إمتصاصية تم الحصول عليها هي (α=0.92) عندما كان سمك الطلاء (0.23 μm) والإنبعاثية ($\varepsilon_{100^{\circ}c}$=0.14) لأساس من الألمنيوم، وأن أفضل إمتصاصية تم الحصول عليها هي (α=0.90) لسمك الطلاء (0.25 μm) والإنبعاثية ($\varepsilon_{100^{\circ}c}$=0.13) لأساس من الحديد المغلون وذلك عندما كانت درجة حرارة سطح المسخن الكهربائي (290 °C) (±2 °C) ونسبة خلط المحلول (M/2 Nickel nitrate :M/2 Thiourea) هي (1 : 1.28).

قام الباحث **[John, 1994]** باستخدام الطلاء الكهربائي لترسيب طبقة من النحاس- النيكل الأسود باستخدام محلول الكتروليتي مكونا من كبريتات النيكل (Sulphate Nickel) (40g/l) و كبريتات النحاس (Copper Sulphate) (20g/l) و خلات الامونيوم (Ammonium Acetate) (15g/l). واجريت عملية الطلاء في محلول عند درجة حرارة (35°C) ومقدار حامضية

(ph=5.5) وتم تجهيز اقطاب جهاز الطلاء بتيار كهربائي كثافته ($4A/dm^2$) وزمن تغطيس (30) ثانية. أظهرت النتائج ان قيمة الامتصاصية للأشعة الشمسية (α) تصل إلى (0.98) والانبعاثية الحرارية (ε) تصل إلى (0.10).

قام الباحث **[Wackelgard, 1998]** بدراسة خصائص الطلاء الكهربائي للنيكل الأسود باستخدام محاليل تحتوي على كلوريد النيكل (Nickel Chlorine) وكلوريد الصوديوم(Sodium Chlorine) حيث تم الحصول على امتصاصية (α) قيمتها (0.96) وانبعاثية (ε) مقدارها (0.10). تم اختبار استقرارية الطلاء تحت ظروف رطوبة عالية وقد وجد أن الامتصاصية تتغير خلال الساعات الأولى من التعرض للرطوبة ولكنها بعد ذلك تستقر، ومن ذلك تم التوصل إلى أن طلاء النيكل الأسود مقاوم لدرجات الحرارة العالية والرطوبة.

مما سبق يتبين ان عملية صناعة الاسطح الانتقائية للاقطات الشمسية ذات الاسطح المستوية امر اساسي لتحسين الاداء، ويهدف البحث الحالي الى بناء منظومة تصنيع اسطح انتقائية لاساس من الحديد والحديد المغلون والالمنيوم المتوفر تجاريا بطريقتين هما الطلاء الكهربائي والرش الكيميائي الحراري وذلك باستخدام محاليل طلاء ذات تراكيز تختلف عن التراكيز المذكورة في البحوث السابقة.

الجانب العملي

1- منظومة الطلاء الكهربائي

أجزاء منظومة الطلاء الكهربائي المستخدمة موضحة بالشكل (3) وتتكون من الاجزاء التالية:

1- مجهز قدرة (Power supply) من النوع الرقمي (Digital) ذو مواصفات (30V) و(3A).
2- حوض (Bath) مصنوع من البلاستك اسطواني الشكل ذو قطر (17.8 cm) وارتفاع (18 cm).
3- أعمدة تثبيت مصنوعة من البلاستك لتثبيت كل من القطبين على الحوض.
4- أسلاك توصيل من النحاس.

إن مكونات حوض الطلاء بالنيكل الأسود موضحة بالجدول (1)**[وزارة الصناعة والتصنيع العسكري ،المعهد المتخصص للصناعات الهندسية، 1989]**. في البداية تم تحضير (2.5 l) من محلول الطلاء وذلك بخلط كل من كلوريد النيكل (Nickel chloride) وكلوريد الامونيوم (Ammonium chloride) وثايوسيانات الصوديوم (Sodium thiocyanate) مع كمية من الماء المقطر حيث إن كل مادة تخلط على حدة، أما كلوريد الزنك (Zinc chloride) يخلط مع كمية من الماء المقطر عند درجة حرارة ($40\ ^0C$) وبعد التأكد من ذوبان كل مادة جيدا بالماء تم خلطها معا وقيس الحجم وأضيف الماء المقطر لإكمال الحجم إلى (2.5 l). بعد ذلك بعدة ساعات قيست حامضية المحلول وكانت بحدود (ph=4.3).

2- منظومة الرش الكيميائي الحراري (Chemical Thermal Spray Pyrolysis)

تتألف منظومة الرش الكيميائي الحراري من عدة أجهزة بسيطة وهي المرذذ (atomizer) والمسخن الكهربائي والمزدوج الحراري والقارئ الرقمي لدرجة الحرارة وجهاز السيطرة على درجة الحرارة واسطوانة غاز النتروجين ومنظم للتحكم بضغط الغاز، رتبت كما في الشكل (4) بحيث يمكن الاستفادة منها في رش العينات، بالاضافة الى وجود مروحة لإزالة الأبخرة المتكونة من الرش، وإن أهم جزء في هذه المنظومة هو المرذذ الموضح بالشكل (5). صنع المرذذ محليا من الزجاج الاعتيادي، يحتوي على خزان اسطواني بسعة (110 ml) مفتوح من الأعلى بفتحة قطرها (4 cm) وإرتفاعه (9 cm) يوضع فيه المحلول المراد رشه، وهذا الخزان متصل من الأسفل بصمام الغرض منه التحكم بمقدار المحلول الساقط إلى أنبوبة شعرية قطرها (0.1cm)، تحيط هذه الأنبوبة غرفة زجاجية

منتفخة ذات شكل مخروطي مغلقة من جهة الصمام ومفتوحة من الأسفل بحيث تحيط بفتحة الأنبوبة الشعرية لتكون الفتحتان في النهاية بمستوى واحد، وتحتوي الغرفة الزجاجية على فتحة جانبية تسمح بمرور الغاز المضغوط داخلها والذي يعمل على خلخلة الضغط داخل الغرفة الزجاجية وبالتالي تحويل القطرة الساقطة من الأنبوبة الشعرية إلى رذاذ مخروطي الشكل بإتجاه العينة المراد ترسيب المحلول عليها، ومن العوامل المهمة التي يجب مراعاتها في تصميم المرذذ الدقة في أن تكون نهاية الأنبوبة الشعرية في منتصف نهاية الغرفة الزجاجية، وان يكون سطحها الداخلي خاليا من الخدوش أو التكسرات، ويثبت المرذذ على حامل معدني (Holder) يمكن التحكم من خلاله على ارتفاعه العمودي، ويثبت أيضا بالحامل ويكون في أسفل المرذذ قدح الغرض منه جمع قطرات المحلول المنسابة من المرذذ أثناء مدة التحكم بفتح وغلق الصمام.

3- تحضير المحلول المستخدم في جهاز الرش الكيميائي الحراري

لتحضير محلول الطلاء بالنيكل الاسود إستعملت مادتا نترات النيكل ($Ni(NO_3)_2$) وهي مادة على شكل مسحوق اخضر اللون وزنها الجزيئي (182.71 g/mol)، وكذلك مادة الثايوريا (NH_2SCNH_2) وهي مادة على شكل مسحوق أبيض اللون وزنها الجزيئي (76.12 g/mol). بنسبة خلط (M/2 Nickel nitrate :M/2 Thiourea) هي (1 : 1.28).

تم تحضير محلول الرش بدرجة حرارة الغرفة اذ مزج (2.2840 g) من نترات النيكل المذابة في (25 ml) من الماء المقطر مع(1.2179g) من الثايوريا المذابة في (32ml) من الماء المقطر. وللحصول على الوزن المراد إذابته للمادتين في أعلاه تم استعمال المعادلة (1) **[عوض و آخرون، 1982]**:

$$M = (W_t / M_{wt}).(1000/ V) \qquad (1)$$

حيث ان :

M: مولارية المادة (mol/l) .

M_{Wt}: الوزن الجزيئي للمادة (g/mol) .

V: حجم الماء المقطر الذي تمت فيه الاذابة (ml) .

W_t: الوزن المطلوب اذابته (g).

وبعد اكمال عملية الإذابة يترك المحلول المحضر لعدة ساعات، وبعدها يكون جاهزا لوضعه في خزان المرذذ.

4- طريقة الإختبار

بداية ربطت منظومة الطلاء وتم اخذ قطعة من النيكل وربطت بالقطب الموجب لمجهز الطاقة (.P.S) واما القطب السالب لجهاز (.P.S) فقد ربط بالعينة (النموذج المراد طلاءه). قسمت العينات الى ثلاث مجموعات رئيسية المجموعة الاولى كانت ذات مساحة مساوية تقريبا لمساحة الانود (القطب الموجب) والمجموعة الثانية ذات مساحة تقدر بضعف مساحة الانود والمجموعة الثالثة ذات مساحة تصل الى ثلاثة اضعاف مساحة الانود. اما البعد بين الانود والكاثود تم اخذه بحدود (6 cm) ومن ثم قلل الى (3 cm) وذلك لدراسة تأثير البعد بين الانود والكاثود على خواص الطلاء.

زمن الطلاء (زمن التغطيس بالحوض) هو (30) دقيقة **[وزارة الصناعة والتصنيع العسكري ،المعهد المتخصص للصناعات الهندسية، 1989]**، ولكن لدراسة تأثير هذا المتغير تم اختبار العينات لزمن تغطيس هو (40,30,20) دقيقة. أيضا تم دراسة تأثير تغير كثافة التيار وذلك للمجموعتين الثانية والثالثة فقط لعدم تجانس الطلاء في كليهما. بالنسبة لسبائك الألمنيوم تم دراسة تأثير تغير كل من كثافة التيار و زمن التغطيس والبعد بين الانود والكاثود. تم تغطيس جميع العينات بعد الانتهاء من طلائها بزيت

محركات الديزل وذلك لملء الفجوات التي من الممكن ان تكون قد تكونت وبذلك تعمل كطبقة حماية للطلاء**[وزارة الصناعة والتصنيع العسكري ،المعهد المتخصص للصناعات الهندسية، 1989].**

5- منظومة إختبار أداء العينات

لاختبار اداء العينات تم قياس درجة حرارة سطحها عند بدء تعريضها لاشعة الشمس وبعد تعريضها لاشعة الشمس بفترة زمنية وذلك لحساب كمية الحرارة المخزونة في كل عينة والمقارنة بينها وبين عينة بدون طلاء واخرى مطلية بطلاء اسود بدون لمعة وتم توجيه المنظومة باتجاه الجنوب. الشكل (6) يوضح المنظومة والتي تتكون من الاجزاء التالية:-

1- إطار حديدي مستطيل الشكل أبعاده (215x83 cm).

2- لوح خشبي أبعاده (190x83 cm).

3- عازل حراري أبعاده (200x93 cm).

4- أربعة قطع حديدية لتثبيت كل من اللوح الخشبي والعازل الحراري على الاطار الحديدي.

5- قاعدة حديدية وعددها (2) على شكل مقلوب حرف (T) تُربط مع الإطار الحديدي بحيث تسمح بحرية حركته حركة دورانية.

تم تثبيت العينات على السطح العازل بمادة لاصقة (السليكون)، وتم قياس درجة حرارة سطحها بعد مرور ساعة، حيث تم أخذ خمسة قراءات لكل عينة بدأ من الساعة (12:00) ظهرا وحتى ما يقارب (04:30) بعد الظهر وتم تقسيم العينات الى مجموعات والمقارنة فيما بينها من حيث كمية الحرارة المخزونة فيها بعد ذلك تم إختيار العينة الفضلى من كل مجموعة والمقارنة فيما بينها لمعرفة العينة الفضلى من حيث الاداء وتحديد ظروف الطلاء الامثل لتحسين اداء هذه العينات، ويوضح الشكل (7) العينات التي تم استخدامها وطريقة طلائها والمتغيرات التي تم استخدامها لكل طريقة طلاء، وتم اجراء (33) عملية فحص لجميع العينات.

أجهزة القياس المستخدمة

1- درجة الحرارة

لقياس درجة الحرارة الماء المراد اذابة **كلوريد الزنك** (Zinc chloride) **فيه** تم استخدام مزدوج حراري نوع (K) حيث تم ربطه بجهاز قياس درجة الحرارة (Digital thermometer) ذو قناتين كما هو موضح بالشكل(8). ومدى درجات الحرارة الممكن قياسها به يتراوح من (^{0}C 4-) الى (^{0}C 1200)، تم اجراء عملية معايرة له وذلك بوضع متحسس المزدوج الحراري في اناء يحتوي على ماء مقطر مع جريش الثلج فكانت قراءة المحرار الزئبقي (^{0}C 0.0) اما جهاز قياس درجة الحرارة (Digital thermometer) فكانت قراءته (^{0}C 2) ومن ثم سخن الماء الى درجة الغليان فكانت قراءة المحرار الزئبقي وجهاز قياس درجة الحرارة (Digital thermometer) (^{0}C 100).

من خلال النتائج تم الحصول على معادلة خطية (2)و(3) معتمدة على القراءتين في اعلاه :

$$y = a + bx \tag{2}$$

$$y = 2 + 0.98\,x \tag{3}$$

حيث ان:

a هي 2 وb هي 0.98. والشكل (8) يوضح مخطط المعايرة للمزدوج الحراري.

2- قياس الحامضية

تم قياس حامضية المحلول المستخدم في الطلاء الكهربائي بجهاز (ph meter) وذلك باخذ عينات من المحلول المستخدم لقياسها بهذا الجهاز كما هو موضح في الشكل (9). تمت معايرة جهاز (ph meter) وذلك بإستخدامه لقياس حامضية محلولين من المحاليل المنظمة (Buffer solutions) قيمة الحامضية لهما هي (4 و 6). بداية تم غسل متحسس الجهاز بالماء المقطر، وبعد ذلك تم تجفيفه حتى لا يؤثر على قيمة الحامضية للمحلول المطلوب فحصه، وضع متحسس الجهاز في وعاء يحتوي على المحلول المنظم الذي قيمة الحامضية له (4) وكانت قراءة الجهاز (4). بعد ذلك تم غسل المتحسس للجهاز بالماء المقطر واعيدت التجربة السابقة ولكن باستخدام المحلول المنظم الذي قيمة الحامضية له (6) وكانت قراءة الجهاز (6)، بعدها تم غسل متحسس الجهاز بالماء المقطر وذلك للمحافظة على نظافته. من ذلك يتضح أن قيمة الحامضية التي يقيسها جهاز (ph meter) هي القيمة الحقيقية لحامضية المحلول المطلوب فحصه.

3- قياس كتلة العينات

تم إستخدام ميزان حساس لقياس كتلة العينات ذو دقة قراءة (10^{-4} g)، وإن لهذا الميزان حيزاً مغلقاً مصنوعاً من البلاستك مبيناً في الشكل(10) وذلك لمنع دخول دقائق قد تكون موجودة في المحيط الخارجي ولمنع تيارات الهواء من الدخول والتأثير على قراءة الجهاز. هذا الحيز له بابان جانبيان وباب من الاعلى لإدخال العينة منه وإن أقصى وأقل كتلة يمكن قياسها به تصل إلى(220 g) و (0.0005 g) على التوالي، وهناك أيضاً فقاعة هوائية خلف الجهاز حيث تعتبر جزء من معايرة الجهاز، و يجب أن تبقى هذه الفقاعة في الوسط. بعد ذلك تم معايرة الجهاز بوضع عينة قياسية (معلومة الكتلة) كتلتها (200 g) على المنصة داخل الحيز المغلق واغلقت الأبواب، وبعد فترة كانت قراءة الجهاز(200 g). من ذلك يتضح أن القيمة التي يقرؤها الجهاز هي القيمة الحقيقية لكتلة العينة المطلوب فحصها.

4- معايرة جهاز قياس درجة حرارة سطح العينات

لقياس درجة حرارة سطح العينات تم استخدام الجهاز الموضح في الشكل (11) حيث تتراوح مدى درجات الحرارة الممكن قياسها به من ($-50\ ^0$C) الى ($700\ ^0$C) وكانت اسم الشركة المصنعة له (technoterm 5500)، وللتأكد من صحة قراءة الجهاز اجريت عملية المعايرة بوضع متحسس الجهاز في اناء يحتوي على ماء مقطر مع جريش الثلج فكانت قراءة المحرار الزئبقي(0.0^0C) اما جهاز قياس درجة الحرارة فكانت قراءته ($-1.9\ ^0$C) و من ثم سخن الماء الى درجة الغليان فكانت قراءة المحرار الزئبقي ($94\ ^0$C) و قراءة جهاز قياس درجة الحرارة ($98.3\ ^0$C).

من خلال النتائج تم الحصول على معادلة خطية(4)و(5) معتمدة على القراءتين اعلاه :

$$y = a + bx \tag{4}$$

$$y = -1.9 + (501/470)\,x \tag{5}$$

حيث ان:

a هي -1.9 و b هي (501/470) .

الشكل (11) يوضح مخطط المعايرة لجهاز قياس درجة حرارة سطح العينات.

<u>حساب النتائج</u>

1- معدل كمية الحرارة المخزونة في العينة

تم حساب كمية الحرارة المخزونة في العينات تبعاً للمعادلة التالية:

كمية الحرارة المخزونة في العينة = كمية الحرارة الساقطة على سطحها– كمية الحرارة المفقودة منها وكما في المعالتين (6)و (7) ادناه:

$$Q = Q_{solar} - Q_{Losses} \tag{6}$$

$$= Q_{solar} - (Q_{Conv.} + Q_{Rad.}) \tag{7}$$

ولكن بسبب تعذر قياس الاشعاع الشمسي والانبعاثية للسطح تم استخدام المعادلة (8) التالية:

$$Q = m.C.\Delta T/\Delta t \tag{8}$$

2- حساب نسب الزيادة في الخزن الحراري

$$\text{اكبر نسبة زيادة في الخزن الحراري عند بداية فحص اداء العنيات} = \left(\frac{\text{أكبركمية حرارة مخزونة في العينة – أكبركمية حرارة مخزونة في العينة بدون طلاء}}{\text{أكبركمية حرارة مخزونة في العينة}} \right) \times 100\% \tag{9}$$

$$\text{اصغر نسبة زيادة في الخزن الحراري عند نهاية فحص اداء العينات} = \left(\frac{\text{أقل كمية حرارة مخزونة في العينة – أقل كمية حرارة مخزونة في العينة بدون طلاء}}{\text{اقل كمية حرارة مخزونة في العينة}} \right) \times 100\% \tag{10}$$

<u>النتائج والمناقشة</u>

تم حساب كمية الحرارة المخزونة في عينات البحث ورسمها مع زمن قياس درجة حرارة سطحها، وتم بداية تقسيم العينات الى مجموعات والمقارنة فيما بينها من حيث كمية الحرارة المخزونة فيها بعد ذلك تم إختيار العينة الفضلى من كل مجموعة والمقارنة فيما بينها لمعرفة العينة الفضلى من حيث الاداء وتحديد ظروف الطلاء الامثل لتحسين اداء هذه العينات، وان ظروف طلاء كل عينة موضحة في الجدول (2). يبين الشكل (12) العلاقة بين كمية الحرارة المخزونة في عينات الحديد (1,2&3) والحديد المغلون (Black paint &Without paint) مع الزمن، وكما نلاحظ من الشكل ان هناك تقارباً في اداء عينات الحديد مما يدل على ان زمن الطلاء (سمك الطلاء) بالزنك والكروم لم يكن له تأثير كبير في اختلاف اداء هذه العينات عن بعضها البعض عند ثبوت زمن الطلاء بالنيكل الاسود (20) دقيقة. ان عينات الحديد سجلت ارتفاع في كمية الحرارة المخزونة فيها ومن ثم هبوطاً سريعاً في هذه الكمية مما يدل على ان قيمة الانبعاثية لها عالية مقارنة بقيمتها لعينات الحديد المغلون وقد يرجع ذلك الى وجود طبقة الكروم التي تم ترسيبها على عينات الحديد مما جعل قيمة كمية الحرارة المخزونة فيها اعلى، وان افضل اداء ضمن هذه المجموعة كان للعينة (1)، وإن القيمة السالبة لكمية الحرارة المخزونة في العينات كانت بسبب حدوث انخفاض في درجة حرارة سطحها.

الشكل (13) يوضح العلاقة بين كمية الحرارة المخزونة في العينات (1,11,35,51,Without paint& Black paint) مع الزمن، تم اختيار العينة الفضلى من حيث الاداء من مجموعات سابقة تبعا لتصنيف العينات مع عينة من الحديد المغلون بدون طلاء والمقارنة فيما بينها, وكما نلاحظ من الشكل ان افضل اداء كان للعينة (11) حيث سجلت اعلى كمية حرارة مخزونة فيها

وان هناك هبوطاً سريعاً في هذه الكمية مما يدل على ان قيمة الانبعاثية لها اعلى مما للعينات الاخرى. من ذلك يتبين ان افضل اداء لعينات الحديد بوصفها أسطحاً انتقائية هو بطلائها بطبقة من الزنك بطريقة الطلاء الكهربائي (وليس بطريقة الغلونة) ومن ثم طلائها بالنيكل الاسود بطريقة الطلاء الكهربائي ايضا. نلاحظ ايضا من الهبوط في كمية الحرارة المخزونة للعينات المذكورة سابقا ان قيمة الانبعاثية يمكن ان تكون متقاربة فيما بينها ولكن افضل اداء كان يعود للعينة (11) مما يدل على ان قيمة الامتصاصية لها اعلى منها في العينات الاخرى وهذا ما حسن من ادائها، وقد بلغت نسبة الزيادة في الخزن الحراري لهذه العينة (عينة الطلاء الكهربائي) إلى عينة الحديد المغلون بدون طلاء بداية فحص اداء العينات (58.23%) وعند نهاية فحصها (44.97%).. كما نلاحظ من الشكل (13) أن كلما كانت نسبة الاداء عند بداية الفحص أكبر ما يمكن هذا يعني أن اعلى كمية حرارة مخزونة في العينة (11) هو اكبر منها في العينة بدون طلاء اي ان ادائها في هذه الفترة جيد وهناك تحسن في اداء هذه العينة، وأن كلما كانت نسبة الاداء عند نهاية الفحص أقل ما يمكن هذا يعني أن كمية الحرارة المفقودة من العينة (11) أقل منها في العينة بدون طلاء.

الشكل (14) يوضح العلاقة بين كمية الحرارة المخزونة في عينات الالمنيوم (54,55,56,57, Without paint& Black paint) مع الزمن، وكما نلاحظ من الشكل ان افضل اداء كان للعينة (Without paint) حيث سجلت اعلى كمية حرارة مخزونة فيها مقارنة بالعينات الاخرى، وان هناك هبوطاً سريعاً في كمية الحرارة المخزونة في العينة (Black paint) مما يدل على ان قيمة الانبعاثية لها عالية مقارنة بالعينات المتبقية. نلاحظ ايضا ان هناك تقارباً في اداء العينات التي تم طلاؤها بالنيكل الاسود مما يدل على انه لم يكن لتغيير كثافة التيار تأثير كبير على اداء العينات بثبوت زمن الطلاء بالنيكل الاسود (30) دقيقة والبعد بين القطبين (3 cm).

الشكل (15) يوضح العلاقة بين كمية الحرارة المخزونة في عينات الالمنيوم (62,66, Without paint& Black paint) وبين الزمن من مجموعات سابقة تبعا لتصنيف العينات مع عينة من الالمنيوم بدون طلاء والمقارنة فيما بينها, نلاحظ ان افضل اداء كان للعينتين(62&66)، وأن هناك تقارباً شديداً في ادائهما. نلاحظ ايضا من الشكل في اعلاه ان كمية الحرارة المخزونة في العينتين (Black paint&Without paint) في البداية تكون اعلى من كمية الحرارة المخزونة في العينتين (62&66) ولكن بعد ذلك نلاحظ انحداراً سريعاً في كمية الحرارة المخزونة فيهما مما يدل على ان قيمة الانبعاثية لهما اعلى من قيمتها للعينتين (62&66) وهذا ما جعل اداء تلك العينتين أفضل من أداء العينتين الاخريين. من ذلك يتبين أن بالإمكان تحسين أداء عينات الالمنيوم بطريقتين هما اولا طريقة الطلاء الكهربائي وذلك بطلاء العينة من الالمنيوم بالنيكل الاسود لمدة (20) دقيقة باستخدام بعد بين القطبين (6 cm) وكثافة تيار مقداره ($0.15\ A/dm^2$). ثانيا طريقة الرش الكيميائي الحراري وذلك بطلاء العينة من الالمنيوم بالنيكل الاسود لمدة (16) ثانية والبعد بين فتحة المرذذ وسطح العينة (27 cm) وكمية الجريان (4.8 ml/min.) وضغط الغاز (1 bar) ودرجة حرارة سطح العينة ($290\ ^0C$).

الإستنتاجات

من خلال هذه الدراسة تم إستنتاج ما يأتي:-

1- إمكانية تحسين أداء عينات الحديد، حيث كانت أفضل عينة هي التي تم طلاؤها اولا بطبقة من الزنك طلاءً كهربائياً حيث كان زمن الطلاء دقيقتين وثانياً بطبقة من النيكل الأسود وزمن الطلاء كان (20) دقيقة والبعد بين القطبين (6 cm) وكثافة التيار ($0.15\ A/dm^2$) ونسبة مساحة وجه واحد للعينة الى مساحة وجه واحد للقطب تساوي (1)، إذ بلغت نسبة زيادة الخزن الحراري لعينة الطلاء الكهربائي الى عينة الحديد المغلون بدون طلاء عند بداية فحص اداء العينات (58.23%) وعند نهاية فحصها (44.97%).

د. طالب كشاش مرتضى
د. قصي جهاد عبد الغفور
زينب بهجة كريم

2- إمكانية تحسين أداء عينات الالمنيوم، حيث كان أفضل أداء (كمية الحرارة المخزونة) لعينات الالمنيوم يعود لعينتين تم طلاء احداهما بطريقة الكهربائي والثانية بطريقة الرش الكيميائي الحراري. حيث ان عينة الطلاء الكهربائي قد تم طلاؤها بالنيكل الاسود لمدة (20) دقيقة باستخدام كثافة تيار مقدارها ($0.15\ A/dm^2$) والبعد بين القطبين (6 cm) ونسبة مساحة وجه واحد للعينة الى مساحة وجه واحد للقطب تساوي (1)، وأما عينة الرش الكيميائي الحراري فقد تم طلاؤها بطبقة من النيكل الأسود عندما كان زمن الطلاء (16) ثانية، والبعد بين فتحة الخزان وسطح العينة (27 cm) و كمية الجريان (4.8 ml/min.) و ضغط الغاز (1 bar) و درجة حرارة سطح العينة ($290\ ^0C$).

3- أن العينات التي تم طلاؤها بطلاء اسود بدون لمعة (متوفر تجاريا) لها امتصاصية عالية وانبعاثية عالية ايضا حيث ان الانحدار السريع في كمية الحرارة المخزونة في العينة والموضح في الاشكال (13و 14 و15) تدل على ذلك.

المصادر

- P.K.Gogna and K.L.Chopra,"Structure – dependant thermal and optical properties of black nickel coatings",Thin Solid Film, 57(1979)299-302.
http://www.sciencedirect.com/science/article/pii/0040609079901676.

- M. Madhusudana and H.K. Sehgal ,"spray-deposited black nickel selective absorber surfaces for solar thermal conversion ", Applied 10(1982)65-74.
http://www.sciencedirect.com/science/article/pii/0306261982900605.

- هادي كاظم عوض، صالح محمد سعيد، جواد سلمان البدري، عبد الكريم هاشم الشلال، "الأساسيات النظرية للتحليل الكمي والوزني والحجمي للكيمياء التحليلية اللاعضوية "،مديرية دار الكتب للطباعة والنشر. الموصل (1982).

- وزارة الصناعة والتصنيع العسكري ،المعهد المتخصص للصناعات الهندسية ،"دليل الطلاء الكهربائي للمعادن" ،دائرة التعامل الكيمياوي ،بغداد (1989) .

- S. John , "Black nickel-copper solar selective coatings", spie digital library, proc.SPIE, vol.2255,(1994)137-148.
http://proceedings.spiedigitallibrary.org/proceeding.aspx?articleid=969218

-Wackelgard E. ,"Characterization of black nickel solar absorber coatings electroplated in a nickel chlorine aqueous solution ",Journal title , solar energy material and solar cells 56(1998) 35- 44.

http://www.sciencedirect.com/science/article/pii/S0927024898001135

الرموز المستخدمة

الرمز	المعنى	الوحدة
α	الامتصاصية	----
ε	الانبعاثية	----
T	درجة الحرارة	^oC
Q	كمية الحرارة المخزونة في العينة	kW

kg	كتلة العينة	m
$kJ/kg.^oC$	الحرارة النوعية لمعدن العينة	C
^oC	الفرق بين درجة حرارة سطح العينة في اي وقت ودرجة حرارة سطحها الابتدائية	ΔT
sec.	الفرق بين زمن فحص درجة حرارة سطح العينة في اي وقت وزمن فحص درجة حرارة سطحها الابتدائية	Δt

المصطلحات المستخدمة

المعنى	**المصطلح**
هو عملية طلاء العينة بطبقة من الزنك ومن ثم بالكروم طلاءا كهربائيا	التخميد
هو عملية طلاء العينة بطبقة من الزنك طلاءا كهربائيا	الاساس

جدول (1)

مكونات وظروف الطلاء بالنيكل الاسود

الكمية (g/L)	**المادة المستخدمة**
75	كلوريد النيكل ` $NiCl_2.6H_2O$
30	كلوريد الامونيوم NH_4Cl
30	كلوريد الزنك $ZnCl_2$
15	ثايوسيانات الصوديوم NaCNS
ظروف الطلاء	
5.5 – 3.5	درجة الحموضة PH
درجة حرارة الغرفة	درجة الحرارة
(A/dm^2) 0.15	كثافة التيار

د. طالب كشاش مرتضى
د. قصي جهاد عبد الغفور
زينب بهجة كريم

جدول (2)

مواصفات العينات التي تم طلاؤها

رقم العينة	نوعها	البعد بين القطبين في عملية الطلاء الكهربائي (cm)	كثافة التيار (A/dm^2)	زمن الطلاء بالنيكل الاسود (min.)
1	حديد (تخميد(2))	6	0.15	20
2	حديد (تخميد(4))	6	0.15	20
3	حديد (تخميد(8))	6	0.15	20
11	حديد (اساس(2))	6	0.15	20
35	حديد مغلون	3	0.15	30
54	المنيوم	3	0.15	30
55	المنيوم	3	0.25	30
56	المنيوم	3	0.35	30
57	المنيوم	3	0.45	30
62	المنيوم	6	0.15	20
رقم العينة	**نوعها**	**البعد بين العينة وفتحة خزان الجهاز في عملية الرش الكيميائي الحراري (cm)**	**زمن الرش (min. :sec.)**	**كمية الجريان لمحلول الرش (ml/min.)**
51	حديد مغلون	22	0:15	4.16
66	المنيوم	27	0:16	4.8

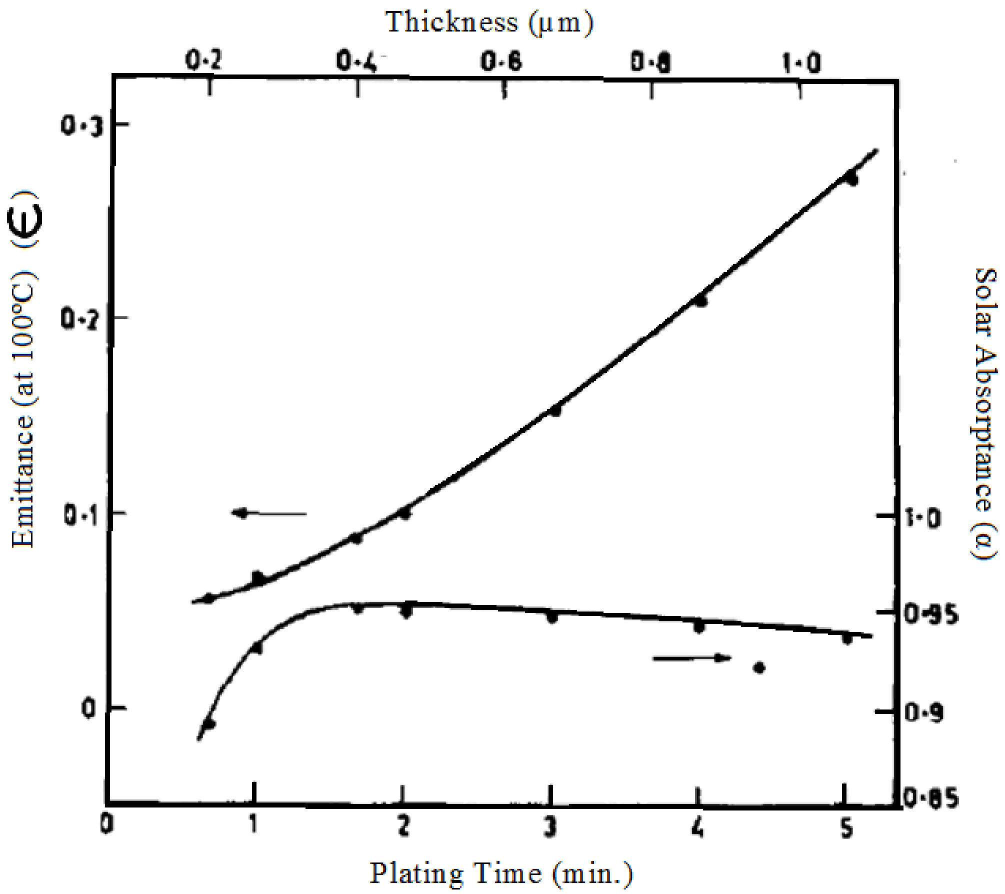

شكل(1): تغير الامتصاصية (α) والانبعاثية (ε) مع زمن التغطيس بالحوض وسمك الطلاء[Gogna & Chopra, 1979]

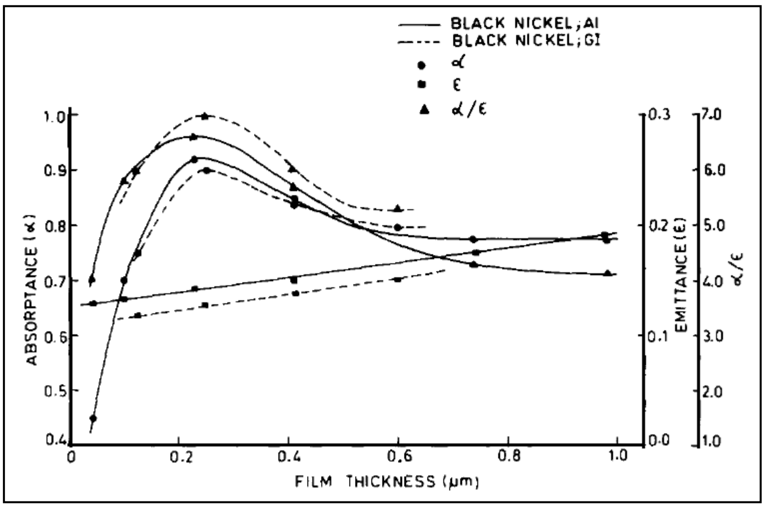

شكل (2): تغير الامتصاصية والانبعاثية ونسبة الامتصاصية الى الانبعاثية مع سمك الطلاء عند نسبة خلط (1 : 1.28)

ودرجة حرارة سطح المسخن الكهربائي (290 ℃)[Madhusudan & Sehgal, 1982]

د. طالب كشاش مرتضى
د. قصي جهاد عبد الغفور
زينب بهجة كريم

شكل (3): اجزاء منظومة الطلاء الكهربائي

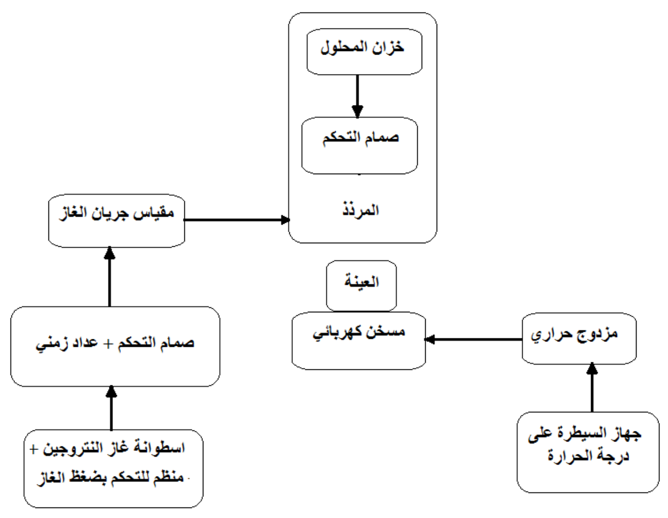

شكل (4): مراحل عمل منظومة الرش الكيميائي الحراري المستعملة في العمل الحالي مع صورة فوتوغرافية للمنظومة

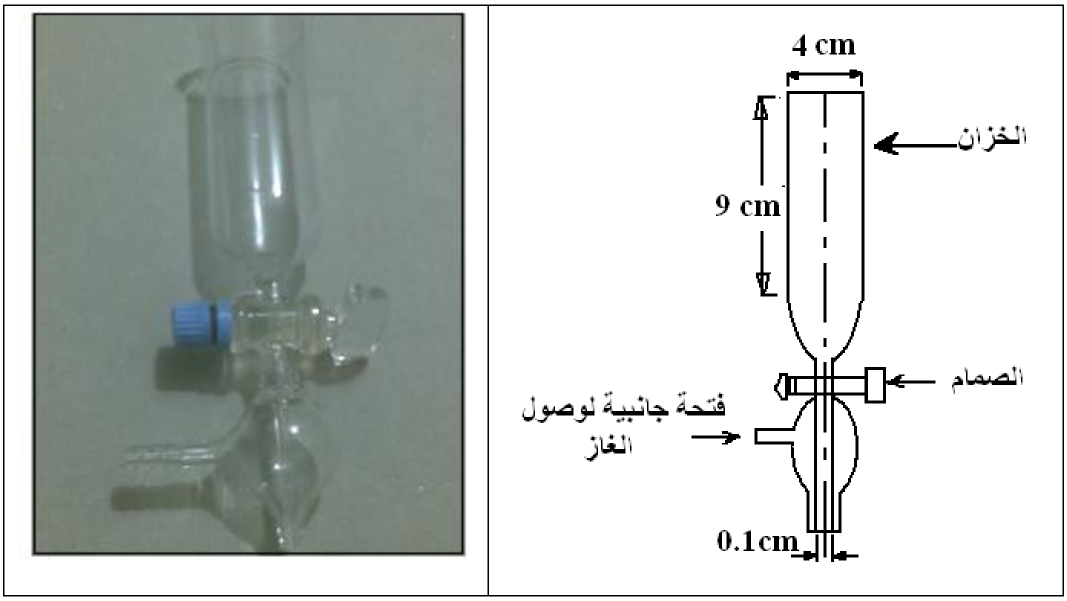

شكل (5): مخطط توضيحي للمرذذ مع صورة فوتوغرافية له

شكل (6): منظومة اختبار اداء العينات

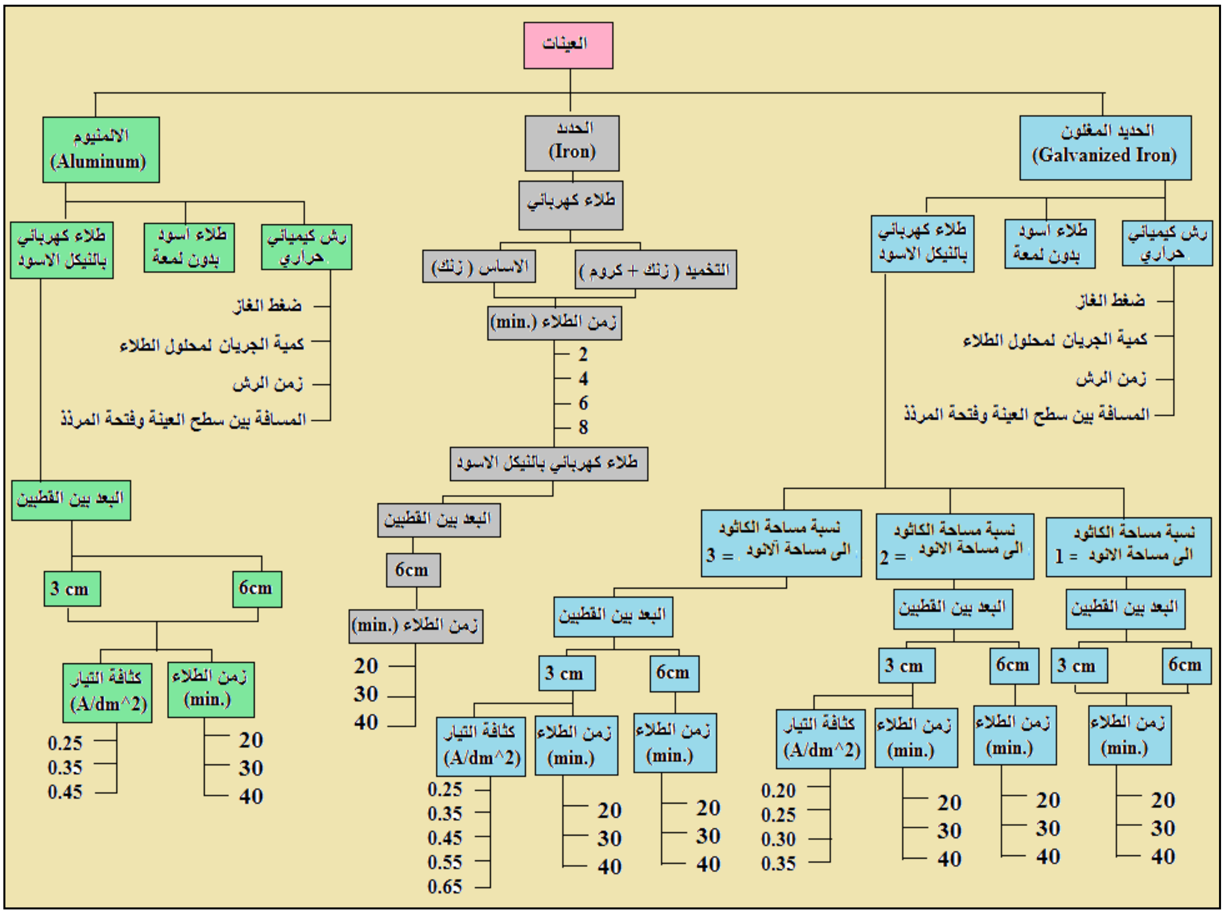

شكل (7): العينات التي تم استخدامها وطريقة طلائها والمتغيرات المستخدمة تبعا لكل طريقة طلاء

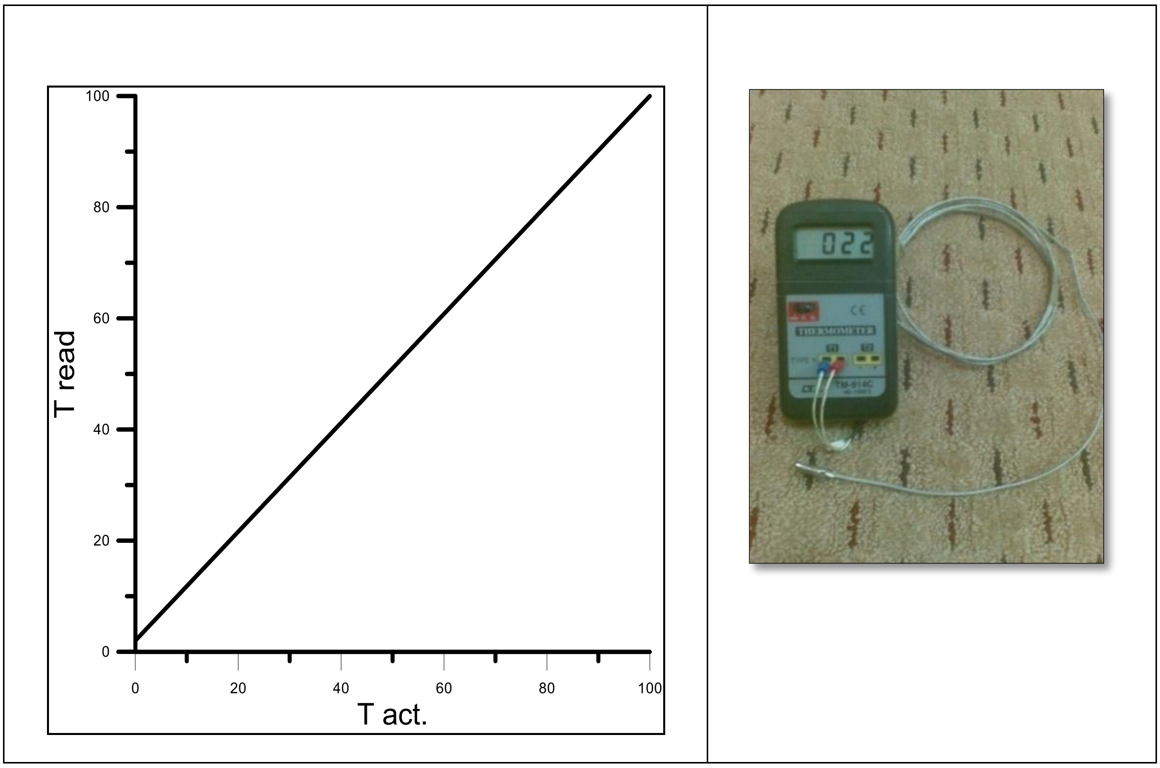

شكل (8): معايرة المزدوج الحراري مع صورة فوتوغرافية له بعد ربطه بجهاز قياس درجة الحرارة (Digital thermometer)

شكل (9): جهاز قياس الحامضية (ph meter)

شكل (10): ميزان حساس لقياس الكتلة

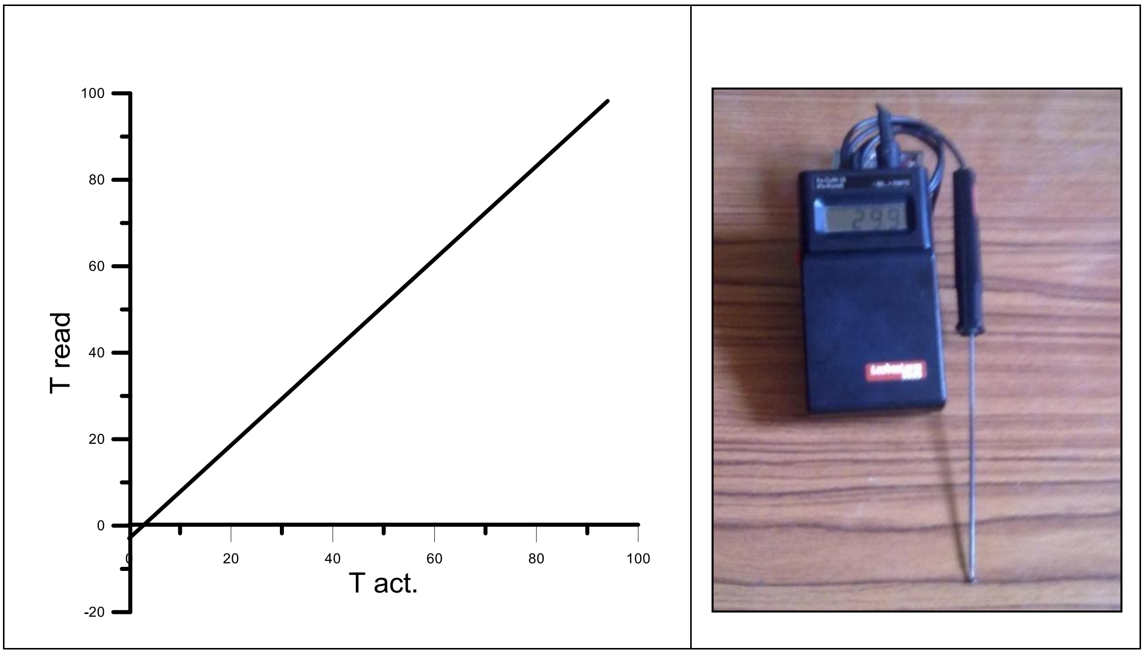

شكل (11): معايرة جهاز قياس درجة حرارة سطح العينات مع صورة فوتوغرافية له

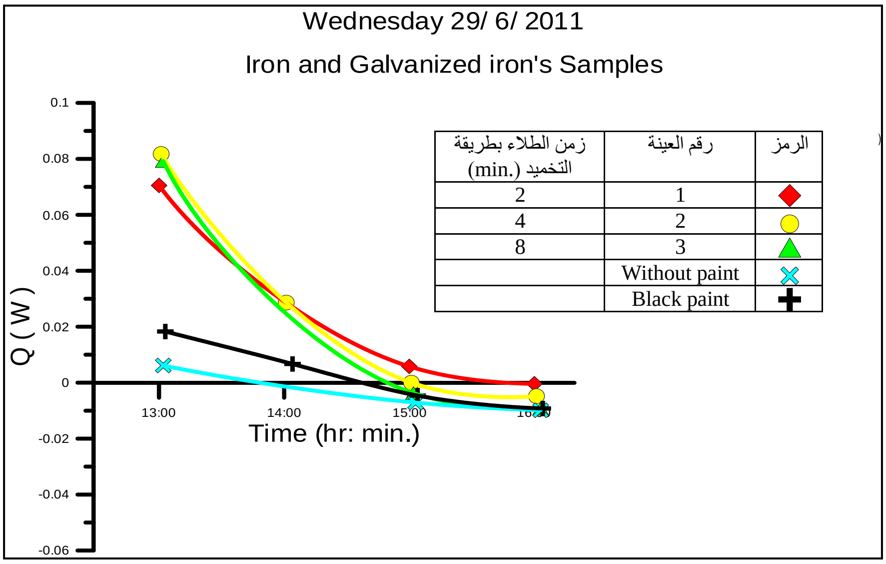

شكل (12): تغير كمية الحرارة المخزونة في عينات الطلاء الكهربائي (1,2&3) والعينتين (Black paint &Without paint) مع الزمن بثبوت زمن الطلاء بالنيكل الاسود (20) دقيقة وكثافة التيار (0.15 A/dm²) والبعد بين القطبين (6 cm)

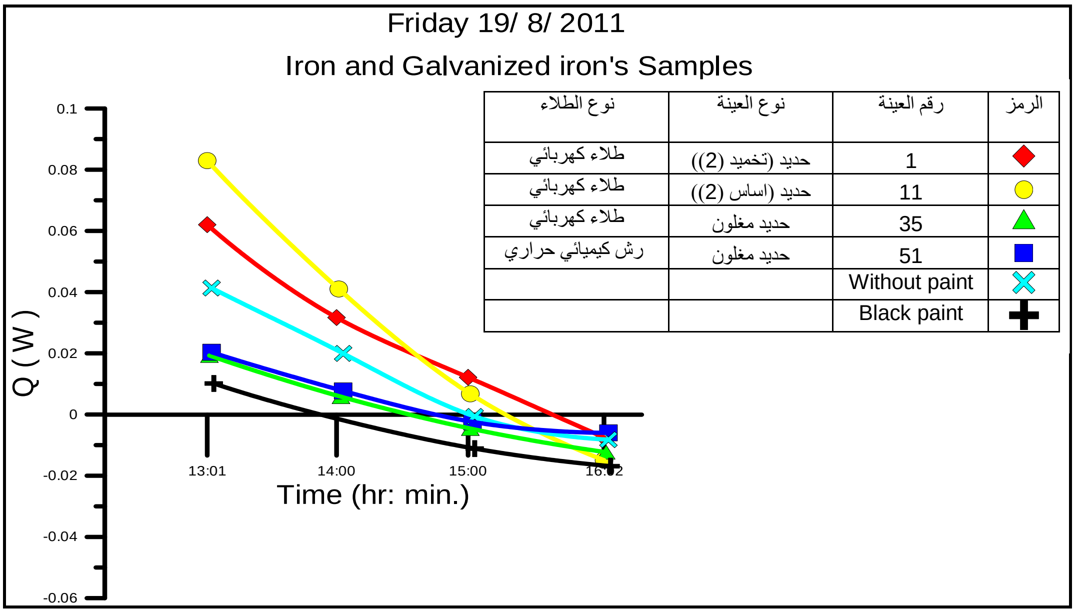

شكل (13): تغير كمية الحرارة المخزونة في العينات (1,11,35,51,Without paint& Black paint) مع الزمن

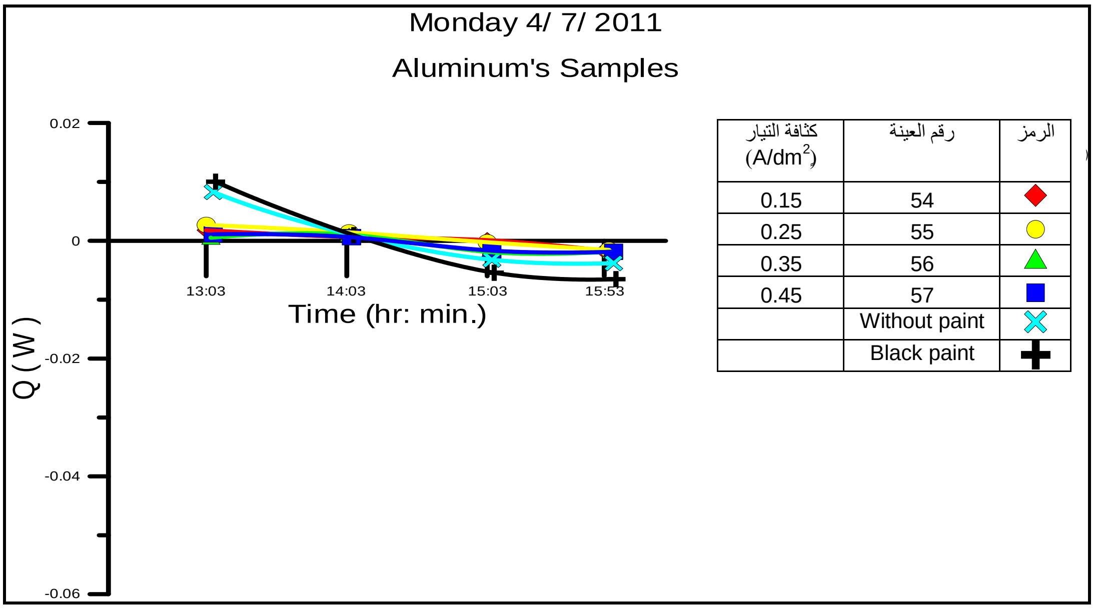

شكل (14): تغير كمية الحرارة المخزونة في عينات الطلاء الكهربائي (54,55,56&57) والعينتين (Black paint &Without paint) مع الزمن بثبوت زمن الطلاء بالنيكل الاسود (30) دقيقة والبعد بين القطبين (3cm)

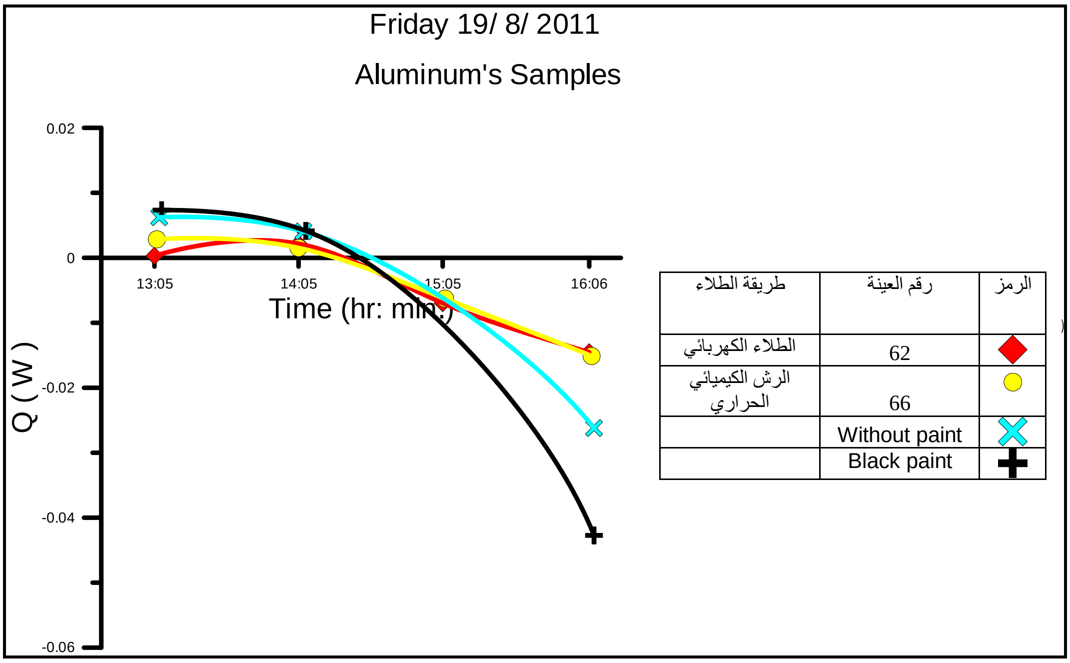

شكل (15): تغير كمية الحرارة المخزونة في العينات (62,66, **Without paint& Black paint**) مع الزمن